Overcoming Challenges in Reversible Addition–Fragmentation Chain Transfer Polymerization using Photoinduced Electron/Energy Transfer Catalysis

Jared G. Baker

Dissertation submitted to the faculty of the Virginia Polytechnic Institute and State University in partial fulfillment of the requirements for the degree of

Doctor of Philosophy
In
Chemistry

C. A. Figg, Committee Chair
J. B. Matson
M. D. Schulz
J. C. Worch

02/04/2026
Blacksburg, VA

Keywords: RAFT, PET-RAFT, Photocatalysis, SUMI, Blocking Order, Organogels, RDRP

Overcoming Challenges in Reversible Addition–Fragmentation Chain Transfer Polymerization using Photoinduced Electron/Energy Transfer Catalysis

Jared G. Baker

ABSTRACT

The development of polymerization methodologies is discussed, with an emphasis on addressing two limitations in reversible addition–fragmentation chain transfer (RAFT) polymerization. Both methods employ photoinduced electron/energy transfer (PET) catalysis to generate radicals within the polymerization system. PET catalysis was selected as the initiation pathway because the rate of radical introduction is tunable across a wide range of conditions, including, but not limited to, photocatalyst identity, photocatalyst concentration, wavelength of light, light intensity, and temperature.

The first limitation that is discussed is the incorporation of a single monomer unit at a defined position within the backbone of a polymer chain. Previously, a single monomer unit could be incorporated only at the beginning or end of a polymer chain in reversible-deactivation radical polymerization (RDRP), or otherwise, single units could undergo multiple incorporations. Using expansive condition screening with PET-RAFT polymerization, a set of conditions was identified that resulted in a single-unit monomer insertion (SUMI) within the polymer backbone. The reaction depended on polymer concentration, monomer concentration, and temperature, and resulted in no detectable double- or higher-order insertions.

The second limitation addressed was the blocking order requirements associated with both RAFT polymerization and RDRP. This limitation had previously been studied in the field, but it either exhibited termination reactions or applied only to specific systems. Using in-depth kinetic experiments and computational studies, we identified unique conditions that enabled us to overcome the blocking-order requirements associated with RDRP. Polymer and photocatalyst concentrations were crucial to the success of the reaction. Using this method, the impact of blocking order on material properties was evaluated and found to affect material behavior significantly. The method yielded a novel high-molecular-weight thermoplastic elastomer that retained its shape.

Expanding on the second method, we sought to maximize chain end fidelity and further elucidate the underlying rates of the technique. By coupling the development of new characterization methods to quantify rates within the system and extensive kinetic experiments, the ratio of the rate of trithiocarbonate activation to the rate of trithiocarbonate termination could be measured. By optimizing conditions to achieve a high ratio of trithiocarbonate activation to termination, a significant increase in chain end fidelity relative to the previously identified conditions was achieved and led to a deeper understanding of which conditions are vital to the method.

Lastly, the impact of PET-RAFT polymerization on the uniformity and properties of polymer networks is discussed. In this study, PET-RAFT polymerization yielded controlled networks initially, but could not yield controlled chain extended networks, resulting from decreased chain mobility in the networks. However, PET-RAFT polymerization enabled access to tunable properties, resulting in changes to the hydrophobicity and swelling ratios of the networks.

Overcoming Challenges in Reversible Addition–Fragmentation Chain Transfer Polymerization using Photoinduced Electron/Energy Transfer Catalysis

Jared G. Baker

GENERAL AUDIENCE ABSTRACT

The development of new polymerization techniques will be discussed, with an emphasis on addressing two limitations in the polymer chemistry community. Both methods employ light to overcome the existing limitations. Light was selected as the stimulus because the rate of the reaction can be tuned using a variety of different factors.

The first limitation discussed is the incorporation of a single functional group into the polymer chain to mimic biological systems. Previously, a single functional group could be placed only at the beginning or end of a polymer, or multiple functional groups were incorporated, limiting our ability to mimic biological systems. By exploring a variety of factors including temperature, light source, and dilution, a set of conditions was identified that resulted in a single functional group being included in the polymer chain. The reaction resulted in only single incorporations, and no double- or higher-order insertions were detected. This method brings us one step closer to mimicking biological systems.

Inspired by our first polymerization technique, the second limitation addressed was the order in which different monomers could be polymerized. This limitation prevents the formation of different polymer sequences, thereby reducing the range of accessible properties. This limitation had previously been studied in the field, but could be applied only in specific cases, thereby limiting the accessible sequences still. Using computational studies and exploring the reaction landscape, we identified conditions that enabled us to overcome the order in which monomers are polymerized. Temperature, polymer, and light conditions were found to be crucial to the success of the reaction. Using this method, the effect of monomer order on polymer properties was evaluated and found to be significant. With this method, new polymer sequences, and thus new polymer properties, can be accessed.

Expanding on the second method, we focused on further understanding the mechanism and rates of the reaction. A new characterization technique was developed to quantify the rates of the reaction to help understand the mechanism through extensive screenings. The ratio of polymer chains started to polymer chains finished prematurely was elucidated. The elucidated ratio significantly increased our understanding of the mechanism and the rates of the reaction. This study further enhances the number of new polymer sequences that can be accessed.

Lastly, the impact of light-initiated polymerizations on the uniformity of polymer networks, such as contact lenses, is discussed. Light-initiated polymerizations were found to yield homogeneous starting gels, but could not yield homogeneous gels after the initial polymerization. Further polymerization led to heterogeneous networks, but enabled properties of the gels to be tuned, including how much the gels could swell in water.

Acknowledgements:

I would first like to thank my mentor, Dr. Adrian Figg, for shaping me into not only the scientist, but the person that I have become over the past 5 years. I will forever be grateful that you took a chance on me and allowed me to be your first graduate student. None of this dissertation would have been possible without your all-encompassing support over the years, and thank you for everything you've done for me, especially all of the times you went above and beyond what was expected.

Next, I would like to thank my groupmates (Stephen, Ian, Darwin, Joey, Morgan, and Mikayla) for always being a confidant and friend; we all know that working together has made graduate school much more enjoyable. Also, thank you all for being great lab mates and for inspiring the scientific creativity in our group.

I want to thank my committee members: Dr. John Matson, Dr. Michael Schulz, Dr. Josh Worch, and Dr. James Tanko. Thank you for always making time for me and for taking an interest in my research and my scientific success.

Thank you to my family for all of their support over the past 5 years and for encouraging me to pursue my interests in science from an early age. Specifically, thank you, Mom and Dad, for always being there for me and for being my biggest supporters.

Lastly, I want to thank Amanda for dealing with me day in and day out on this journey and for always encouraging me to focus on the positives. I can't imagine having gone through these 5 years without you by my side, and I owe a lot of my success to your constant encouragement and support.

Contributions:
Chapter 1: JGB wrote the initial paper draft, edited and revised the draft, and developed the concept of the paper. JG edited and revised the draft and developed figures for the paper. CAF edited and revised the draft, developed the concept of the paper, administered the project, and provided supervision.

Chapter 2: JGB wrote and edited the chapter. CAF edited and revised the chapter.

Chapter 3: JGB conducted the data collection and data curation, formal analysis, and wrote and revised the draft. RZ conducted data collection for the SUMI condition screening and chain extensions. CAF edited and revised the draft, developed the concept of the paper, administered the project, funded the project, and provided supervision and insight.

Chapter 4: JGB conducted the data collection and data curation, conceptualized the project, conducted formal analysis, and wrote, edited, and revised the draft. SJK conducted data collection for testing different activation pathways and revised the draft. KJW conducted the density functional theory calculations for the paper. DT conducted and oversaw the density functional theory calculations for the paper and provided insight into the mechanism of the tertiary amine. JG conducted data collection for the polymerization method without tertiary amine present including catalyst loading experiments. ICA conducted data collection for the polymerization with tertiary amine present including tertiary amine and catalyst loading experiments. DCG conducted data collection for testing different activation pathways including macroCTA concentration experiments. CAF conceptualized the project, funded the project, provided insight and data analysis, edited and revised the draft, and oversaw the experimental work.

Chapter 5: MG and JGB contributed equally to this manuscript about authorship. MG conducted the data collection and data curation, conducted formal analysis, wrote, edited, revised the draft, and developed Python scripts for data curation. JGB conducted the data collection and data curation, conducted formal analysis, wrote, edited, and revised the draft, and conceptualized the project. SJK conducted the density functional theory calculations for the paper, conducted data collection and curation, conceptualized the project, and developed HPLC methods for the project. CAF provided insight and data analysis, edited and revised the draft, funded the project, and oversaw the experimental work.

Chapter 6: ZB and JGB contributed equally to this manuscript about authorship. ZB conducted the data collection and curation, conducted formal analysis, and wrote, edited, and revised the draft. JGB conducted the data collection and curation, conducted formal analysis, and wrote, edited, and revised the draft. MJH conducted data collection and formal analysis for the daughter gels. JDN conducted data collection and formal analysis for the swelling experiments. MG conducted data collection and formal analysis for the parent gels. NT conducted data collection and formal analysis for the degraded gels. JW conducted data collection and formal analysis for the rheology experiments. CAF

conceptualized the project, conducted data curation and formal analysis, administered the project, supervised the experimental work, and edited and revised the draft.

Chapter 7: JGB wrote, edited, and revised the chapter. CAF edited and revised the chapter.

Table of contents:

List of Figures:

List of Tables:

List of Abbreviations:

RDRP	Reversible-deactivation radical polymerization
ATRP	Atom transfer radical polymerization
RAFT	Reversible addition–fragmentation chain transfer
PC	Photocatalyst
PCRP	Photocatalyzed radical polymerizations
PET	Photoinduced electron/energy transfer
ARGET	Activator regenerated by electron transfer
ICAR	Initiators for continuous activator regeneration
ED	Electron donor
CTA	Chain transfer agent
TCT	thiocarbonylthioyl
STEM	Structurally tailored and engineered macromolecular
DMAc	*N*,*N*-dimethylacetamide
SEC	Size-exclusion chromatography
RI	Refractive index
BDE	Bond dissociation energy
UHMW	Ultra-high molecular weight
DFT	Density functional theory
SUMI	Single-unit monomer insertion
NMR	Nuclear magnetic resonance
PheoA	Pheophorbide a
ROMP	Ring-opening metathesis polymerization
PMA	Poly(methyl acrylate)
BVE	Benzyl vinyl ether
DTPA	2-(dodecylthiocarbonothioylthio) propionic acid
AH	Anilinium hypophosphite
2-ClEVE	2-chloroethyl vinyl ether
n-BuVE	*n*-butyl vinyl ether
Iso-BuVE	*Iso*-butyl vinyl ether
DEGVE	Di(ethylene glycol) vinyl ether
MALDI-TOF MS	Matrix assisted laser desorption/ionization time-of-flight mass spectrometry
MA	Methyl acrylate
TTC	Trithiocarbonate
PMMA	Poly(methyl methacrylate)
TPE	Thermoplastic elastomer
HMW	High molecular weight
MMA	Methyl methacrylate
TEOA	Triethanolamine
PDMA	Poly(*N*,*N*-dimethylacrylamide)
M_n	Number average molecular weight
$Đ$	Dispersity
BTPA	2-(butylthiocarbonothioylthio)propanoic acid
HPLC	High-performance liquid chromatography
TEA	Triethylamine

PMDTA	*N*,*N*,*N'*,*N''*,*N''*-pentamethyldiethylenetriamine
HMTETA	1,1,4,7,10,10-hexamethyltriethylenetetramine
Me_6TREN	Tris[2-(dimethylamino)ethyl]amine
TEMED	*N*,*N*,*N'*,*N'*-tetramethylethylenediamine
MALS	Multi-angle light scattering
DMA	*N*,*N*-dimethylacrylamide
DP	Degree of polymerization
DSDA	Disulfide-based diacrylate
G'	Storage modulus
G"	Loss modulus
DTT	Dithiothreitol

Chapter 1: Leveraging Reactivity to Gain Precise Control over Macromolecular Structures with Photocatalysis in Reversible-Deactivation Radical Polymerizations*

Authors: Jared G. Baker, Joey Gloriod, and C. Adrian Figg

1.1 Abstract

Photocatalysis has gained a prominent role in reversible-deactivation radical polymerization (RDRP) techniques. Photocatalyzed polymerizations are appealing due to ease of implementation, oxygen tolerance, spatiotemporal and orthogonal control, and increased uniformity in polymer chain ends compared to exogenous initiation. Due to these attractive features, photocatalysis has been widely used and incorporated into atom transfer radical polymerization (ATRP) and reversible addition–fragmentation chain transfer (RAFT) polymerization. Herein, recent examples of photocatalysis in RDRP techniques at the macroscopic, topological, and primary sequence levels of control are presented to highlight how photocatalysis has led to advances at all levels of polymer chemistry. For example, photocatalysis can be used for the selective photoactivation of distinct end-groups, enabling the synthesis of sequence-defined oligomers/polymers, or complex polymer topologies. However, there are still significant gaps in photocatalyzed RDRP (e.g., kinetic understanding of photocatalyst (PC) interplay with different chain ends, PC development, and effects of reaction conditions on PC performance). By identifying how photocatalysis and reaction conditions can be tuned to mediate polymerization kinetics and selectivity, more defined and controlled polymer sequences, topologies, and macroscopic properties will be unlocked.

*Adapted and reproduced with permission from *Chem. Sci.* **2025**, *16*, 15298-15309.

1.2 Introduction

The first report of photocatalysis was published almost 50 years ago by Kellogg and coworkers.[17] However, a resurgence in this field has occurred over the past 15 years, driven by the synthetic ease and tunability of photophysical properties of catalysts, resulting in diverse photocatalyst (PC) derivatives.[18] Photocatalysis is widely used in synthetic transformations, with over 35 applicable organic/metal-centered catalysts being used.[18–20] Photocatalysis has been widely adopted to facilitate previously difficult transformations such as hydrogen atom transfer reactions,[21–23] carbon–heteroatom bond formations,[24–26] carbon–carbon bond formations,[27–29] amine α-functionalization,[30–32] and enantioselective transformations.[33–35] The adoption of photocatalysis in small molecule chemistry has led to significant advances in drug discovery and synthetic methodology.[36–38] Although photocatalysis has made a lasting impact on small molecule transformations, photocatalyzed reactions have also been used in method development for polymer synthesis.

Light and photocatalysis have been used in polymer chemistry since the beginning of the 21st century, but significantly fewer PCs have been employed in photocatalyzed radical polymerizations (PCRP) compared to in small molecule transformations.[39–41] Despite differences in PC development, implementing light and photocatalysis in polymerizations has been shown at all levels of polymer synthesis, from the macroscopic scale down to the primary sequence.[39] Using light in polymer chemistry has led to advances in 3D printing,[42–44] surface coatings,[45,46] self-healing properties,[47,48] syntheses of copolymer architectures,[49–51] and sequence-defined polymers.[11,15]

Reversible-deactivation radical polymerization (RDRP) techniques have seen widespread implementation of photocatalysis with atom transfer radical polymerization (ATRP),[52] first reported in 2012 by Hawker and coworkers,[53] and with reversible addition–fragmentation chain transfer (RAFT) polymerization,[54] first reported in 2014 by Boyer and coworkers.[55] There are various types of photocatalyzed ATRP—photoinduced electron/ energy transfer (PET) ATRP, photoinduced organocatalyzed ATRP, metal-free ATRP, etc.—which we will refer to collectively as photocatalyzed ATRP throughout this perspective. For RAFT polymerization, only PET-RAFT polymerizations will be highlighted, as the mechanism is distinct from photoiniferter[56] and photoRAFT (which requires the degradation of a photoinitiator to introduce radicals).[57] Readers interested in photoiniferter and/or photoinduced ATRP are referred to recent reviews/ perspectives on these mechanisms.[56,58] Photocatalyzed ATRP and PET-RAFT polymerizations enable oxygen tolerant polymerizations,[59–61] higher chain-end fidelity,[62] and more uniform polymer end groups compared to RAFT polymerizations using exogenous initiators,[41,57] leading to facile polymer synthesis with fewer polymer chain end defects. Photocatalysis can be performed with low-energy red, near IR, or white light as opposed to more energy-intensive routes, such as heat or UV/ blue light.[63–66] Herein, the advantages, disadvantages, and limitations of PCRPs will be discussed by highlighting the uses and innovations of photocatalysis in polymer chemistry at the macroscopic, topological, and primary sequence levels. Subsequently, by focusing future efforts on the less-understood aspects of PCRPs (tailoring PCs to target selective photoactivation, interplay of PCs and other reaction conditions, and PC derivatization/development),[67–69] PCRPs will provide access to defined,

complex topologies and sequences to parallel the significant advances that photocatalysis has afforded for small molecule synthesis.

1.3 Polymerization Methods

Photocatalyzed ATRP and PET-RAFT polymerizations provide reaction tunability according to catalyst and incident wavelength of light, leading to straightforward ways to gain spatiotemporal control and selective photoactivation. Additionally, in PET-RAFT polymerization, a PC introduces a new mechanism for control: activation–deactivation of the chain end by the PC.

1.3.1 ATRP

Transition metal-mediated RDRP was introduced in 1995.[70–72] Specifically, the Matyjaszewski group introduced ATRP using copper as a transition metal catalyst.[73,74] ATRP is governed by the equilibrium between dormant and active chains, which is mediated by a transition-metal catalyst, typically a Cu(I) species (**Figure 1.1A**).[52] The catalyst can cleave a carbon–halogen (or pseudo–halogen) bond, leading to the formation of a Cu(II)X species and an active radical on the chain end that can propagate with monomer in solution. The active chain end can be reversibly deactivated back to a dormant species by reducing the Cu(II)X species, forming a (pseudo-) halogen chain end, and restoring the Cu(I) catalyst. ATRP controls the growth of most chains through the ATRP equilibrium, which limits the fraction of dead chains to a small fraction of total chains in the system, leading to a controlled polymerization.[75] Using photocatalysis in ATRP allows for lower Cu loadings (in addition to non-photocatalyzed methods, including activator regenerated by electron transfer (ARGET),[76] initiators for continuous activator

regeneration (ICAR),[77] and photoinduced ATRP),[78–81] providing down to ppb levels of Cu or entirely replacing Cu with a PC.

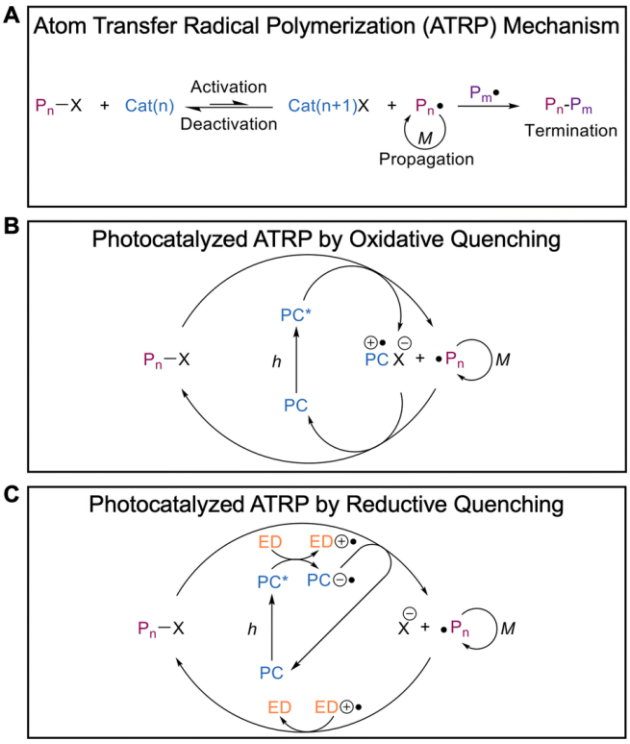

Figure 1.1. A) General mechanism of atom transfer radical polymerization (ATRP) highlighting mechanistic steps of control, where X can be a halogen or a pseudo-halogen. B) General mechanism of photocatalyzed ATRP through the oxidative quenching pathway (PC = photocatalyst). C) General mechanism of photocatalyzed ATRP through the reductive quenching pathway (ED = electron donor).[52]

Photocatalyzed ATRP, first reported by the Hawker group,[53] is compatible with both metal-centered PCs[8] and organic PCs.[82,83] Within photocatalyzed ATRP, the activation–deactivation cycle of chains can proceed through either an oxidative- or reductive quenching cycle, with both proceeding through electron transfer (**Figure 1.1B and C**).[41,84] Although the chemistry on the chain end remains the same in both instances, the activation mechanisms vary. In the oxidative-quenching pathway, the excited PC directly reduces the alkyl halide to activate the chain end, which can then propagate with monomer in solution (**Figure 1.1B**). The resultant radical cation PC oxidizes the chain end

and deactivates it, completing the catalytic cycle. In the reductive quenching pathway, the excited PC is initially reduced by a sacrificial electron donor (ED)—commonly an amine—and the radical anion PC reduces the alkyl halide to activate the chain end (**Figure 1.1C**). Activating the chain end restores the PC to the ground state through oxidation. Separately, the radical cation ED oxidizes the active chain end to complete the catalytic cycle, yielding the alkyl halide. Although photocatalyzed ATRP can proceed through two mechanistic pathways, both yield the same polymers. A variety of different PCs have been employed in ATRP including, but not limited to, phenothiazines,[85] phenoxazines,[86] dihydrophenazines,[83] xanthene dyes,[87,88] perylene,[82] $Ir(ppy)_3$,[53] and porphyrins.[89]

1.3.2 RAFT Polymerization

RAFT polymerization was first introduced in 1998 by Rizzardo, Moad, and Thang.[90] Prior to RAFT polymerization, photoiniferter mediated by xanthates had been used in the 1980s.[91–93] RAFT polymerization is governed by a degenerative chain transfer process instituted by the presence of a chain transfer agent (CTA).[54] CTAs containing a thiocarbonylthioyl (TCT) group can be xanthates, dithiocarbamates, dithiobenzoates, or trithiocarbonates. In a typical RAFT polymerization, radicals are introduced by exogenous compounds such as azo initiators (**Figure 1.2A**, initiation step).[54] After the initiator undergoes addition to monomer, the carbon-centered radical chain end will add to a C=S bond in the TCT and cleave the R-group, initiating a new chain (**Figure 1.2A**, pre-equilibrium step). Once all R-groups have been initiated and added to monomer (re-initiation step), degenerative chain transfer between CTAs and active chain ends ensues, resulting in a controlled polymerization (**Figure 1.2A**, main equilibrium step).

Degenerative chain transfer is how control is garnered in RAFT polymerization, as the process readily activates and deactivates chain ends.[94]

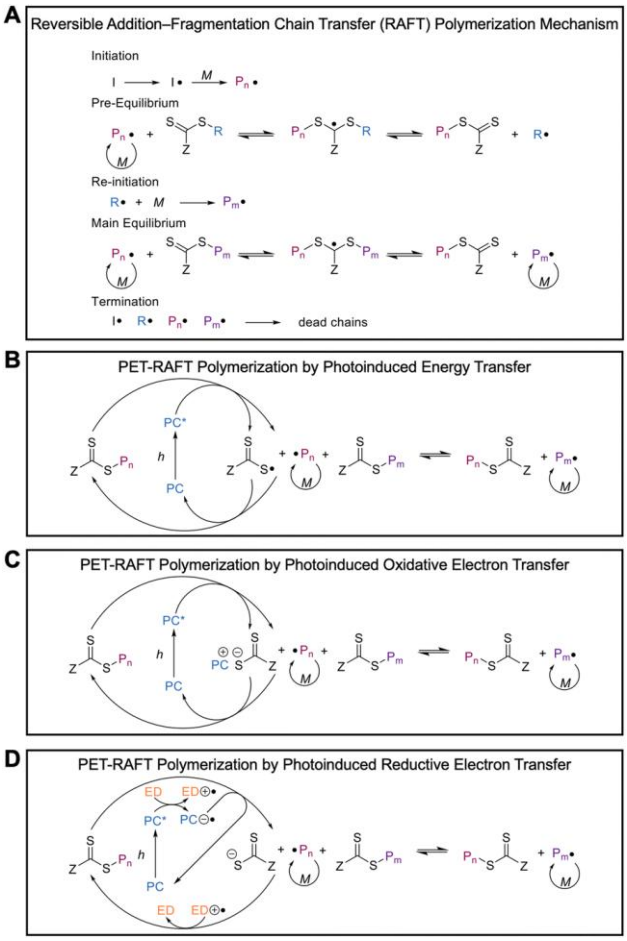

Figure 1.2. A) General mechanism of reversible addition–fragmentation chain transfer (RAFT) polymerization highlighting mechanistic steps for control. B) General mechanism of photoinduced electron/energy transfer (PET) RAFT polymerization through the photoinduced energy transfer pathway (PC = photocatalyst). C) General mechanism of PET-RAFT polymerization through the photoinduced oxidative electron transfer pathway. D) General mechanism of PET-RAFT polymerization through the photoinduced reductive electron transfer pathway (ED = electron donor).

PET-RAFT polymerization, first reported by the Boyer group,[55,66,95–97] has been performed with metal-centered PCs and organic PCs. Photocontrolled interconversion of radical and cationic polymerization methods using PCs has been shown using RAFT polymerization from the Fors group.[10,98,99] PET-RAFT polymerization is unique, as the

activation–deactivation of chains can occur through three pathways: photoinduced energy transfer, photoinduced oxidative electron transfer, or photoinduced reductive electron transfer (**Figure 1.2B–D**).[100] Photoinduced energy transfer most often occurs with metal-centered catalysts in which the excited PC releases photothermal energy upon relaxation, resulting in homolytic cleavage of the R-group C–S bond on the TCT (**Figure 1.2B**). The homolytic cleavage results in a carbon-centered radical on the chain end and a sulfur-centered radical on the TCT. The chain ends are deactivated through reversible combination or through chain transfer. In photoinduced oxidative electron transfer, the excited PC reduces the TCT, resulting in an oxidized PC, anionic TCT, and a carbon-centered radical on the chain end (**Figure 1.2C**). In photoinduced reductive electron transfer, the excited PC is first reduced by an ED—typically a tertiary amine—and the reduced PC is oxidized by the TCT, resulting in a neutral PC, oxidized ED, anionic TCT, and a carbon-centered radical on the chain end (**Figure 1.2D**). Deactivation of the chain end can occur through degenerative chain transfer, but regeneration of the PC must occur through electron transfer to close the catalytic cycle.

All three mechanisms will result in the same polymeric material being synthesized. A variety of PCs have been employed in PET-RAFT polymerization including, but not limited to, $Ir(ppy)_3$,[9,61] porphyrins,[95,101] $Ru(bpy)_3$,[59] xanthene dyes,[102,103] and photoactive proteins.[104]

1.4 PCRP innovation on the macroscopic level

Spatiotemporal control with oxygen tolerance can be achieved by using PCRPs,[1] leading to PCRP use in various applications including 3D printing and surface patterning. PET-RAFT polymerization is used for the synthesis of 3D and 4D materials due to fast

reaction times, oxygen tolerance, and spatiotemporal control (**Figure 1.3A**).[1,2,105] A 4D material is when a 3D material undergoes a transformation in response to an external stimuli (e.g., light, pH, temperature) over time.[3] Another advantage of using PCRP for 3D and 4D materials is that prints can be chemically modified after the initial polymerization. Due to the retention of chain ends, chain extensions can be performed to modify material properties, while selectively retaining or changing the overall shape of the initial print.[2–4,106] Jin and coworkers used PCRPs to synthesize 3D materials and transform them into 4D materials by using light as an external stimulus to induce bending, changing the print shape (**Figure 1.3B**).[2] Retaining chain ends also aids in the synthesis and expansion of structurally tailored and engineered macromolecular (STEM) gel networks. The chain ends enable modification of physical properties and self-healing networks by introducing additional monomer(s) (**Figure 1.3C**).[4,107–109] We have previously demonstrated network expansion and physical property modifications using PCRPs. This work resulted in 1.5× larger organogels compared to the starting gels, impacting swelling properties in N,N-dimethylacetamide (DMAc) and water (**Figure 1.3D**).[4] Network expansion of STEM gels can be performed through other light-mediated methods such as photoiniferter.[110–112] However, without a PC, the polymerization requires degassing and UV or blue light, while PCRPs can be performed at longer wavelengths of light without degassing.

Spatiotemporally controlled PCRPs have been used for surface-initiated polymerizations.[5–7,113–119] Patterning surfaces is integral for the fabrication of electronics,[120] microarrays of cells,[121] sensors,[122] and photonic crystals.[123,124] Surface-initiated polymerizations previously could be performed with thermal or redox initiators with limited spatial control, but light-mediated/initiated or photocatalyzed polymerizations

lead to significantly better control over surface patterning.[125] PCRP development led to the synthesis of patterns and gradients on surfaces using photomasks, where only selected areas are irradiated to induce polymerization (**Figure 1.4A and B**).[6]

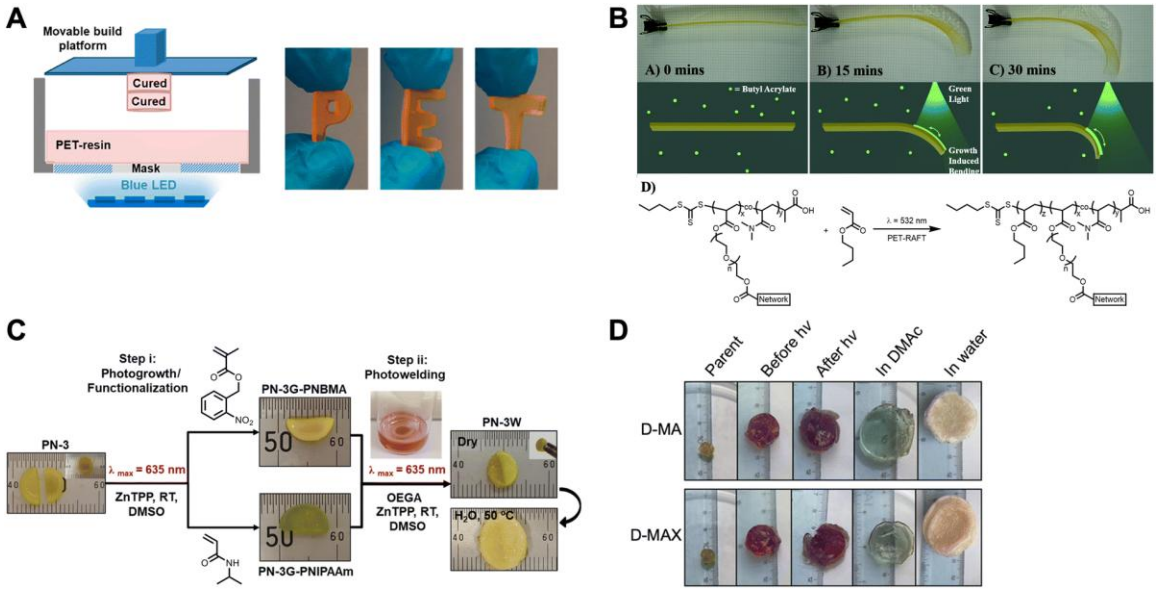

Figure 1.3. A) Bottom-up digital light processing 3D printer and images of letters printed using photoinduced electron/energy transfer reversible addition–fragmentation chain transfer (PET-RAFT) polymerization. Reproduced with permission from ref. [1]. Copyright 2020, American Chemical Society. B) Growth-induced bending of a 4D printed material using PET-RAFT polymerization. Reproduced with permission from ref. [2]. Copyright 2020, Royal Society of Chemistry. (C) Photogrowth and photowelding of polymer networks using PET-RAFT polymerization. Reproduced with permission from ref. [3]. Copyright 2021, American Chemical Society. (D) Photogrowth of polymer networks to change materials properties using PET-RAFT polymerization. Reproduced with permission from ref. [4]. Copyright 2024, Royal Society of Chemistry.

Selectively irradiating and polymerizing regions of interest introduces complex multi-layer 3D pattern synthesis[5] with micron length scale resolution,[126] which were inaccessible using RDRP before light-mediated/ photocatalyzed polymerizations. Spatiotemporally controlled surface patterning has led to surface modifications for materials with antifouling (**Figure 1.4C**),[7,118] antifogging,[127] self-healing properties,[128] and the development of reusable heterogeneous catalysts.[129] Overall, PCRPs have led to

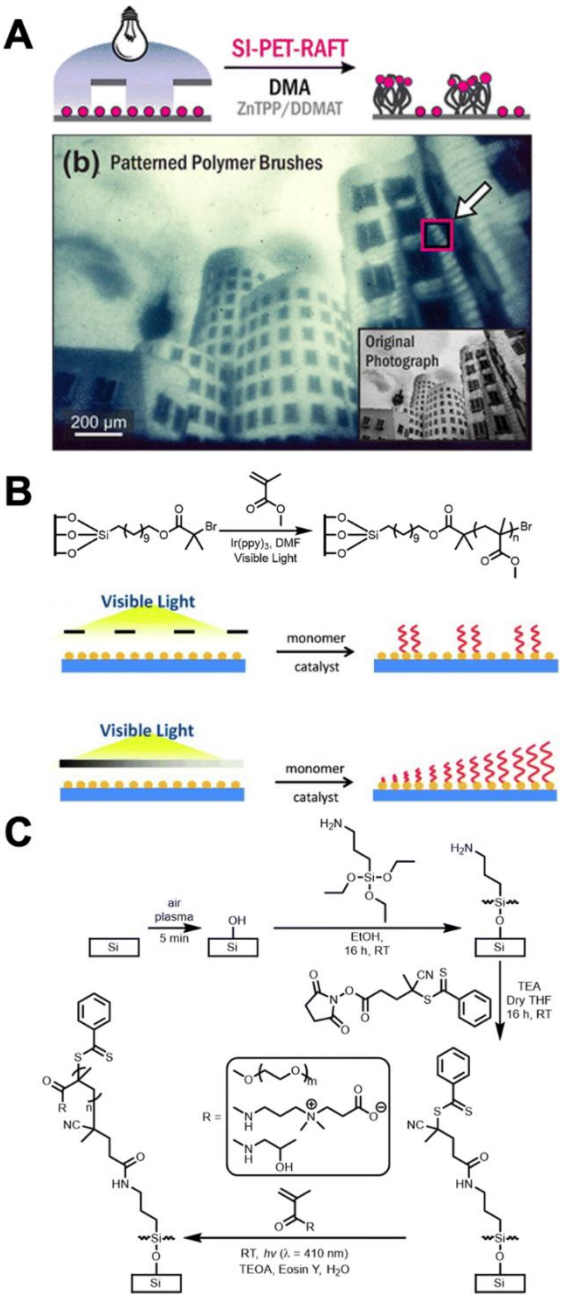

Figure 1.4. A) Schematic of surface-initiated polymerizations using photomasks and an optical micrograph using photoinduced electron/energy transfer reversible addition–fragmentation chain transfer (PET-RAFT) polymerization. Reproduced with permission from ref. [5]. Copyright 2019, American Chemical Society. B) Schematic for performing surface-initiated polymerizations using photomasks or neutral density filters using photocatalyzed atom transfer radical polymerization (ATRP). Reproduced with permission from ref. [6]. Copyright 2013, Wiley Online Library. C) Synthetic scheme for the surface-initiated PET-RAFT polymerization of antimicrobial polymers on silicon surfaces for antifouling applications. Reproduced with permission from ref. [7]. Copyright 2020, American Chemical Society.

advances in polymer synthesis at the macroscopic scale by enabling the modification of print/gel material properties and multi-layer surface patterning.

1.5 PCRP innovation on the topological level

Controlling polymer topology is important because it ultimately dictates the physical properties and applications.[130] PCRPs can be used to synthesize homopolymers, statistical, gradient, and block copolymers,[55,63,83,131] with polymer architectures including linear, star, brush, or hyperbranched structures.[132–136] Although these polymers can be synthesized through non-photocatalyzed RDRP techniques, photocatalysis provides high chain end fidelity and more uniform chains compared to those prepared by exogenous initiators.[55,137]

Light-mediated photoiniferter polymerizations and PCRPs lead to better uniformity in block copolymer syntheses due to the elimination of exogenous initiators, which start new chains.[137,138] Uniform block copolymers with high end-group fidelity are exemplified in polymerization-induced self-assembly[51,60,139] and block copolymer networks using photocatalysis.[4,108] PCRPs also offer the unique advantage of overcoming blocking-order limitations in RDRP techniques (**Figure 1.5A and B**).[8] Prior to PCRP, blocking order could be overcome in ATRP using a halogen-exchange reaction (requiring end-group modification).[140] However, Hawker and coworkers reported that blocking order can be reversed using photocatalyzed ATRP with $Ir(ppy)_3$ without the need for a halogen-exchange (**Figure 1.5A**).[8] In RAFT polymerization, both photoiniferter and PET-RAFT polymerization can be used to reverse blocking order. Sumerlin and coworkers showed that reversing blocking order could be performed with photoiniferter using xanthates (which are better suited for less-activated monomers) due to the lower C–S bond dissociation

energy (BDE) compared to other TCTs, but could not be performed with trithiocarbonates (which are better suited for more-activated monomers).[141] We reported that conventional blocking order in RDRP can be reversed with trithiocarbonates using PET-RAFT polymerization, leading to the synthesis of novel triblock copolymers (**Figure 1.5B**).[9] Furthermore, using photocatalysis for block copolymer syntheses provides access to orthogonal stimuli to synthesize novel block copolymers. Fors and coworkers switched between cationic and radical RAFT polymerizations using selective PCs and discrete wavelengths, leading to previously unattainable vinyl ether and acrylic multiblock copolymers (**Figure 1.5C**).[10,99] These reports demonstrate that by selecting PCs with desired photophysical properties, polymerization mechanisms can be switched by changing the irradiation wavelength. The opportunity to readily switch between radical, cationic, and/or anionic polymerization through photocatalytic conditions (e.g. PC, wavelength of light, temperature) will facilitate greater control and tunability in copolymer syntheses.

PCRPs have also been advantageous in the synthesis of graft copolymers, either from a polymer backbone or a protein. One main advantage to performing these polymerizations using light-mediated polymerizations is orthogonal control (**Figure 1.6A and B**). Moad, Hawker, and Boyer used a chemoselective approach for the one-pot synthesis of polymer architectures using a two CTA system (**Figure 1.6B**).[11,12,51] A CTA with a lower BDE compared to the other CTA was selectively activated by lower energy green light via photoiniferter, while the other CTA remained uninitiated. Subsequently, introducing a PC activated both CTAs by PET, leading to the divergent synthesis of one-

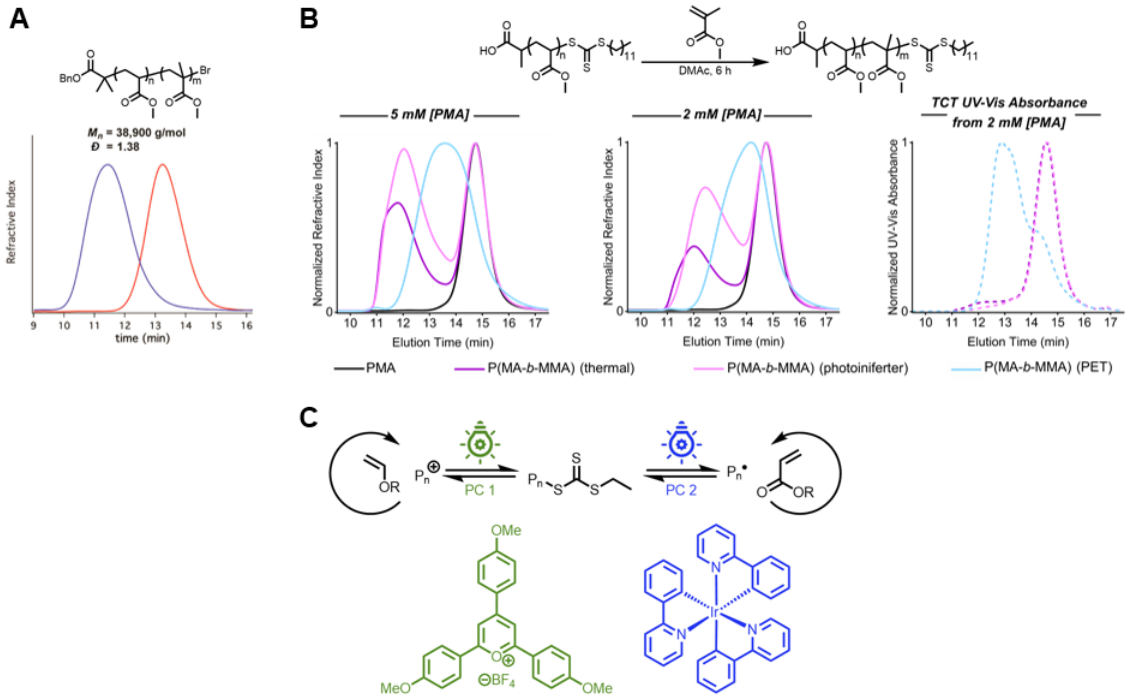

Figure 1.5. A) Size-exclusion chromatography (SEC) refractive index (RI) traces of block copolymers going against conventional blocking order in reversible-deactivation radical polymerization (RDRP) using photocatalyzed atom transfer radical polymerization (ATRP). Reproduced with permission from ref. [8]. Copyright 2014, American Chemical Society. B) SEC RI traces of block copolymers going against conventional blocking order using thermal initiation, photoiniferter, or photoinduced electron/energy transfer (PET) initiation in reversible addition–fragmentation chain transfer (RAFT) polymerization at different concentrations. Reproduced with permission from ref. [9]. Copyright Wiley Online Library. C) Schematic of converting between cationic and radical polymerizations using selective photocatalysts and wavelengths in RAFT polymerization. Reproduced with permission from ref. [10]. Copyright 2021, American Chemical Society.

pot graft copolymers with simultaneous control over the backbone and side-chain lengths using an inimer (a molecule containing a polymerizable and initiating group). Finally, photocatalysis has also led to metal-free grafting-from polymerizations on proteins. For example, PET-RAFT polymerizations with Eosin Y have been used to perform fast, metal-free polymerizations from proteins or cells at room temperature (**Figure 1.6C**).[13,142,143]

Lastly, photocatalyzed ATRP and PET-RAFT polymerizations are used to synthesize higher-order polymer architectures including stars,[132,133] hyperbranched

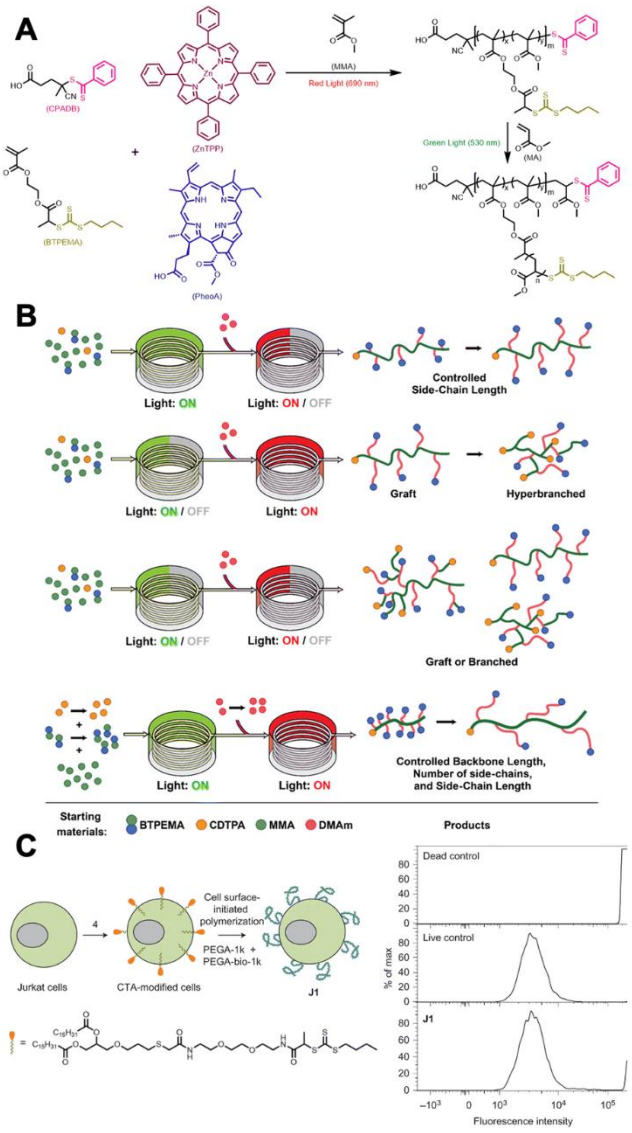

Figure 1.6. (A) Schematic of selective photoactivation for the one-pot synthesis of a graft copolymer using an inimer using photoinduced electron/energy transfer reversible addition–fragmentation chain transfer (PET-RAFT) polymerization. Reproduced with permission from ref. [11]. Copyright 2016, American Chemical Society. B) Schematic of a divergent approach to synthesize different architectures depending on light on/off events and duration in flow through selective photoactivation using PET-RAFT polymerization. Reproduced with permission from ref. [12]. Copyright 2021, American Chemical Society. C) Schematic of grafting-from proteins using PET-RAFT polymerization and cell viability post-polymerization. Reproduced with permission from ref. [13]. Copyright 2017, Springer Nature.

polymers,[132–136] and ultrahigh molecular weight (UHMW) polymers. Light-mediated polymerizations lead to the facile synthesis of UHMW polymers under atmospheric

conditions.[144–149] Prior to using light to perform UHMW polymerizations, high-pressure (5–6 kbar) and exogenous initiators were required, leading to longer polymerizations with higher disperisties.[150] Using light has enabled the synthesis of >1 × 10^6 g mol−1 UHMW polymers at atmospheric conditions in water or organic solvents in minutes to hours.[147,151–153]

Future work focusing on ATRP and RAFT polymerization end group BDEs will aid in efforts to selectively activate polymer end groups with photocatalysis. For example, BDE differences of over 11 kcal mol^{-1} have been reported for different R–X bonds in RAFT polymerization (R–S(=S)–Z) and ATRP (R–Br) using density functional theory calculations (DFT).[154–156] The 11 kcal mol^{-1} energy difference presents an opportunity to leverage the reduction potential of PCs for the selective activation of different bonds, leading to the facile synthesis of defined polymer architectures.

1.6 PCRP innovation on the primary sequence level

The primary sequence is the most difficult level of polymerization to control due to monomer energetics and RDRP following a Poisson distribution model in ideal cases.[94] Sequence-defined oligomers/polymers can be accessed using selective photoactivation in RDRP by studying the photophysical properties of PCs and chain end BDEs. Currently, when performing PCRPs, a PC is chosen that has a high enough reduction potential to cleave all the chain ends regardless of the chemical identity. However, as shown by DFT calculations,[154–156] orthogonal control to target and cleave specific bonds through PC selection is possible using PCRP. Thus, catalyst choice, wavelength of light selection, and polymerization conditions will be imperative for controlling the primary sequence. The selection of a PC for a desired BDE leads to sequence-defined/controlled polymers by

performing sequential single-unit monomer insertion (SUMI) reactions through selective photocatalysis.[11,15] However, currently only short oligomers (50 monomer units) could be achieved. Also, as discussed above, orthogonal and/or chemoselective control will enable easier syntheses of higher-order architectures or offer chemical handles for subsequent alterations to physical properties, topology, or molecular weight.

Photocatalyzed polymerizations have only been shown at the primary sequence level through SUMI reactions (**Figure 1.7A–D**). To modulate the primary sequence, PCRP SUMI reactions are used for the installation of functional units within a polymer backbone. For example, we were able to perform a SUMI reaction within an acrylic backbone using PET-RAFT polymerization (**Figure 1.7A**).[14] Through a combination of temperature and photocatalytic control (using $Ir(ppy)_3$ at low temperatures) a single vinyl ether could be inserted into an acrylic backbone.

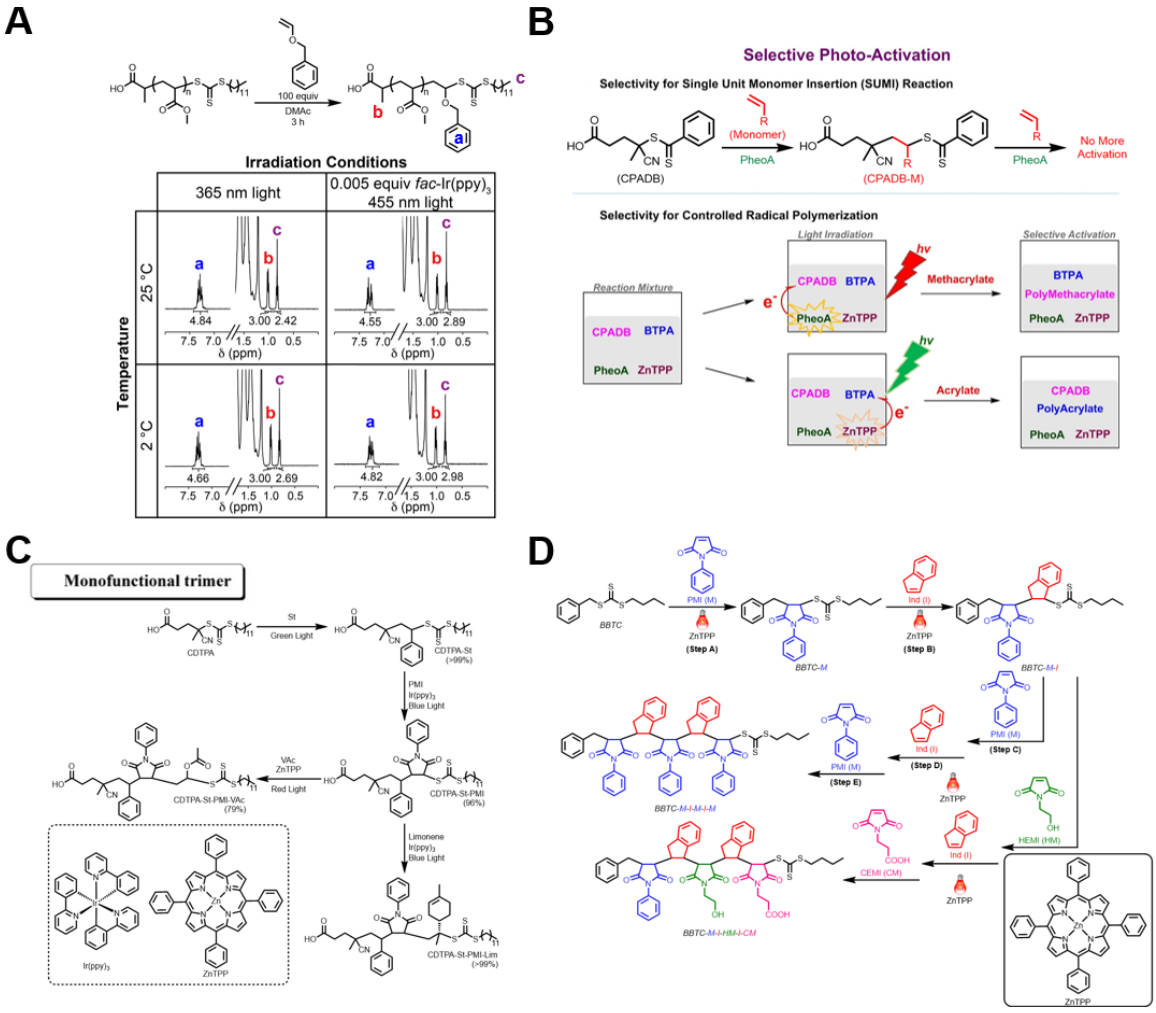

Figure 1.7. A) Schematic and ^{1}H nuclear magnetic resonance (NMR) spectra for a single unit monomer insertion (SUMI) reaction within an acrylic backbone using photoinduced electron/energy transfer reversible addition–fragmentation chain transfer (PET-RAFT) polymerization. Reproduced with permission from ref. [14]. Copyright 2024, American Chemical Society. B) Schematic of selective photoactivation for SUMI reactions and divergent synthesis using PET-RAFT polymerization. Reproduced with permission from ref. [11]. Copyright 2016, American Chemical Society. C) Schematic for iterative SUMI reactions for the synthesis of sequence-defined trimers using PET-RAFT polymerization. Reproduced with permission from ref. [15]. Copyright 2016, Wiley Online Library. D) Schematic for the synthesis of sequence-defined pentamers using iterative SUMI reactions via PET-RAFT polymerization. Reproduced with permission from ref. [16]. Copyright 2018, American Chemical Society.

Although most SUMI reports using PCRP techniques also rely on the poor homopolymerization of specific monomers,[157] photocatalysis is imperative for the uniformity of chains. If these polymerizations were performed using exogenous initiators,

each iterative SUMI reaction would have compounding defects due to initiator-derived chains.[11,15,158] However, by using PCRPs, Boyer and coworkers utilized the reduction potentials of specific PCs to perform SUMI reactions with no initiator-derived defects. In these examples, pheophorbide a (PheoA) had a high enough reduction potential to cleave the 4-cyanopentanoic acid C–S bond with a lower BDE on the R-group of the TCT. However, after a SUMI reaction using methyl methacrylate, no subsequent polymerization occurred because PheoA does not have a high enough reduction potential to cleave the new C–S bond with a higher BDE that was formed between methyl methacrylate and the TCT (**Figure 1.7B**). By using selective photoactivation, sequence-defined trimers were synthesized (**Figure 1.7C**). Recently, higher-order sequence-defined structures of up to 18 monomer units were synthesized using PCRP SUMI reactions (**Figure 1.7D**).[16,159]

Although only oligomers have been synthesized by iterative SUMI reactions, there is still a significant unmet opportunity to synthesize sequence-defined structures with higher degrees of polymerization using selective photoactivation to mimic nature. Rather than proceeding through subsequent protection–deprotection steps like in solid-phase peptide synthesis,[160] selective photoactivation simply requires changing photocatalytic conditions, which will be aided by advances in heterogeneous catalysis and flow chemistry.

1.7 Future outlook

Photocatalysis is an essential process in organic and polymer chemistry, aiding in transformations that were previously inaccessible. PCRP has led to many significant advances in polymer synthesis, but the full potential of photocatalysis has not been explored. In small molecule transformations, PCs with desirable photophysical properties (e.g., redox potential, excited state lifetime) are readily chosen to perform difficult

transformations,[161–163] while comparatively fewer PCs are used for specific photophysical properties to conduct PCRPs. Previously, PCRPs have predominantly been used to synthesize materials in a more environmentally friendly manner,[40] to provide access to polymers with various architectures,[12] and to polymerize difficult monomers (e.g., fluorinated monomers).[139] However, the distinct mechanism of polymer activation and the unique decoupling of radical introduction from other reaction conditions (e.g., temperature) have not been widely used to access novel sequences and/or architectures.

Synthesizing more defined polymers and architectures using PCRP has been limited due to understudied aspects of how PCs and photocatalysis are impacted by differences in reaction conditions including, but not limited to, temperature, solvent, wavelength of light, light intensity, chain end identity, and polymerization additives (e.g., amines/ligands). This gap in fundamental knowledge has ultimately limited how photocatalysis can be applied to RDRP techniques. For example, studying the corresponding photoredox processes, desirable photophysical properties of PCs, polymerization kinetics across different reaction conditions, and the reactivities of chain ends and PCs will provide insight into how photocatalysis can be used as a tunable chemical handle through various factors (e.g. wavelength of light and temperature) in RDRP (**Figure 1.8**). These insights will address an unmet need to access polymers with defined sequences, architectures, and topologies through selective activation. Furthermore, using photocatalysis through photoactive proteins[104] to perform PCRPs could provide stereocontrol by leveraging the constricted active site of the protein, which is unattainable with current PCs. Combining selective photoactivation and photocatalysis with post-polymerization modifications (e.g., metamorphosis,[164] selective depolymerization,[165,166]

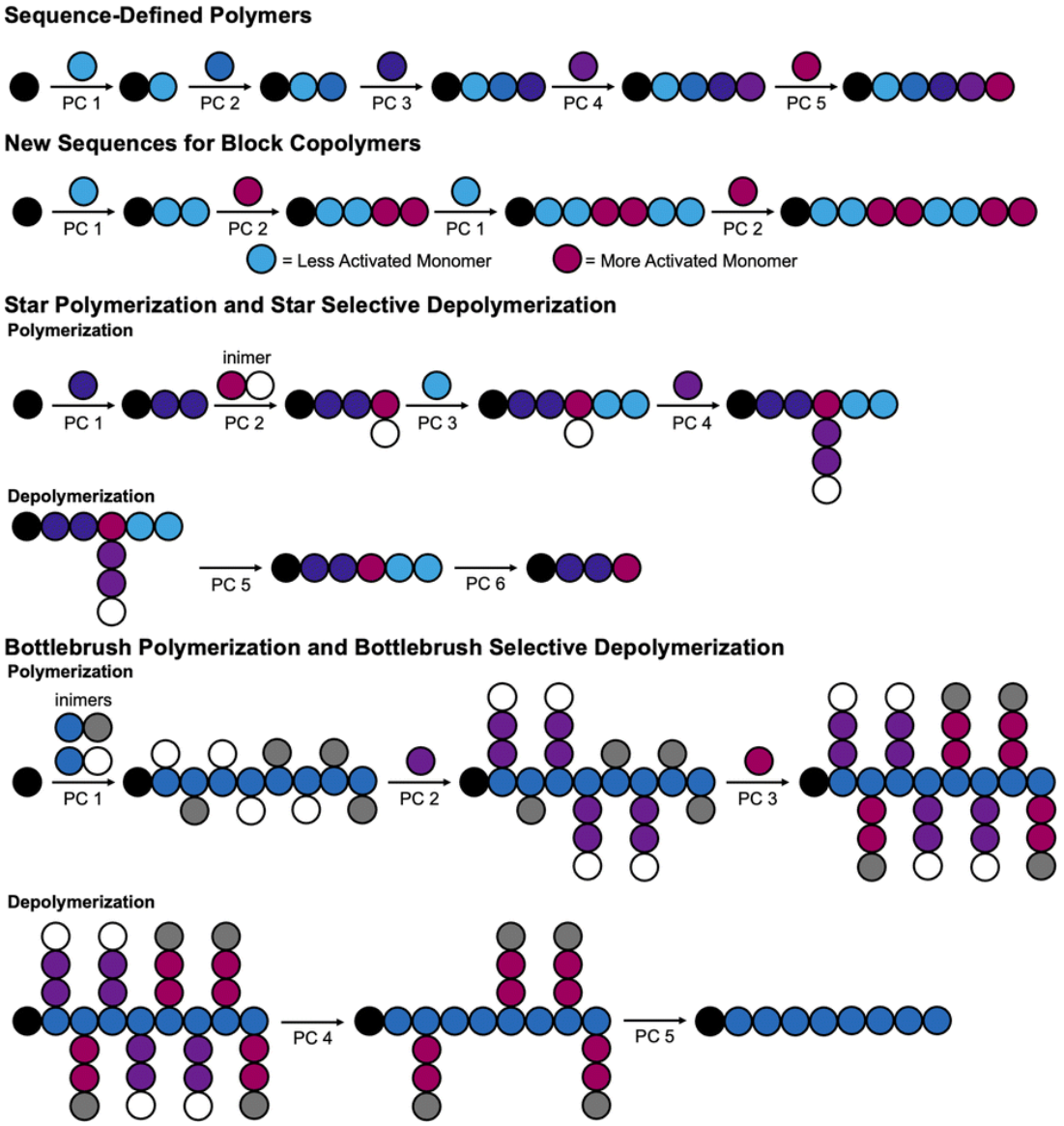

Figure 1.8. Cartoon representation of how photocatalysis and selective photoactivation can lead to the synthesis of sequence-defined polymers, new block copolymer sequences, facile defined architecture synthesis, and for post-polymerization modifications.

backbone functionalization,[167–169] and photoligation[170–173]) can lead to advanced and responsive architectures beyond what is accessible with PCRPs alone. Photocatalysis could be used to target and activate specific chain ends leading to new block copolymer sequences, the polymerization of a wider range of monomers, and possibly sequence-defined polymers. Enhanced control over these types of structures will lead to advances

ranging from fundamental structure–function relationships of high-performance materials to addressing societally impactful challenges, like plastic recycling, drug development, and the fabrication of organoelectronics.

1.8 Take-home messages for improving photocatalysis use in RDRP techniques

Explore photophysical properties. PCs are understudied in how rates of activation are impacted by PC choice, temperature, wavelength of light, and/or light intensity variation in polymerization systems. A better understanding of rates of activation via PC across reaction conditions will provide fundamental insight, leading to more defined polymerization systems.

Emphasize selective photoactivation. PCs are primarily chosen in PCRPs because they are compatible with the polymerization technique being used (RAFT polymerization and/or ATRP) and the reduction potential of the PC is high enough to cleave all of the chain ends in solution. By leveraging the reduction potentials of PCs against the BDEs of chain ends, PCs can be chosen to perform specific transformations resulting in selective photoactivation of desired chains leading to sequence-defined polymers.

Investigate orthogonal control. Photocatalysis is rarely used in the presence of two separate initiators because most common PCs have a reduction potential high enough to cleave both sets of chain ends. Further investigation into initiator activation rates with differing PCs, wavelengths of light, and light intensities can lead to new synthetic pathways using inimers for the polymerizations of stars, brushes, and hyperbranched polymers.

Combine photocatalysis with post-polymerization modification. Photocatalysis use in RAFT polymerization and ATRP has mainly focused on performing polymerizations but has not widely been incorporated into post-polymerization modifications. A better

understanding of the interplay between PCs and chain ends/pendent groups through redox potential and BDE or electron/energy transfer and functional groups can lead to selective depolymerization and/or modification of the backbone.

Chapter 2: Research Objectives

The purpose of this research was to develop new polymerization methodologies that enable access to well-defined novel structures for biomimicry and next-generation materials.

Reversible addition–fragmentation chain transfer (RAFT) polymerization has been used as a reversible-deactivation radical polymerization (RDRP) technique since its introduction in 1998. Although RAFT polymerization has been employed to synthesize various architectures, topologies, and polymers, limitations remain. Using photoinduced electron/energy transfer (PET) catalysis, two challenges in RAFT polymerizations were addressed. Photocatalysis is advantageous in RDRP, as PET introduces unique activation mechanisms that provide a chemical handle to address these challenges.

The first limitation addressed in Chapter 3 is that inserting a single monomer into a polymer backbone is difficult because the polymer ideally follows a Poisson distribution. RAFT polymerization ideally follows a Poisson distribution because of the chain transfer agent (CTA); the CTA is rapidly converting dormant chain ends to active chain ends, and vice versa, providing all chain ends with an equal likelihood of being activated to propagate, resulting ideally in a Poisson distribution of monomer units being added across all of the chain ends in the polymerization. Using unique PET-RAFT polymer conditions, decreased temperature and increased trithiocarbonate (TTC) concentration, we inserted exactly one vinyl ether at a defined point within the polymer backbone using a single-unit monomer insertion (SUMI) reaction. This methodology enabled near-quantitative incorporation of the single monomer (>96%), with no double- or higher-order insertions

observed by mass spectrometry. The insertion could be performed using various vinyl ethers, with no change in incorporation percentages observed; the vinyl ether could then be chain extended, allowing the SUMI site to be placed at any point in the polymer backbone.

Next, the second limitation addressed in Chapters 4 and 5 is the long-standing blocking order requirements for RDRP. Previously, monomer order in block copolymers was restricted by the requirement that more stable radical species be polymerized first, followed by less stable ones. By increasing the photocatalyst loading, using a dilute [TTC], and introducing a reversible redox pathway to stabilize the TTC, the blocking order could be reversed (Chapter 4). This methodology enabled access to previously inaccessible triblock copolymers. The impact of blocking order on physical properties was investigated, and it was found that reversing the blocking order changes the material from brittle to elastomeric behavior. Ultimately, this methodology was used to synthesize a novel high-molecular-weight thermoplastic elastomer that can be strained by >1600%. This method was then expanded to improve TTC retention and enable further chain extension (Chapter 5). Using extensive kinetic studies, we focused on the underlying reaction rates: the rates for TTC activation ($k_{a,TTC}$) and TTC termination ($k_{t,TTC}$). By evaluating [TTC], photocatalyst loadings, temperature, and monomer equivalents through kinetic studies, new sets of reaction conditions were identified that increased the activation-to-termination ratio, reaching a maximum of 4.1.

Lastly, in Chapter 6, the impact of using PET-RAFT polymerization to synthesize and chain extend organogels on polymer uniformity was evaluated. It was found that PET-RAFT polymerization results in well-defined organogels, but result in uncontrolled chain

extensions. Nevertheless, PET-RAFT polymerization was used to modulate the overall properties of the organogels resulting in changes in hydrophobicity and swelling ratios.

Overall, methods have been developed to address limitations in RDRP by employing PET-RAFT polymerizations to insert a single monomer unit into a polymer backbone and to overcome conventional blocking order requirements. These innovations will enable the synthesis of novel polymers and materials and advance biomimicry, high-performance materials, and the use of photocatalysts in RDRP.

Chapter 3: Installing a Single Monomer within Acrylic Polymers Using Photoredox Catalysis*

Authors: Jared G. Baker, Richard Zhang, and C. Adrian Figg

3.1 Abstract

Incorporating exactly one monomer at a defined position during a chain polymerization is exceptionally challenging due to the statistical nature of monomer addition. With RAFT polymerization ideally following a Poisson distribution, at any point in the polymerization, a chain end could have a different degree of polymerization than the average chain end in solution, making it difficult to insert a single monomer at a defined position in every chain, as each chain has a statistical average number of repeat units present. Herein, photoinduced electron/energy transfer (PET) enables the incorporation of exactly one vinyl ether into polyacrylates synthesized via reversible addition−fragmentation chain transfer (RAFT) polymerization. Near-quantitative addition (>96%) of a single vinyl ether is achieved while retaining >99% of the thiocarbonylthio chain ends. Kinetic studies reveal that performing the reactions at 2 °C limits unwanted chain breaking events. Finally, the syntheses of diblock copolymers are reported where molecular weights and dispersities are well-controlled on either side of the vinyl ether. Overall, this report introduces an approach to access acrylic copolymers containing exactly one chemical handle at a defined position, enabling novel macromolecular architectures to probe structure−function properties, introduce sites for de/reconstruction, store information, etc.

*Adapted and reproduced with permission from *J. Am. Chem. Soc.* **2024**, *146*, 106-111.

3.2 Introduction

Functionality plays a critical role in polymer properties.[174–177] For example, routes to synthesize sequence-defined and sequence-controlled polymers are pursued to mimic the complexity of and information stored in biomacromolecules (e.g., proteins, DNA, polysaccharides).[178–183] However, there are very few examples demonstrating the synthesis of polymers with defined functional group placement using chain polymerization techniques.[16,158,184–190] In these examples, the functional group placement is either preprogrammed into the monomers, or only oligomers can be synthesized (**Figure 3.1**). This lack of examples is surprising given that the position of just a single moiety can have substantial impacts on properties. For example, a single ionic charge placed at different positions within an amphiphilic polypeptoid affected assembly properties.[191] This observation suggests that the analogous modulation of acrylic polymer properties could be tuned via the incorporation of single functionalities. However, incorporating a single monomer within a polymer chain at a defined position is challenging because the inherent statistical growth process of common chain polymerization techniques must be overcome.[192] When a monomer that can homopolymerize is used in chain polymerization, the monomer is added to polymer chains via propagation and follows a statistical average, also known as a Poisson distribution. Even if only 1 equivalent of monomer, with respect to polymer chain ends, is used in the polymerization, monomer insertions of 0, 1, 2, 3, and some higher-order degrees of polymerization will occur because of this distribution, leading to poor uniformity of the polymer chains due to the statistical order in which polymerization occurs in chain growth polymerizations. This distribution ultimately makes a single insertion at a defined position in a polymer chain difficult.

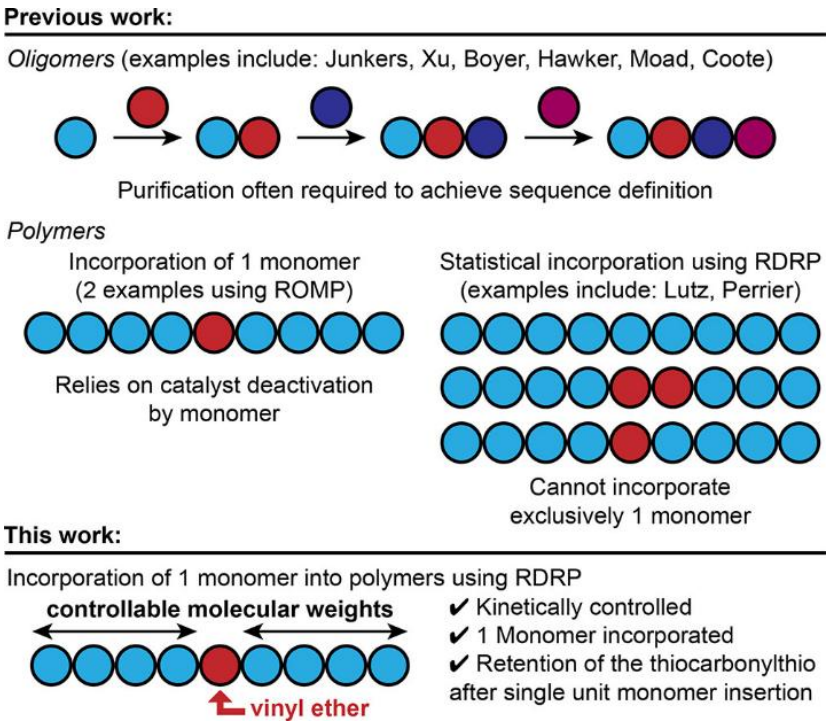

Figure 3.1. Previous work incorporating successive single-unit monomer insertion reactions to access oligomers, exactly 1 monomer into polymers by ring-opening metathesis polymerization (ROMP), and statistically incorporating monomers into polymers using reversible–deactivation radical polymerization (RDRP) versus the incorporation of exactly 1 vinyl ether monomer into polyacrylates using RDRP.

Monomer design can be used to place single functionalities in polynorbornenes using ring-opening metathesis polymerization (ROMP, **Figure 3.1**).[193,194] However, accessing analogous structures using reversible-deactivation radical polymerization (RDRP) has not been accomplished because radical polymerizations rely entirely upon monomer addition kinetics. A chain end deactivation approach similar to the one used for ROMP is inaccessible due to the radical nature of RDRP. Notable examples approaching this goal were pioneered by Lutz leveraging the poor homopolymerizability of maleic anhydride and maleimides.[195–197] However, these monomers undergo minor homopolymerization, so defects of 0 and 2 additions exist in the polymer products, limiting access to precise macromolecular structures.[157,198,199] There are no examples that use RDRP

to insert exactly 1 monomer at a defined position in a macromolecule because previous strategies have relied upon monomer addition kinetics without sufficient selectivity. Previous RDRP examples have primarily used acrylates and maleimides, which are capable of homopolymerization in radical polymerizations.[16,158,187] Due to the homopolymerization ability of the monomers being used, equivalents of monomer and reaction time need to be leveraged to obtain the highest percent of single monomer insertions, while limiting double and higher-order insertions since the monomers can homopolymerize. This method will still require purification when performed directly to the chain transfer agent to obtain uniform polymer chains.[16,158,187] However, when performed in a polymer chain, kinetic selectivity over monomer addition is paramount because defects of 0 and 2 additions cannot be purified out of polymer samples, a distinct challenge compared to oligomeric single-unit monomer insertion (SUMI) approaches.[16,158,186,187] Therefore, delineating the effects of precise monomer stoichiometry and position on properties (e.g., solution/bulk assembly, antimicrobials, information storage) would be convoluted by the defects in functionalities.

Herein, the slow radical polymerization kinetics of vinyl ethers[200], due to vinyl ethers failure to homopropagate in radical polymerizations, are used to control the insertion of exactly one monomer within an acrylic polymer (**Figure 3.1**). Because vinyl ethers cannot homopolymerize via radical polymerization, polymerization kinetics can be leveraged to incorporate exactly one, as cross-propagation is available in radical polymerizations with vinyl ethers. Vinyl ethers are usually only used in radical polymerizations as comonomers or to switch polymerization mechanisms.[99,200,201] The Barner-Kowollik lab used vinyl ethers to end-cap polymers synthesized via reversible addition−fragmentation chain transfer (RAFT) polymerization.[202] However, multiple

additions occurred, and substantial amounts of the thiocarbonylthio (TCT) chain end were lost due to irreversible termination. Even if single additions and minimal loss of the TCT had been achieved, chain extensions from vinyl ethers (less-activated monomers) with acrylates (more-activated monomers) are unfavorable and contradict blocking order requirements of traditional RAFT polymerization.[203] RDRP techniques following blocking order guidelines to ensure complete chain extensions are achieved. Typically, monomers with more stable propagating radical species are polymerized first (e.g. methyl methacrylate) followed by monomers with less stable propagating radical species (e.g. *N*,*N*-dimethylacrylamide). Going in the opposite direction typically results in incomplete chain extensions and bimodal distributions as polymer chains capped with less stable propagating radical species will remain inactive once a more stable propagating radical species is introduced and begins to polymerize.

We hypothesized that photoinduced electron/energy transfer (PET) reactions[19] can be used to insert a single vinyl ether within a polyacrylate. PET-mediated radical introduction leads to fewer termination events and more uniform polymer end groups than other initiation techniques.[55,204] We anticipated that these qualities would lead to the retention of the TCT during the SUMI reaction. If successful, chain extension of the TCT-terminated polymer containing a single vinyl ether could be possible adapting a recent photomediated approach to flip blocking order.[141] This process would result in the first synthetic method to access acrylic copolymers with defined lengths and low dispersities on either side of exactly 1 monomer, a critical first step toward incorporating defined functional group sequences within polymers.

3.3 Results and Discussion

Poly(methyl acrylate) (PMA, **Figure A1**) synthesized using PET-RAFT conditions and terminated with a trithiocarbonate was used to study the SUMI reaction with benzyl vinyl ether (BVE) (**Figure 3.2A**). Three different initiation methods were screened: thermal at 75 °C,[90] photoiniferter at 25 °C with 365 nm light,[153,205] and PET using *fac*-$Ir(ppy)_3$ at 25 °C with 455 nm light.[55] The thermal activation method led to vinyl ether oligomerization and termination (**Figure A2**). Photoactivation pathways led to significant incorporation of BVE by ^{1}H NMR spectroscopy analysis with photoiniferter leading to a 97% incorporation of BVE (**Figure 3.2B**, a) and PET leading to 91% incorporation of BVE (**Figure 3.2C**, a). While the photoiniferter method resulted in near-quantitative BVE incorporation, ^{1}H NMR spectroscopy indicated that ~20% of the TCT was lost during the reaction (**Figure 3.2B**, c), analogous to reported results. Conversely, the PET initiation pathway led to minimal loss of the TCT (4%, **Figure 3.2C**, c).[55] However, longer reaction times at 25 °C did not improve BVE incorporation (**Figure A3**).

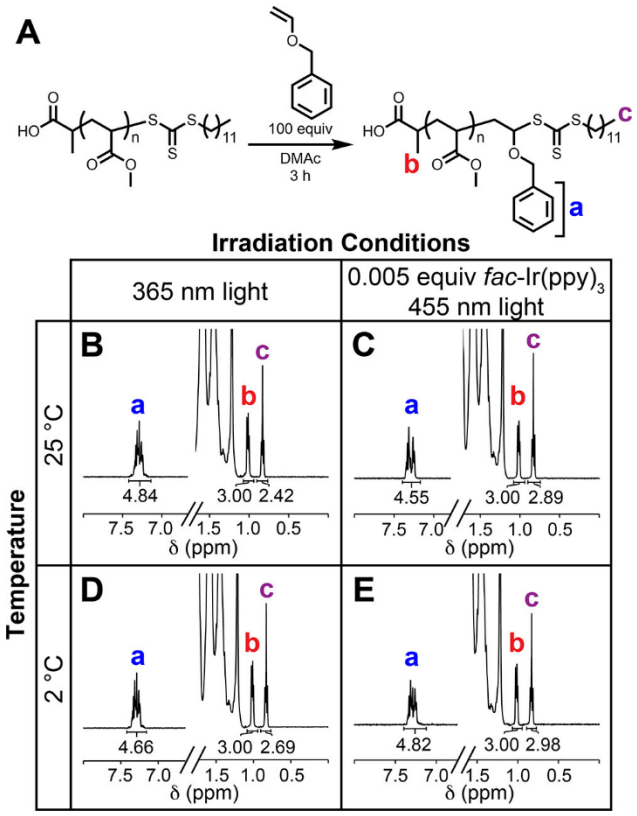

Figure 3.2. A) Scheme of the single-unit monomer insertion reaction, B) ^{1}H NMR spectrum of PMA-BVE at 25 °C using 365 nm light, C) 25 °C using 455 nm light, D) 2 °C using 365 nm light, and E) 2 °C using 455 nm light.

We hypothesized that lower reaction temperatures would lead to high BVE incorporation before a significant loss of TCT occurs. We expected that TCT loss was primarily occurring by termination and unproductive chain transfer events between a vinyl ether and a radical species, which will ultimately result in terminated polymer chains (**Figure A4**), so cooling down the temperature would slow down these processes and result in higher retention of the TCT.[206] At 2 °C, retention of the TCT was improved using either photoactivation approach. However, PET activation led to >99% retention of TCT and >96% BVE incorporation by ^{1}H NMR spectroscopy (**Figure 3.2E**, a and c; **Figure A5**) compared to 90% retention of TCT and 93% BVE incorporation using a photoiniferter pathway (**Figure 3.2D**, a and c).

Trapping studies were conducted to probe if 2 °C slowed down rates of TCT activation by both PET and chain transfer during the SUMI reaction (**Figure 3.3A**).[100,207,208] We hypothesized that the TCT rate of activation by the PET catalyst ($k_{A,\ PET}$) would not be as affected by the temperature compared to the TCT activation by chain transfer ($k_{A,\ CT}$).[209,210] Importantly, these experiments solely measured the rate of TCT consumption via either radical quenching or monomer addition; they did not measure the rates of degenerative chain transfer characteristic of RAFT processes.

The disappearance of the methine proton adjacent to the TCT (δ = 4.68 ppm) of 2-(dodecylthiocarbonothioylthio) propionic acid (DTPA) was monitored to extract an apparent rate constant of DTPA consumption (k_{DTPA}, **Figure 3.3B**).[102] The rate of consumption of DTPA under different conditions was then used to identify the proportion of $k_{A,\ PET}$ versus $k_{A,\ CT}$ occurring during the addition of a single vinyl ether.

Anilinium hypophosphite (AH), a radical-scavenging hydrogen atom source,[102] was used in 15-fold excess to prevent TCT activation via chain transfer (**Figure A6**). The *fac*-Ir(ppy)$_3$ and DTPA concentrations were kept constant throughout the different conditions. Resultantly, these rates represent radical introduction and consumption of DTPA when all other possible chain transfer and monomer addition events are eliminated. Therefore, the k_{DTPA} values measured in the presence of AH at 25 °C (**Figure 3.3C**, entry 1) and 2 °C (**Figure 3.3C**, entry 4) are directly proportional to $k_{A,\ PET}$. Since radical concentration is assumed to be constant, increases in k_{DTPA} under different conditions will provide insight into the relative rates of $k_{A,\ PET}$ versus $k_{A,\ CT}$. An increased rate in k_{DTPA} means that DTPA is activated by chain transfer in addition to PET.

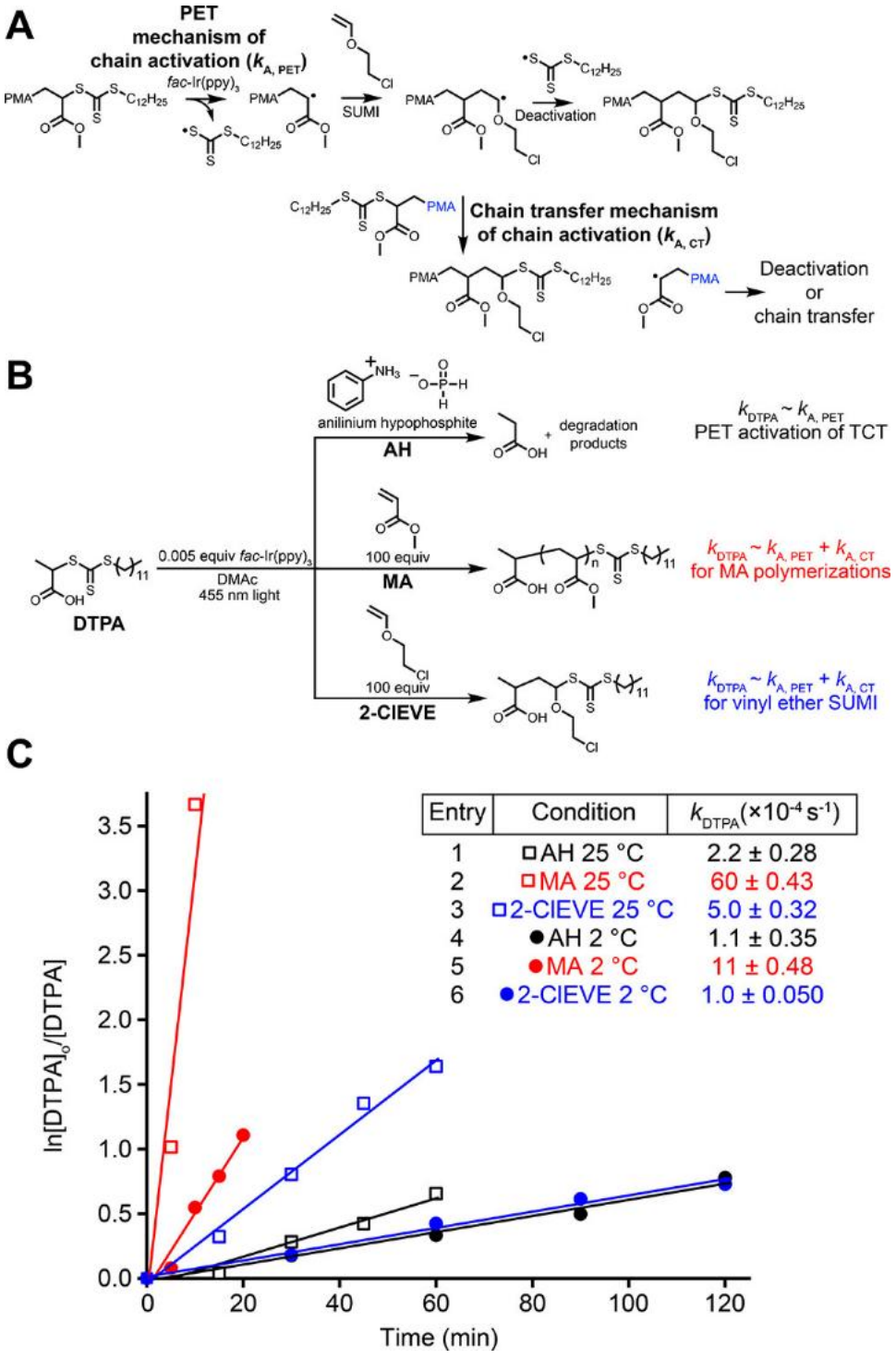

Figure 3.3. A) Scheme describing chain activation via PET catalysis and chain transfer; B) Schemes of different conditions to study the consumption of 2-(dodecylthiocarbonothioylthio) propionic acid (DTPA); C) Kinetic data for the consumption of DTPA with methyl acrylate (MA), 2-chloroethyl vinyl ether (2-ClEVE), or anilinium hypophosphite (AH). All experiments monitored the disappearance of the methine proton of DTPA at δ = 4.68 ppm via ^{1}H NMR spectroscopy.

The k_{DTPA} in the presence of AH decreased from 2.2×10^{-4} s^{-1} at 25 °C to 1.1×10^{-4} s^{-1} at 2 °C, indicating that $k_{A,\,PET}$ is slowed down by 50% at 2 °C compared to 25 °C. This result indicates that lowering the temperature decreases the overall number of radicals introduced into the system via PET, leading to fewer termination events.

The k_{DTPA} in the presence of MA decreased from 60×10^{-4} s^{-1} at 25 °C (**Figure 3.3C**, entry 2) to 11×10^{-4} s^{-1} at 2 °C (**Figure 3.3C**, entry 5; **Figure A7**). The decrease in rate suggests that $k_{A,\,CT}$ is more affected by temperature than $k_{A,\,PET}$. At 25 °C, the difference in rate between AH and MA increases by 30×, while the difference in rate between the two conditions at 2 °C only increases by 10×. Additionally, DTPA is consumed significantly faster in the presence of MA. Therefore, activation by chain transfer ($k_{A,\,CT}$) is the predominate mode of DTPA consumption in the presence of monomers that homopolymerize because k_{DTPA} is significantly faster than $k_{A,\,PET}$. These results confirm that conventional PET-RAFT activation of TCTs occurs predominately via degenerative chain transfer, instead of PET.

The k_{DTPA} in the presence of 2-ClEVE decreased from 5.0×10^{-4} s^{-1} at 25 °C (**Figure 3.3C**, entry 3) to 1.0×10^{-4} s^{-1} at 2 °C (**Figure 3.3C**, entry 6; **Figure A8**). These results show that (1) DTPA consumption in the presence of vinyl ethers decreases with temperature and (2) at 2 °C, the k_{DTPA} is the same value as k_{DTPA} in the presence of AH. Therefore, we concluded that chain transfer does not play a significant role in DTPA consumption in the presence of vinyl ethers. Furthermore, these observations suggested that chain breaking events, unproductive chain transfer between vinyl ethers and a radical species (**Figure A4**), were also significantly slowed down at the lower temperatures.

Next, we sought to confirm that (1) exactly one vinyl ether was added to each chain and (2) the conditions were amenable to other vinyl ethers. SUMI reactions were performed with five vinyl ethers: BVE, 2-ClEVE, *n*-butyl vinyl ether (*n*-BuVE), *iso*-butyl vinyl ether (*iso*-BuVE), and di(ethylene glycol) vinyl ether (DEGVE) and analyzed using matrix assisted laser desorption/ionization time-of-flight mass spectrometry (MALDI-TOF MS) (**Figure 3.4** and **Figures A9−A14**).

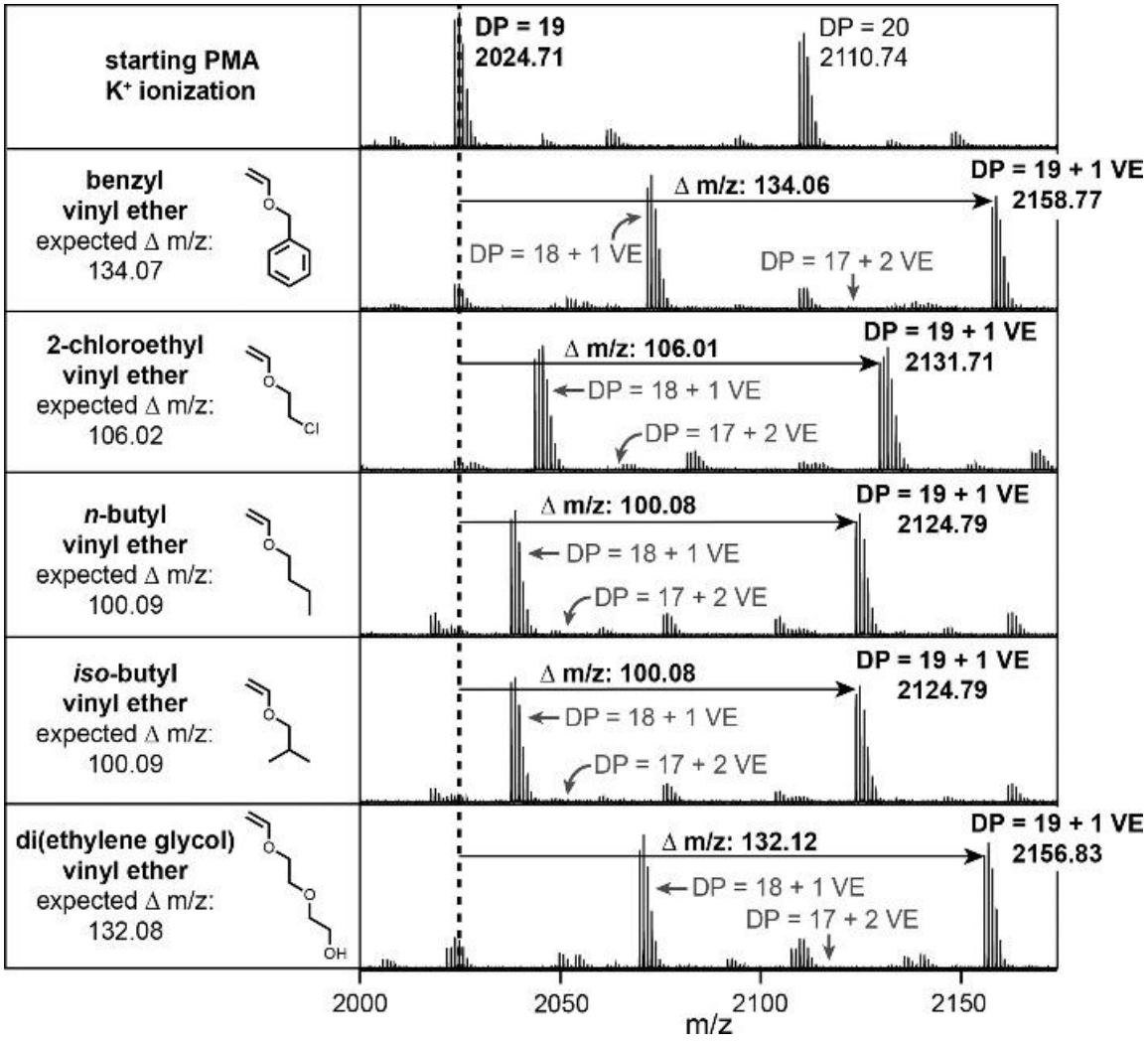

Figure 3.4. MALDI-TOF MS spectra of 5 vinyl ethers (BVE, 2-ClEVE, *n*-BuVE, *iso*-BuVE, and DEGVE) added to poly(methyl acrylate) (PMA).

The expected m/z shift of each vinyl ether was observed. For BVE, a shift of 134.07 m/z was expected and a shift of 134.06 m/z was observed. No double-addition peaks of BVE were observed. The main potassium adduct peak corresponds to PMA-BVE with a TCT on the chain end. Analogous observations of single addition, retention of TCT, and minimal starting PMA were observed for 2-ClEVE, *n*-BuVE, *iso*-BuVE, and DEGVE.

Size-exclusion chromatography (SEC) analysis was used to confirm that no vinyl ether polymerization occurred. No shift in retention time was observed, indicating no vinyl ether polymerization (**Figure 3.5**). A minor distribution at lower retention times following the SUMI reaction potentially results from termination and/or chain breaking events, unproductive chain transfer events between vinyl ethers and radical species due to the labile protons on vinyl ethers, leading to termination events (**Figure A4**), leading to polymer−polymer coupling of the resultant pendent or backbone radical with another polymer. This distribution is double the molecular weight of the starting PMA (**Figure A15**) and accounts for ~4 mol % of the total population. Considering the ^{1}H NMR spectra, MALDI-TOF MS spectra, and SEC chromatograms, exactly one vinyl ether is added to each chain end.

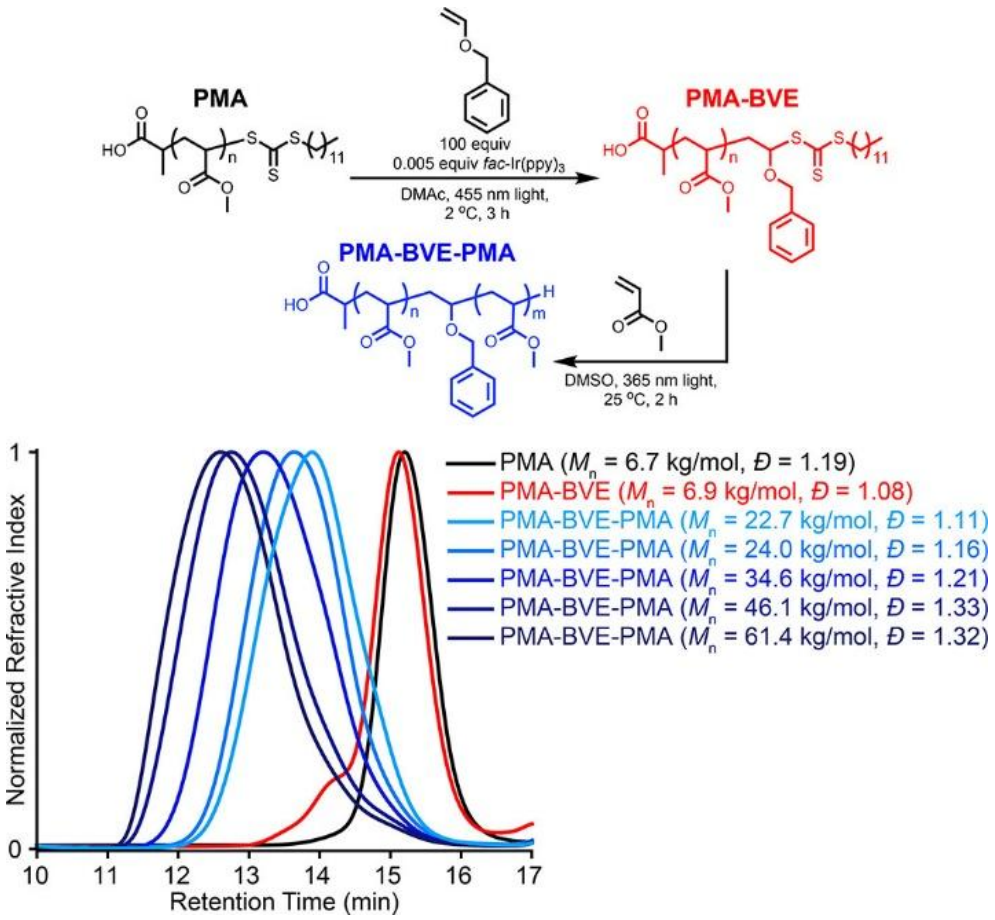

Figure 3.5. Scheme and size-exclusion chromatograms of the insertion of BVE into a PMA chain and subsequent chain extensions from poly(methyl acrylate)-benzyl vinyl ether (PMA-BVE) using methyl acrylate to achieve PMA-BVE-PMA.

Chain extensions with methyl acrylate (MA) were performed to confirm TCT retention on the chain end (**Figure 3.5, Figure A16**). Photoiniferter conditions were used, as PET-RAFT conditions led to multimodal traces (**Figure A17**).[141] Polymerizations were set up targeting different molecular weights (**Figure 3.5**). Uniform shifts to higher molecular weights of 22.7, 24.0, 34.6, 46.1, and 61.4 kg/mol were observed when 100, 200, 300, 400, and 500 equiv of MA were used, respectively (**Figure 3.5** and **Figures A16, A18−A21**). However, loss of the TCT occurred during this step, indicated by a loss of absorbance at the TCT absorption at 365 nm (**Figure A22**). Importantly, these data

demonstrate that the molecular weight of the polymer following the SUMI reaction can be controlled.

3.4 Conclusion

In conclusion, photochemistry enabled the placement of exactly one vinyl ether within the acrylic polymers. These results are a significant step toward sequence-defined polymers and new polymer architectures. We expect that these architectures will play a critical role in (1) probing structure−function properties, (2) incorporating sites for controllable polymer deconstruction and reconstruction, and (3) accessing macromolecular architectures where the placement of defined chemical moieties dictate function (e.g., polymer−protein conjugates, ionic polymers, antimicrobial polymers, information-storage polymers, etc.).

The remaining challenge in incorporating a single monomer unit into the backbone of a polymer chain lie in the chain extension. Although we were able to chain extend from the vinyl ether and target different molecular weights, following the chain extension, no chain end fidelity remains, limiting the number of single monomer unit sites that can be incorporated in the backbone, while other methods performed on small molecules can retain full chain end fidelity for up to 18-mers. Being able to overcome this limitation with near quantitative chain end fidelity would enable us to incorporate more sites for further interests and applications, such as programming the polymer chain to recognize specific protein surfaces based on functionality and distance between sites. A deficiency in the methodology that we would like to overcome is the use of such an excess of monomer. Currently, to drive the incorporation to quantitative levels, we use 100 equivalents, while only 1 equivalent is functional. This requires us then to subsequently use commercially

available monomers and limits the functionalities that can be installed, unless a post-polymerization modification is performed. Nevertheless, this report remains the only one to be able to incorporate a single monomer unit within the backbone of a polymer chain at a defined position, and has inspired the use of vinyl ethers in more recent papers that are trying to perform single unit monomer insertion reactions.

3.5 Experimental

3.5.1 Materials

Anilinium hypophosphite (Sigma-Aldrich, 97%) was used as received. Methyl acrylate (MA, Thermo Scientific, 99%), benzyl vinyl ether (BzVE, Synthonix, 97%), 2-chloroethyl vinyl ether (2-ClEVE, Acros Organics, 95%), *n*-butyl vinyl ether (*n*BuVE, Alfa Aesar, 98%), *iso*-butyl vinyl ether (*iso*BuVE, TCI, 99%), and diethylene glycol vinyl ether (DiEGVE, TCI, 96%) were filtered through basic alumina prior to use. *fac*-Ir(ppy)$_3$ (Strem Chemicals, 95%) was prepared as a 10 mg/mL solution in *N*,*N*-dimethylacetamide (DMAc) prior to use. 2-(Dodecylthiocarbonothioylthio)propionic acid (DTPA) was adapted and synthesized from a previous report.[211] All solvents were used as received.

For a visible light source, 76.2 cm Supernight Blue or Green LED Light Strips were purchased from Amazon and placed on a Xnrtop Silver Tone Aluminum Radiator Heatsink Heat Sink 150 × 80 × 27 mm from Amazon. For an ultraviolet light source, an Everbeam 365 nm 50 W UV LED Black Light from Amazon was used.

3.5.2 Characterization

^{1}H NMR spectroscopy was conducted on either an Agilent U4-DD2 400 MHz or a Bruker Avance II 500 MHz at 25 °C. DMSO-d_6 (Cambridge Isotopes Laboratories, Inc., 99.9%) and $CDCl_3$ (Cambridge Isotopes Laboratories, Inc., 99.8%) were used as received.

Size Exclusion Chromatography (SEC) was performed in *N*,*N*-dimethylacetamide (DMAc) with 50 mM LiCl at 50 °C at a flow rate of 0.5 mL min^{-1} (Agilent isocratic pump, degasser, and autosampler, columns: TOSOH TSKgel Guard Alpha and TOSOH TSKgel Alpha-3000: molecular weight range 0–1 × 10^5 g mol^{-1}). Detection consisted of a Wyatt Optilab refractive index detector operating at 785 nm, a Wyatt DAWN multi-angle light scattering detector operating at 783 nm, and an Agilent MWD operating at 365 nm. Absolute molecular weights and dispersities were calculated with the Wyatt ASTRA software and off-line d*n*/d*c* analysis.

Visible light intensity was measured with an International Light Technologies ILT-350 illuminance spectrophotometer with a NIST traceable ISO17025 accredited calibration.

Matrix-assisted laser desorption/ionization time-of-flight mass spectrometry (MALDI-TOF MS) was performed on a Bruker timsTOF fleX MALDI-2 instrument. Analysis of poly(methyl acrylate) and SUMI reaction products was performed by mixing *trans*-2-[3-(4-*tert*-butylphenyl)-2-methyl-2-propenylidene]malonitrile (DCTB) matrix (10 mg/mL in THF), polymer solution (1.0 mg/mL in THF), and potassium trifluoroacetic acid (1.0 mg/mL in THF) at a v:v:v ratio of 5:2:2 matrix:polymer:salt, and 3 μL were spotted on a stainless steel Bruker MTP 384 target polished steel BC plate and air dried.

3.6 Procedures

3.6.1 Example polymerization for starting poly(methyl acrylate)

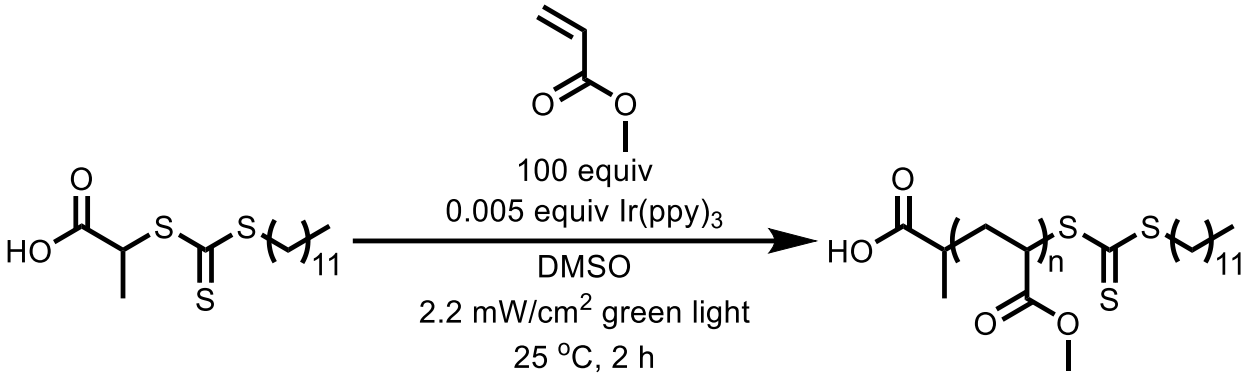

DMAc (33.6 mL), MA (18.4 g, 214 mmol), 2-(Dodecylthiocarbonothioylthio)propionic acid (750 mg, 2.14 mmol), and *fac*-Ir(ppy)$_3$ (7.01 mg, 1.07 × 10^{-2} mmol) were combined in a 50 mL Schlenk flask. The mixture was covered in aluminum foil and degassed with Argon for 30 min. The mixture was irradiated with a green LED strip (2.2 mW/cm^2) for 2 h at room temperature until achieving a conversion of 85% by 1H NMR spectroscopy. The reaction mixture was then precipitated into an excess of chilled methanol 2×, and then dried under vacuum and characterized by ^{1}H NMR spectroscopy and SEC.

3.6.2 Example procedure for trapping studies

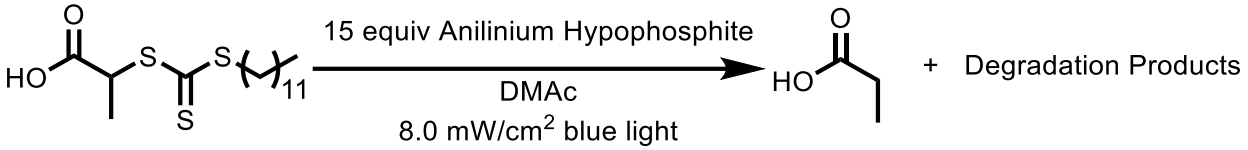

Anilinium Hypophosphite (71.6 mg, 4.50 × 10^{-1} mmol), 2-(Dodecylthiocarbonothioylthio)propionic acid (10.5 mg, 3.00 × 10^{-2} mmol), *fac*-Ir(ppy)$_3$ (9.83 × 10^{-2} mg, 1.50 × 10^{-4} mmol) were dissolved in DMAc (3.00 mL) with DMF as an internal standard in 2-dram vials and capped with rubber septum. After degassing the

solution for 5 min with Argon, the vials were placed in the 2 °C fridge and equilibrated for 1 h before turning the blue LED strip on (8.0 mW/cm^2). Vials were removed at 30 min, 60 min, 90 min, and 120 min and quenched by opening the vial to air. Conversion was determined by ^{1}H NMR spectroscopy using DMSO-d_6 as a solvent and tracking the disappearance of the methine peak at δ = 4.64 ppm.

3.6.3 Example procedure for vinyl ether small molecule analog studies

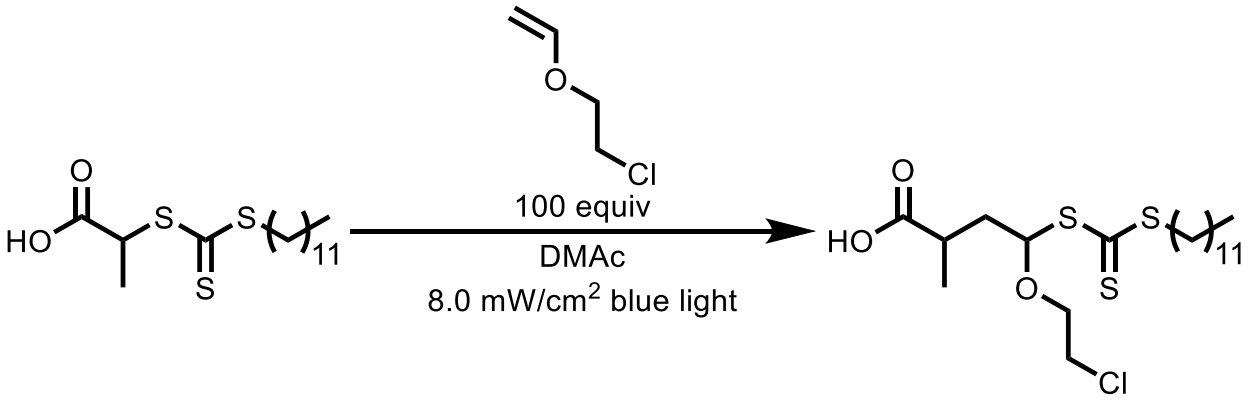

2-chloroethyl vinyl ether (1.26 g, 11.9 mmol), 2-(Dodecylthiocarbonothioylthio)propionic acid (41.6 mg, 1.19 × 10^{-1} mmol), *fac*-Ir(ppy)$_3$ (3.88 × 10^{-1} mg, 5.93 × 10^{-4} mmol) were dissolved in DMAc (1.46 mL) with DMF as an internal standard in 2-dram vials and capped with rubber septum. After degassing the solution for 5 min with Argon, the vials were placed in the 2 °C fridge and equilibrated for 1 h before turning the blue LED strip on (8.0 mW/cm^2). Vials were removed at 30 min, 60 min, 90 min, and 120 min and quenched by opening the vial to air. Conversion was determined by ^{1}H NMR spectroscopy using DMSO-d_6 as a solvent and tracking the disappearance of the methine peak at δ = 4.64 ppm.

3.6.4 Example procedure for methyl acrylate small molecule analog studies

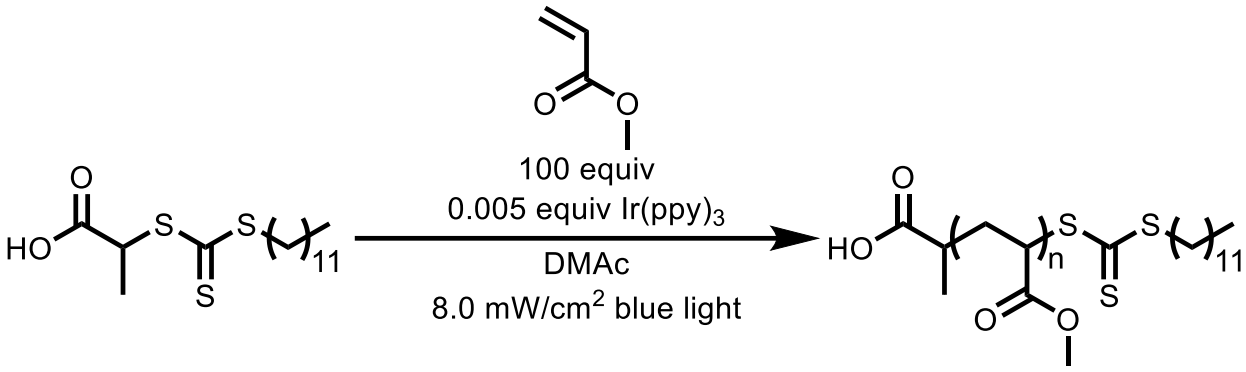

Methyl acrylate (1.02 g, 11.9 mmol), 2-(Dodecylthiocarbonothioylthio)propionic acid (41.6 mg, 1.19×10^{-1} mmol), *fac*-Ir(ppy)$_3$ (3.88×10^{-1} mg, 5.93×10^{-4} mmol) were dissolved in DMAc (1.57 mL) with DMF as an internal standard in 2-dram vials and capped with rubber septa. After degassing the solution for 5 min with Argon, the vials were placed in the 2 °C fridge and equilibrated for 1 h before turning the blue LED strip on (8.0 mW/cm^2). Vials were removed at 30 min, 60 min, 90 min, and 120 min and quenched by opening the vial to air. Conversion was determined by ^{1}H NMR spectroscopy using DMSO-d$_6$ as a solvent and tracking the disappearance of the methine peak at $\delta = 4.64$ ppm.

3.6.5 Example procedure for Single-Unit Monomer Insertion Reaction

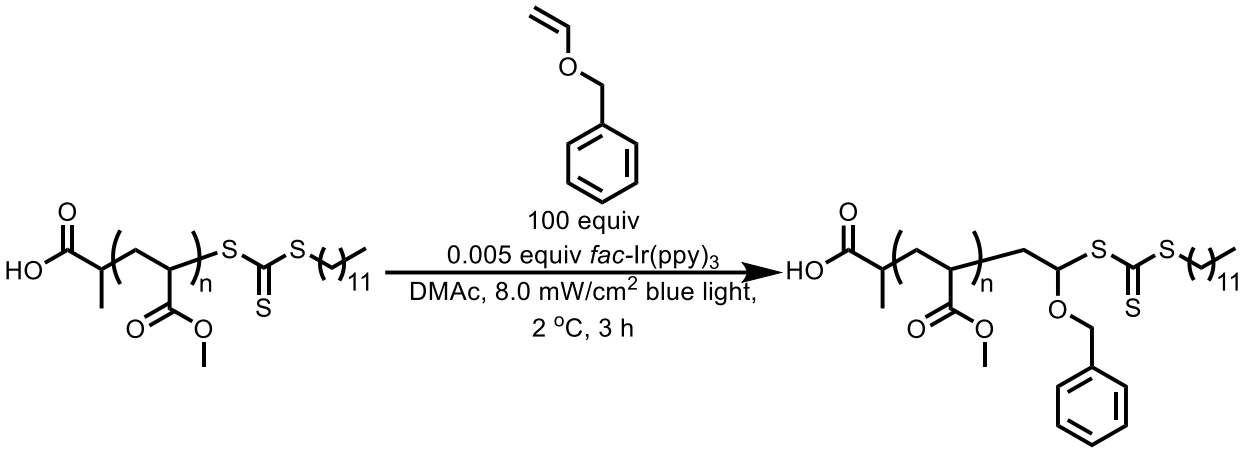

PMA (M_n = 8000 g/mol, $Đ$ = 1.06, 250 mg, 3.13 × 10^{-2} mmol), benzyl vinyl ether (419 mg, 3.13 mmol), *fac*-Ir(ppy)$_3$ (1.03 × 10^{-1} mg, 1.56 × 10^{-4} mmol) were dissolved in DMAc (0.269 mL) in a 2-dram vial and capped with a rubber septum. After degassing the solution for 5 min with Argon, the vial was placed in the 2 °C fridge and equilibrated for 1 h before turning the blue LED strip on (8.0 mW/cm^2). The sample was irradiated for 3 h and quenched by opening the vial to air. The reaction mixture was then precipitated into an excess of chilled methanol 2×, and then dried under vacuum and characterized by ^{1}H NMR spectroscopy and SEC.

3.6.6 Example procedure for chain extension

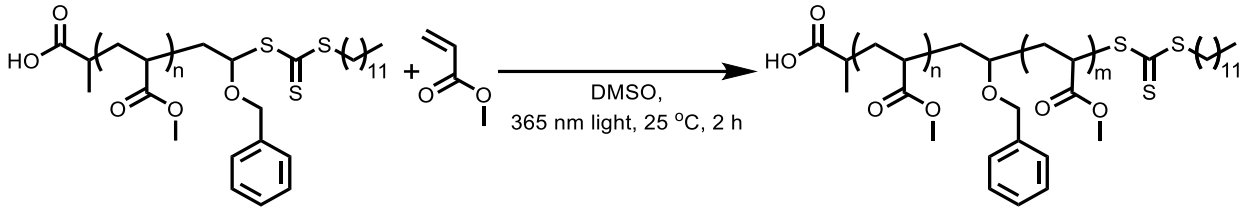

PMA-BVE (M_n = 8134 g/mol, $Đ$ = 1.10, 250 mg, 3.07 × 10^{-2} mmol) and MA (660 mg, 7.67 mmol) were dissolved in DMAc (3.14 mL) in a 2-dram vial and capped with a rubber septum. After degassing the solution for 5 min with Argon, the vial was placed approximately 4 cm from the 365 nm light source. The sample was irradiated for 2 h at 25 °C and quenched by opening the vial to air. The reaction mixture was then precipitated into an excess of chilled methanol 2×, and then dried under vacuum and characterized by ^{1}H NMR spectroscopy and SEC.

3.6.7 Example procedure for control SUMI studies (blue light)

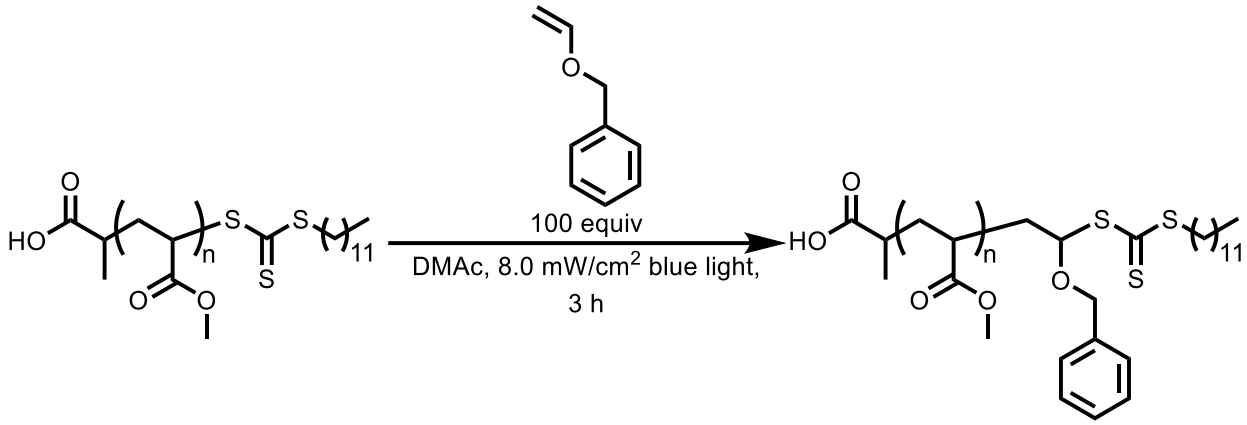

PMA (M_n = 8000 g/mol, $Đ$ = 1.06, 250 mg, 3.13 × 10^{-2} mmol) and benzyl vinyl ether (419 mg, 3.13 mmol) were dissolved in DMAc (0.279 mL) in a 2-dram vial and capped with a rubber septum. After degassing the solution for 5 min with Argon, the vial was either placed in the 2 °C fridge and equilibrated for 1 h or kept at room temperature before turning the blue LED strip on (8.0 mW/cm^2). The sample was irradiated for 3 h and quenched by opening the vial to air. The reaction mixture was then precipitated into an excess of chilled methanol 2×, and then dried under vacuum and characterized by ^{1}H NMR spectroscopy and SEC.

3.6.8 Example procedure for control SUMI studies (365 nm light)

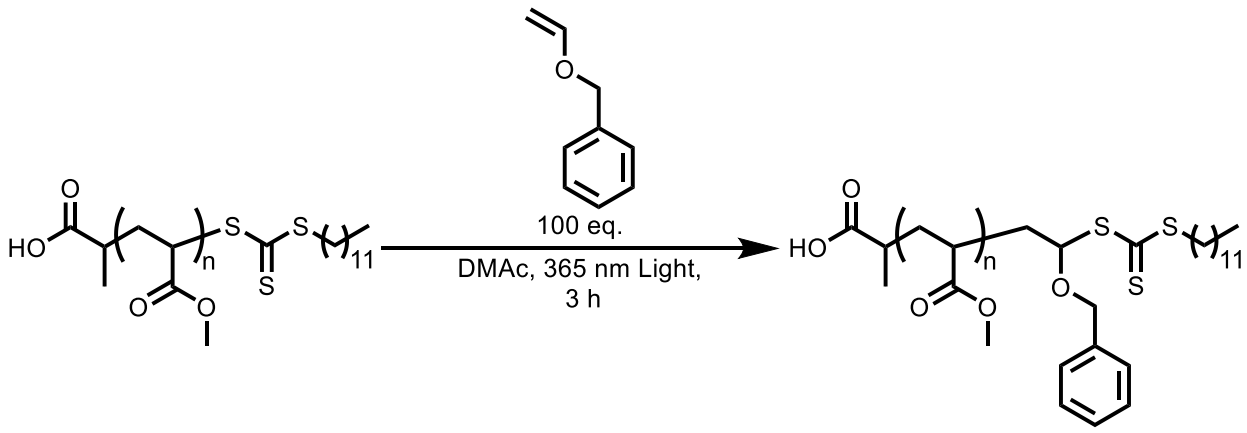

PMA (M_n = 8000 g/mol, $Đ$ = 1.06, 250 mg, 3.13 × 10^{-2} mmol) and benzyl vinyl ether (419 mg, 3.13 mmol) were dissolved in DMAc (0.279 mL) in a 2-dram vial and capped with a rubber septum. After degassing the solution for 5 min with Argon, the vial was either placed in the 2 °C fridge and equilibrated for 1 h or kept at room temperature before turning the 365 nm light on. The sample was irradiated for 3 h and quenched by opening the vial to air. The reaction mixture was then precipitated into an excess of chilled methanol 2×, and then dried under vacuum and characterized by ^{1}H NMR spectroscopy and SEC.

Chapter 4: Reverse Blocking Order of Trithiocarbonate-Mediated RAFT Polymerizations Using Photocatalysis*

Authors: Jared G. Baker, Stephen J. Koehler, Katherine J. Wood, Diego Troya, Joey Gloriod, Ian C. Anderson, Darwin C. Gomez, and C. Adrian Figg

4.1 Abstract

Many acrylic–methacrylic block copolymer sequences remain inaccessible due to synthetic limitations. Herein, photoinduced electron/energy transfer (PET) catalysis is leveraged to reverse blocking order limitations in trithiocarbonate (TTC)-mediated reversible addition–fragmentation chain transfer (RAFT) polymerization. We synthesized poly(methylacrylate-*b*-methyl methacrylate) by PET-RAFT using *fac*-Ir(ppy)$_3$, achieving predictable, linear increases in molecular weight with conversion. Kinetics studies showed that adding a tertiary amine (triethanolamine) introduced a reversible redox reaction to stabilize the TTC radical during chain extensions, leading to more uniform block copolymers ($Đ$ < 1.47) compared to block copolymers synthesized without amine ($Đ$ < 1.56). To highlight the utility of this method, triblock copolymers of poly(methyl acrylate) and poly(methyl methacrylate) blocks were investigated. The order of acrylic and methacrylic blocks impacted the physical properties of compositionally similar polymeric materials. For example, a high molecular weight triblock copolymer (P(MMA-*b*-MA-*b*-MMA), M_n = 564 kg mol^{-1}) thermoplastic elastomer showed exceptional strain (>1600%). Overall, we report (i) a new methodology to unlock synthetic access to acrylic–methacrylic block copolymers using TTCs and photocatalysis, (ii) insight into photocatalyst-mediated radical polymerization, and (iii) synthesis of new high-performance materials.

*Adapted and reproduced with permission from *Angew. Chem., Int. Ed.* **2025**, *64*, e202509029. Copyright 2025, Wiley Online Library.

4.2 Introduction

Acrylic block copolymers find wide use in lithography,[212–214] drug delivery,[215–217] adhesives,[218,219] and thermoplastic elastomers (TPE).[220–225] Synthetic routes toward block copolymers include reversible deactivation radical polymerization (RDRP),[184,226–228] anionic polymerization,[229–231] cationic polymerization,[98,232,233] and Lewis pair polymerization.[234,235] However, these techniques do not enable access to many acrylic–methacrylic block copolymers as they have limitations such as blocking order requirements, minimal chain-end fidelity, or limited monomer scope.

Blocking order requirements are dictated by the relative radical stabilities of active chain ends and restrict RDRP techniques.[203,236] More stable monomers (e.g., methacrylates—3° radicals) must be polymerized before less stable monomers (e.g., acrylates—2° radicals) to avoid incomplete reinitiation. This limitation in RDRP leads to high fractions of homopolymer impurities (**Figure 4.1a**), limiting access to many discrete AB diblock and subsequent ABA/ABC triblock copolymer sequences, which are promising for polymer compatibilization,[237–239] biomimicry,[240,241] and high-strength materials.[242,243]

Few approaches exist to reverse RDRP blocking limitations. A halogen exchange reaction or photocatalysis can be used in atom transfer radical polymerization (ATRP) to chain-extend polyacrylates with methacrylates.[8,140] However, obtaining the correct combination of halogen, catalyst, ligand, and monomers for acrylic–methacrylic block copolymers can be resource-intensive and limit access to multiblock copolymers.[244–247] Additionally, achieving high molecular weight (HMW) polymers (>150 kg mol^{-1}) using ATRP requires high pressure reaction conditions, heterogeneous systems, or dual catalysis,

and halogen-exchange on HMW polymers from ATRP is not reported.[144,150,248–252] In reversible addition–fragmentation chain transfer (RAFT) polymerization, ultra-high molecular weight polymers can be readily synthesized.[150,151] HMW polymers are of interest for applications due to the increase in entanglements (crosslinks) that are present, which can enhance material properties such as tensile strength.[253] Direct photolysis of xanthate RAFT agents can extend polyacrylates with methacrylates.[141] However, controlling molecular weights during the chain extension is challenging, only works with xanthates due to the lower carbon─sulfur bond dissociation energy (C─S BDE = 38.06 kcal mol^{-1}) compared to more commonly used trithiocarbonate RAFT agents (TTC, C─S BDE = 41.50 kcal mol^{-1}, **Figure 4.1a**),[254] and has not been reported for polymers >40 kg mol^{-1}. The limited accessibility of HMW acrylic–methacrylic block copolymers limits the ability to probe copolymer properties and applications.

Monomer-order limitations can be bypassed during a TTC-mediated RAFT polymerization by using minimal equivalents of a comonomer, but this yields a non-discrete, gradient block copolymer.[255] These impurities affect applications (e.g., lithography) that rely on distinct separation of polymer phases.[177,256] Overall, synthetic methods to access discrete acrylic–methacrylic block copolymers using RDRP are limited. We set out to develop a method to overcome monomer restrictions with TTC-mediated RDRP that would enable a broader range of accessible block copolymers, resulting in a novel P(MA-*b*-MMA-*b*-MA) triblock copolymer.

Chain transfer makes reversing blocking limitations with TTCs difficult. For example, during a chain extension of poly(methyl acrylate) (PMA, macroinitiator) with methyl methacrylate (MMA), the intermediate radical species (**Figure 4.1b**) must fragment

into **2** to initiate PMA chains for chain extension. However, the energy barrier to **2** ($\Delta G^{\ddagger}$ = +16.8 kcal mol^{-1}) exceeds fragmentation into **3** ($\Delta G^{\ddagger}$ = +11.6 kcal mol^{-1}). Fragmentation into **3** leaves PMA chains un-activated and results in free-radical polymerization of MMA.[203] To address this limitation, we expected that photoinduced electron/energy

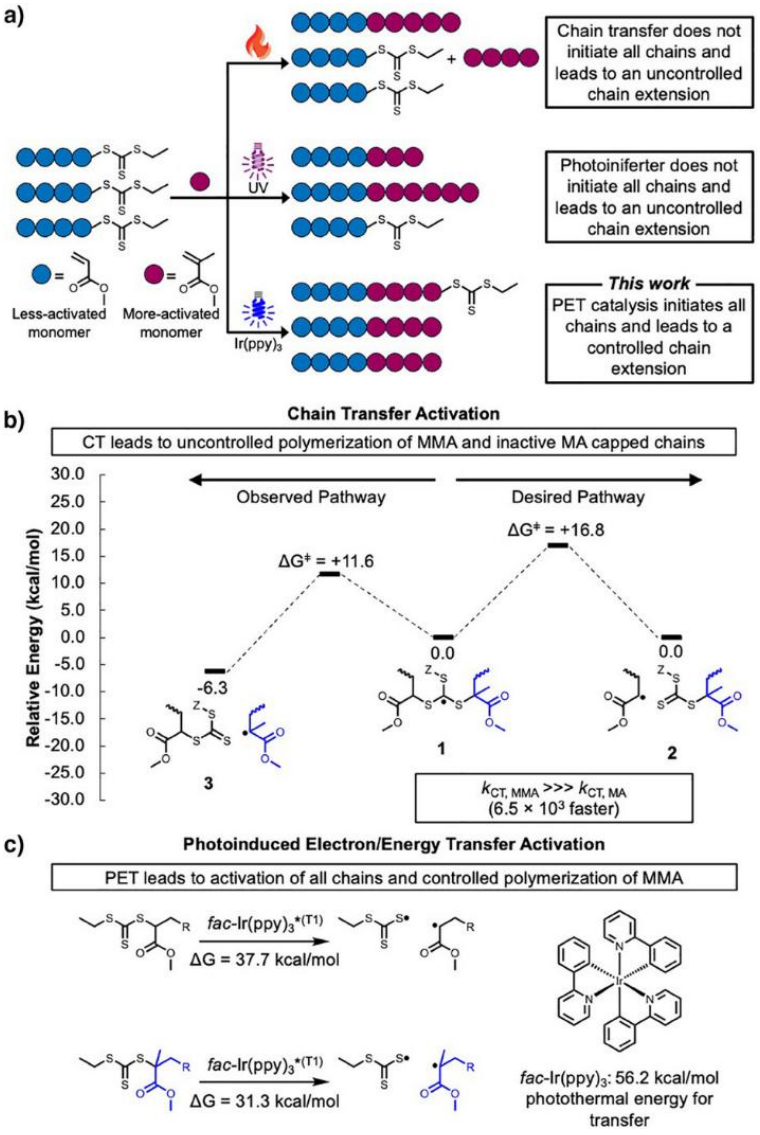

Figure 4.1. a) Initiation methods and subsequent polymer distributions when polymerizing against conventional blocking order with thermal, photoiniferter, or PET initiation methods. b) Reaction coordinate diagram depicting the chain transfer mechanism with an MA- or MMA-capped chain end. c) DFT calculations of energy required to undergo homolytic cleavage of MA- and MMA-capped chains and the amount of photothermal energy *fac*-Ir(ppy)$_3$ can provide.[207]

transfer (PET) catalysis using *fac*-Ir(ppy)$_3$ will overcome blocking-order requirements in TTC-mediated RAFT polymerization and minimize differences in chain-end BDE (**Figure 4.1a**). PET-RAFT polymerization, first reported by the Boyer group,[55,66,97] can be performed with various photocatalysts across the visible light spectrum. Compared to photoiniferter, direct photolysis of the C─S bond on the R-group of a RAFT polymerization chain transfer agent (CTA),[57] PET-RAFT polymerization uses a photocatalyst to cleave the C─S bond of the R-group on the CTA, leading to a wider variety of wavelengths and initiation pathways (e.g., energy transfer, oxidative electron transfer, reductive electron transfer).[57,100]

Our model density functional theory (DFT) calculations of MA and MMA chains capped with a TTC predict bond dissociation energies (BDE) of 37.7 and 31.3 kcal mol^{-1}, respectively (**Figure 4.1c**). The photocatalyst, *fac*-Ir(ppy)$_3$,[14,55] liberates 56.2 kcal mol^{-1} of photothermal energy following excitation;[257] thus, *fac*-Ir(ppy)$_3$ could readily achieve direct C─S homolysis of both TTC-capped species. We hypothesized that *fac*-Ir(ppy)$_3$, which goes through an energy transfer pathway,[100,207,258] would enable us to reverse conventional blocking order limitations with TTCs. In sum, we envisioned that the blocking order limitations that have plagued TTC-mediated RDRP could be overcome using PET catalysis, enabling synthetic access to previously inaccessible and potentially useful (multi)block copolymers.

4.3 Results and Discussion

A thermally initiated RAFT polymerization yielded the first block of PMA (13.3 kg mol^{-1}, $Đ$ = 1.06). Next, we compared chain extension polymerizations with MMA under thermally initiated RAFT (purple traces), photoiniferter (pink traces), or PET-RAFT (blue

traces) polymerization conditions using size-exclusion chromatography (SEC, **Figure 4.2a–c**). We chose polymerization conditions according to common (PET-)RAFT polymerizations (**Figure 4.2a**, 300 equiv MMA, 5 mM [PMA], 0.1 equiv 4,4′-azobis(4-cyanovaleric acid) or 0.005 equiv *fac*-Ir(ppy)$_3$ when applicable). The light-mediated polymerizations at 25 °C yielded broad SEC traces (**Figure B1**); thus, we increased the temperature to 40 °C to increase the rate of activation by PET,[14] leading to faster activation of chain-ends and more uniform polymer chains, which resulted in narrower SEC traces than at 25 °C. Both thermally initiated RAFT and photoiniferter polymerizations yielded bimodal chromatograms. These bimodal traces, characteristic of TTC-mediated polymerizations going against monomer blocking-order restrictions, suggested populations of unreacted PMA, the desired P(MA-*b*-MMA) copolymers, and uncontrolled PMMA.[141] The PET-RAFT polymerization showed a monomodal shift to lower retention times with a corresponding shift in the UV–vis absorbance of the TTC (**Figure B2**). These results suggested that the distinct initiation mechanism of PET-RAFT polymerization can be used to overcome monomer restrictions in TTC-mediated polymerizations. However, the PET-RAFT trace was broad ($Đ$ = 1.33) and did not align with expected number-average molecular weights (M_n, $M_{n,theory}$ = 33.4 kg mol^{-1} versus $M_{n,SEC}$ = 18.4 kg mol^{-1})

To investigate how to improve molecular weight agreement, we investigated the effect of macroinitiator concentration. We expected that unimolecular and bimolecular processes affect interchain proximity and radical concentration, which impact the activation–deactivation, chain transfer, and termination reactions (**Figure 4.2d–g**).[259] As termination occurs bimolecularly in RAFT polymerizations,[259] we expected that decreased [PMA] would decrease the amount of termination. Decreasing the concentration of PMA

in solution results in a decrease in the concentration of radical species. We expected that by decreasing [radical] by decreasing [PMA], there would be less termination. To measure the effect of [PMA], we performed polymerizations at 2 mM [PMA] (**Figure 4.2b**, 250 equiv MMA, 0.1 equiv 4,4′-azobis(4-cyanovaleric acid) or 0.01 equiv *fac*-Ir(ppy)$_3$ when

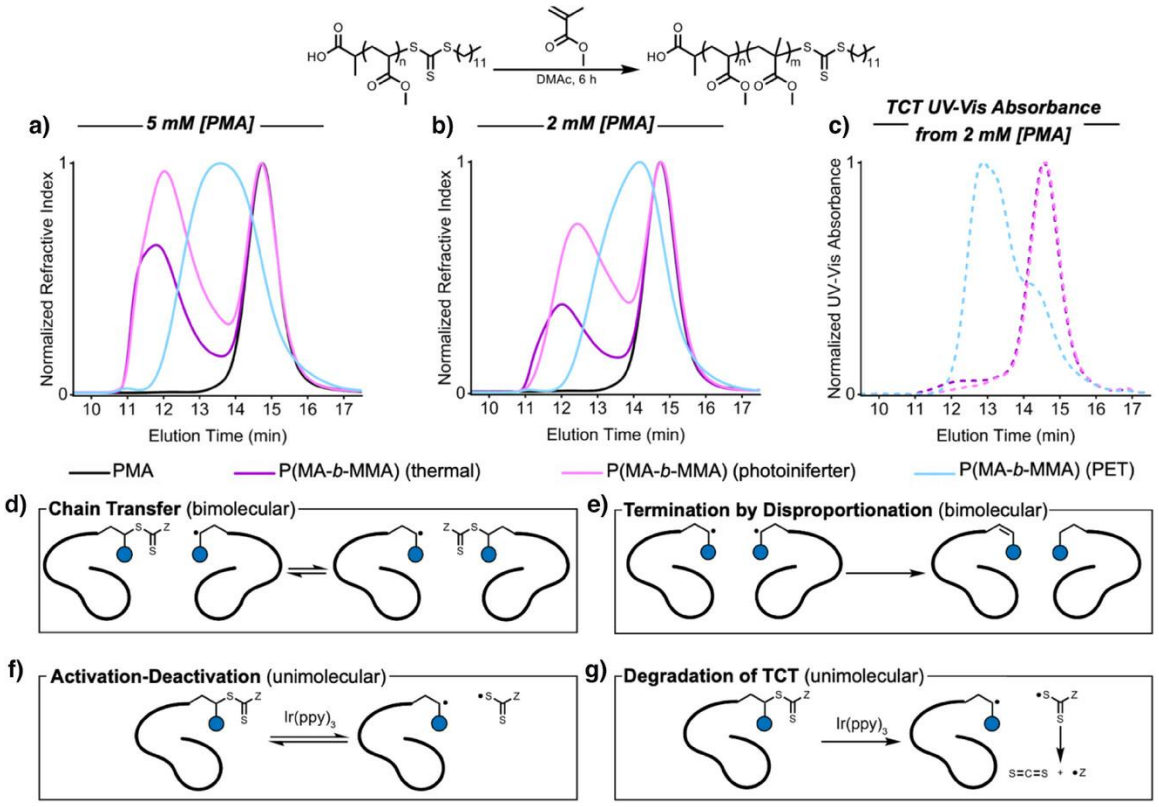

Figure 4.2. Refractive index traces of PMA chain extensions with MMA using thermal, photoiniferter, or PET initiation at 5 mM a) or 2 mM b) [PMA]. c) UV–vis traces of P(MA-b-MMA) following chain extension at 2 mM [PMA]. Cartoon representations of bimolecular chain end activation d), bimolecular termination e), unimolecular chain end activation f), and unimolecular termination g).

applicable). We compared these conditions to conventional PET-RAFT conditions (where [PMA] = 5 mM, **Figure 4.2a**). As expected, we observed bimodal chromatograms for thermal and photoiniferter while the PET-RAFT polymerization conditions showed a narrower chromatogram compared to when [PMA] = 5 mM.

These data suggest that higher [PMA] favors unproductive bimolecular chain transfer reactions (**Figure 4.2d**) and termination (**Figure 4.2e**) that led to higher *Đ* values (1.33), while decreased [PMA] led to lower *Đ* values (1.20) determined by multi-angle light scattering. Following PET activation (**Figure 4.2f**), we suspect that the TTC radical degrades, contributing to termination by loss of the deactivating species (**Figure 4.2g**), as the sulfur-centered TTC radicals resulting from PET activation can degrade or initiate new chains.[260] To counteract this we introduced a competing TTC stabilization pathway.

Tertiary amines can reduce a TTC radical to a TTC anion, preventing degradation or initiation of new chains.[105,106,153,261–263] To stabilize the TTC radical via a tertiary amine mediated reversible redox pathway, triethanolamine (TEOA) was added to the system. Experiments comparing [PMA] and *fac*-Ir(ppy)$_3$ loading (**Figures B3–B8**) in the presence of TEOA showed that [PMA] = 2 mM and 0.01 equiv of *fac*-Ir(ppy)$_3$ yielded narrow and symmetric SEC traces with increasing molar masses and low *Đ* values. However, the UV–vis absorbance traces from the PET-RAFT polymerizations with TEOA showed slightly higher absorbance values compared to no TEOA (**Figure B2**).

We investigated polymerization kinetics to further evaluate the impact of TEOA on PET-RAFT polymerizations. Reaction aliquots were taken during a 6 h chain extension polymerization of PMA with MMA with 0 or 1 equiv of TEOA. Without TEOA, the pseudo-first-order kinetics plot showed a linear relationship up to 4 h. After 4 h, we observed a minor decrease in the apparent rate, indicating a decrease in radical concentration likely due to TTC degradation/termination (**Figure 4.3a**). The M_n versus conversion plot agreed with the expected molar masses measured by ^{1}H nuclear magnetic resonance (NMR) spectroscopy monomer conversion and the experimental molecular

weights measured by SEC using PMMA standards, but $Đ$ increased with conversion (MMA conversion = 38 ± 2% and $Đ$ = 1.56 at 6 h, **Figure 4.3b**). The SEC refractive index (RI) traces shifted to lower elution times with increasing monomer conversion, showing a minor shoulder throughout (**Figure 4.3c and B9**). Similar kinetics were observed with the addition of 1 equiv of TEOA (**Figure 4.3d–f and B10**). However, lower $Đ$ values persisted throughout the polymerization (MMA conversion = 39 ± 2% and $Đ$ = 1.47 at 6 h). Deconvolution of the 6 h RI traces showed that polymerizations with TEOA increased the number of extended chains from 86% to 91% (**Figure B11 and B12**). We observed similar kinetic data with poly(*N*,*N*-dimethylacrylamide) (PDMA) as the macroinitiator and the difference in the starting polymer seemed to only minorly affect the efficiency of the chain extensions (**Figure B13**). Overall, kinetics indicated a controlled MMA chain-extension polymerization from polyacrylates and polyacrylamides by using *fac*-Ir(ppy)$_3$ combined with TEOA showing linear pseudo-first-order kinetics, linearly increasing M_n with conversion, and moderate $Đ$.

To further compare if TEOA stabilized TTCs during the PET-RAFT polymerizations, absorbance at 365 nm in-line with SEC was used to quantify TTC throughout the polymerization. When TEOA was present, up to a 12% improvement in TTC retention was observed compared to reactions without TEOA during the first 3 h (**Figure 4.3g**). We expected that TEOA undergoes a reversible redox reaction with the TTC radical to form the more stable TTC anion and an amine radical cation.[105,106,153,261–263] However, a continuous decline in UV–vis absorbance occurred throughout the chain extension. The decline in TCT UV–vis absorbance indicated termination events, which are substantiated by the increase in $Đ$ values. We investigated if additional TEOA could retain

more chain-ends in the reaction. However, using 2 or 5 equiv of TEOA resulted in decreased UV–vis absorbance compared to 1 equiv of TEOA (**Figures B14–B17**). These results show increasing TEOA does not improve or prolong chain-end retention.

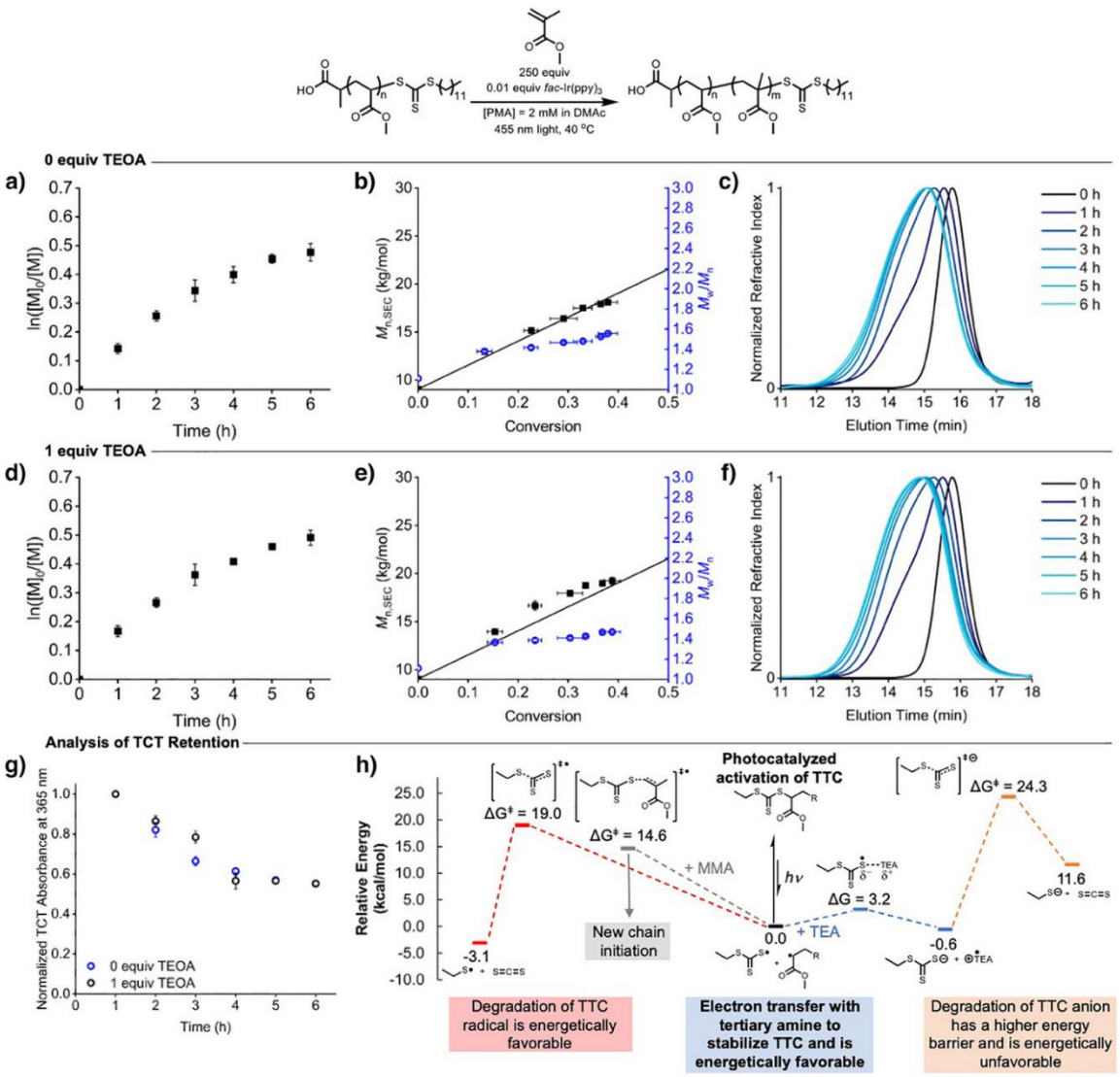

Figure 4.3. Pseudo-first-order kinetics plot with 0 a) or 1 (d) equiv TEOA. M_n and $Đ$ plot with 0 b) or 1 (e) equiv TEOA versus PMMA standards. RI traces of polymerization progress with 0 c) or 1 (f) equiv TEOA. g) UV–vis absorbance versus time with 0 and 1 equiv TEOA. h) DFT calculations of accessible routes for the TTC radical species presented in an energy coordinate diagram.

DFT calculations were performed to investigate the energetics for the reversible redox reaction introduced by the amine (**Figure 4.3h**). These calculations indicated that

electron transfer between the TTC radical and the amine is nearly thermoneutral (ΔG = −0.6 kcal mol^{-1}) via an accessible [TTC-amine] radical complex (ΔG = +3.2 kcal mol^{-1}). We predicted that degradation of the TTC anion via decarboxylation ($\Delta G^{\ddagger}$ = +24.9 kcal mol^{-1}, ΔG = +12.1 kcal mol^{-1}) is much less likely than decarboxylation from the radical form ($\Delta G^{\ddagger}$ = +19.0 kcal mol^{-1}, ΔG = −3.1 kcal mol^{-1}). Interestingly, the most likely predicted control-limiting mechanistic pathway for the TTC radical is addition to MMA, which showed an energy barrier like MMA homopropagation ($\Delta G^{\ddagger}$ = +14.6 kcal mol^{-1}). However, we expect this pathway to be minimized in the presence of TEOA. These data suggest that TEOA plays a minor role in limiting the degradation of the deactivating species (TTC) during the polymerization by introducing a reversible redox pathway to stabilize the TTC radical. Future studies into more reducing tertiary (multi)amines or other reducing agents capable of performing a TTC radical reduction redox reaction could further improve chain-end retention of TTC during the chain extension.

To delineate the effects of discrete block sequence order on physical properties, we synthesized P(MMA-*b*-MA-*b*-MMA) and P(MA-*b*-MMA-*b*-MA) using a bis-TTC to achieve bidirectional growth of block copolymers (**Figure 4.4a**). These block sequences impacted physical properties with the triblock copolymer following conventional monomer blocking order (P(MA-*b*-MMA-*b*-MA)) exhibiting brittle behavior and 8.6 MPa stress and 3.6% strain at break (**Figure B18**), while the triblock copolymer made by the reported PET conditions (P(MMA-*b*-MA-*b*-MMA)) exhibited elastomeric behavior compared to the counterpart, but more fittingly can be described as a ductile material with a 19 MPa stress and 33% strain at break (**Figure B19**). The change in block sequence (P(MMA-*b*-MA-*b*-MMA) versus P(MA-*b*-MMA-*b*-MA)) resulted in over a 200% greater stress and 900%

greater strain at break. These data confirm that the block sequences accessible using PET-RAFT polymerization directly impact physical properties. However, recent observations indicate that although the overall molecular weights and monomer weight fractions are similar, the block lengths differ between the two samples for the hard and soft segments. To elucidate the effects of changes in block order on physical properties, an additional set of block copolymers would need to be synthesized, keeping the lengths of the outer and inner blocks constant while varying the monomers, as well as keeping one block constant while the others are varied. As previously shown in the literature, both the hard and soft segment block lengths alter the thermal properties of the bulk material, such as the glass transition temperature (T_g), while also affecting physical properties, including tensile stress and strain.[264–272] Due to these factors, further testing needs to be performed to properly explore the impact of soft-hard-soft and hard-soft-hard triblock copolymers that were synthesized in this study.

Finally, because TTC-mediated polymerizations provide unprecedented access to HMW acrylic polymers, we synthesized a HMW P(MMA-*b*-MA-*b*-MMA) block copolymer using a bis-TTC (M_n = 564 kg mol^{-1}, **Figure 4.4b**). The HMW TPE did not break up to 1600% strain (1.6 MPa stress) when subjected to tensile testing, but rather thinned and slipped out of the clamps (**Figure B20**). To investigate if the sample had shape recovery, we subjected it to further tensile testing. The sample (starting length = 26 mm) was pulled to 1001% strain and allowed 10 min to recover. The HMW TPE fully recovered to a final length of 27 mm while remaining transparent. HMW are desirable for applications as the additional effective chain entanglements can lead to improvements in properties such as tensile stress, while also impacting melt viscosity and shear modulus, and provides

access to unique properties.[273,274] Notably, two discrete glass transition temperatures are observed for the low molecular weight samples that correspond to the MA and MMA blocks at ~19 °C for MA and ~125 °C for MMA, indicating that phase separation is occurring within the system or only 1 T_g would be visible. Although these values do not directly align with literature values for these respective polymers they are within 15 °C. However, the HMW sample only has 1 T_g that corresponds to the MA region. Due to the T_g appearing at ~19 °C, it does not indicate that the blocks are no longer phase separated, but rather that the T_g of the MMA portion was suppressed beyond detection levels. To further confirm this small angle X-ray scattering could be performed to confirm that phase separation is still present in the sample. These results suggested this PET-RAFT polymerization method can be used to produce a variety of acrylic/methacrylic "superelastomeric" materials.[222,275]

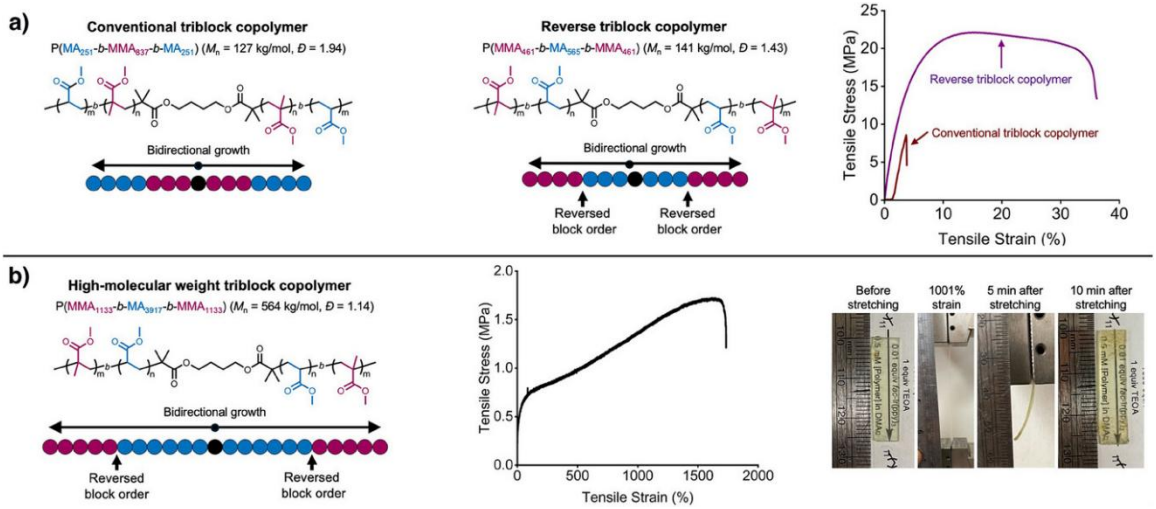

Figure 4.4. a) Copolymer sequences synthesized with representative cartoons and stress versus strain curves. b) HMW block copolymer synthesized by bifunctional growth, stress versus strain curve, and images depicting the sample before, during, and after being pulled to 1001% strain.

4.4 Conclusions

In this study, we found that PET catalysis can reverse conventional blocking order requirements in TTC-mediated RAFT polymerizations and provide access to HMW acrylic–methacrylic block copolymers. Using greater catalyst loadings (0.01 equiv) and lower macroinitiator concentrations (2 mM) than typical for PET-RAFT polymerizations showed a controlled polymerization. TEOA stabilized the TTC radical through an electron transfer, corroborated by DFT calculations, and enhanced chain-end retention compared to polymerizations without TEOA. These advances enabled access to novel block copolymer sequences that were inaccessible by RAFT polymerization or ATRP with significantly different physical properties according to the block sequence, exemplified by a HMW superelastomeric P(MMA-*b*-MA-*b*-MMA) TPE. Overall, this work provides critical insight into how photocatalysis can be used to access novel high-performance polymeric materials.

4.5 Experimental

4.5.1 Materials

Methyl acrylate (MA, Thermo Scientific, 99%), methyl methacrylate (MMA, Thermo Scientific, 99%), *N*,*N*-dimethylacrylamide (DMA, TCI, >99%), ethyl acrylate (EA, Sigma Aldrich, 99%), isobutyl acrylate (*i*BA, Sigma Aldrich, 99+%), n-butyl methacrylate (*n*BMA, Fluka, >99%) and tert-butyl methacrylate (*t*BMA, Sigma Aldrich, 98%) were filtered through basic alumina prior to use. *fac*-Ir(ppy)$_3$ (Strem Chemicals, 95%) was prepared as a 10 mg/mL solution in *N,N*-dimethylacetamide (DMAc) prior to use. Triethanolamine (TEOA, Sigma Aldrich, >99%) was prepared as a 20x dilution in DMAc prior to use. 4,4-azobis(4-cyanovaleric acid) (ACVA, Sigma Aldrich, >98%) was

prepared as a 20 mg/mL solution in reaction solvent prior to use. 2-(Dodecylthiocarbonothioylthio)propionic acid (DTPA) and 2-(dodecylthiocarbonothioylthio)-2-methylpropionic acid were synthesized according to a previous report.[211] Butane-1,4-diyl bis(2-(((dodecylthio)carbonothioyl)thio)-2-methylpropanoate) (bis-TTC) was synthesized using a modified approach from a previous report.[276] *N*,*N*-dimethylacetamide (Thermo Scientific, 99%), dimethyl sulfoxide (Thermo Scientific, 99.7%), and *N*,*N*-dimethylformamide (Acros Organics, 99.8%) were used as received.

For a visible light source, 76.2 cm Supernight Blue Light Strips were purchased from Amazon and placed on a Xnrtop Silver Tone Aluminum Radiator Heat Sink 150 × 80 × 27 mm from Amazon. For an ultraviolet light source, an Everbeam 365 nm 50 W UV LED Black Light from Amazon was used. For a heating source a Thermo Scientific MaxQ 6000 shaker deck was used.

4.5.2 Characterization

^{1}H NMR spectroscopy was conducted on an Agilent U4-DD2 400 MHz. DMSO-d_6 (Cambridge Isotopes Laboratories, Inc., 99.9%) and $CDCl_3$ (Cambridge Isotopes Laboratories, Inc., 99.8%) were used as received.

Size Exclusion Chromatography (SEC) was performed in *N*,*N*-dimethylacetamide (DMAc) with 50 mM LiCl at 50 °C at a flow rate of 0.5 mL min^{-1} (Agilent isocratic pump, degasser, and autosampler, columns: TOSOH TSKgel Guard Alpha and a TOSOH TSKgel Alpha-3000: molecular weight range 0–1 × 10^5 g mol^{-1} or a TOSOH TSKgel Alpha-4000: molecular weight range 0–1 × 10^6 g mol^{-1}). Detection consisted of a Wyatt Optilab refractive index detector operating at 785 nm, a Wyatt DAWN multi-angle light scattering

detector operating at 783 nm, and an Agilent MWD operating at 365 nm. Absolute molecular weights and dispersities were calculated with the Wyatt ASTRA software and d*n*/d*c* values were determined by performing refractive index 100% recovery methods in the Wyatt ASTRA software. Or SEC was performed in *N*,*N*-dimethylacetamide (DMAc) with 50 mM LiCl at 50 °C at a flow rate of 0.5 mL min^{-1} (Agilent 1260 Infinity II isocratic pump, degasser, and autosampler, columns: TOSOH TSKgel Guard Alpha and a TOSOH TSKgel Alpha-3000: molecular weight range 0–1 × 10^5 g mol^{-1} or a TOSOH TSKgel Alpha-4000: molecular weight range 0–1 × 10^6 g mol^{-1}). Detection consisted of an Agilent VWD operating at 365 nm and an Agilent RID. Molecular weights and dispersities were calculated using column calibration with poly(methyl methacrylate) standards with molecular weights in the range of 902 to 116,000 g/mol, which corresponds to a linear calibration region of 12.3 to 18.6 minutes.

Differential Scanning Calorimetry (DSC) was performed using a heat/cool/heat cycle between -40 °C and 150 °C at heating/cooling rate of 10 °C/min under a nitrogen stream of 50 mL/min on a Discovery DSC2500 (TA Instruments). The samples were prepared by annealing at 140 °C for 72 hours under vacuum following synthesis and end-group removal.

Tensile testing was performed on an Instron 68TM-30 with a 30 kN capacity. The samples were prepared by annealing at 140 °C for 72 hours under vacuum following synthesis and end-group removal. After annealing, the samples were melt pressed at 150 °C, and cut into 12.7 mm by 6.35 mm rectangles for testing.

Visible light intensity was measured with an International Light Technologies ILT-350 illuminance spectrophotometer with a NIST traceable ISO17025 accredited calibration.

4.5.3 Density Functional Theory Calculations

All geometry optimizations and harmonic frequency calculations were conducted with the ωB97X-D functional[277] and 6-311+G(d,p) basis set as implemented in Gaussian09.[278] An "ultrafine" integration grid and standard cutoffs were used in all calculations. Implicit solvation with *N,N*-dimethylacetamide was accomplished via the SMD model.[279] The calculations use a reduced-dimensionality ethyl trithiocarbonate to model the dodecyl trithiocarbonate chain-transfer agent used in the experiments. Triethanolamine was modeled as triethylamine. All reported energies correspond to Gibbs energies at 298 K and 1 atm.

4.6 Procedures

4.6.1 Synthesis of Butane-1,4-diyl bis(2-(((dodecylthio)carbonothioyl)thio)-2-methylpropanoate) (DiTTC)[276]

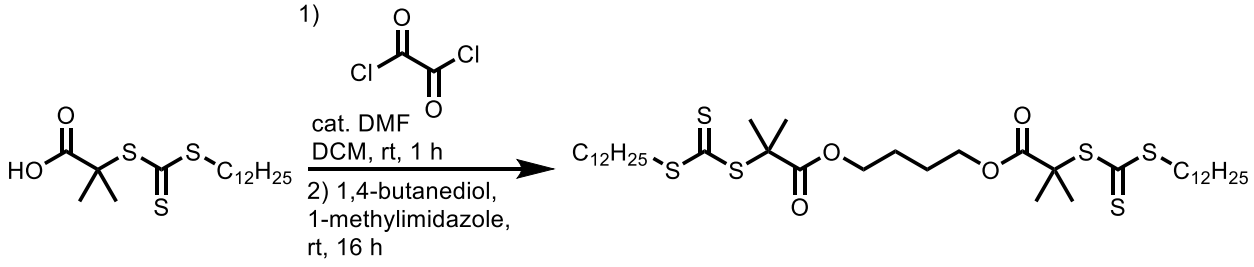

2-(dodecylthiocarbonothioylthio)-2-methylpropionic acid (2.179 g, 5.98 mmol), DCM (25 mL), and a catalytic amount of *N*,*N*-dimethylformamide (0.05 mL) were combined in a flame dried 100 mL round bottom flask under argon. Oxalyl chloride (6.28 mmol) was immediately added to the round bottom flask under argon and the reaction was

stirred for 1 hour at room temperature. Next, 1,4-butanediol (3.29 mmol) was added dropwise over the course of one minute. Lastly, 1-methylimidazole (6.58 mmol) was added immediately to quench the HCl produced. The reaction was stirred overnight at room temperature. The reaction was diluted with more DCM (10 mL) and washed with water (3× 100 mL) and brine (3× 100 mL). The organic layers were collected and dried with magnesium sulfate and the organic phase was rotovapped to dry. The bis-TTC was yielded as a dark yellow/orange oil (45%) after purification by precipitation and trituration with cold methanol. ^{1}H NMR (400 MHz, $CDCl_3$): δ = 0.80 (t, -CH_2-C$\underline{H}_3$, 6H), 1.10-1.36 and 1.65-1.75 (m, -(C$\underline{H}_2$)$_{10}$-CH_3, 40H), 1.60 (s, -C(C$\underline{H}_3$)$_2$, 12H), 3.18 (t, S-C$\underline{H}_2$, 4H), and 4.03 (m, O-C$\underline{H}_2$, 4H).

4.6.2 Example polymerization for starting poly(methyl acrylate) (PMA)

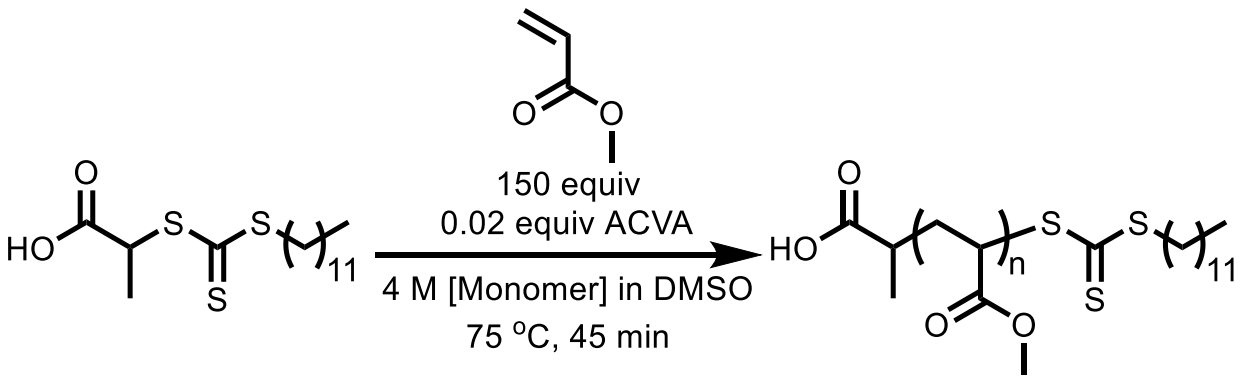

DMSO (33.8 mL), MA (18.4 g, 214 mmol), 2-(Dodecylthiocarbonothioylthio)propionic acid (500 mg, 1.42 mmol), and ACVA (7.98 mg, 2.85×10^{-2} mmol) were combined in a 50 mL Schlenk flask. DMF was added as an internal ^{1}H nuclear magnetic resonance (NMR) spectroscopy standard. The mixture was covered in aluminum foil and degassed with Argon for 30 min. The mixture was placed in a preheated 75 °C oil bath for 45 minutes. The reaction was then stopped by opening the flask to air and removing from the oil bath, the mixture was then precipitated into an excess

of chilled methanol 2×, and then dried under vacuum and characterized by ^{1}H NMR spectroscopy and SEC.

4.6.3 Example polymerization for starting poly(N,N-dimethylacrylamide) (PDMA)

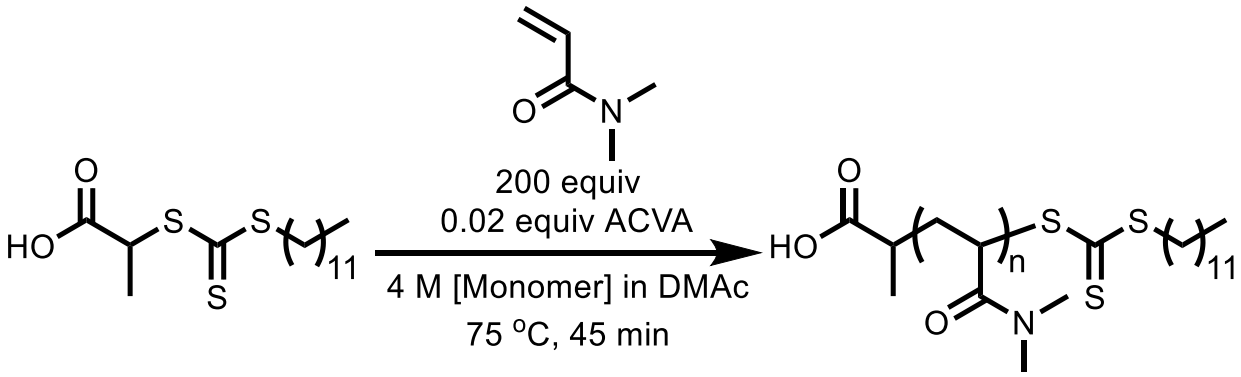

DMAc (24.9 mL), DMA (16.9 g, 171 mmol), 2-(Dodecylthiocarbonothioylthio)propionic acid (300 mg, 0.855 mmol), and ACVA (4.78 mg, 1.71 × 10^{-2} mmol) were combined in a 50 mL Schlenk flask. DMF was added as an internal ^{1}H nuclear magnetic resonance (NMR) spectroscopy standard. The mixture was covered in aluminum foil and degassed with Argon for 30 min. The mixture was placed in a preheated 75 °C oil bath for 45 minutes. The reaction was then stopped by opening the flask to air and removing from the oil bath, the mixture was then precipitated into an excess of chilled diethyl ether 2×, and then dried under vacuum and characterized by ^{1}H NMR spectroscopy and SEC.

4.6.4 Example procedure for 5 mM reverse blocking order controls

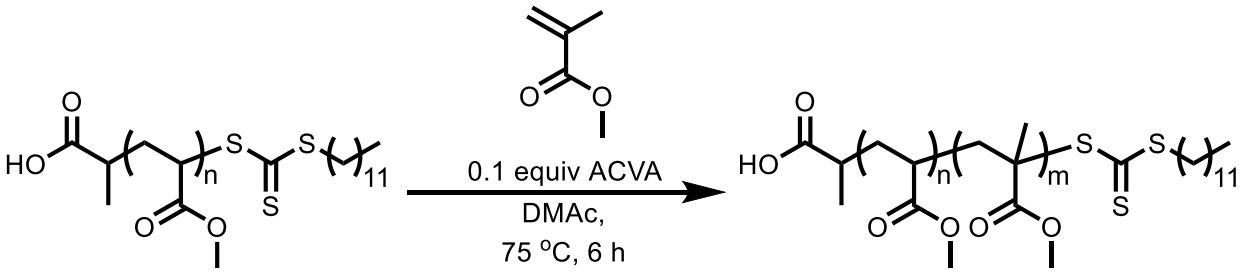

Condition 1 (Purple Trace):

DMAc (1.80 mL), MMA (0.342 g, 3.42 mmol, 300 equiv), 13.3 kg/mol PMA terminated with a trithiocarbonate (152 mg, 1.14×10^{-2} mmol, 1 equiv), and ACVA (0.319 mg, 1.14×10^{-3} mmol, 0.1 equiv) were combined in a 25 mL Schlenk flask. DMF was added as an internal ^{1}H nuclear magnetic resonance (NMR) spectroscopy standard. The mixture was covered in aluminum foil and degassed with Argon for 10 min. The mixture was placed in a preheated 75 °C oil bath for 6 hours. The reaction was then stopped by opening the flask to air and removing from the oil bath, the mixture was then precipitated into an excess of chilled methanol 2×, and then dried under vacuum and characterized by ^{1}H NMR spectroscopy and SEC.

Condition 2 (Pink Trace):

DMAc (1.78 mL), MMA (0.336 g, 3.36 mmol, 300 equiv), and 13.3 kg/mol PMA terminated with a trithiocarbonate (149 mg, 1.12×10^{-2} mmol, 1 equiv) were combined in a 2 dram scintillation vial. DMF was added as an internal ^{1}H nuclear magnetic resonance (NMR) spectroscopy standard. The mixture was covered in aluminum foil and degassed with Argon for 10 min. The mixture was placed over a 365 nm light 2 cm away from the light source for 6 hours. The reaction was then stopped by opening the vial to air and turning off the light, the mixture was then precipitated into an excess of chilled methanol 2×, and then dried under vacuum and characterized by ^{1}H NMR spectroscopy and SEC.

Condition 3 (Blue Trace):

DMAc (1.86 mL), MMA (0.351 g, 3.51 mmol, 300 equiv), 13.3 kg/mol PMA terminated with a trithiocarbonate (156 mg, 1.17×10^{-2} mmol, 1 equiv), and *fac*-Ir(ppy)$_3$ (0.0384 mg, 5.85×10^{-5} mmol, 0.005 equiv) were combined in a 2 dram scintillation vial. DMF was

added as an internal ^{1}H nuclear magnetic resonance (NMR) spectroscopy standard. The mixture was covered in aluminum foil and degassed with Argon for 10 min. The mixture was equilibrated for 1 hour at 40 °C and placed over a 455 nm light, 2 cm away from the light source for 6 hours. The reaction was then stopped by opening the vial to air and turning off the light, the mixture was then precipitated into an excess of chilled methanol 2×, and then dried under vacuum and characterized by ^{1}H NMR spectroscopy and SEC.

4.6.5 Example procedure for 2 mM reverse blocking order controls

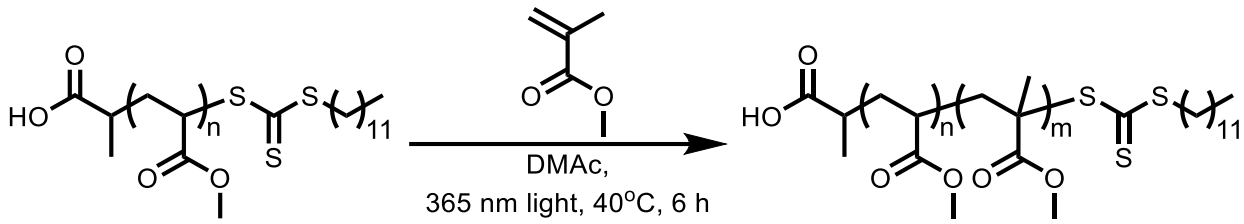

Condition 1 (Purple Trace):

DMAc (5.33 mL), MMA (0.287 g, 2.87 mmol, 250 equiv), 13.3 kg/mol PMA terminated with a trithiocarbonate (153 mg, 1.15×10^{-2} mmol, 1 equiv), and ACVA (0.322 mg, 1.15×10^{-3} mmol, 0.1 equiv) were combined in a 25 mL Schlenk flask. DMF was added as an internal ^{1}H nuclear magnetic resonance (NMR) spectroscopy standard. The mixture was covered in aluminum foil and degassed with Argon for 10 min. The mixture was placed in a preheated 75 °C oil bath for 6 hours. The reaction was then stopped by opening the flask to air and removing from the oil bath, the mixture was then precipitated into an excess of chilled methanol 2×, and then dried under vacuum and characterized by ^{1}H NMR spectroscopy and SEC.

Condition 2 (Pink Trace):

DMAc (5.82 mL), MMA (0.313 g, 3.13 mmol, 250 equiv), and 13.3 kg/mol PMA terminated with a trithiocarbonate (167 mg, 1.25×10^{-2} mmol, 1 equiv) were combined in a 2 dram scintillation vial. DMF was added as an internal ^{1}H nuclear magnetic resonance (NMR) spectroscopy standard. The mixture was covered in aluminum foil and degassed with Argon for 10 min. The mixture was placed over a 365 nm light 2 cm away from the light source for 6 hours. The reaction was then stopped by opening the vial to air and turning off the light, the mixture was then precipitated into an excess of chilled methanol 2×, and then dried under vacuum and characterized by ^{1}H NMR spectroscopy and SEC.

Condition 3 (Blue Trace):

DMAc (5.34 mL), MMA (0.288 g, 2.88 mmol, 250 equiv), 13.3 kg/mol PMA terminated with a trithiocarbonate (153 mg, 1.15×10^{-2} mmol, 1 equiv), and *fac*-Ir(ppy)$_3$ (0.0754 mg, 1.15×10^{-4} mmol, 0.01 equiv) were combined in a 2 dram scintillation vial. DMF was added as an internal ^{1}H nuclear magnetic resonance (NMR) spectroscopy standard. The mixture was covered in aluminum foil and degassed with Argon for 10 min. The mixture was equilibrated for 1 hour at 40 °C and placed over a 455 nm light, 2 cm away from the light source for 6 hours. The reaction was then stopped by opening the vial to air and turning off the light, the mixture was then precipitated into an excess of chilled methanol 2×, and then dried under vacuum and characterized by ^{1}H NMR spectroscopy and SEC.

4.6.6 Example procedure for reverse blocking order kinetics with PMA

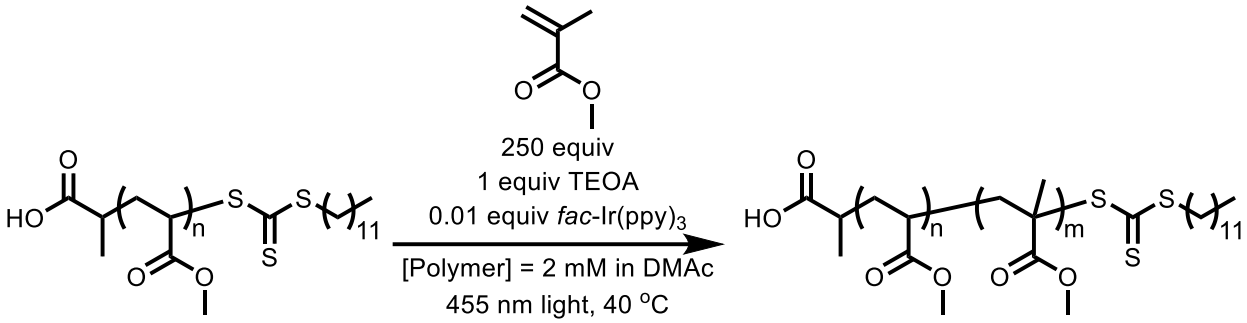

DMAc (48.3 mL), MMA (2.68 g, 26.8 mmol, 250 equiv), 13.3 kg/mol PMA terminated with a trithiocarbonate (1.42 g, 0.107 mmol, 1 equiv), *fac*-Ir(ppy)$_3$ (0.700 mg, 1.07×10^{-3} mmol, 0.01 equiv), and TEOA (15.9 mg, 0.107 mmol, 1 equiv) were combined in a 50 mL Schlenk flask. DMF was added as an internal ^{1}H nuclear magnetic resonance (NMR) spectroscopy standard. The mixture was covered in aluminum foil and degassed with Argon for 30 min. The mixture was equilibrated for 1 hour at 40 °C and placed over a 455 nm light, 2 cm away from the light source for 1, 2, 3, 4, 5, and 6 hours. The reaction was stopped by opening the flask to air and turning off the light, the mixture was then precipitated into an excess of chilled methanol 2×, and then dried under vacuum and characterized by ^{1}H NMR spectroscopy and SEC.

4.6.7 Example procedure for reverse blocking order kinetics with PDMA

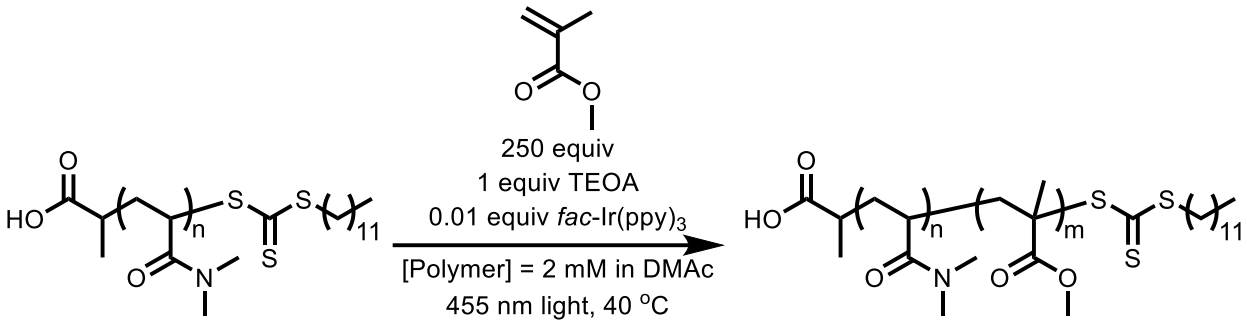

DMAc (36.2 mL), MMA (2.03 g, 20.3 mmol, 250 equiv), 19.3 kg/mol PDMA terminated with a trithiocarbonate (1.57 g, 0.0812 mmol, 1 equiv), *fac*-Ir(ppy)$_3$ (0.532 mg,

8.12×10^{-4} mmol, 0.01 equiv), and TEOA (12.1 mg, 0.0812 mmol, 1 equiv) were combined in a 100 mL beaker. DMF was added as an internal ^{1}H nuclear magnetic resonance (NMR) spectroscopy standard. The reaction mixture was evenly dispersed into ten 2 dram scintillation vials. The mixture was covered in aluminum foil and degassed with Argon for 10 min. The mixture was equilibrated for 1 hour at 40 °C and placed over a 455 nm light, 2 cm away from the light source for 0.5, 1, 1.5, 2, 3, 4, 5, 6, 9, or 12 hours. The reaction was stopped by opening the vial to air and turning off the light, the mixture was then precipitated into an excess of chilled diethyl ether 2×, and then dried under vacuum and characterized by ^{1}H NMR spectroscopy and SEC.

4.6.8 Example procedure for reverse blocking order kinetics with PMA with no TEOA

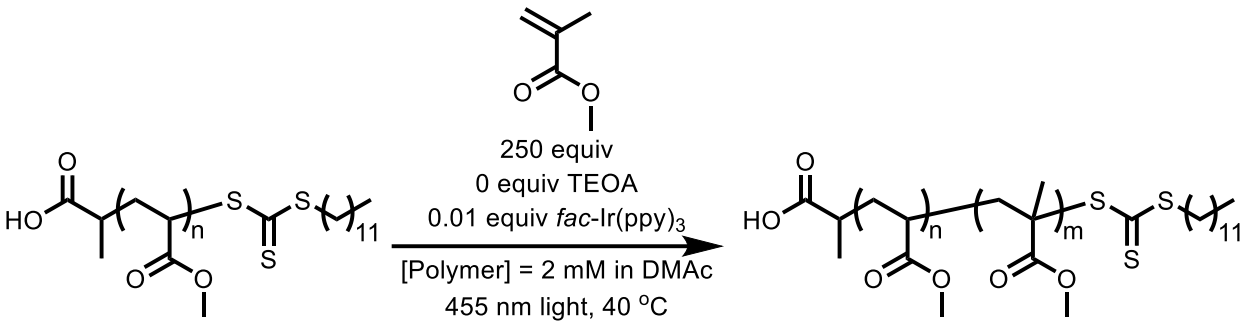

DMAc (23.2 mL), MMA (1.33 g, 13.3 mmol, 250 equiv), 13.3 kg/mol PMA terminated with a trithiocarbonate (0.709 g, 0.0533 mmol, 1 equiv), and *fac*-Ir(ppy)$_3$ (0.349 mg, 5.33×10^{-4} mmol, 0.01 equiv) were combined in a 100 mL beaker. DMF was added as an internal ^{1}H nuclear magnetic resonance (NMR) spectroscopy standard. The reaction mixture was evenly dispersed into ten 2 dram scintillation vials. The mixture was covered in aluminum foil and degassed with Argon for 10 min. The mixture was equilibrated for 1 hour at 40 °C and placed over a 455 nm light, 2 cm away from the light source for 0.5, 1, 1.5, 2, 3, 4, 5, 6, 9, or 12 hours. The reaction was stopped by opening the vial to air and

turning off the light, the mixture was then precipitated into an excess of chilled methanol 2×, and then dried under vacuum and characterized by ^{1}H NMR spectroscopy and SEC.

4.6.9 Example procedure for PMA with DiTTC

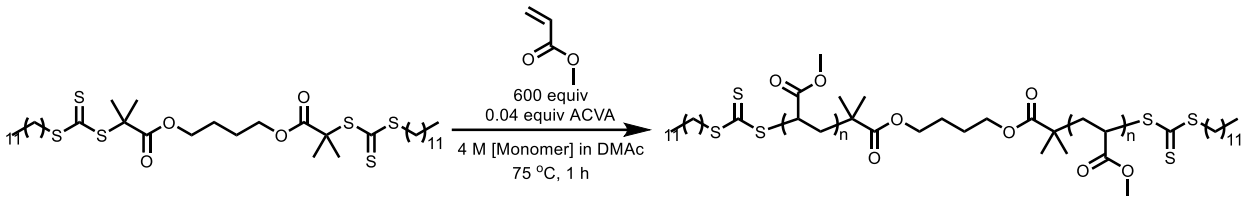

DMAc (33.4 mL), MA (19.8 g, 230 mmol), Butane-1,4-diyl bis(2-(((dodecylthio)carbonothioyl)thio)-2-methylpropanoate) (300 mg, 0.383 mmol), and ACVA (4.29 mg, 1.53×10^{-2} mmol) were combined in a 50 mL Schlenk flask. DMF was added as an internal ^{1}H nuclear magnetic resonance (NMR) spectroscopy standard. The mixture was covered in aluminum foil and degassed with Argon for 30 min. The mixture was placed in a preheated 75 °C oil bath for 2 h. The reaction was then stopped by opening the flask to air and removing from the oil bath, the mixture was then precipitated into an excess of chilled methanol 2×, and then dried under vacuum and characterized by ^{1}H NMR spectroscopy and SEC.

4.6.10 Example procedure for PMMA with DiTTC

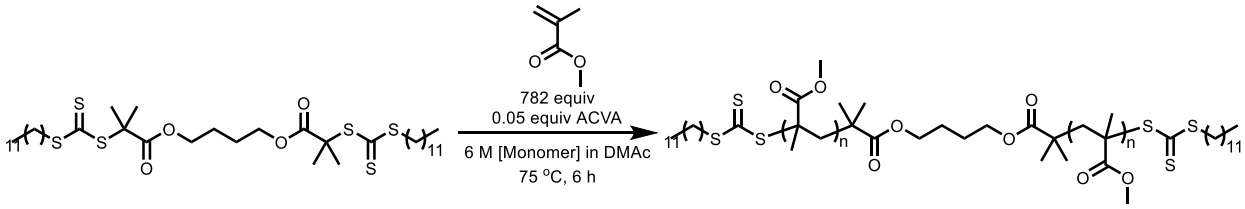

DMAc (10.3 mL), MMA (23.0 g, 230 mmol), Butane-1,4-diyl bis(2-(((dodecylthio)carbonothioyl)thio)-2-methylpropanoate) (230 mg, 0.294 mmol), and ACVA (4.29 mg, 1.53×10^{-2} mmol) were combined in a 50 mL Schlenk flask. DMF was added as an internal ^{1}H nuclear magnetic resonance (NMR) spectroscopy standard. The

mixture was covered in aluminum foil and degassed with Argon for 30 min. The mixture was placed in a preheated 75 °C oil bath for 6 hours. The reaction was then stopped by opening the flask to air and removing from the oil bath, the mixture was then precipitated into an excess of chilled methanol 2×, and then dried under vacuum and characterized by ^{1}H NMR spectroscopy and SEC.

4.6.11 Example procedure for HMW PMA with DiTTC

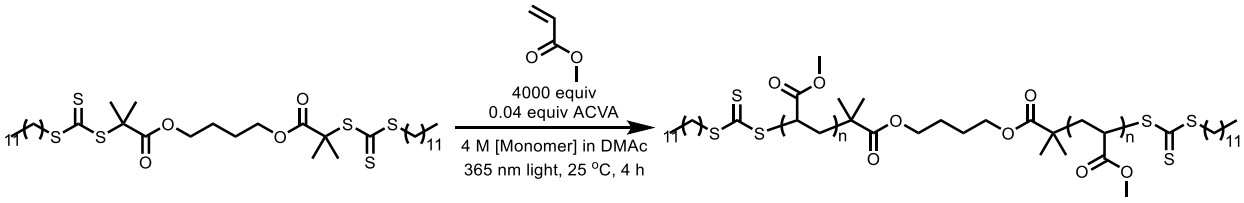

DMAc (8.66 mL), MA (4.78 g, 55.6 mmol), and Butane-1,4-diyl bis(2-(((dodecylthio)carbonothioyl)thio)-2-methylpropanoate) (10.9 mg, 1.39 × 10^{-2} mmol) were combined in a 25 mL Schlenk flask. DMF was added as an internal ^{1}H nuclear magnetic resonance (NMR) spectroscopy standard. The mixture was covered in aluminum foil and degassed with Argon for 30 min. The mixture was placed 2 cm away from a 365 nm light source at 25 °C for 4 hours. The reaction was then stopped by opening the flask to air and turning off the light, the mixture was then precipitated into an excess of chilled methanol 2×, and then dried under vacuum and characterized by ^{1}H NMR spectroscopy and SEC.

4.6.12 Example procedure for HMW PMA chain extension with MMA

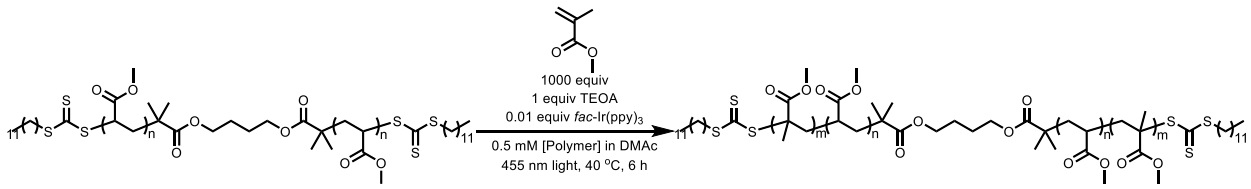

DMAc (7.18 mL), MMA (0.531 g, 5.31 mmol), 337 kg/mol PMA terminated with a trithiocarbonate (1.79 g, 5.31×10^{-3} mmol), *fac*-Ir(ppy)$_3$ (0.0348 mg, 5.31×10^{-5} mmol), and TEOA (0.791 mg, 5.31×10^{-3} mmol) were combined in a 25 mL Schlenk flask. DMF was added as an internal ^{1}H nuclear magnetic resonance (NMR) spectroscopy standard. The mixture was covered in aluminum foil and degassed with Argon for 30 min. The mixture was equilibrated for 1 hour at 40 °C and placed over a 455 nm light, 2 cm away from the light source for 6 hours. The reaction was then stopped by opening the vial to air and turning off the light, the mixture was then precipitated into an excess of chilled methanol 2×, and then dried under vacuum and characterized by ^{1}H NMR spectroscopy and SEC.

Chapter 5: Measuring Activation and Termination of Reverse-Blocking-Order PET-RAFT Chain Extension Polymerizations

Authors: Morgan Gunter,[†] Jared G. Baker,[†] Stephen J. Koehler, and C. Adrian Figg

5.1 Abstract

Acrylic–methacrylic block copolymers are synthetically challenging due to blocking order limitations in reversible–deactivation radical polymerizations. Recently, a photoinduced electron/energy transfer (PET) catalysis method was introduced to access acrylic–methacrylic block copolymers during trithiocarbonate (TTC)-mediated reversible addition–fragmentation chain transfer (RAFT) polymerizations. Herein, the effects of tertiary amines, [TTC], photocatalyst loading, monomer equivalents, and temperature on TTC retention were investigated. From these experiments, a metric to estimate TTC retention—the ratio of the TTC activation rate constant to the TTC termination rate constant ($k_{a,TTC}/k_{t,TTC}$)—is introduced to evaluate polymerizations. Notably, $k_{a,TTC}/k_{t,TTC}$ peaked at 60 °C with 0.1 mM [TTC] and 0.1 mol% *fac*-Ir(ppy)$_3$ with a value of 4.1, suggesting the highest TTC retention, but dispersity increased with time. These data suggest a complex relationship between reaction conditions and PET-RAFT polymerizations. The analysis method will prove critical for addressing blocking order limitations by evaluating how reaction conditions affect rate constants to maximize $k_{a,TTC}/k_{t,TTC}$.

5.2 Introduction

Block copolymers are used for photolithography[212–214] and in adhesives, sealants, and coatings.[218,219,280,281] Due to synthetic ease, they are commonly synthesized in

academic labs via reversible–deactivation radical polymerization (RDRP) techniques.[184,228] However, the range of accessible acrylic-methacrylic block copolymers available using RDRP is limited because block copolymer structures must follow a specific blocking order.[203,236] The relative radical stability of the propagating radical dictates the monomer order. Monomer classes with more stable propagating radicals (e.g., methacrylates and methacrylamides) must be polymerized before those with less stable propagating radicals (e.g., acrylates and acrylamides) to avoid homopolymer impurities.

Blocking order requirements can be reversed using atom transfer radical polymerization (ATRP) ((pseudo-)halogen exchange reaction, photocatalysis)[8,140] and RAFT polymerization (use of a comonomer, photoiniferter with xanthates).[141,255] However, most methods suffer from poor chain-end retention of the functionality required for subsequent chain extensions. Additionally, and critically, reversing blocking order has not been demonstrated with trithiocarbonates (TTC), which are thiocarbonyl thio units widely used in photoiniferter, RAFT, and PET-RAFT polymerizations. We reported a photoinduced electron/energy transfer (PET) catalyzed TTC-mediated RAFT polymerization system that circumvents the blocking order requirements associated with RDRP.[9] The photocatalyst *fac*-Ir(ppy)$_3$ was used to perform the polymerization of methyl methacrylate (MMA) from a poly(methyl acrylate) (PMA) with a TTC chain end in a controlled polymerization. Additionally, we modified conventional PET-RAFT polymerization conditions by diluting the TTC concentration, increasing the concentration of *fac*-Ir(ppy)$_3$, and increasing the reaction temperature to 40 °C. Although novel multiblock copolymer structures could be synthesized, achieving higher-order block copolymers requires further improvements to the method, as the loss of TTC led to poor

chain-end fidelity, limiting access to acrylic multiblock (tetra- and higher-order) copolymers. Also, although poor chain end fidelity occurred the polymerization was controlled for the first 6 hours of the polymerization before deviations to the pseudo-first-order kinetics plot were observed. To partially address this limitation, a tertiary amine was used to introduce a reversible redox pathway and stabilize the TTC radical intermediate;[106,153,261–263] however, significant termination still occurred. We expected that a complex interplay of reaction conditions, catalyst loading, and polymer concentration would affect the activation and termination reactions.

The kinetics of key mechanistic steps, such as activation, termination, and propagation, in RDRP techniques, including ATRP,[52,75,154,156,282–289] (PET-)RAFT polymerization,[61,69,94,100,137,207,208,258,290–300] and photoiniferter[148,301–308] have been well studied since the advent of these techniques. PET-RAFT polymerization, first introduced by the Boyer group,[55] has been mechanistically studied and used for surface-initiated polymerizations,[5,103,113,116,125,126,280] the synthesis of block copolymers/higher-order architectures,[11,12,131,132,137,309] and for single-unit monomer insertion reactions.[11,14–16,310] However, the rates of activation and termination in the reverse-blocking-order PET-RAFT polymerization system we reported have not yet been investigated.

The rate constants of TTC activation ($k_{a,TTC}$) and TTC termination ($k_{t,TTC}$) are of interest because both influence chain-end retention in reverse-blocking-order PET-RAFT polymerizations. The $k_{a,TTC}$ is important because all chain ends must be initiated by PET catalysis. The degenerative chain transfer method of chain activation in the RAFT pre-equilibrium preferentially cleaves the more stable radical species, leading to incomplete initiation of PMA chains in the presence of MMA.[9,57] Consequently, to achieve uniformity

in chain extensions, PMA chain ends must be activated by PET quickly, as they will otherwise not be initiated by MMA-capped chains via chain transfer. Therefore, we expect that $k_{a,TTC}$ must be maximized for complete initiation, which can be readily modulated via photocatalyst concentration, temperature, and/or the intensity of the irradiation source.[14,69,311,312] The $k_{t,TTC}$ directly relates to chain-end retention. Termination events in PET-RAFT polymerizations can proceed through combination or disproportionation reactions, which are coupled with TTC degradation.[260] To limit these termination events, $k_{t,TTC}$ can be modulated by temperature, TTC concentration, and photocatalyst concentration.[68,298,300]

Although these rate constants are measured independently, the ratio of $k_{a,TTC}/k_{t,TTC}$ serves as a metric of success for reverse-blocking-order PET-RAFT polymerization. This metric is analogous to the ATRP equilibrium constant,[52,289] which is maximized to limit the fraction of dead chains and achieve a controlled polymerization. Specifically, the $k_{a,TTC}/k_{t,TTC}$ ratio indicates the fraction of activated chain ends that are terminated during polymerization, thereby representing the upper limit of chain end retention in the system. For example, if our $k_{a,TTC}/k_{t,TTC}$ ratio is equal to 1, every chain that is affected is terminated, but if our ratio is 5, for every 5 chains activated, 1 is terminated. An ideal system would maximize the $k_{a,TTC}/k_{t,TTC}$ ratio as the higher the ratio the higher the chain end fidelity within the system. However, the interdependence of both rate constants on reaction conditions poses challenges in determining how to maximize chain activation while limiting termination to fully address blocking-order limitations. We hypothesized that $k_{t,TTC}$ could be reduced more than $k_{a,TTC}$ by lowering [TTC] and the *fac*-Ir(ppy)$_3$ loadings, thereby increasing $k_{a/TTC}/k_{t,TTC}$ values and improving chain-end fidelity. We set out to test

this hypothesis by measuring and mapping the interdependence between activation and termination on reaction parameters, thereby establishing a foundation for understanding PET activation of TTCs.

Herein, we establish an analytical framework to enable facile determination of both $k_{a,TTC}$ and $k_{t,TTC,}$ and we provide rate constant landscapes for *fac*-Ir(ppy)$_3$-catalyzed reverse-blocking-order PET-RAFT polymerizations of PMA or 2-(butylthiocarbonothioylthio)propanoic acid (BTPA) (**Figure 5.1**). First, reverse-blocking-order PET-RAFT polymerizations of PMA were performed in the presence of other tertiary amines to determine whether tertiary amine structure affects TTC chain-end retention, as only triethanolamine (TEOA) had been used previously.[9] In this study common ATRP ligands were chosen with varying reduction potentials as these tertiary amines are readily accessible in polymer laboratories. Then, the effect of concentration of the TTC and the mol% of the photocatalyst (*fac*-Ir(ppy)$_3$) on the $k_{a,TTC}$ and $k_{t,TTC}$ was evaluated using BTPA and MMA. For $k_{a,TTC}$, high-performance liquid chromatography (HPLC) was used to separate activated from inactivated TTC, enabling quantification of activation throughout the polymerization. For $k_{t,TTC}$, UV-Vis spectroscopy was used to monitor the decrease in absorbance at 309 nm, corresponding to TTC concentration, throughout the polymerization.[313] This methodology was also used to evaluate the $k_{a,TTC}$ and $k_{t,TTC}$ across a range of temperatures and MMA equivalents. Finally, the conditions identified through the screening studies were assessed a PMA macro chain transfer agent (macroCTA) chain extended with MMA to determine the retention of chain-end functionality. While full retention of the TTC after reverse-blocking-order PET-RAFT polymerizations remains inaccessible, the protocol reported here establishes a methodological approach to maximize

chain activation and limit termination in multi-variable polymerizations, complementing established polymerization characterization methods.

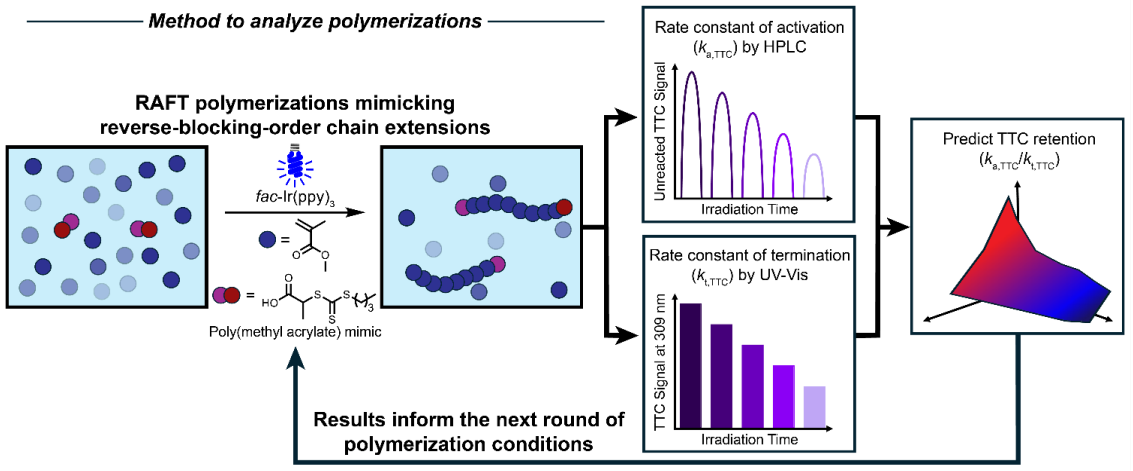

Figure 5.1. Schematic representation of analyses performed on reverse-blocking-order trithiocarbonate (TTC)-mediated photoinduced electron/energy transfer (PET) reversible addition–fragmentation chain transfer (RAFT) polymerizations for the determination of the rate constant of TTC activation ($k_{a,TTC}$) and the rate constant of TTC termination ($k_{t,TTC}$) to predict TTC retention.

5.3 Results and Discussion

Chain extensions of PMA or BTPA (MA R-group mimic) with MMA using *fac*-Ir(ppy)$_3$ as the photocatalyst were selected as a model system for condition analysis (**Figure 5.1**). Previously, the presence of a tertiary amine, TEOA, increased chain end retention by introducing a reversible redox pathway that reduced the TTC radical intermediate to the more stable TTC anion.[105,106,153,261–263] However, only a limited improvement was observed. Using density functional theory (DFT) calculations, energy barriers of six tertiary amines were calculated for the reduction of a TTC radical to a TTC anion (**Figure C1**). The tertiary amines investigated included species that are commonly used in small molecule reactions or as ATRP ligands[75,285]: TEOA, triethylamine (TEA), *N*,*N*,*N'*,*N''*,*N''*-pentamethyldiethylenetriamine (PMDTA), 1,1,4,7,10,10-

hexamethyltriethylenetetramine (HMTETA), tris[2-(dimethylamino)ethyl]amine (Me_6TREN), and *N*,*N*,*N'*,*N'*-tetramethylethylenediamine (TEMED). The relative energy barriers of the tertiary amines were calculated to be 1.78 kcal/mol for TEOA, -0.41 kcal/mol for TEA, -0.62 kcal/mol for PMDTA, 0.51 kcal/mol for HMTETA, -5.06 kcal/mol for Me_6TREN, and -1.02 kcal/mol for TEMED. These values indicate that the reduction of a TTC radical to a TTC anion using Me_6TREN is the most energetically favorable but may be non-reversible. Moreover, the previously used TEOA is the least energetically favorable.

The six tertiary amines were then used in kinetics experiments to determine the extent of chain end retention (monitored by UV-Vis spectroscopy at 309 nm) and compared to a no-tertiary amine control (**Figure C2**). Regardless of the tertiary amine identity, improvements in chain-end retention were marginal compared to the control (**Figure 5.2**). Within the first hour of polymerization, the best-performing amines, HMTETA and Me_6TREN, both resulted in 36% chain-end retention, compared with 17% for the control. However, after 2 hours of irradiation, none of the tertiary amines retained more than 21% of chain ends. Although HMTETA and Me_6TREN resulted in higher chain-end retention than in the absence of an amine, merely changing the tertiary amine identity only marginally improved chain-end retention. Moreover, no trend was observed between the calculated relative energy barriers and the ability of the tertiary amines to retain chain ends. We believe that no trend was observed as the reduction potentials of these tertiary amines are similar and that more reducing compounds would need to be tested to observe a trend, if present.[314] These findings revealed that the chain extension conditions require further

investigation, as altering the tertiary amine did not enhance chain end retention. For all subsequent studies, TEOA was used.

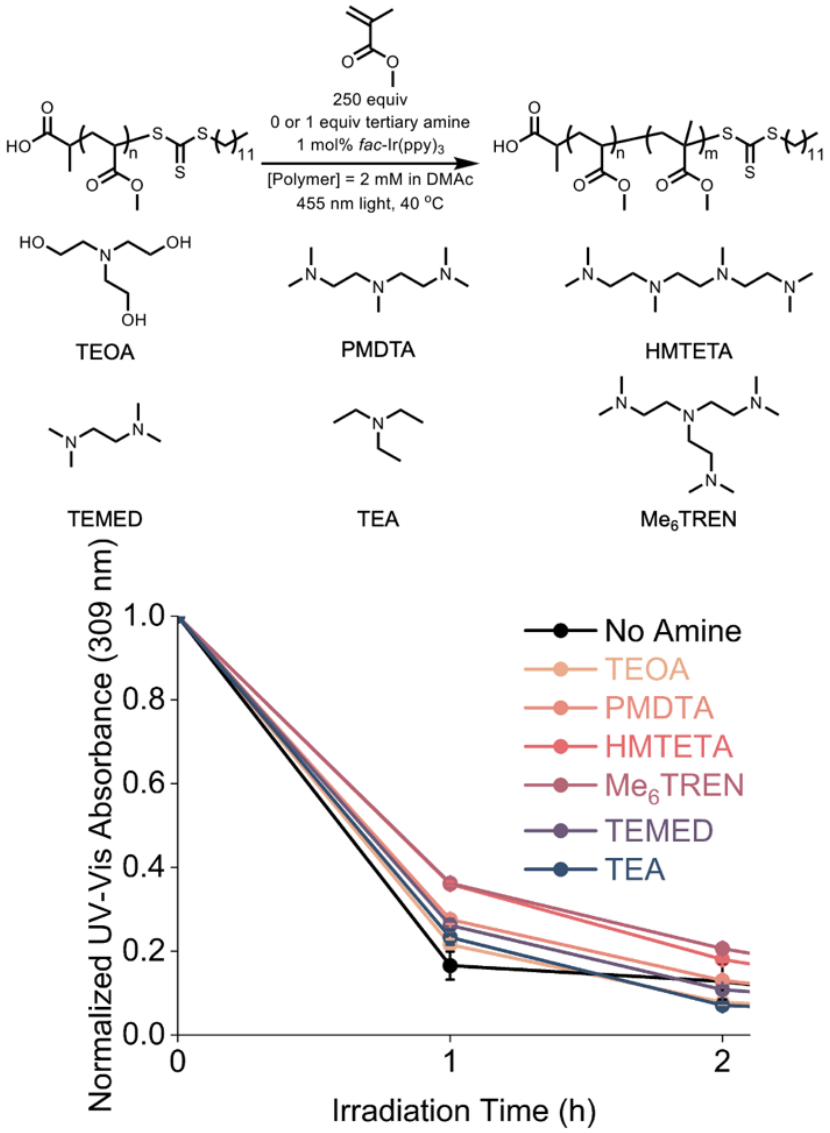

Figure 5.2. Normalized UV-Visible absorbance of 6 different amines and no amine over the course of 2 hours in the reverse-blocking-order photoinduced electron/energy transfer reversible addition–fragmentation chain transfer polymerization system.

We expected that both $k_{a,TTC}$ and $k_{t,TTC}$ can be modulated by changes to *fac*-Ir(ppy)$_3$ loading, [TTC], and temperature, so we used a combinatorial approach to analyze chain extensions of BTPA with MMA in combination with HPLC to measure $k_{a,TTC}$ (**Figure 5.3A, B**) and UV-vis spectroscopy to measure $k_{t,TTC}$ (**Figure 4.3C, D**).

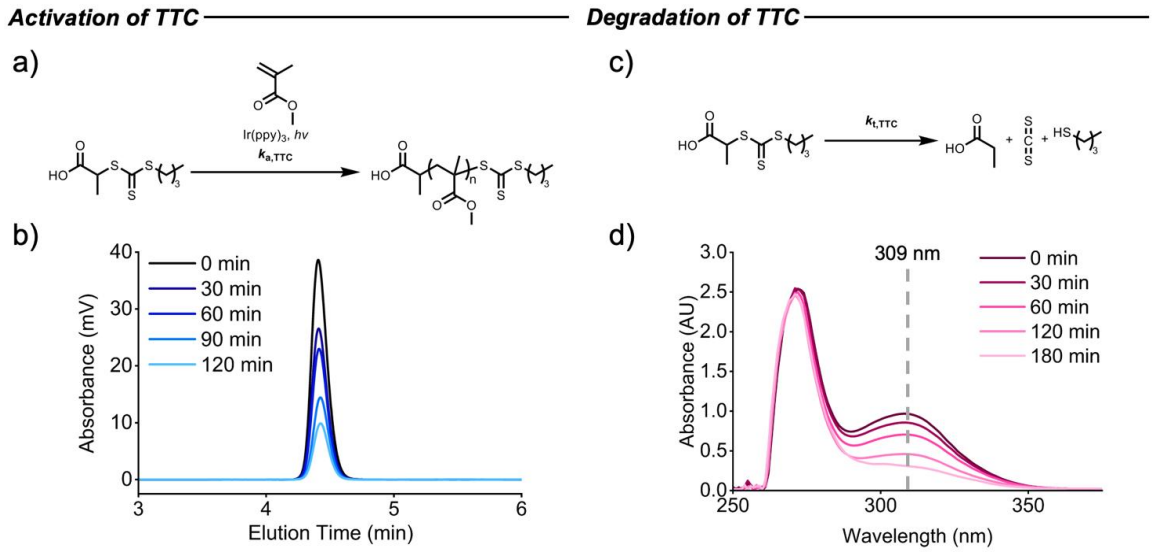

Figure 5.3. A) Activation pathway for methyl acrylate mimic R-group trithiocarbonates (TTC) with methyl methacrylate via photoinduced electron/energy transfer reversible addition–fragmentation chain transfer (PET-RAFT) polymerization. B) High-performance liquid chromatography chromatograms of unactivated BTPA over the course of the polymerization. C) TTC termination pathway for methyl methacrylate polymerizations in PET-RAFT polymerization. D) UV-Vis spectra of the reaction solution, highlighting the extent of TTC termination over the course of the polymerization.

Kinetic studies of $k_{a,TTC}$ in RAFT polymerization systems typically employ ^{1}H nuclear magnetic resonance (NMR) spectroscopy to monitor TTC activation.[14,313] However, this approach has limited sensitivity and requires the presence of a distinguishable, unambiguous proton on the R-group of the TTC that shifts upon monomer addition. Due to these restrictions, we developed an HPLC-based method to measure $k_{a,TTC}$. In PET-RAFT polymerizations, activation of the TTC can occur by PET ($k_{a,PET}$) or by chain transfer ($k_{a,CT}$) (**Figure C3**). The activation pathway cannot be distinguished by direct measurement. For both pathways, one monomer unit must be added to the propagating R-group of the TTC for activation to be quantified. Therefore, regardless of how activation occurs ($k_{a,PET}$ or $k_{a,CT}$), the sum of these events ($k_{a,TTC}$) can be analyzed by isolating and quantifying unreacted TTC via HPLC. For our system, unreacted BTPA was separated from activated BTPA using a C4 column with methanol and 0.05% acetic acid as the

mobile phase at a flow rate of 1.5 mL/min (**Figure 5.3B**). Throughout the polymerization, the peak at 4.4 minutes, corresponding to unreacted BTPA, decreases in intensity. The area beneath the peak can then be integrated and compared to the peak area at t = 0 minutes to calculate the relative amount of unreacted BTPA as a function of reaction time.

To measure $k_{t,TTC}$, we evaluated TTC degradation during polymerization using UV-Vis spectroscopy (**Figure 5.3D**). Termination events can either result from or lead to TTC degradation (**Figure C4**). Consequently, TTC degradation was assumed to be directly proportional to the number of terminated chains and was used to evaluate $k_{t,TTC}$. The $k_{t,TTC}$ was measured following a similar method reported by the Qiao group: the absorbance at 309 nm, corresponding to the $\pi \rightarrow \pi^*$ transition of TTC, was monitored and used to determine the relative amount of degraded TTC compared to a t = 0 timepoint.[313] Quantifying TTC degradation by UV-Vis spectroscopy is advantageous because it can be applied to both concentrated and dilute systems and does not require prior purification.

Experiments were conducted to determine the relative effects of [TTC] and *fac*-Ir(ppy)$_3$ loadings on $k_{a,TTC}$ and $k_{t,TTC}$. Previously, we reported chain extensions of PMA with MMA using 1 mol% of *fac*-Ir(ppy)$_3$ and 2 mM [TTC].[9] Therefore, loadings/concentrations of 0.1 mol%, 1 mol%, and 2.5 mol% were evaluated for *fac*-Ir(ppy)$_3$ and 0.1 mM, 0.5 mM, 2.0 mM, and 5.0 mM were evaluated for [TTC].

A distinct trend was observed when analyzing the impact of *fac*-Ir(ppy)$_3$ loading and [TTC] on $k_{a,TTC}$ via HPLC: increasing [TTC] or *fac*-Ir(ppy)$_3$ loading led to higher $k_{a,TTC}$ (**Figure 5.4A-D and Table C1-C12**).

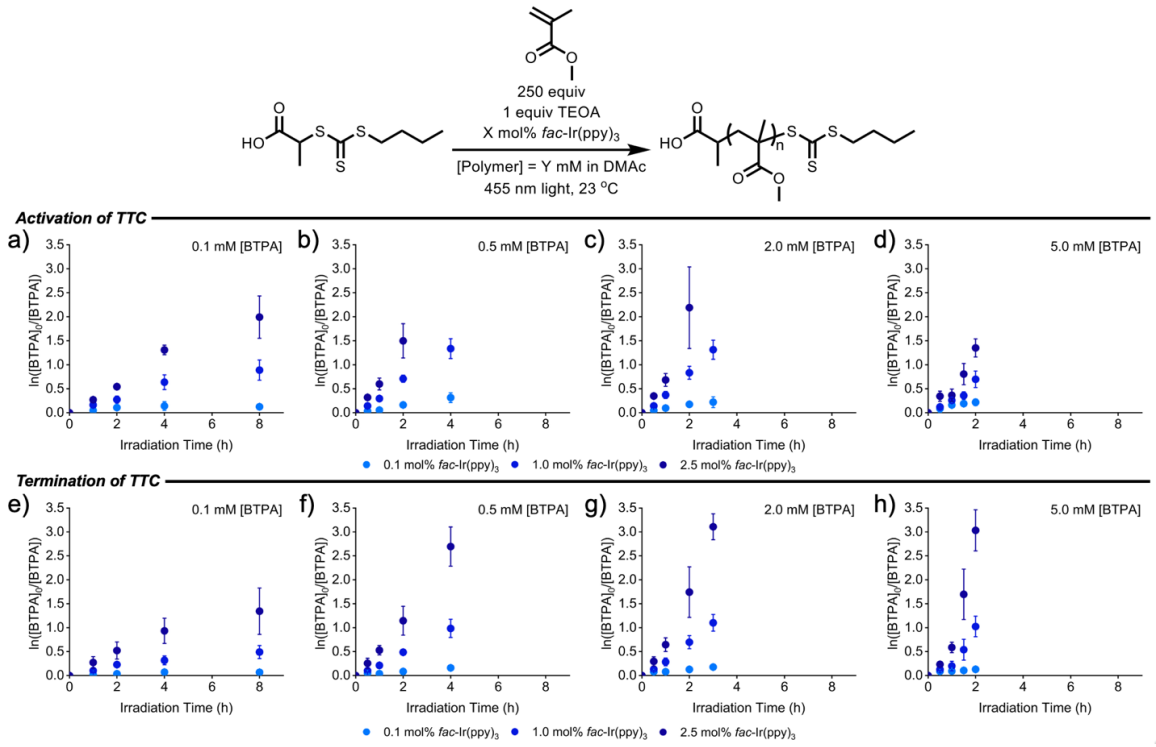

Figure 5.4. Pseudo-first-order kinetics plots for the activation of trithiocarbonate (TTC) with a) 0.1 mM [TTC], b) 0.5 mM [TTC], c) 2.0 mM [TTC], or d) 5.0 mM [TTC] with 0.1, 1.0, or 2.5 mol% *fac*-Ir(ppy)$_3$. Pseudo-first-order kinetics plots for the termination of TTC with e) 0.1 mM [TTC], f) 0.5 mM [TTC], g) 2.0 mM [TTC], or h) 5.0 mM [TTC] with 0.1, 1.0, or 2.5 mol% *fac*-Ir(ppy)$_3$.

The increase in $k_{a,TTC}$ with increasing [TTC] or *fac*-Ir(ppy)$_3$ loading was consistent with our expectations: increasing either the TTC concentration or the photocatalyst loading enhances $k_{a,TTC}$ because a collision between a TTC and an excited photocatalyst becomes more likely, thereby increasing the likelihood of activation events.[69] Increasing the *fac*-Ir(ppy)$_3$ loading from 0.1 mol% to 2.5 mol% increased $k_{a,TTC}$ by 10-fold, while increasing the concentration of TTC from 0.1 mM to 5 mM only increased $k_{a,TTC}$ by 3.5-fold. Together, increasing [TTC] from 0.1 mM to 5 mM and *fac*-Ir(ppy)$_3$ loading from 0.1 mol% to 2.5 mol% increased $k_{a,TTC}$ by 28-fold. Overall, an increase in [TTC] or *fac*-Ir(ppy)$_3$ loading enhanced $k_{a,TTC}$, indicating better uniformity of polymer chains.

A trend was also observed for the relationship between [TTC] and *fac*-Ir(ppy)$_3$ loading and $k_{t,TTC}$ (**Figure 5.4E-H and Table C1-C12**). As with $k_{a,TTC}$, increasing either the TTC concentration or the photocatalyst loading increased $k_{t,TTC}$. These observations were expected for two reasons. First, for [TTC], increasing TTC concentration increases the likelihood of termination reactions by increasing the frequency of collisions between two active chain ends.[315] Second, for *fac*-Ir(ppy)$_3$ loading, increasing the photocatalyst concentration increases the number of radicals in solution. Higher radical concentrations will increase TTC degradation because termination is also more prevalent.[69,316] Increasing the *fac*-Ir(ppy)$_3$ loading from 0.1 mol% to 2.5 mol% increased $k_{t,TTC}$ by 16-fold, while increasing the concentration of TTC from 0.1 mM to 5 mM increased $k_{t,TTC}$ by 6.6-fold. Meanwhile, increasing both factors, [TTC] = 0.1 mM to 5 mM and *fac*-Ir(ppy)$_3$ loading = 0.1 mol% to 2.5 mol%, increased $k_{t,TTC}$ by 120-fold. These findings indicate that [TTC] and *fac*-Ir(ppy)$_3$ loading impact $k_{t,TTC}$ significantly more than they impact $k_{a,TTC}$.

Next, $k_{a,TTC}$ and $k_{t,TTC}$ were plotted against [TTC] and *fac*-Ir(ppy)$_3$ loading (**Figure 5.5A-B and Table C13**). Evaluating the simultaneous influence of both factors on $k_{a,TTC}$ revealed notable observations compared to the 2D plots (**Figure 5.5A**). The highest $k_{a,TTC}$ value did not occur at the highest [TTC] value, but rather at 2 mM (28×10^{-5} s^{-1}). Conversely, the highest *fac*-Ir(ppy)$_3$ loading corresponded to the highest $k_{a,TTC}$ for any [TTC], as expected. Additionally, [TTC] only marginally impacted $k_{a,TTC}$ at the lowest *fac*-Ir(ppy)$_3$ loading (0.1 mol%). When evaluating $k_{t,TTC}$ as a function of [TTC] and *fac*-Ir(ppy)$_3$, a similar correlation was observed compared to $k_{a,TTC}$ (**Figure 5.5B**). The lowest $k_{t,TTC}$ value (0.30×10^{-5} s^{-1}), or highest chain end retention, corresponded to the lowest catalyst loading and [TTC] (**Figure 5.5B**). Consequently, the most desirable $k_{t,TTC}$, lowest

rate of TTC termination, value falls opposite of where the most desirable $k_{a,TTC}$, highest rate of TTC activation, arises.

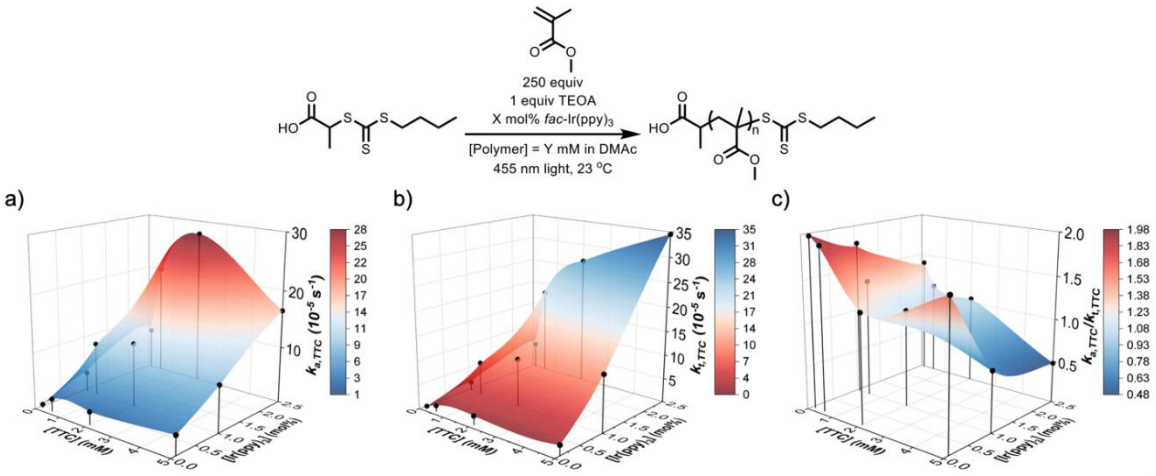

Figure 5.5. a) 3D plot of the rate of activation of the trithiocarbonate (TTC) ($k_{a,TTC}$) versus [TTC] and *fac*-Ir(ppy)$_3$ loading. b) 3D plot of the rate of termination of the TTC ($k_{a,TTC}$) versus [TTC], *fac*-Ir(ppy)$_3$ loading. c) 3D plot of $k_{a,TTC}/k_{t,TTC}$ versus [TTC] and *fac*-Ir(ppy)$_3$ loading.

To better compare the relative influence of reaction conditions on activation and termination, and to identify where we expected the highest chain-end fidelity, the ratio $k_{a,TTC}/k_{t,TTC}$ was plotted against [TTC] and the *fac*-Ir(ppy)$_3$ loading (**Figure 5.5C and Table C13**). Overall, the lowest $k_{a,TTC}/k_{t,TTC}$ value (0.48) occurred at the highest [TTC] and photocatalyst loading, while the highest $k_{a,TTC}/k_{t,TTC}$ value (1.98) occurred at the lowest [TTC] and photocatalyst loading. Notably, the previously reported conditions resulted in a $k_{a,TTC}/k_{t,TTC}$ of 1.14,[9] which is significantly lower than the highest value obtained in these experiments. The highest $k_{a,TTC}/k_{t,TTC}$ values were observed at the lowest *fac*-Ir(ppy)$_3$ loading and across three different [TTC] (0.1, 0.5, and 5 mM), corresponding to $k_{a,TTC}/k_{t,TTC}$ values of 1.64–1.98. Interestingly, the *fac*-Ir(ppy)$_3$ loading has a greater impact on $k_{a,TTC}/k_{t,TTC}$ than on [TTC], as at 0.1 mol% photocatalyst loading, TTC concentration only slightly diminishes $k_{a,TTC}/k_{t,TTC}$. Overall, these findings indicate that although reducing the

concentration of either factor lowers $k_{a,TTC}$ (negatively), $k_{t,TTC}$ is more positively affected (lower rates) by fewer radicals in solution.

With promising polymerization conditions identified, the impact of MMA equivalents was evaluated. To determine if [MMA] impacted the $k_{a,TTC}/k_{t,TTC}$ values, experiments using 250 or 5000 equiv of MMA across 6 conditions were performed (**Figure C5 and Table C14-C19**). The reaction conditions evaluated were 0.1 or 0.5 mM [TTC] and 0.1, 1, or 2.5 mol% *fac*-Ir(ppy)$_3$. These conditions were selected because lower [TTC] concentrations resulted in the highest $k_{a,TTC}/k_{t,TTC}$ values (**Figure 5.6**). Notably, no significant differences were observed in the $k_{a,TTC}/k_{t,TTC}$ values between systems with 250 and 5000 equiv, indicating that [monomer] has little to no effect on $k_{a,TTC}/k_{t,TTC}$ values (**Figure C6-C7 and Table C20**). This result was expected because monomer species do not participate in the processes that dictate $k_{a,TTC}$ and $k_{t,TTC}$: we expect that the rate-determining step of activation is the homolytic cleavage of the C–S bond on the TTC R-group, and that all termination pathways are independent of monomer concentration.[14] The minuscule impact of [MMA] on $k_{a,TTC}/k_{t,TTC}$ enables an extensive range of molecular weights to be targeted during chain extension via reverse-blocking-order PET-RAFT polymerization.

The impact of temperature on $k_{a,TTC}/k_{t,TTC}$ was also evaluated due to the strong influence of temperature on reaction rates. Temperature has been shown to increase both the rate of activation and the rate of termination in RAFT polymerizations.[14,298] However, the impact that temperature has on $k_{a,TTC}/k_{t,TTC}$ in the reverse-blocking-order PET-RAFT polymerization system has not been evaluated. To investigate how temperature affected $k_{a,TTC}$ and $k_{t,TTC}$ in the system, polymerizations with 250 equiv of MMA; 0.1, 0.5, or 5 mM

[TTC]; and 0.1 mol% *fac*-Ir(ppy)$_3$ at 40 (**Figure C8 and Table C21-C23**) and 60 °C (**Figure C9 and Table C24-C26**) were performed and analyzed.

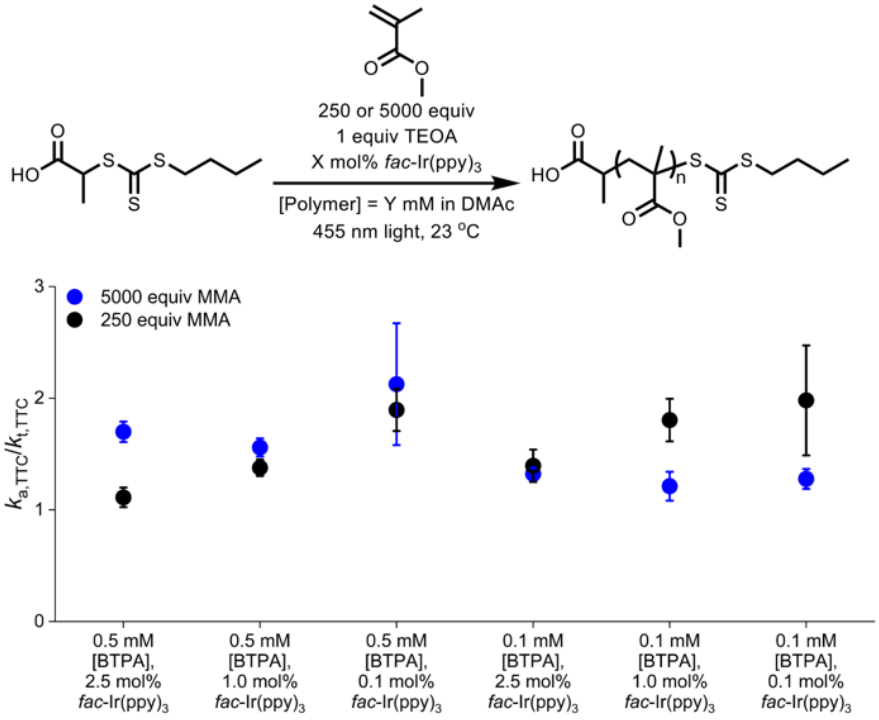

Figure 5.6. Comparison of the ratio of the rate of activation of the TTC ($k_{a,TTC}$) to the rate of termination of the TTC ($k_{t,TTC}$) for systems containing 5000 equiv of methyl methacrylate (MMA) versus 250 equiv MMA across different [trithiocarbonate (TTC)] and *fac*-Ir(ppy)$_3$ loadings.

Increasing temperature resulted in higher $k_{a,TTC}$ and $k_{t,TTC}$ values when 0.1 mM [TTC] was used (**Figure 5.7A and 5.7B**). However, when [TTC] was 0.5 mM or 5 mM, $k_{a,TTC}$ increased between 23 and 40 °C but decreased between 40 and 60 °C. This trend may be due to the boiling point of carbon disulfide at 46.2 °C,[317] leading to further TTC degradation. Notably, $k_{a,TTC}$ increased by 7.3-fold from 23 to 60 °C, while $k_{t,TTC}$ only increased by 3.5-fold for 0.1 mM [TTC]. For 0.5 mM [TTC], $k_{a,TTC}$ increased by 2.2-fold from 23 to 60 °C, while $k_{t,TTC}$ increased by 1.9-fold. Finally, $k_{a,TTC}$ increased by 1.7-fold and $k_{t,TTC}$ decreased by 0.80-fold for 5 mM [TTC]. These data indicate that $k_{a,TTC}$ is more impacted by temperature than $k_{t,TTC}$. Using previous data, $k_{a,TTC}/k_{t,TTC}$ values can be

compared as a function of temperature. Increasing the polymerization temperature from 23 °C to 60 °C increased $k_{a,TTC}/k_{t,TTC}$ by 2.1-fold at 0.1 mM [TTC], yielding a high $k_{a,TTC}/k_{t,TTC}$ value of 4.1 (**Figure 5.7C**). The increase in temperature also increased $k_{a,TTC}/k_{t,TTC}$ by 2.1-fold at 5 mM [TTC] and 1.6-fold at 0.5 mM [TTC].

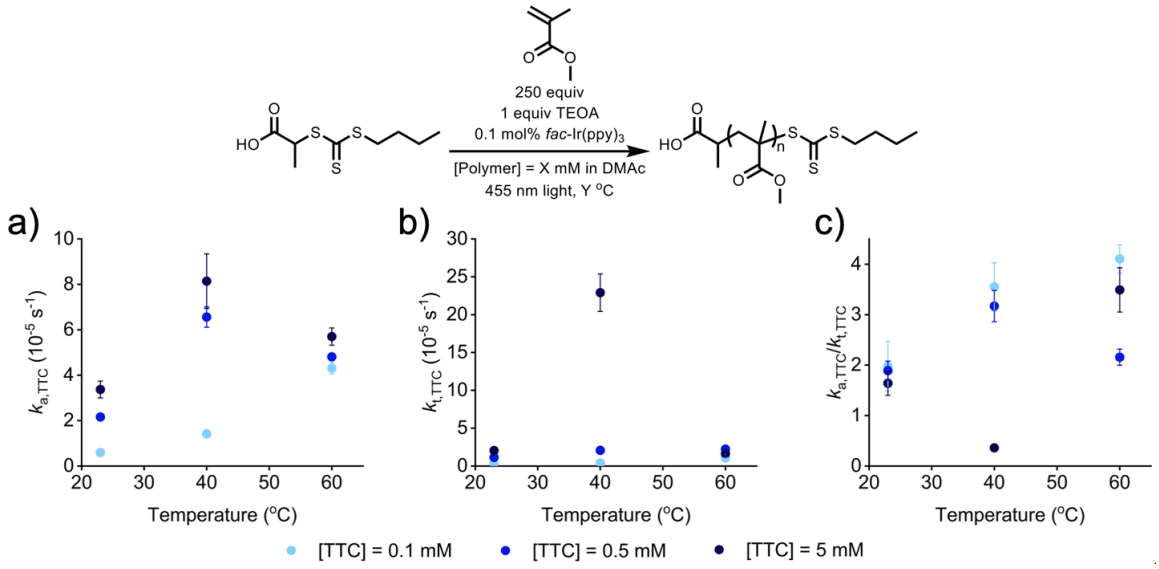

Figure 5.7. a) Effect of temperature on the rate of activation of trithiocarbonates (TTC) ($k_{a,TTC}$) at different TTC concentrations. b) Effect of temperature on the rate of termination of TTCs ($k_{t,TTC}$) at different TTC concentrations. c) Effect of temperature on $k_{a,TTC}/k_{t,TTC}$ at different TTC concentrations.

To determine how translatable the protocol is, we then applied the conditions identified via small-molecule measurements to a macroCTA by chain-extending an 8 kg/mol PMA with MMA. Although the highest $k_{a,TTC}/k_{t,TTC}$ was obtained with 0.1 mM [TTC] and 0.1 mol% *fac*-Ir(ppy)$_3$ at 60 °C, the traces broadened rather than shifted and showed increasing dispersity over time (**Figure C10**). This observation, alongside the greater compatibility of high TTC concentrations with large-scale material synthesis, led us to choose 5 mM [TTC] for chain extension experiments. Additionally, the low absolute value of $k_{a,TTC}$ at 40 °C with 0.1 mM [TTC and 0.1 mol% *fac*-Ir(ppy)$_3$ necessitates a reaction time of over 45 h to activate 90% of the chains, which would likely lead to high termination

rates unaccounted for in the small-molecule studies. Consequently, a kinetics study was performed for 16 hours using 5 mM [TTC] and 0.1 mol% *fac*-Ir(ppy)$_3$. In the pseudo-first-order kinetics plot, a linear relationship was observed, indicating a constant radical concentration throughout the polymerization (**Figure 5.8A**).

Molecular weight increased with conversion, and the experimental molecular weights from SEC-MALS align with the theoretical molecular weights from GC-MS (**Figure 5.8B**). The normalized differential refractive index (dRI) traces from SEC-MALS show a larger population of chain-extended products over time, but unreacted PMA (~20%) remained even after 16 h of irradiation (**Figure 5.8C and Figures C11-C17**). Lastly, different MMA equivalents (250, 500, 750, or 1000) were used to target different molecular weights (**Figure 5.8D and Table c27**). A shift to lower elution times was observed with increasing MMA equivalents; however, unreacted PMA remained present across all equivalents. The kinetics studies revealed that this method can be applied to a PMA macroCTA to achieve controlled polymerization with targetable molecular weights; however, poor chain end retention and incomplete activation persisted, indicating the need for further condition screening. These results indicate that to overcome blocking order requirements, conditions that yield a higher $k_{a,TTC}$ must be identified through reaction screening, as even after 15 hours, unreacted PMA remains, while maintaining a low $k_{t,TTC}$ value.

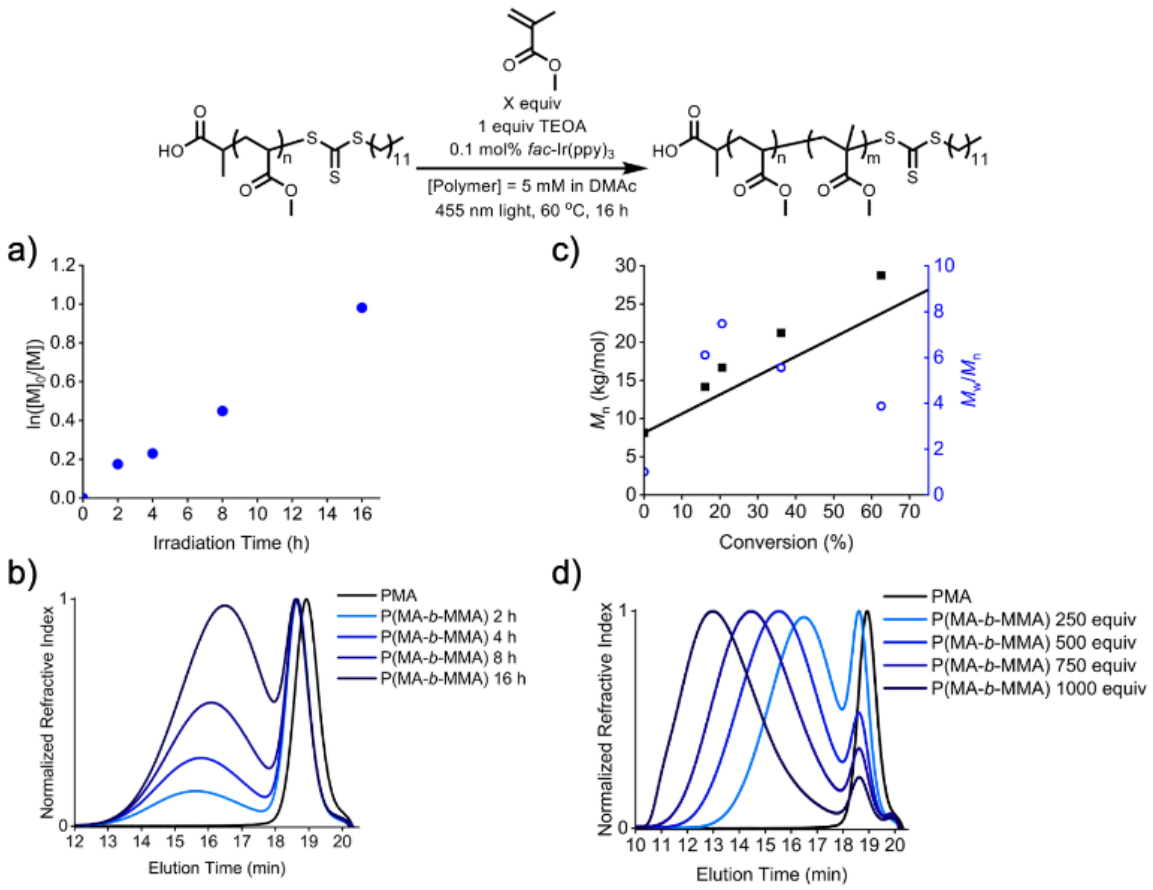

Figure 5.8. a) Pseudo-first-order kinetics plot. b) Molecular weight (M_n) and dispersity ($Đ$) versus conversion using multi-angle light scattering size exclusion chromatography (SEC-MALS). c) Refractive index (RI) traces from SEC-MALS across four timepoints. d) RI traces from SEC-MALS of polymerizations with 250, 500, 750, or 1000 equivalents of methyl methacrylate.

5.4 Conclusions

In this study, a quantitative methodology for characterizing $k_{a,TTC}$ and $k_{t,TTC}$ using HPLC and UV-Vis spectroscopy was employed to measure chain end retention in reverse-blocking-order PET-RAFT polymerizations. This approach provided multiple insights into the interplay of PET-RAFT polymerization reagents. We found that tertiary amine identity had a minimal effect on TTC retention, whereas [TTC], *fac*-Ir(ppy)$_3$ loading, and temperature directly impacted $k_{a,TTC}$, $k_{t,TTC}$, and $k_{a,TTC}/k_{t,TTC}$. Nonetheless, since only tertiary amines were explored other classes of compounds could prove better, such as

phenoxazines. Monomer concentration had no effect on $k_{a,TTC}/k_{t,TTC}$ under these conditions, confirming that molecular weights could be targeted without affecting the polymerization results. Temperature impacted $k_{a,TTC}$ more than it impacted $k_{t,TTC}$ and yielded the highest $k_{a,TTC}/k_{t,TTC}$ values (4.1 compared to 1.2, that was previously reported[9]), suggesting that temperature will be an important input for fully addressing reverse-blocking-order PET-RAFT polymerizations. This protocol will enable further investigation into catalysts and conditions that maximize $k_{a,TTC}/k_{t,TTC}$ to achieve multiblock copolymers without blocking order limitations. We believe that photocatalysts that proceed through electron transfer vs. energy transfer in the PET process will improve $k_{a,TTC}/k_{t,TTC}$, as the trithiocarbonate will automatically be reduced to the more stable anionic species preventing degradation of the TTC. Furthermore, we believe that further exploration into our 3D surfaces can find a new high $k_{a,TTC}/k_{t,TTC}$ value as our area explored is small. We also expect that this approach will be highly amenable to high-throughput syntheses, thereby further establishing robust insights into how rate constants affect polymerization outcomes. Overall, this methodological framework will provide fundamental insights into photocatalysis, activation, and termination in polymer systems, enabling access to novel polymer architectures and sequences.

5.5 Experimental

5.5.1 Materials

Methyl acrylate (MA, Thermo Scientific, 99%) and methyl methacrylate (MMA, Thermo Scientific, 99%) were filtered through basic alumina prior to use. *fac*-Ir(ppy)$_3$ (Strem Chemicals, 95%) was prepared as a 10 or 1 mg/mL solution in *N*,*N*-dimethylacetamide (DMAc) prior to use. Triethanolamine (TEOA, Sigma Aldrich, >99%),

1,1,4,7,10,10-hexamethyltriethylenetetramine (HMTETA, Sigma Aldrich, 97%), *N*,*N*,*N'*,*N''*,*N''*-pentamethyldiethylenetriamine (PMDTA, TCI Chemicals, >99.0%), tris[2-(dimethylamino)ethyl]amine (Me_6TREN, TCI Chemicals, >98.0%), (TEMED, MP Biomedicals), and triethylamine (TEA, Sigma Aldrich) were prepared as 10 mg/mL solutions in DMAc prior to use. 4,4'-azobis(4-cyanovaleric acid) (ACVA, Sigma Aldrich, >98%) was prepared as a 20 mg/mL solution in reaction solvent prior to use. 2-(butylthiocarbonothioylthio)propionic acid (BTPA) and 2-(dodecylthiocarbonothioylthio)propionic acid (DTPA) were synthesized according to a previous report.[211] *N*,*N*-dimethylacetamide (Thermo Scientific, 99%), dimethyl sulfoxide (Thermo Scientific, 99.7%), and *N*,*N*-dimethylformamide (Acros Organics, 99.8%) were used as received.

5.5.2 Characterization

For a visible light source, 76.2 cm Supernight Blue Light Strips were purchased from Amazon and placed on a Xnrtop Silver Tone Aluminum Radiator Heat Sink 150 × 80 × 27 mm from Amazon. For a heating source a Thermo Scientific MaxQ6000 Incubated/Refrigerated Stackable Shaker was used.

^{1}H nuclear magnetic resonance (NMR) spectroscopy was conducted on a JEOL ECZL400 with a RoyalHFX probe. DMSO-d_6 (Cambridge Isotopes Laboratories, Inc., 99.9%) and $CDCl_3$ (Cambridge Isotopes Laboratories, Inc., 99.8%) were used as received.

UV-Visible (UV-Vis) spectroscopy was performed on an Agilent Cary 60 UV-Vis.

Gas chromatography-mass spectrometry (GC-MS) was performed on an Agilent 7890A GC System with an Agilent 5975C VL MSD with Triple-Axis Detector. Helium was used as the carrier gas at a flow rate of 1 mL min^{-1} (column: J&W HP-5ms GC Column,

30 m, 0.25 mm, 0.25 µm, 7 inch cage). A 1 µL injection was used with an inlet temperature of 125 °C, the oven was ramped from 40 – 140 °C at a rate of 40 °C min^{-1} and then from 140 – 290 °C at a rate of 100 °C min^{-1}. The detector was set to 150 °C and had a mass range of 30 – 550 amu, and the ionization source to 230 °C.

Size Exclusion Chromatography Multi-Angle Light Scattering (SEC-MALS) was performed in DMAc with 50 mM lithium chloride at 50 °C at a flow rate of 0.5 mL min^{-1} (Agilent isocratic pump, degasser, and autosampler, columns: TOSOH TSKgel Guard Alpha and a TOSOH TSKgel Alpha-4000 (molecular weight range 0 – 1×10^6 g mol^{-1}). Detection consisted of a Wyatt Optilab refractive index detector operating at 785 nm, a Wyatt DAWN multi-angle light scattering detector operating at 783 nm, and an Agilent MWD operating at 309 nm. Absolute molecular weights and dispersities were calculated with the Wyatt ASTRA software, and d*n*/d*c* values were determined by performing refractive index 100% recovery methods in the Wyatt ASTRA software.

High-performance liquid chromatography (HPLC) was performed in methanol with 0.2% acetic acid at 25 °C at a flow rate of 1.5 mL min^{-1} (Agilent isocratic pump, degasser, and autosampler, column: Princeton Chromatography Inc., 100Å, 10µ, 250 × 4.6 mm, P/N: 250046-03004). Detection consisted of an Agilent VWD operating at 309 nm.

Visible light intensity was measured with an International Light Technologies ILT-350 illuminance spectrophotometer with a NIST traceable ISO17025 accredited calibration.

5.5.3 Density Functional Theory Calculations

All geometry optimizations and harmonic frequency calculations were conducted with the ωB97X-D functional[277] and 6-311+G(d,p) basis set as implemented in

Gaussian09.[278] An "ultrafine" integration grid and standard cutoffs were used in all calculations. Implicit solvation with *N*,*N*-dimethylacetamide was accomplished via the SMD model.[279] The calculations use a reduced dimensionality ethyl trithiocarbonate to model the dodecyl trithiocarbonate chain-transfer agent used in the experiments. All reported energies correspond to Gibbs energies at 298 K and 1 atm.

5.6 Procedures

5.6.1 Example polymerization for starting poly(methyl acrylate) (PMA)

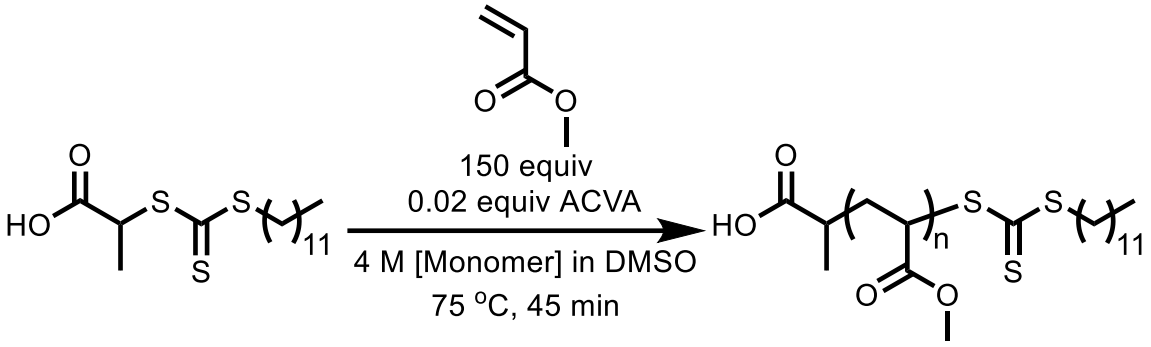

DMSO (33.8 mL), MA (18.4 g, 214 mmol), 2-(Dodecylthiocarbonothioylthio)propionic acid (500 mg, 1.42 mmol), and ACVA (7.98 mg, 2.85×10^{-2} mmol) were combined in a 50 mL Schlenk flask. DMF was added as an internal gas chromatography mass spectroscopy (GC-MS) standard. The mixture was covered in aluminum foil and degassed with argon for 30 min. The mixture was placed in a preheated 75 °C oil bath for 45 minutes. The reaction was then stopped by opening the flask to air and removing it from the oil bath. The polymer was then precipitated into an excess of chilled methanol 2× and then dried under vacuum and characterized by GC-MS and SEC-MALS.

5.6.2 Example polymerization for PMA chain extension with MMA with different tertiary amines

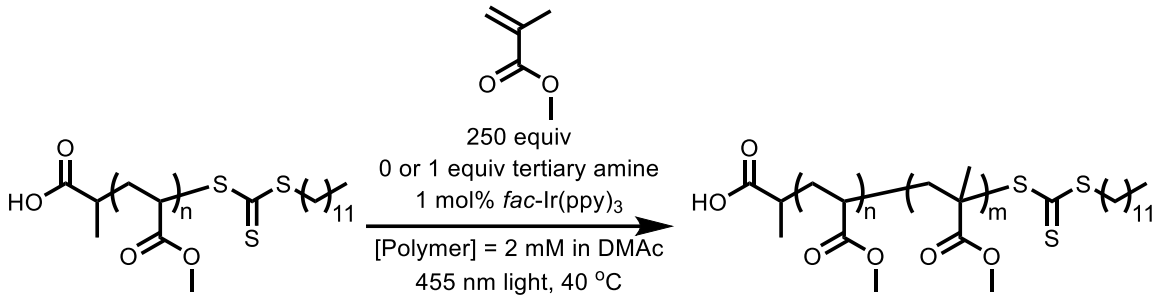

DMAc (26.58 mL), MMA (1.52 g, 15.2 mmol), PMA (M_n = 7406 g/mol, 0.45 g, 0.061 mmol), TEOA (9.03 mg, 0.061 mmol), and *fac*-Ir(ppy)$_3$ (0.397 mg, 6.1×10^{-4} mmol) were combined in a 50 mL Schlenk flask. DMF was added as an internal GC-MS standard. The mixture was covered in aluminum foil and degassed with Argon for 30 min. The mixture was equilibrated for 1 hour at 40 °C and placed over a 455 nm light, 2 cm away from the light source, for 6 hours. The reaction was then stopped by opening the flask to air and turning off the light. The mixture was then precipitated into an excess of chilled methanol 2× and then dried under vacuum and characterized by GC-MS and SEC-MALS.

5.6.3 Example polymerization for chain extension with MMA using small molecule analog BTPA

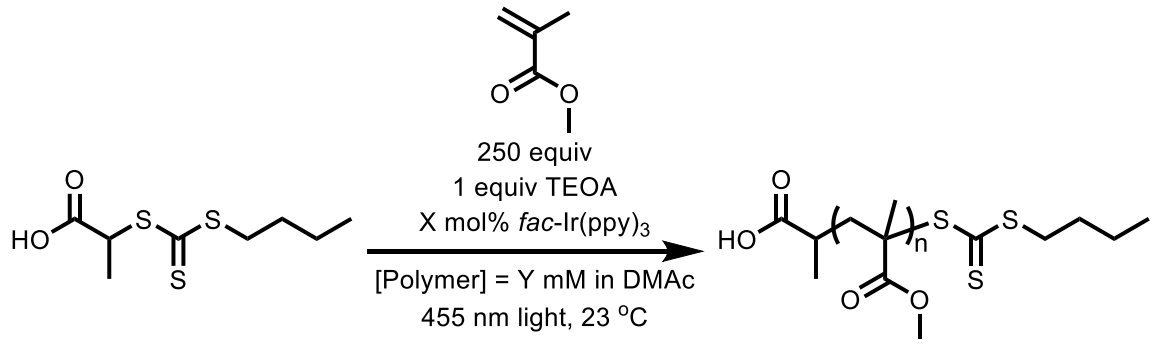

DMAc (45.5 mL), MMA (8 mL, 75 mmol), BTPA (71.5 mg, 0.3 mmol), TEOA (44.8 mg, 0.3 mmol), and *fac*-Ir(ppy)$_3$ (1.97 mg, 3×10^{-3} mmol) were combined in a 100

mL round-bottom flask. DMF was added as an internal GC-MS standard. The mixture was divided equally into 16 vials, which were covered in aluminum foil and degassed with argon for 5 min. The samples were placed over a 455 nm light, 2 cm away from the light source, for 0.5, 1, 1.5, or 2 hours. The reactions were quenched by removing the vials from the reaction vessel and opening the vials to air. Aliquots of the samples were characterized by GC-MS, UV-Vis spectroscopy, and high-performance liquid chromatography (HPLC).

5.6.4 Example polymerization for chain extension with MMA using small molecule analog BTPA at elevated temperatures

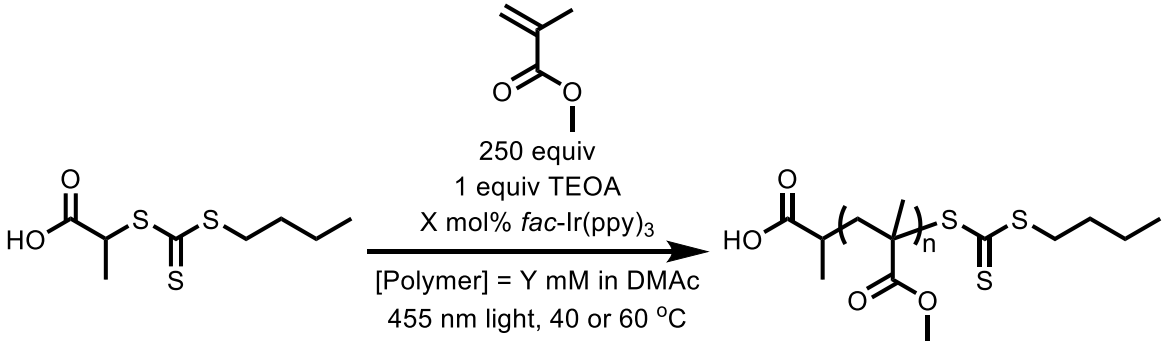

DMAc (59.75 mL), MMA (0.160 mL, 2 mmol), BTPA (14.2 mg, 0.006 mmol), TEOA (8.96 mg, 0.006 mmol), and *fac*-Ir(ppy)$_3$ (5.24 μg, 6×10^{-6} mmol) were combined in a 100 mL round-bottom flask. DMF was added as an internal GC-MS standard. The mixture was divided equally into 12 vials, which were then covered in aluminum foil and degassed with argon for 5 min. The samples were placed over a 455 nm light, 2 cm away from the light source, for 1, 2, 4, or 8 hours. The reactions were quenched by removing the vials from the reaction vessel and opening the vials to air. Aliquots of the samples were characterized by GC-MS, UV-Vis spectroscopy, and HPLC.

5.6.5 Example polymerization for PMA chain extension with MMA using improved conditions

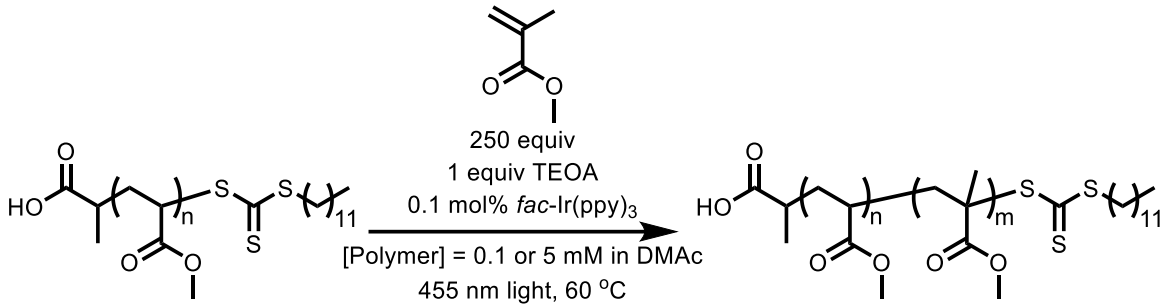

DMAc (28.1 mL), MMA (75.5 µL, 70.8 mmol), PMA (M_n = 8310 g/mol, 23.5 mg, 2.83×10^{-3} mmol), TEOA (0.422 mg, 2.83×10^{-3} mmol), and *fac*-Ir(ppy)$_3$ (1.85 µg, 2.83×10^{-6} mmol) were combined in a 50 Schlenk flask. DMF was added as an internal GC-MS standard. The mixture was covered in aluminum foil, degassed with argon for 30 min, and equilibrated at 60 °C for 1.5 h. The mixture was placed over a 455 nm light, 4 cm away from the light source, for 16 hours. The reaction was stopped by opening the flask to air. The reaction mixture was precipitated into chilled methanol 2× to isolate the polymer. An aliquot of the reaction mixture was characterized by GC-MS and UV-Vis spectroscopy, and the isolated polymer was characterized by SEC-MALS.

5.6.6 Example kinetics study for PMA chain extension with MMA using optimized conditions

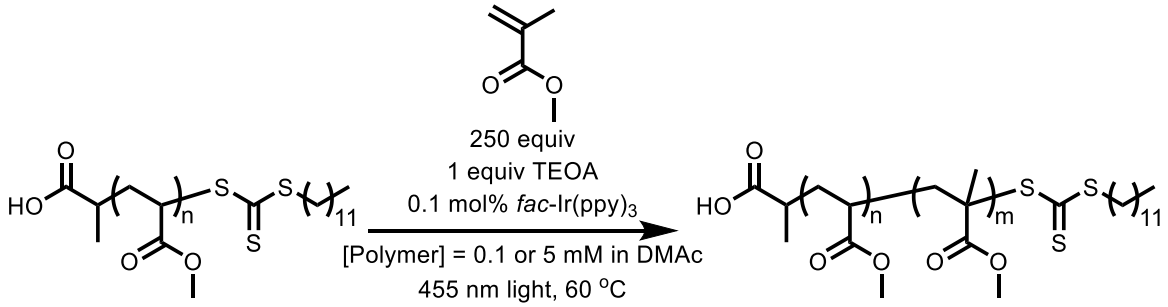

DMAc (28.1 mL), MMA (75.5 µL, 70.8 mmol), PMA (M_n = 8310 g/mol, 23.5 mg, 2.83×10^{-3} mmol), TEOA (0.422 mg, 2.83×10^{-3} mmol), and *fac*-Ir(ppy)$_3$ (1.85 µg, 2.83×10^{-6} mmol) were combined in a 50 mL Schlenk flask. DMF was added as an internal GC-

MS standard. The mixture was covered in aluminum foil, degassed with argon for 30 min, and equilibrated at 60 ºC for 1.5 h. The mixture was placed over a 455 nm light, 4 cm from the light source, for 16 hours. 5 mL of the reaction solution were pulled with a syringe at 2, 4, 8, and 16 h. Aliquots of the reaction mixture were characterized by GC-MS and UV-Vis spectroscopy, and the isolated polymer (precipitated with chilled methanol 2×) was characterized by SEC-MALS.

Chapter 6: Customizing STEM Organogels using PET-RAFT Polymerization*

Authors: Zaya Bowman,† Jared G. Baker,† Madeleine J. Hughes, Jessica D. Nguyen, Mathew Garcia, Nahome Tamrat, Joshua C. Worch, and C. Adrian Figg

6.1 Abstract

Photoinduced electron/energy transfer (PET) reversible addition–fragmentation chain transfer (RAFT) polymerization results in more uniform polymer networks compared to networks synthesized by thermally initiated RAFT polymerizations. However, how PET-RAFT polymerizations affect molecular weight control and physical properties during parent-to-daughter block copolymer network synthesis is unclear. Herein, we synthesized a structurally tailored and engineered macromolecular (STEM) organogel composed of poly(methyl acrylate) and a degradable crosslinker. Chain extensions on the STEM organogel were performed using PET-RAFT polymerization of either methyl acrylate (MA) or *N*,*N*-dimethylacrylamide (DMA) with or without additional crosslinker. We found that physical properties were dependent on monomer composition and crosslinking. The swelling ratios of the diblock networks were similar in DMAc. Conversely, swelling ratios in water increased by 430% for networks extended with MA and 5200% for networks extended with DMA compared to the parent organogels. Rheological analysis showed a tunable modulus from 1000–4000 Pa. However, size exclusion chromatography analysis of the degraded gels revealed that the PET-RAFT polymerization chain extension yielded disperse block copolymers with poor control over the molecular weight. These results indicate that PET-RAFT polymerizations can be used

*Adapted and reproduced with permission from *Polym. Chem.* **2024**, *15*, 3907-3915.

to expand organogel networks to block copolymer networks to modulate physical properties, but control over the chain extension polymerization is lost. Looking forward, this report points to opportunities to gain control over PET-RAFT block copolymer network synthesis via secondary reversible deactivation pathways.

6.2 Introduction

Organogels are a class of polymer networks that consist of an organic liquid phase within a three-dimensional crosslinked network.[318–320] Currently, organogels are used in applications such as anti-icing,[321,322] anti-fouling,[323] drug delivery,[324–326] and food processing.[327,328] Performing chain extension polymerizations on organogel networks provide an opportunity to modify properties such as amphiphilicity,[3,329,330] composition,[112,331–333] shape,[1,2,109] and mechanical properties.[334–337] For example, Chen and Gu et al. showed that parent-to-daughter gel network extensions can be used to maintain or modify gel moduli and introduce copolymers to modify solvophilicity.[107] However, only a few controlled polymerization techniques result in the retention of chain end functionality required to synthesize block copolymer networks.

Complex architectures including block copolymers and block copolymer networks can be synthesized using reversible-deactivation radical polymerization (RDRP) because the polymer chain ends can be reactivated to perform chain extensions.[338] For example, reversible addition–fragmentation chain transfer (RAFT) polymerization is used to synthesize organogels, resulting in more uniform networks compared to free radical polymerization (FRP).[339–341] However, using RAFT polymerization to synthesize network polymers leads to a loss in molecular weight control at higher degrees of polymerization (DP) due to mobility issues in viscous media and because degenerative chain transfer is

required for molar mass control.[339] Photoiniferter and photoinduced electron/energy transfer (PET) initiation pathways are used instead of conventional radical initiators because the added reversible deactivation reaction leads to higher chain end retention,[62,342] providing a platform to access structurally tailored and engineered macromolecular (STEM) gel networks.[2,105,109,110,343,344] However, there is not clarity on how PET-RAFT polymerizations affect both the molecular weight control of STEM organogel chain extensions and the physical property changes that result from these modifications.

We aimed to determine if PET-RAFT polymerization yields well-defined block copolymers and networks with tunable properties by using degradable crosslinkers to characterize the copolymers. The disulfide-based diacrylate (DSDA) crosslinker enables organogel synthesis that is stable under atmospheric conditions but can be cleaved in the presence of a reducing agent.[339] A stable yet degradable crosslinker is important to ensure that physical properties are not compromised by prematurely degraded crosslinkers. We hypothesized that PET-RAFT polymerization can be used to chain extend organogels into block copolymer networks with tunable physical properties, while DSDA will provide a degradable crosslinker to analyze the chain extension molecular weight control.

Herein, poly(methyl acrylate-*stat*-DSDA) (P(MA-*s*-DSDA)) STEM organogels were synthesized as the first block comprising the parent organogel (**Figure 6.1**). To synthesize block copolymer networks with different properties, methyl acrylate (MA) or *N*,*N*-dimethylacrylamide (DMA) were chosen as the second block due to the different physical characteristics of the resulting poly(methyl acrylate) (PMA) or poly(*N*,*N*-dimethylacrylamide) (PDMA) polymers. Each chain extension using MA or DMA was performed with or without additional DSDA to determine the effect of a crosslinked versus

non-crosslinked second block. The resultant gels were then analyzed via swelling ratio studies and rheology to measure network physical properties. Following physical properties testing, the DSDA crosslinks were reduced to thiols to yield linear copolymers that were analyzed via size exclusion chromatography (SEC). Overall, the primary and chain-extended organogels were characterized to determine network physical property differences and molecular weight control.

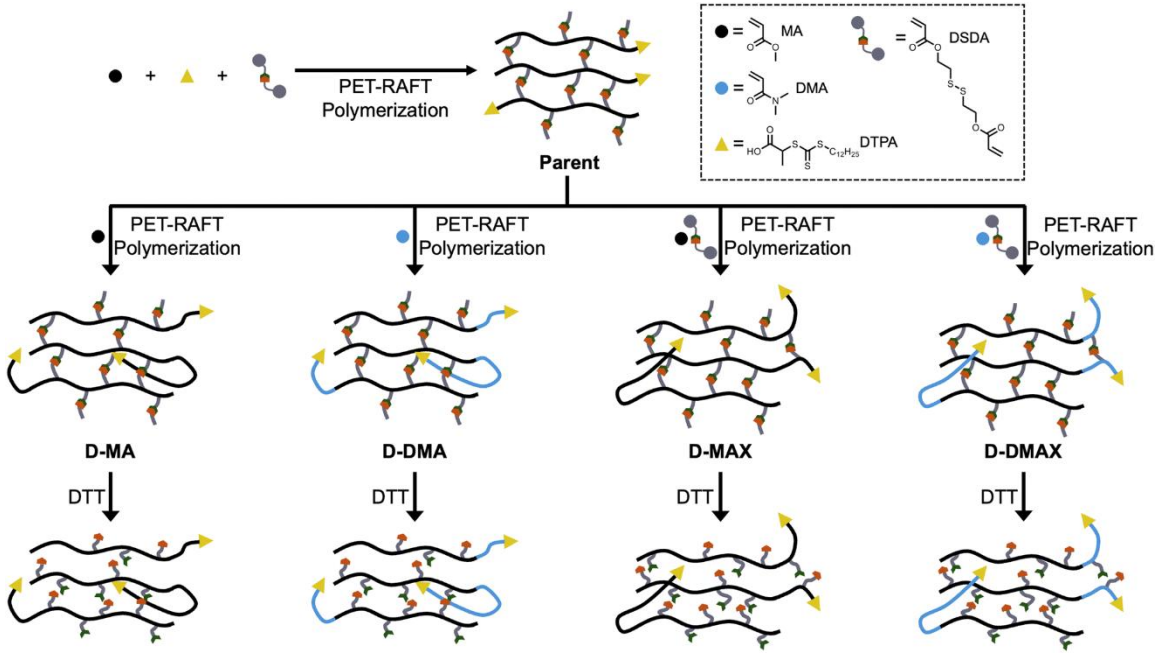

Figure 6.1. Cartoon representation of the block copolymer organogel network chain extensions followed by degradation. All polymerizations used ZnTPP as the photocatalyst.

6.3 Results and Discussion

6.3.1 Synthesis of Parent Gels by PET-RAFT Polymerization

The STEM organogel network was synthesized using oxygen tolerant PET-RAFT polymerization to yield P(MA-*s*-DSDA) copolymers terminated with a trithiocarbonate (**Figure 6.2A**). The parent gel polymerization displayed a linear relationship in the pseudo-first-order kinetics plot (**Figure 6.2B and Table D1**) after an inhibition period of 2 hours.

This inhibition period can occur in PET-RAFT polymerizations performed without deoxygenation.[61] Following blue light irradiation from the bottom of the vial, a layer of the gel was green and showed signs of cracking (noted as bottom of the gel), whereas the majority of the gel was brown and appeared to be homogeneous with no cracking (as top of the gel, **Figure 6.2C and Figure D1**).

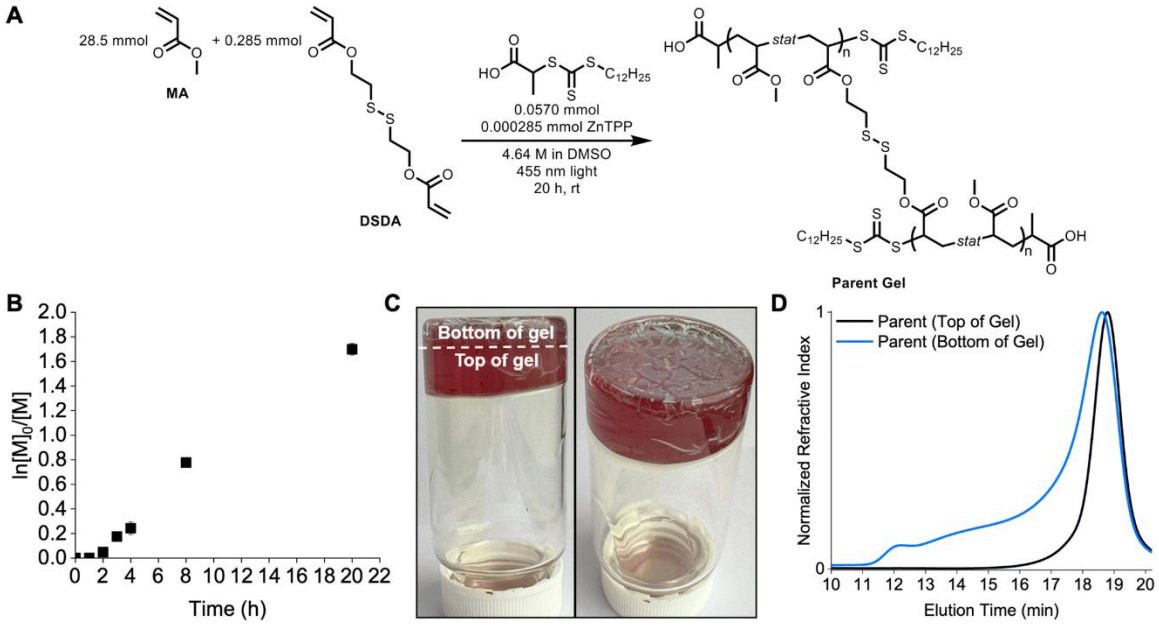

Figure 6.2. A) Scheme of parent gel polymerization. B) Pseudo-first-order kinetic plot of the parent gel polymerization. C) Photographs of the resulting parent gel following irradiation. D) SEC traces of the parent gel with samples taken from the top and bottom of the gel.

To investigate the differences between the top and bottom of the synthesized STEM gel, SEC was used to analyze both regions separately after degradation of the network polymers into linear chains using DTT. The SEC trace of the green (bottom) portion of the parent gel consisted of a broad distribution spanning the elution volume of the column and a number-average molecular weight (M_n) of 34.6 kg mol^{-1} with a dispersity ($Đ$) value of 2.79 (**Figure 6.2D**) according to poly(methyl methacrylate) standards. The SEC trace of the top portion of the degraded gel showed a monomodal trace and M_n = 20.9 kg mol^{-1}

with a low dispersity ($Đ$ = 1.09) (**Figure 6.2D**). The difference between the top and bottom parts of the parent gel is related to the positioning of the light source in the reaction setup. Specifically, the bottom of the vial absorbed the greatest intensity of light, generating a high concentration of radicals, high amounts of termination, and uncontrolled polymerization.[107] The top portion of the vial received fewer photons due to scattering, resulting in a lower radical concentration and a controlled PET-RAFT polymerization. Therefore, only the top portion of the gel was used throughout the rest of the study.

6.3.2 Synthesis of Daughter Gels by PET-RAFT Polymerization

Following STEM gel synthesis, we investigated the effect of PET-RAFT polymerization on the chain extension to achieve block copolymer networks. MA and DMA were used as model monomers to investigate the tunability of the physical properties, while DSDA was used as the crosslinker to maintain network degradability for molecular weight analysis. STEM gel networks were swollen in a combination of DMSO, monomers, and ZnTPP and then irradiated with blue light for 20 hours to yield four discrete daughter gels (**Figure 6.3A**). An MA chain extension without DSDA yielded the daughter gel with a polymer structure of P((MA-*s*-DSDA)-*b*-MA) (D-MA). An MA chain extension with DSDA yielded the daughter gel with a polymer structure of P((MA-*s*-DSDA)-*b*-(MA-*s*-DSDA)) (D-MAX). A DMA chain extension without DSDA yielded the daughter gel with a polymer structure of P((MA-*s*-DSDA)-*b*-DMA) (D-DMA). Lastly, a DMA chain extension with DSDA yielded the daughter gel with a polymer structure of P((MA-*s*-DSDA)-*b*-(DMA-*s*-DSDA)) (D-DMAX). The ratio of monovinyl monomer (i.e., MA or DMA) to the divinyl DSDA monomer was kept constant at 100 : 1.

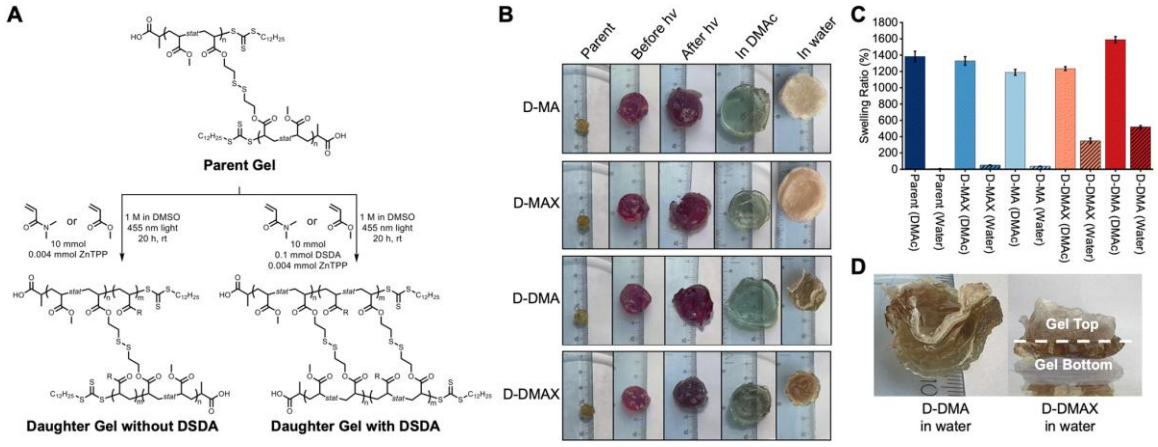

Figure 6.3. A) Scheme of parent-to-daughter gel network extension. B) Photographs of the dried parent networks, parent networks swelled before irradiation, parent networks after irradiation to synthesize daughter gels, daughter gels swelled in DMAc, and daughter gels swelled in water. C) Swelling ratios of parent and daughter gels in DMAc and water. D) Photographs of the side profiles of D-DMA and D-DMAX swelled in water with designations for the top and bottom of the daughter gels.

Following the chain extensions, all the daughter gels became larger in size, indicating that network extension had occurred (**Figure 6.3B**). The daughter gels were washed 3× with methanol and dried under vacuum. Swelling ratios were then performed in excess DMAc (a good solvent for both PMA and PDMA). A decrease in swelling ratios was observed when comparing parent gels (14× swelling ratio) to D-MA (12× swelling ratio, 16% decrease compared to parent gel, **Figure D2**), D-MAX (13× swelling ratio, 4.1% decrease compared to parent gel, **Figure D3**), and D-DMAX (12× swelling ratio, 12% decrease compared to parent gel, **Figure D4**), while D-DMA showed an increase in the DMAc swelling ratio of 16× and a 15% increase compared to the parent gel (**Figure 6.3C, D5, and Table D2**).

Following the DMAc swelling ratio experiments, the gels were placed into excess deionized water for 24 hours (**Figure 6.3B, C, and Table D3**). The parent organogel swelled to 0.082× of the dry mass. An increase in swelling ratios was observed when comparing parent gels to D-MA (0.37× swelling ratio, 350% increase compared to parent

gel, **Figure D6**) and D-MAX (0.50× swelling ratio, 510% increase compared to parent gel, **Figure D7**). When the parent gel was compared to the DMA-containing daughter gels an increase was observed for D-DMA (5.2× swelling ratio, 6200% increase compared to parent gel, **Figure D8**) and D-DMAX (3.5× swelling ratio, 4200% increase compared to parent gel, **Figure D9**). The DMA-containing daughter gels favorable swelling in water was expected since PDMA will impart hydrophilicity to the organogel network, transforming it into an amphiphilic network.

We observed that the chain extensions were spatiotemporally controlled. The polymerizations to synthesize the block copolymer networks were irradiated from the bottom of the Petri dish which resulted in the chain extension polymerization localized to one side of the organogel and asymmetric expansion of the materials (**Figure D10**). For example, the localized chain extensions were observable with D-DMA and D-DMAX block copolymer networks, which showed heterogeneous water swelling. In both examples, the side that was facing the light during the chain extension swelled in water and the side facing away from the light contracted (**Figure 6.3D**).

To further investigate the spatiotemporal control of the block copolymer networks, we synthesized a daughter gel using a checkerboard pattern on the bottom of the Petri dish during an MA without DSDA chain extension polymerization. A lattice structure was imprinted onto the organogel as evidenced by distinct squares on the surface of the gel following the polymerization and swelling in DMAc (**Figure D11**).

6.3.3 Rheology Studies

The parent and bottoms of the daughter organogels were subjected to oscillatory shear rheometry to measure how the chain extensions modified the moduli (storage

modulus (G'), loss modulus (G'')) and overall viscoelastic behavior of the block copolymer networks compared to the STEM organogels. Amplitude, frequency, and time sweeps were run on the parent and daughter samples after being swelled in DMAc for 24 hours.

All block copolymer networks were within an order of magnitude stiffer compared to the parent organogel due to increased numbers of chain entanglements and/or chemical crosslinks (**Figure 6.4A, B, D12, and D13**). The materials chain extended with DMA (D-DMA and D-DMAX) showed a higher modulus than MA chain-extended materials (D-MA and D-MAX), with the samples containing additional crosslinker (D-DMAX and D-MAX) being stiffer than non-crosslinked counterparts (D-DMA and D-MA) (**Figure 6.4A and D14**).

All gels consistently showed a weak frequency dependence up to ~20 rad s^{-1}, after which, inertial effects are likely present (**Figure 6.4A**). These data suggest that the block copolymer networks behave as robust solid-like (i.e., elastic) materials. The amplitude sweep experiments showed that the linear-viscoelastic range was nearly constant for most of the gels (up to ~7% strain, **Figure 6.4B**). Interestingly, D-DMAX did not display an observable cross-over point up to 100% strain suggesting a more solid-like structure compared to the other block copolymer networks.

These rheological data indicate that the organogels became stiffer after the block copolymer network synthesis, and G' can be modulated by a factor of 2–3× via monomer choice. Overall, the swelling ratios and rheological analyses show that the physical properties of organogels can be readily modified via PET-RAFT chain extensions.

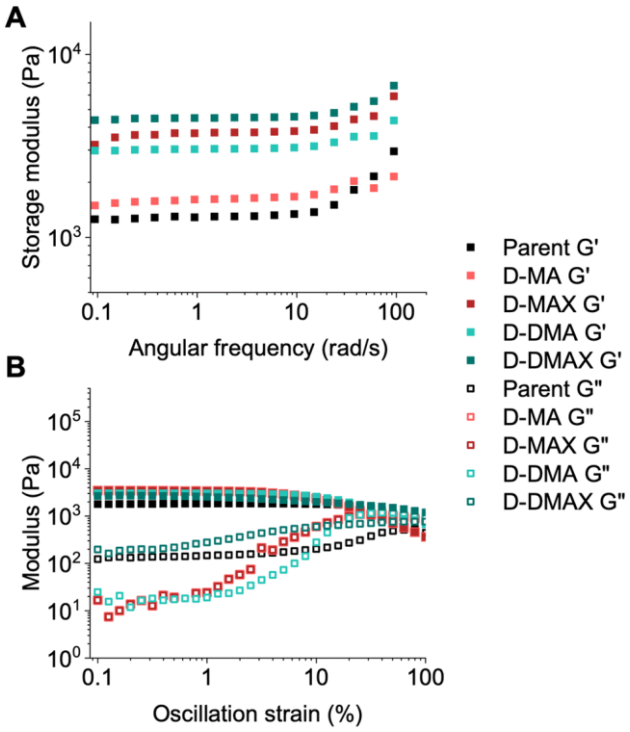

Figure 6.4. A) Frequency sweeps of the parent and daughter gels. B) Amplitude sweeps of the parent and daughter gels where the filled squares correspond to the storage modulus (G') and the empty squares correspond to the loss modulus (G'').

6.3.4 Degradation Studies

Degradation studies were performed on the daughter gels to assess how well the molecular weights were controlled during the organogel network chain extension. Each daughter gel was separated into top and bottom portions and subjected to a solution of dithiothreitol (DTT) at 20 mg mL^{-1} in DMAc at 65 °C for 24 hours to degrade the network into linear chains. MA was then added to the reaction mixture to perform a thiol-Michael addition to prevent oxidation of the sulfides, which would reform the crosslinks. After 24 h at 65 °C, the mixture was diluted and filtered for characterization by SEC (**Figure 6.5A**).

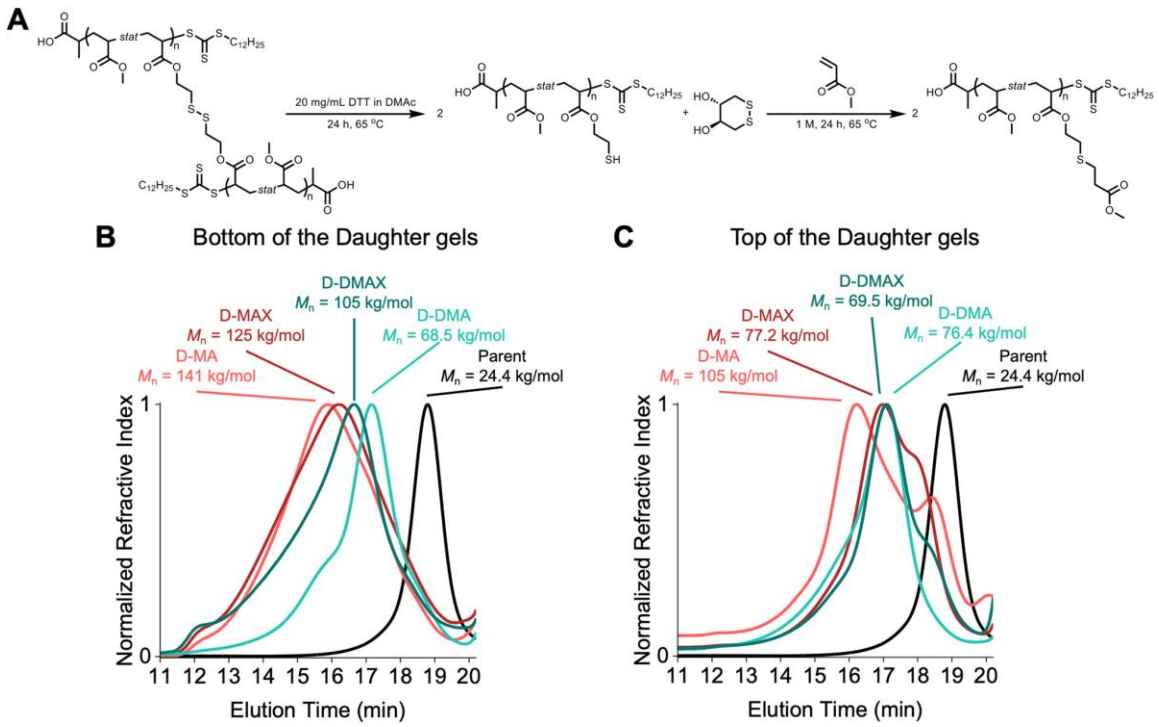

Figure 6.5. A) Scheme of gel degradation with dithiothreitol followed by a thiol-Michael addition. B) SEC traces of parent and bottoms of the daughter gels with molecular weight data calculated using PMMA SEC standards. C) SEC traces of parent and tops of the daughter gels with molecular weight data calculated using PMMA SEC standards.

The SEC traces showed the successful network chain extension of the parent gel, indicating that the trithiocarbonate chain-ends were retained following the synthesis of the STEM organogel. However, all the organogel network chain extension block copolymers showed broad SEC traces that spanned most of the entire column volume (~8 minutes of elution time, **Figure 6.5B**). Two observations can be made about the chain extensions. First, the bottoms of the daughter gels showed higher molecular weights than the top counterparts, except for D-DMA. This observation is attributed to the bottom of the gels being exposed to higher light intensity, which led to a higher radical concentration and resulted in a broader molecular weight distribution, analogous to a free radical polymerization. The chain extensions resulted in heterogeneous networks as the tops and bottoms did not undergo similar chain extension reactions (**Figure 6.5B, C**). Second,

PMA–PMA block copolymers eluted at lower retention times compared to PMA–PDMA block copolymers. This difference is attributed to MA being a better solvent for the parent networks than DMA. Resultantly, more MA diffused into the parent gel network prior to irradiation, leading to higher local concentrations of MA compared to DMA.

The broad dispersity of molecular weights indicated that the PET-RAFT chain extension did not undergo a controlled polymerization. We expect that the limited chain mobility prevented degenerative chain transfer reactions from occurring, which are needed for a controlled RAFT polymerization.[90,236] The limited chain transfer led to free radical polymerization and high amounts of termination. This result disproved our initial hypothesis that using PET-RAFT polymerization would lead to molecular weight control over the parent-to-daughter gel network extensions and suggests that additional degenerative chain transfer reaction pathways are required to maintain control over network block copolymer synthesis.

6.4 Conclusions

In this study, degradable organogels consisting of MA, DSDA, and DMA were synthesized via oxygen tolerant PET-RAFT polymerization. PET-RAFT block copolymer network chain extensions did not result in uniform molecular weight control as the daughter polymer chains showed broad and disperse traces by SEC analysis. Although PET-RAFT polymerization was found to result in poor molecular weight control over block copolymer network chain extensions, tunable physical properties (storage moduli, solvophilicity) according to monomer identity were still achieved. Looking forward, introducing additional reversible deactivation pathways to preserve chain end fidelity could lead to molecular weight control of network chain extensions and better network uniformity,

enabling investigations into how dispersity and molecular weight impact physical properties in block copolymer networks.

6.5 Experimental

6.5.1 Materials

Dimethyl sulfoxide (DMSO, Thermo Scientific, 99.7%), *N*,*N*-dimethylacetamide (DMAc, Thermo Scientific, 99%), *N*,*N*-dimethylformamide (DMF, Acros Organics, 99.8%), acryloyl chloride (Sigma, 97%), bis(2-hydroxyethyl) disulfide (BHEDS, Sigma, technical grade), and triethylamine (Thermo Scientific, 99%) were used as received. Methyl acrylate (MA, Thermo Scientific, 99%) and *N*,*N*-dimethylacrylamide (DMA, TCI, 99%) were filtered through basic alumina prior to use. Zinc tetraphenyl porphyrin (ZnTPP) (TCI, 97%) was prepared as a 10 mg mL^{-1} solution in DMSO prior to use. Dithiothreitol (DTT, Fisher, 99%) was prepared as a 20 mg mL^{-1} solution in DMAc prior to use. Disulfide-based diacrylate (DSDA) was synthesized from a previous report.[339] 2-(Dodecylthiocarbonothioylthio)propionic acid (DTPA) was synthesized using an adapted procedure from a previous report.[211]

For a visible light source, 76.2 cm Supernight Blue LED Light Strips were purchased from Amazon and placed on a Xnrtop Silver Tone Aluminum Radiator Heatsink Heat Sink 150 × 80 × 27 mm from Amazon.

6.5.2 Characterization

^{1}H nuclear magnetic resonance (NMR) spectroscopy was conducted on an Agilent U4-DD2 400 MHz at 25 °C. DMSO-d_6 (Cambridge Isotopes Laboratories, Inc., 99.9%) and $CDCl_3$ (Cambridge Isotopes Laboratories, Inc., 99.8%) were used as received.

Size exclusion chromatography (SEC) was performed in *N*,*N*-dimethylacetamide (DMAc) with 50 mM LiCl at 50 °C at a flow rate of 0.5 mL min^{-1} (Agilent isocratic pump, degasser, and autosampler, columns: TOSOH TSKgel Guard Alpha and TOSOH TSKgel Alpha-4000: exclusion limit of 1×10^6 Da). Detection consisted of an Agilent 1260 Infinity II refractive index detector and an Agilent 1260 Infinity II variable wavelength detector operating at 280 nm. The system was calibrated with poly(methyl methacrylate) standards with molecular weights in the range of 1480 to 1062000 g mol^{-1}, which corresponds to a linear calibration region of 12.8 to 21.6 minutes.

Rheological measurements were performed on an HR 20 Discovery Hybrid Rheometer (TA Instruments) equipped with stainless steel 8 mm parallel plates. Temperature was controlled with an environmental test chamber and maintained at 23 ± 1 °C. Frequency sweeps were performed at 0.5% strain from 0.01 to 15 Hz (0.06 to 94 rad s^{-1}). Strain (amplitude) sweeps were performed at 1 Hz from 0.01 to 200%. Time sweeps were performed at 0.5% strain and 1 Hz over 300 s. Sample thickness was approximately 2 mm and a small normal force (~0.1 N) was used to compress the sample between the plates to reduce slippage.

6.6 Procedures

6.6.1 PET-RAFT Polymerization of the Parent Gels

DMSO (2.81 mL), MA (2.45 g, 28.5 mmol), DSDA (75.0 mg, 0.285 mmol), DTPA (20.0 mg, 0.0570 mmol), and ZnTPP (0.193 mg, 0.000285 mmol, 31.4 ppm) were combined in a 20 mL scintillation vial. The mixture was capped and irradiated with a blue LED strip (7.88 mW cm^{-2}) for 20 h at room temperature (23 °C). The reaction was quenched by turning off the LED strip and opening the vial to air. The gel was then washed

3× with methanol to remove unreacted monomer and catalyst. The gel was then dried overnight *in vacuo* at room temperature (23 °C).

6.6.2 PET-RAFT Polymerizations of the Daughter Gels without DSDA

DMSO, MA or DMA (10.0 mmol), parent gel network (disk = ∼10 mm in diameter by 3 mm tall), and ZnTPP (2.71 mg, 0.004 mmol, 271 ppm) were combined in the bottom of a Petri dish with a diameter of 94 mm at 1 M [monomer]. The mixture was covered with the top of the Petri dish, sealed with parafilm and electrical tape, and equilibrated at room temperature (23 °C) for 24 hours. The mixture was then irradiated with a blue LED strip (7.88 mW cm^{-2}) for 20 h at room temperature (23 °C). The reaction was quenched by turning off the LED strip and opening the Petri dish to air. The gel was then washed 3× with methanol to remove unreacted monomer and catalyst. The gel was then dried overnight *in vacuo* at room temperature (23 °C).

6.6.3 PET-RAFT Polymerizations of the Daughter Gels with DSDA

DMSO, MA or DMA (10.0 mmol), DSDA (26.2 mg, 0.100 mmol), parent gel network (disk = ∼10 mm in diameter by 3 mm tall), and ZnTPP (2.71 mg, 0.004 mmol, 271 ppm) were combined in the bottom of a Petri dish with a diameter of 94 mm at 1 M [monomer]. The mixture was covered with the top of the Petri dish and sealed with parafilm and electrical tape and equilibrated at room temperature (23 °C) for 24 hours. The mixture was then irradiated with a blue LED strip (7.88 mW cm^{-2}) for 20 h at room temperature (23 °C). The reaction was quenched by turning off the LED strip and opening the Petri dish to air. The gel was then washed 3× with methanol to remove unreacted monomer and catalyst. The gel was then dried overnight *in vacuo* at room temperature (23 °C).

6.6.4 Swelling Ratio Experiments

The dried gels (20 mg – 250 mg) were weighed (WD) and placed in excess DMAc or DI water for 24 h at room temperature (23 °C) in sealed vials. The swollen gels were removed from the vials and dabbed dry with paper towels and weighed (WS). The swelling ratios were calculated by eqn (1).

$$Swelling\ Ratios\ (\%) = \frac{W_S - W_D}{W_D}\ x\ 100 \quad (1)$$

6.6.5 Gel Degradation and thiol-Michael Addition for SEC Analysis

A piece of dried gel (~20 mg) was placed in a 2-dram scintillation vial containing 3 mL of 20 mg mL^{-1} DTT solution in DMAc. The vial was subsequently capped with a septum and sparged with argon for 5 minutes. The sparged vial was placed in a 65 °C oil bath for 24 hours. The vial was then uncapped and MA (284 mg, 3.3 mmol) was added. The vial was subsequently capped with a septum and sparged with argon for 5 minutes. The sparged vial was placed in a 65 °C oil bath for 24 hours. The resulting solution was diluted by 50% with DMAc containing 50 mM LiCl and passed through a 0.2 μm PTFE syringe filter prior to SEC analysis.

Chapter 7: Conclusions

PET-RAFT polymerization has been used to address two long-standing limitations in the RDRP community, including: 1) the insertion of a single monomer at a defined position within the polymer backbone and 2) reversing blocking order requirements to access novel block copolymer sequences.

For inserting a single monomer unit, the method proved to be indifferent to chemical functionality on the monomer, resulting in >96% incorporation levels for all monomers tested with the absence of any double- or higher-order insertions. This method remains the only known instance of a single-unit monomer insertion into the backbone of a polymer chain that results in exclusively single insertions with no higher-order insertions observed, and it has inspired the use of vinyl ethers in other single-unit insertion methods. Furthermore, this method offers avenues in advancements for other areas such as studying structure-function relationships in ionomers, synthesizing more advanced polymer architectures, surface immobilization, and protein recognition. However, this method needs to be improved through various ways prior to the advancement of other areas. One way this method needs to be improved is determining how to retain chain end fidelity after the chain extension. Currently, we are restricted to one incorporation due to the poor chain end fidelity, but if we can overcome this limitation multiple sites can be incorporated. Another limitation of the technique is that we require a large excess of monomer. Currently, we need to use 100 equiv of monomer to drive the incorporation of the vinyl ether since it is an unfavorable reaction, but this results in a large excess of unused monomer. This restricts the monomers to those that are commercially available, limiting the functionality

that can be incorporated. In order to overcome this limitation, other conditions need to be explored, such as ionic liquids or deep eutectic solvents. Nonetheless, the method does provide an opportunity to incorporate a functional monomer at a defined position enabling structure-property relationship studies that were previously inaccessible in RAFT polymers.

For reversing blocking order requirements, linear pseudo-first-order kinetics, an increase in molecular weight with conversion, and shifts to lower retention times via SEC with irradiation time were observed, and lower dispersities were achieved with the presence of a tertiary amine serving as a reversible redox pathway to improve TTC stability. This enabled the synthesis of comparable polymers with different blocking orders, demonstrating the substantial impact that blocking order has on resultant material properties. Overall, this report presents a method for synthesizing a previously inaccessible block copolymer, which enabled a structure-function relationship study to be performed regarding blocking order. Although not perfect, this method addressed and partially overcame an existing 30-year limitation in the RAFT polymerization community, and 20 years behind the introduction of the halogen-exchange in ATRP. Further improvement of this method will enable the synthesis of higher-order multiblock copolymers with any desired sequence, regardless of monomer order, thereby benefiting compatibilization efforts in the ongoing plastic crisis and lead to next-generation thermoplastic elastomers.

To further improve upon the previous method, in-depth kinetic studies were performed on the system to determine the underlying rates and to improve the chain end retention. We found that both $k_{a,TTC}$ and $k_{t,TTC}$ were impacted by [TTC] and photocatalyst loading, but that $k_{a,TTC}$ increased more with increasing temperature compared to $k_{t,TTC}$,

leading to the highest $k_{a,TTC}/k_{t,TTC}$ values to date, reaching a value of 4.1 compared to the previous work, which had a maximum ratio of 1.2. These methodologies were unsuccessful when conventional thermal initiators or photoiniferter were used as the initiation method, indicating the necessity of PET catalysis and the advantages of using PET catalysis with RAFT polymerization. Although this report ultimately did not retain quantitative chain ends, improvements were made. To further improve this method multiple areas still need to be explored. The first area that needs to be explored is the photocatalyst choice. Currently, we have only used *fac*-Ir(ppy)$_3$, which proceeds through energy transfer resulting in a trithiocarbonate radical species that is prone to degradation. However, there is an entirely different pathway, electron transfer, that PET-RAFT polymerization compatible photocatalyst can proceed through. This pathway can be beneficial as upon initiation the trithiocarbonate is already in the reduced anionic state, which is more stable in solution and less susceptible to degradation events. Photocatalysts of interest to us include 10-phenylphenothiazine, zinc tetraphenylporphyrin, and zinc phthalocyanine. Furthermore, to improve the $k_{a,TTC}/k_{t,TTC}$, conditions also need to be changed including solvent. Ionic liquids and deep eutectic solvents have been shown to increase the rate of activation and decrease the rate of termination through stabilization events. These solvents could be beneficial to the method as limiting termination is our biggest hurdle. By improving this method we hope to overcome blocking order limitations to access any desired block copolymer sequence. These advances in polymer synthesis will enable the synthesis of novel polymer sequences and polymer architectures, the probing of structure–function relationships, and access to next generation materials.

Appendix:

Appendix A: SUMI Reaction Characterization

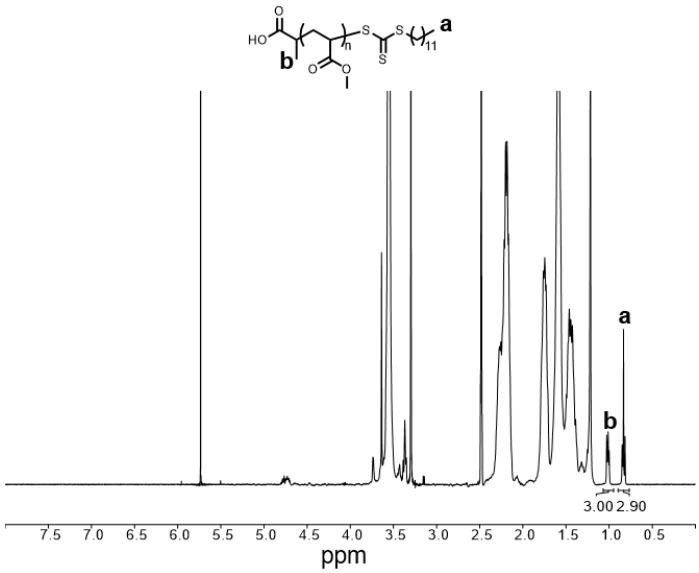

Figure A1. Starting PMA (M_n = 8000 g/mol, $Đ$ = 1.06) ^{1}H NMR spectrum for SUMI reactions.

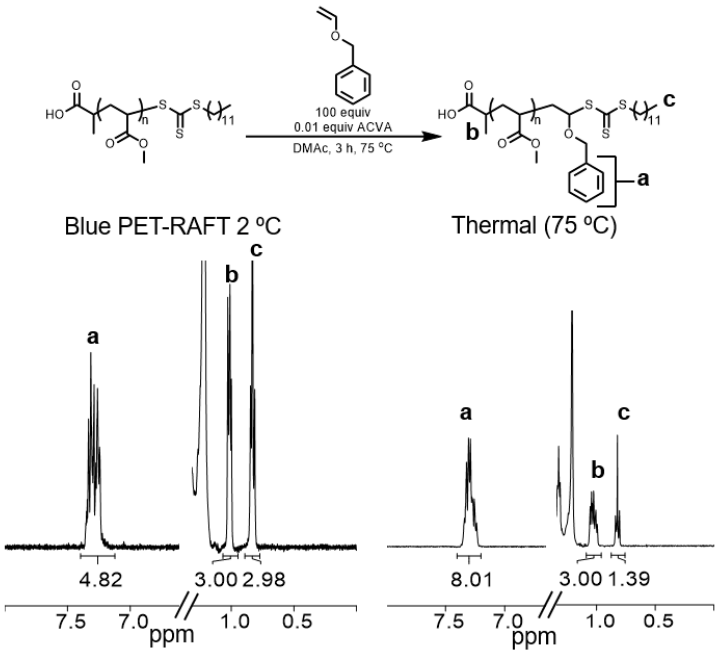

Figure A2. Comparison of PET-RAFT SUMI reactions conducted at 2 °C vs. thermal SUMI reactions conducted at 75 °C via ^{1}H NMR spectroscopy.

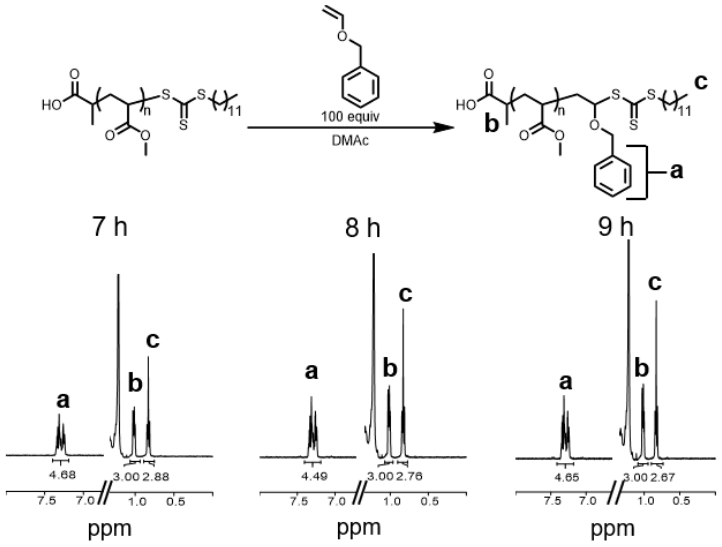

Figure A3. Comparison of SUMI reactions with increasing time at 25 ºC via ^{1}H NMR spectroscopy.

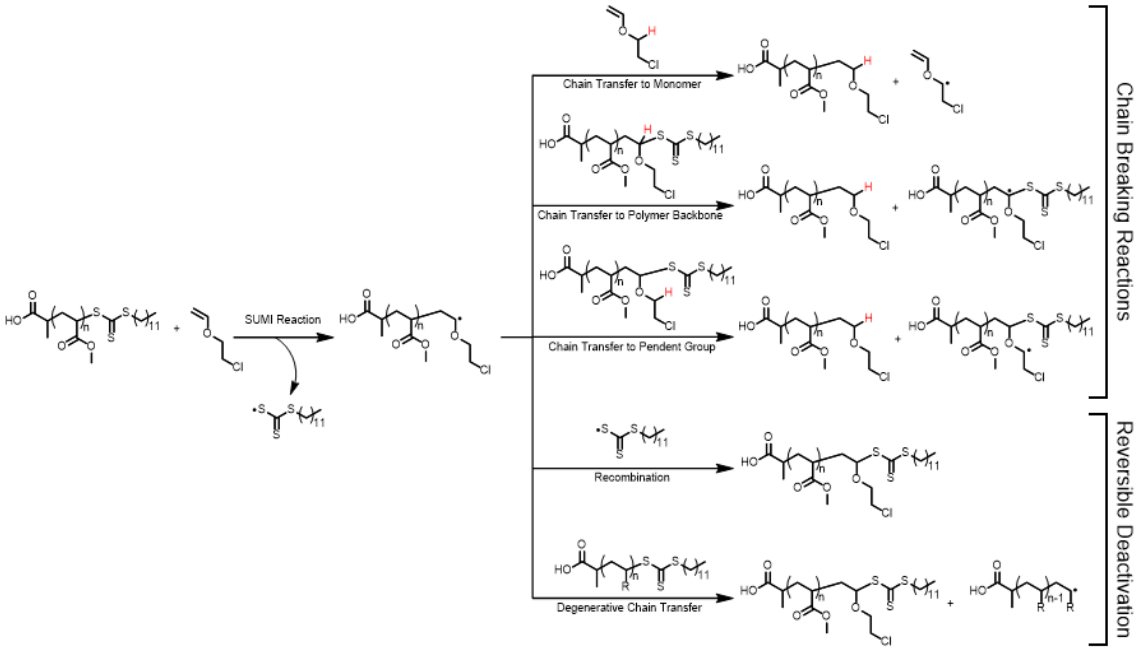

Figure A4. Possible termination and chain transfer events following the SUMI reaction. Chain breaking reaction events result in irreversibly terminated polymer chains. Reversible deactivation events result in polymers with TCT chain ends.

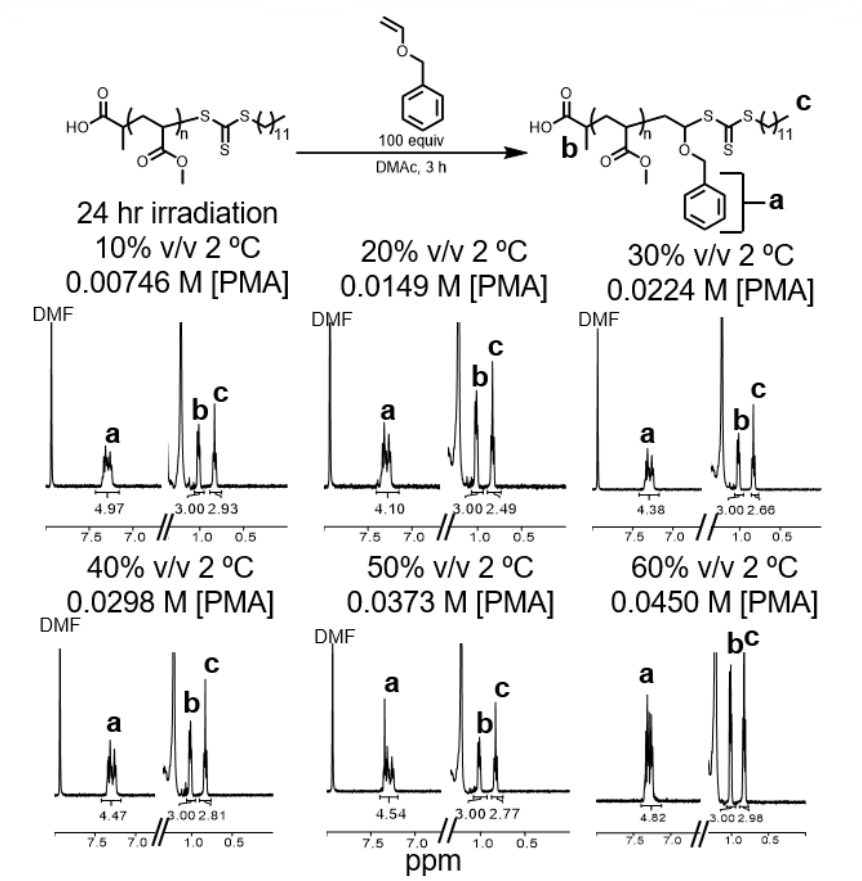

Figure A5. Comparison of SUMI reactions with increasing polymer concentrations conducted at 2 °C via ^{1}H NMR spectroscopy.

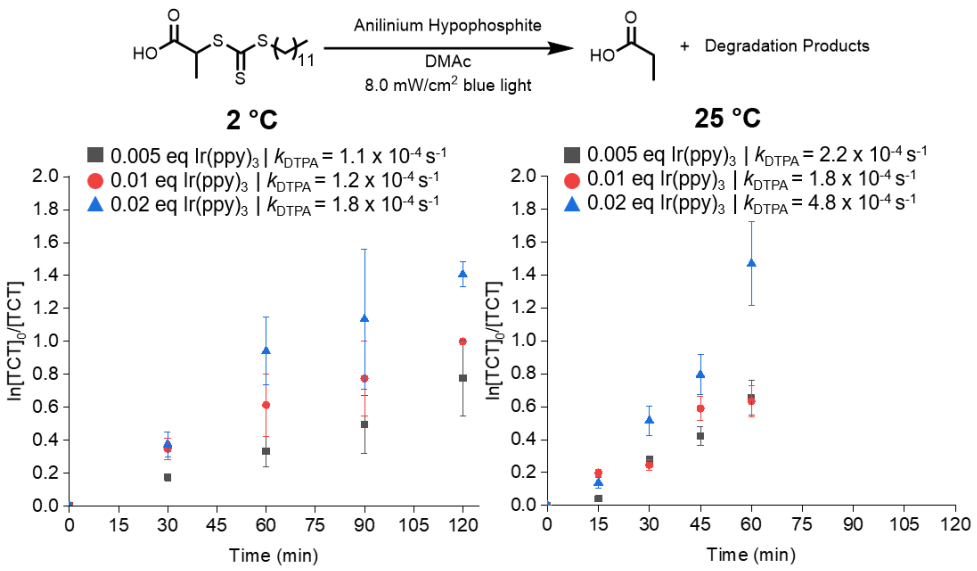

Figure A6. Trapping studies conducted at 2 °C and 25 °C with different catalyst loadings with respect to the concentration of DTPA.

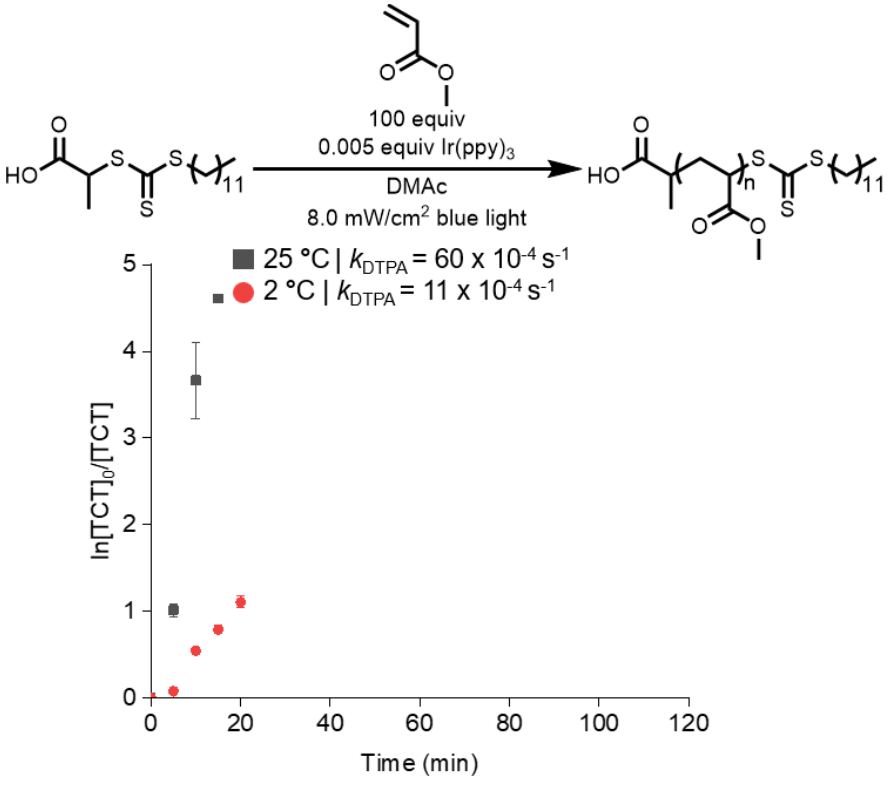

Figure A7. Small molecule studies conducted with MA at 2 °C and 25 °C with a 0.005 eq. catalyst loading with respect to the concentration of DTPA.

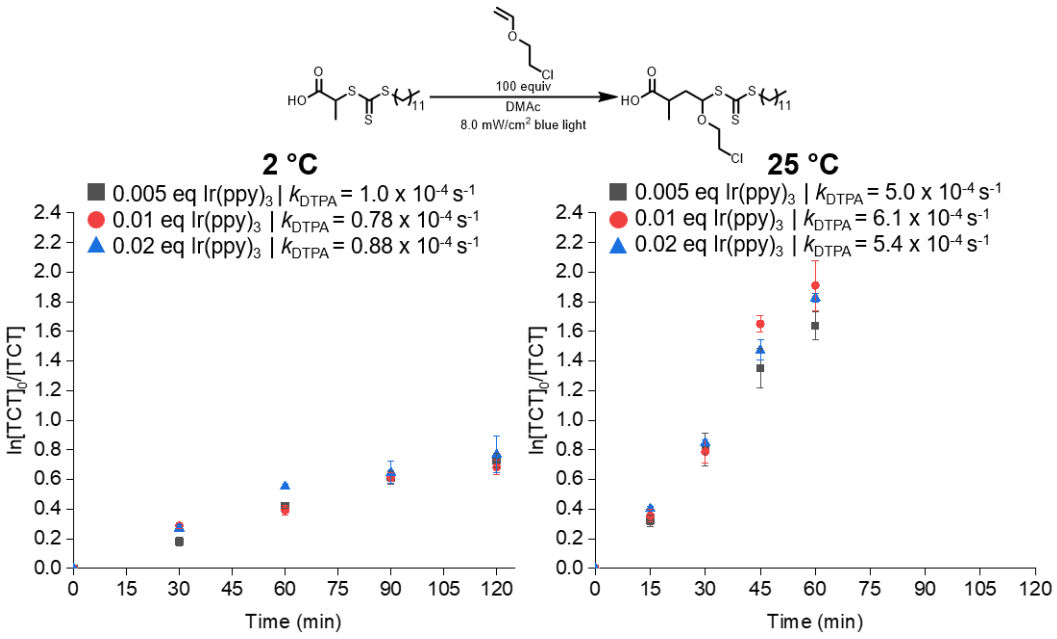

Figure A8. Small molecule studies conducted with 2-ClEVE at 2 °C and 25 °C with different catalyst loadings with respect to the concentration of DTPA.

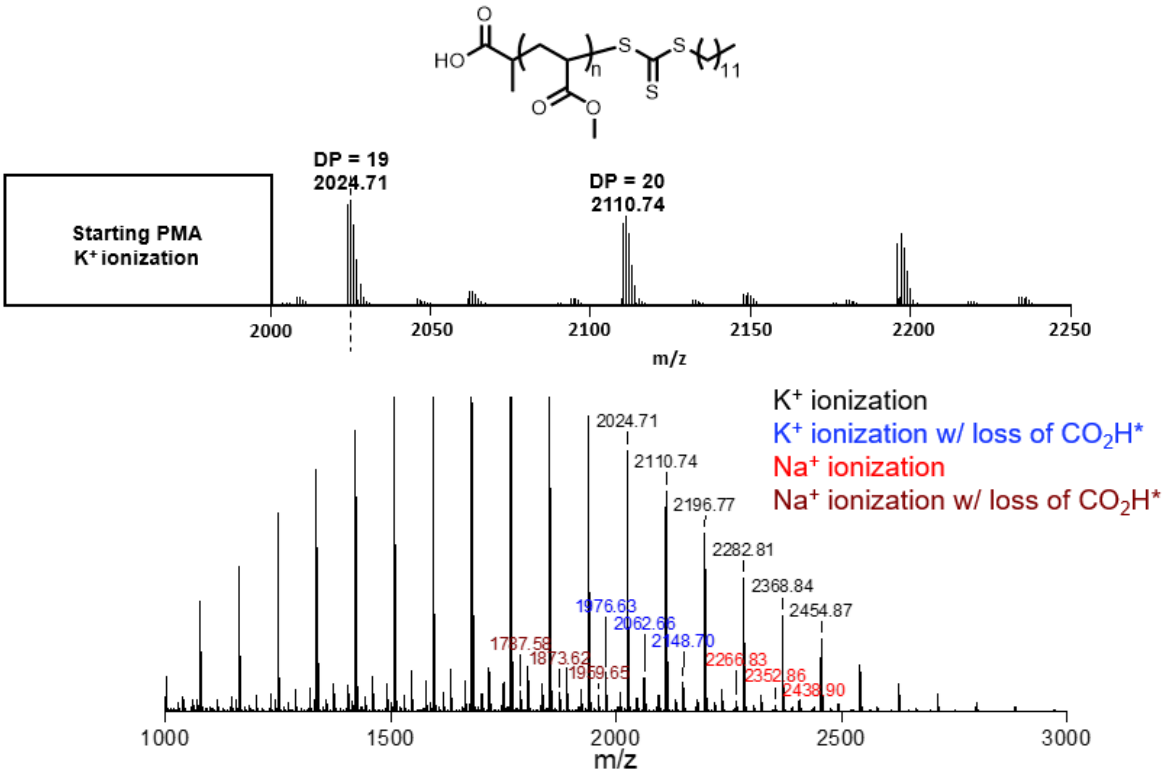

Figure A9. MALDI-TOF spectrum of starting PMA (M_n = 2,800 g/mol, $Đ$ = 1.07). *Proposed fragmentation occurring during the ionization process.[345–348]

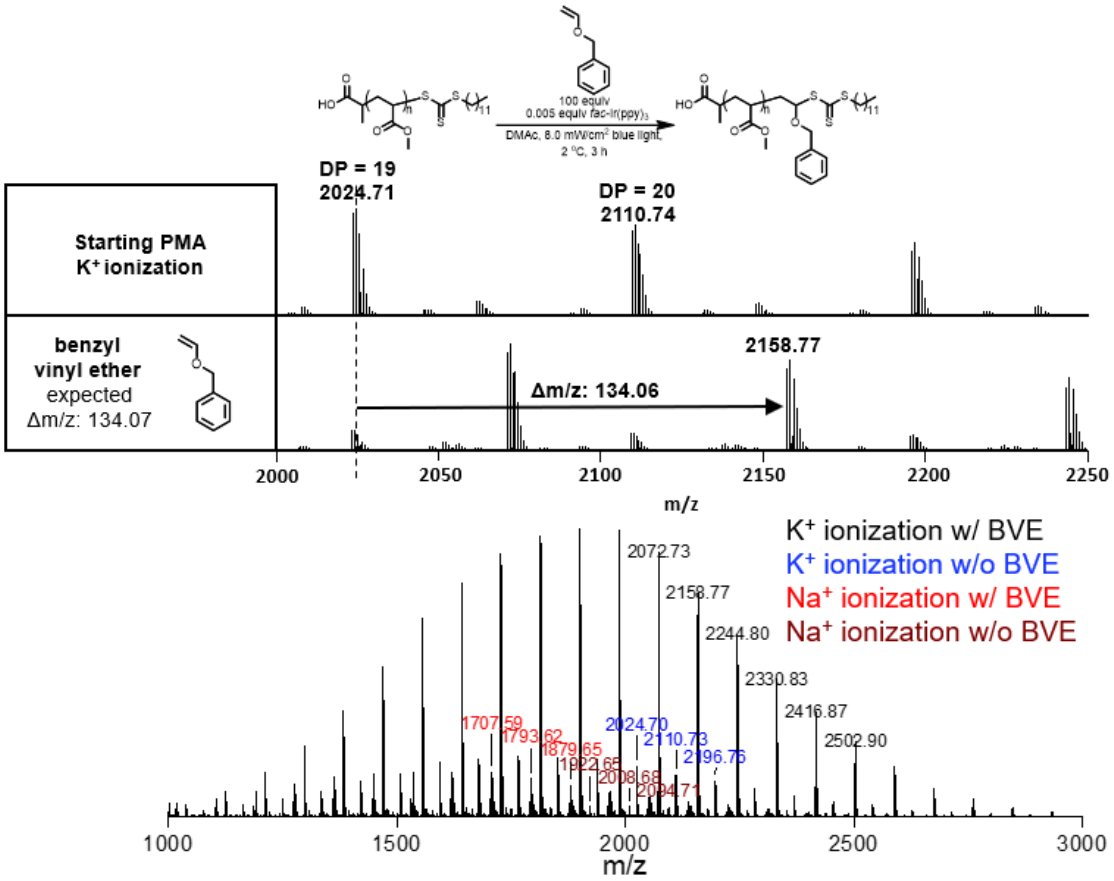

Figure A10. MALDI-TOF spectrum of PMA-BzVE.

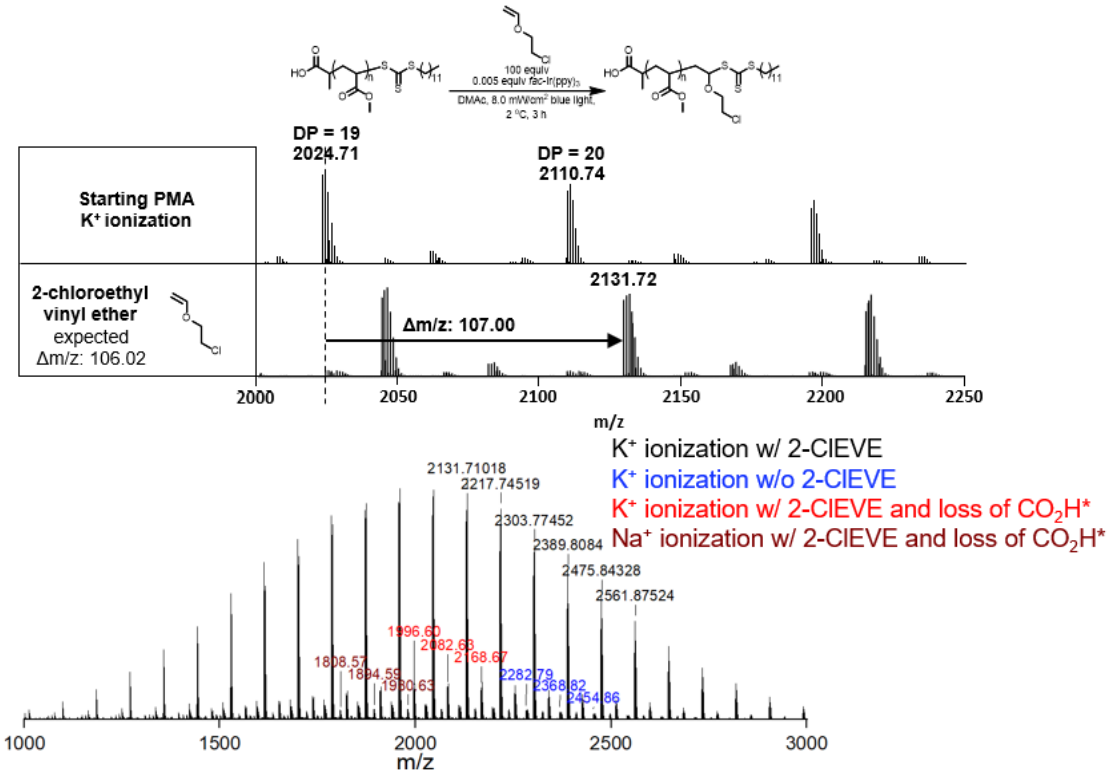

Figure A11. MALDI-TOF spectrum of PMA-(2-ClEVE). *Proposed fragmentation occurring during the ionization process.[345–348]

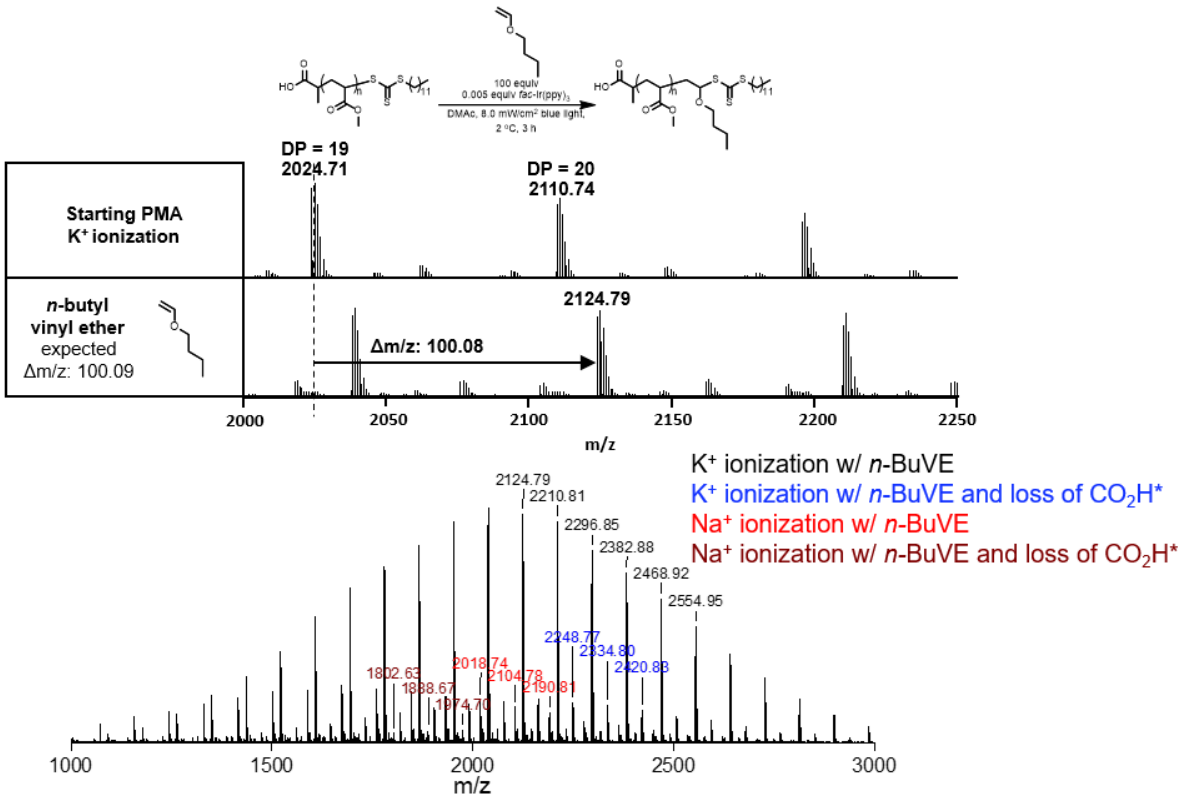

Figure A12. MALDI-TOF spectrum of PMA-(*n*-BuVE). *Proposed fragmentation occurring during the ionization process.[345–348]

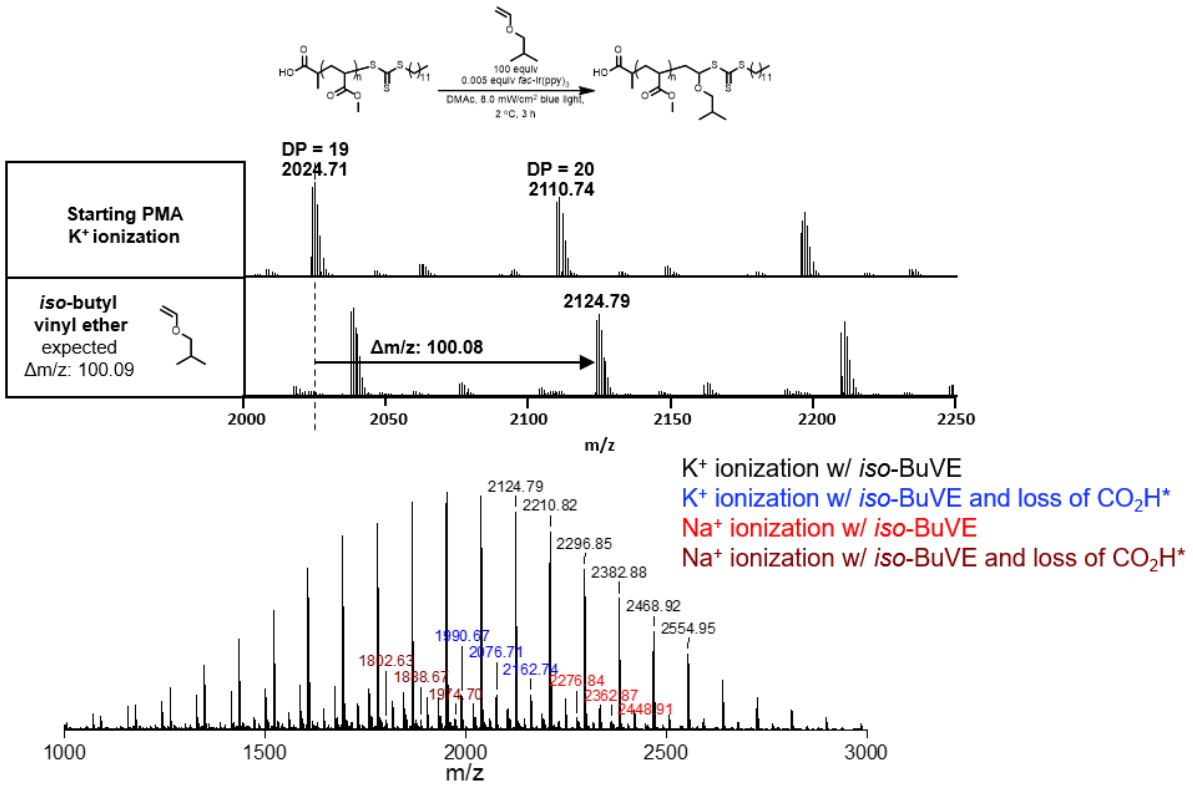

Figure A13. MALDI-TOF spectrum of PMA-(*iso*-BuVE). *Proposed fragmentation occurring during the ionization process.[345–348]

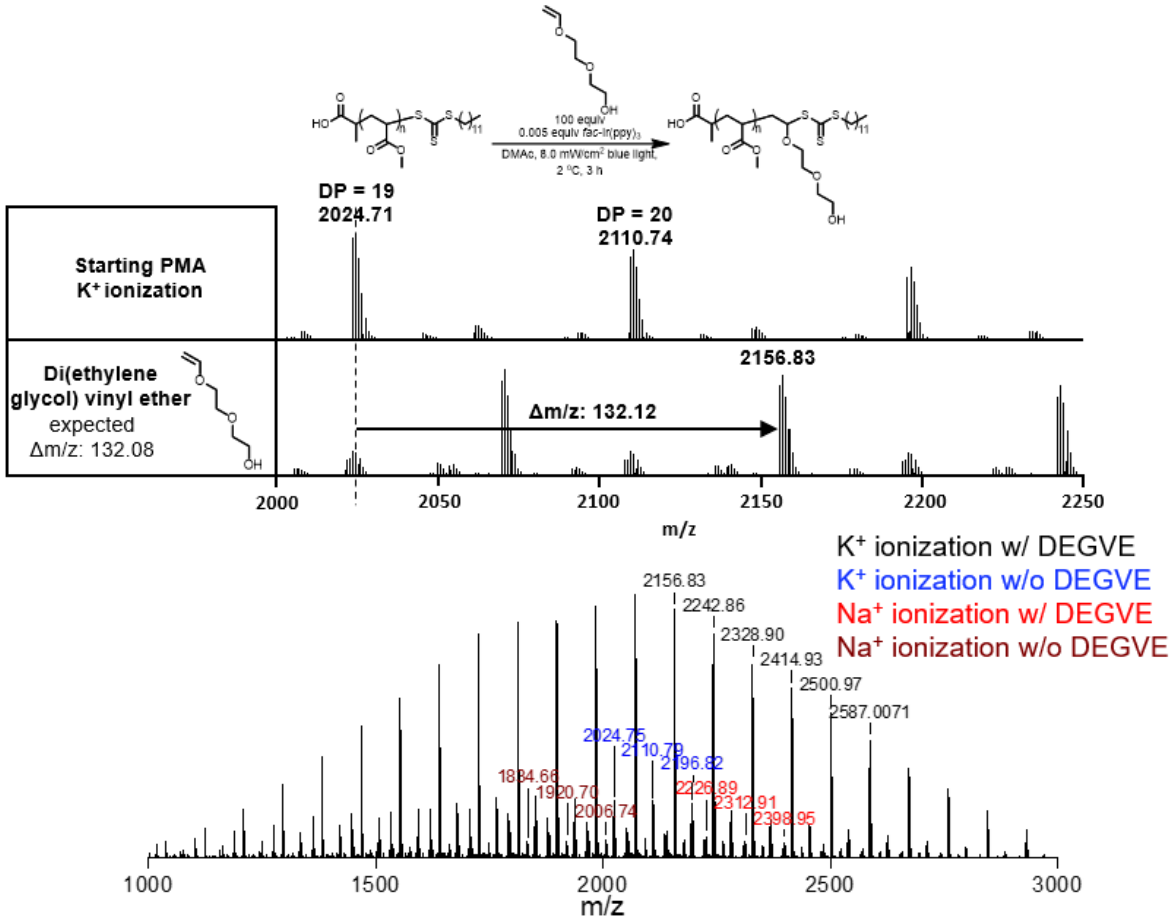

Figure A14. MALDI-TOF spectrum of PMA-DEGVE.

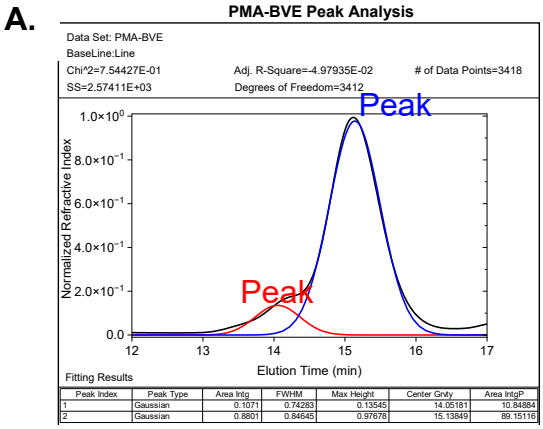

Results

Peak Results

	Peak 1	Peak 2
General (mL/(mg cm))		
UV Ext. Coef. (mL/(mg cm))	0.013	0.011
Masses		
Injected Mass (µg)	1014.00	1014.00
Calculated Mass (µg)	166.94	1220.68
Mass Recovery (%)	16.5	120.4
Molar mass moments (g/mol)		
Mn	1.254×10^{4} (±7.307%)	6.895×10^{3} (±6.267%)
Mw	1.347×10^{4} (±8.382%)	7.082×10^{3} (±7.089%)
Polydispersity		
Mw/Mn	1.074 (±11.120%)	1.027 (±9.462%)

B.

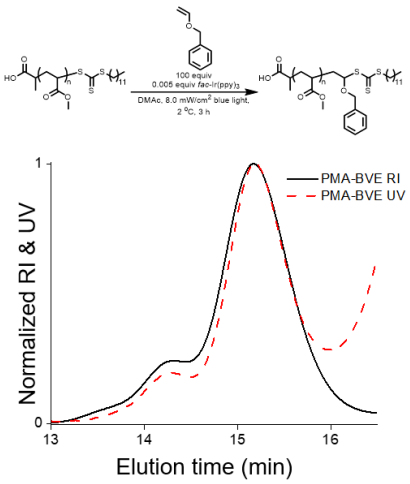

Figure A15. A) Peak analysis of PMA-BVE peaks using deconvolution to assess percentages using Origin Pro and molecular weights of lower elution time species using Astra. Since peak 1 is 2× the molecular weight of peak 2, the area integration was divided by 2 to determine the relative mole percentages of each peak. B. Normalized RI and UV traces are shown for PMA-BVE. The high molecular weight shoulder following the SUMI reaction shows UV absorbance at 365 nm, the wavelength associated with TCTs. This UV absorbance indicates that the chains are not terminated through a conventional chain-chain coupling termination pathway, in which no TCT absorbance would be observed. Instead, the remaining UV absorbance likely stems from chain breaking events either to backbone or vinyl ether pendent groups, which is followed by a polymer-polymer coupling.

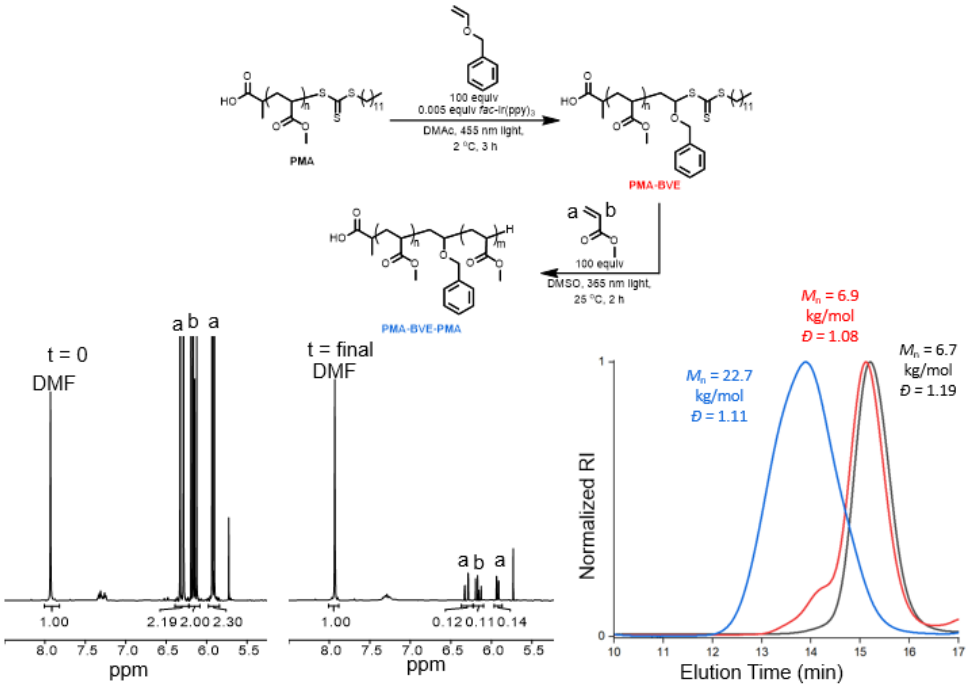

Figure A16. Chain extension of PMA-BVE with 100 equiv MA with t = 0 and final ^{1}H NMR spectra and SEC chromatograms.

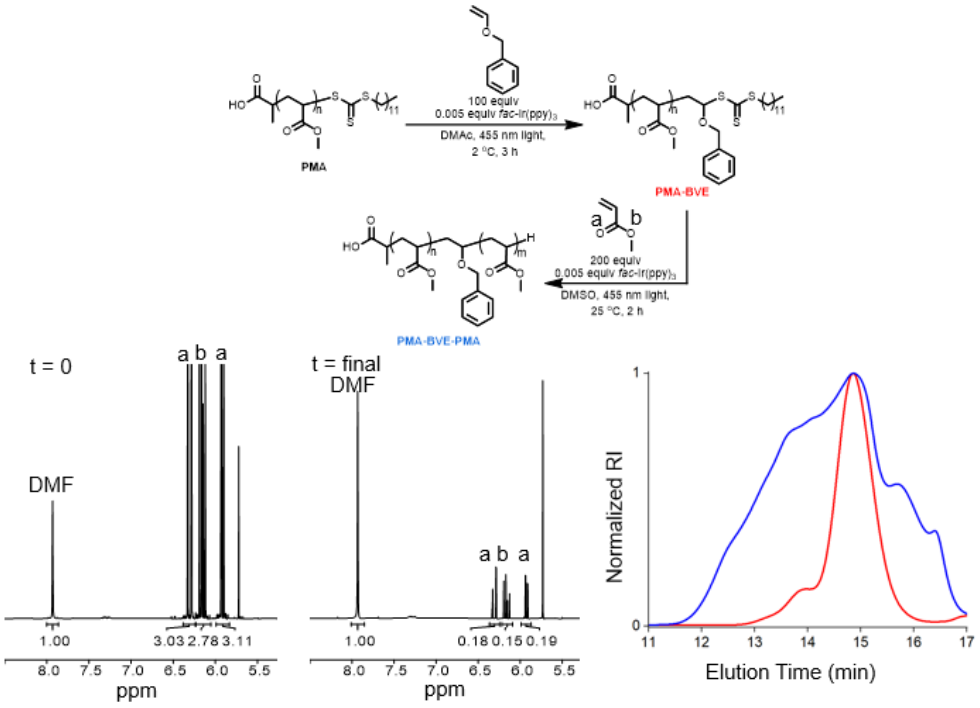

Figure A17. Chain extension using 0.005 equiv $Ir(ppy)_3$ irradiated with 455 nm light of PMA-BVE with 200 equiv MA with t = 0 and final ^1H NMR spectra and SEC chromatograms.

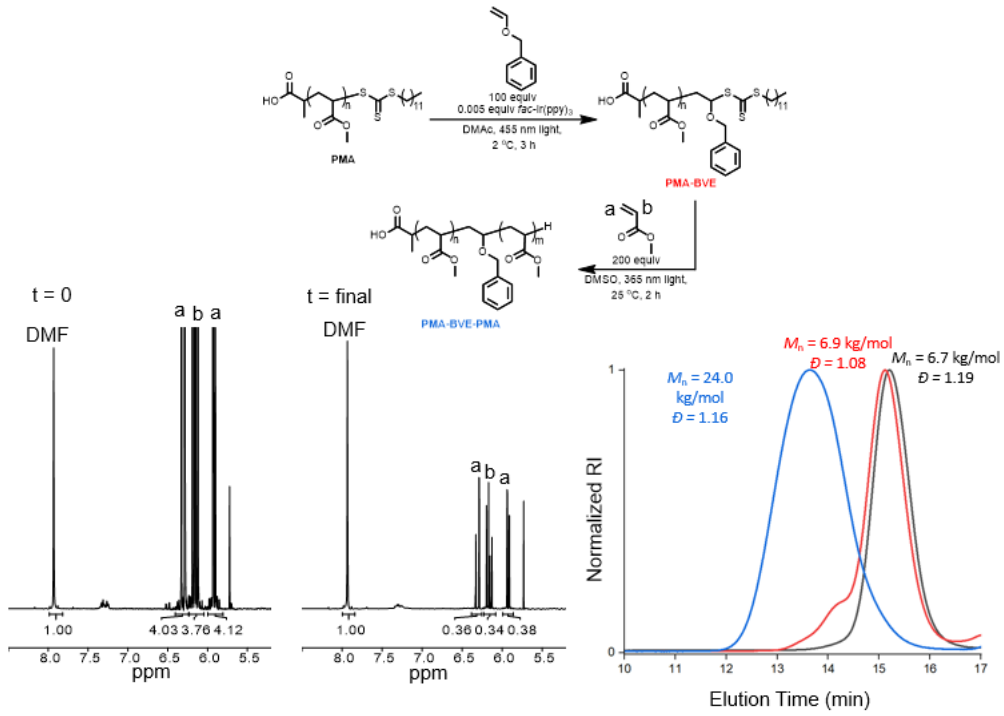

Figure A18. Chain extension of PMA-BVE with 200 equiv MA with t = 0 and final ^{1}H NMR spectra and SEC chromatograms.

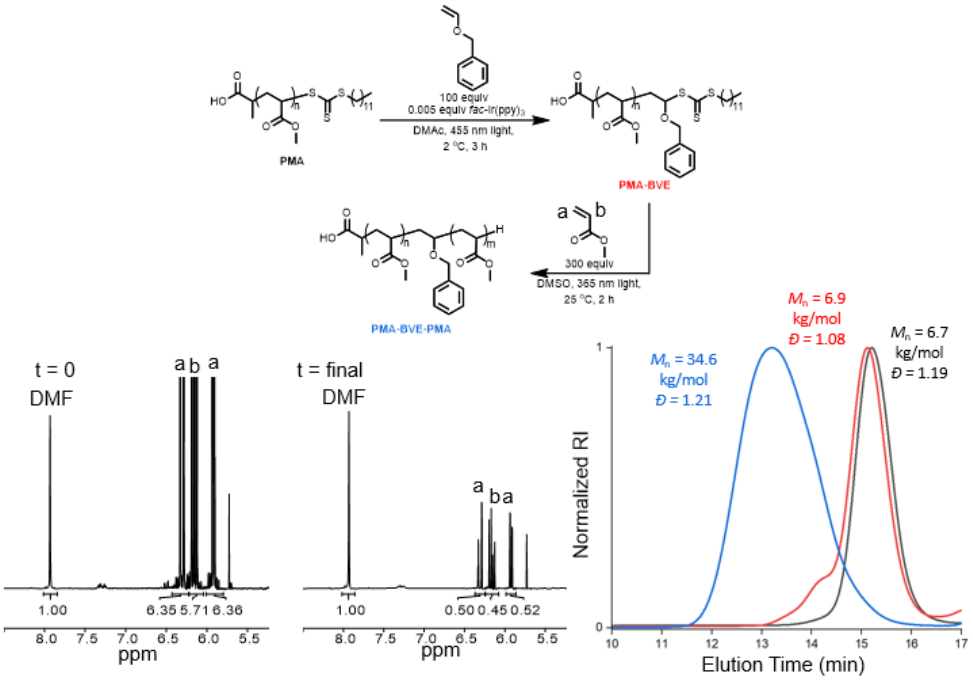

Figure A19. Chain extension of PMA-BVE with 300 equiv MA with t = 0 and final ^{1}H NMR spectra and SEC chromatograms.

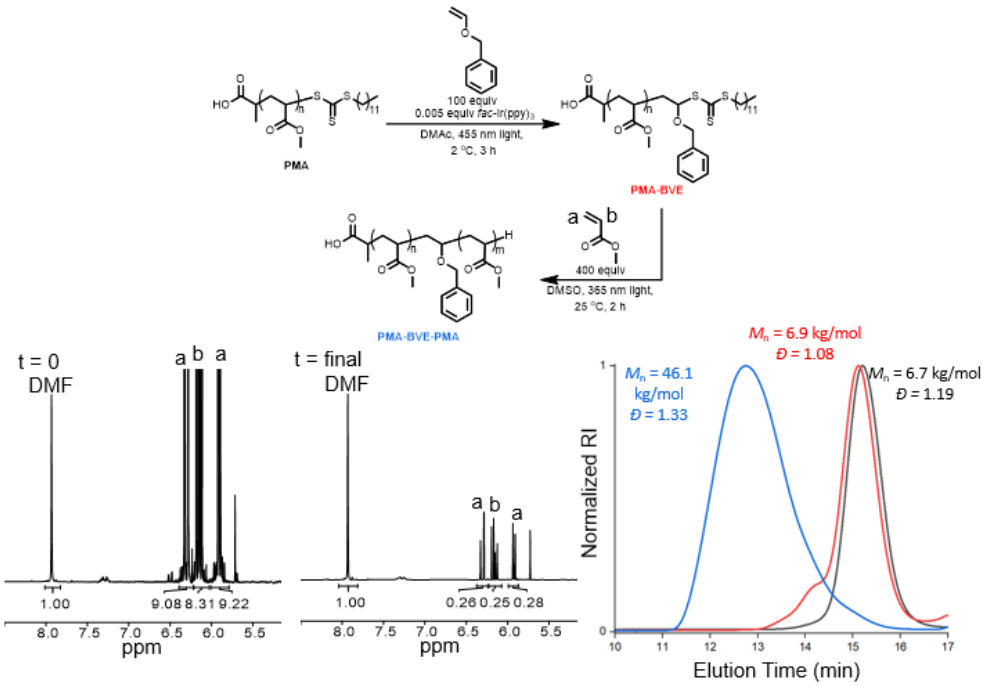

Figure A20. Chain extension of PMA-BVE with 400 equiv MA with t = 0 and final ^{1}H NMR spectra and SEC chromatograms.

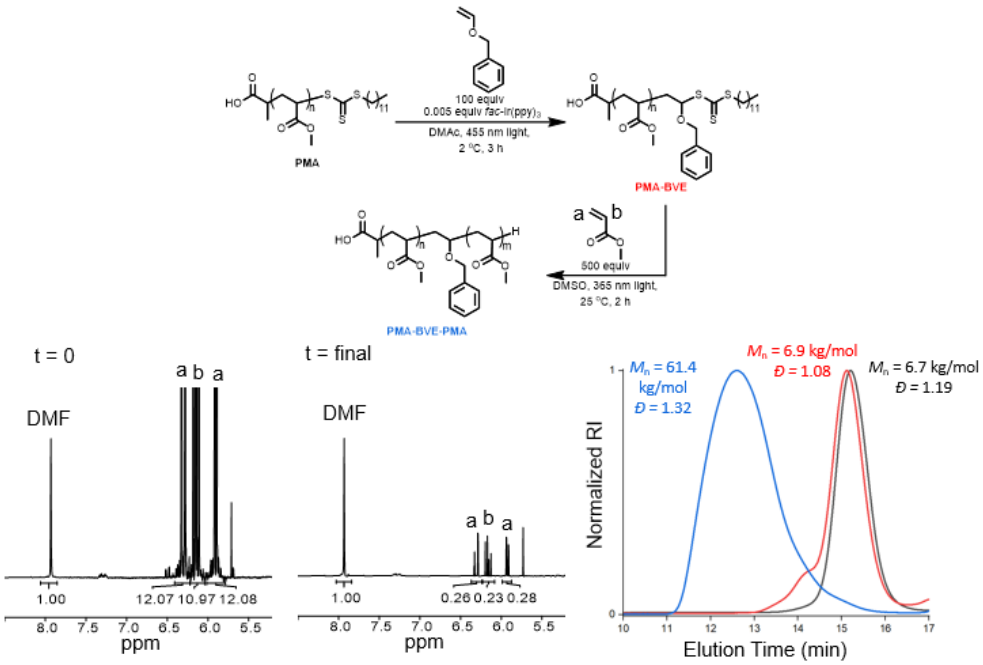

Figure A21. Chain extension of PMA-BVE with 500 equiv MA with t = 0 and final ^{1}H NMR spectra and SEC chromatograms.

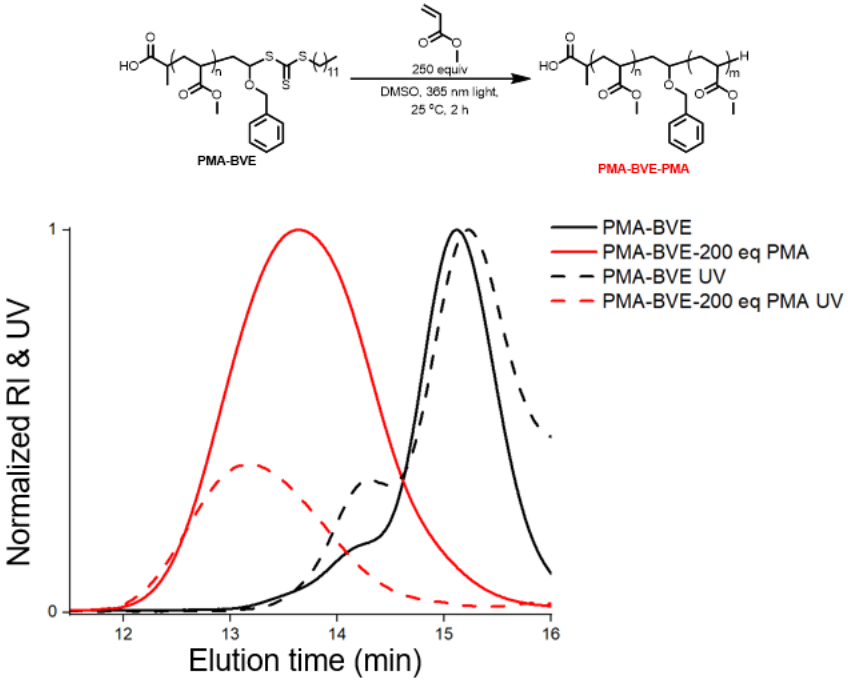

Figure A22. Normalized RI and UV traces for PMA-BVE and PMA-BVE-PMA.

Following the chain extension from PMA-BVE there is a large decrease in UV indicating

large amounts of irreversible termination events occur during the photoiniferter chain extension.

Appendix B: Reversing Blocking Order Using PET Catalysis Characterization

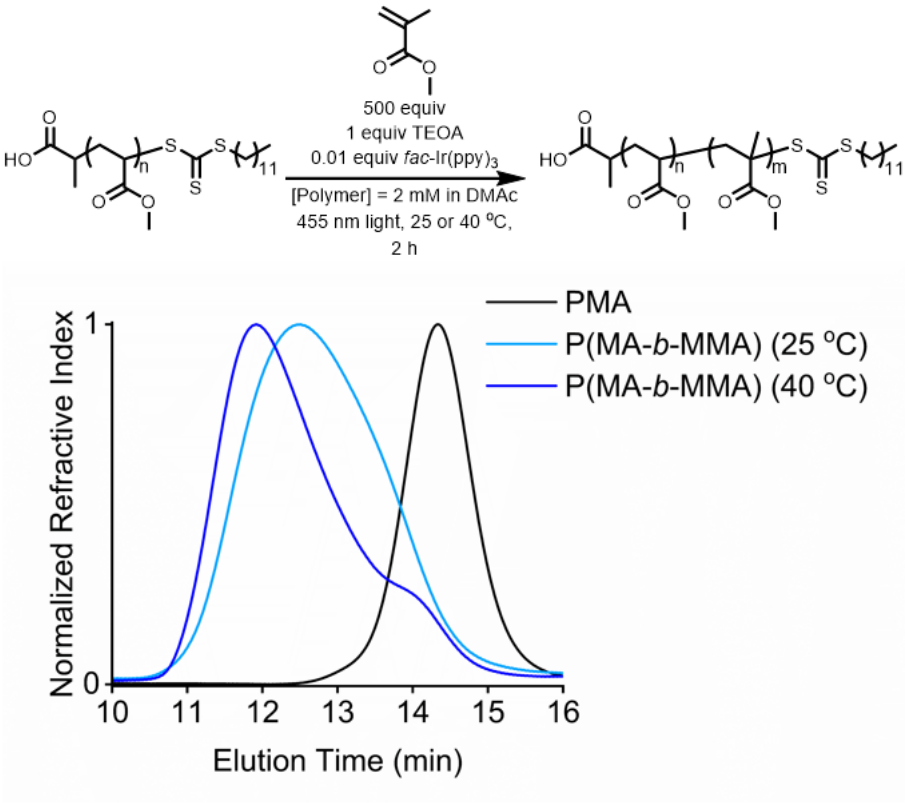

Figure B1. Normalized refractive index (RI) traces of P(MA-*b*-MMA) chain extensions conducted at 25 °C and 40 °C.

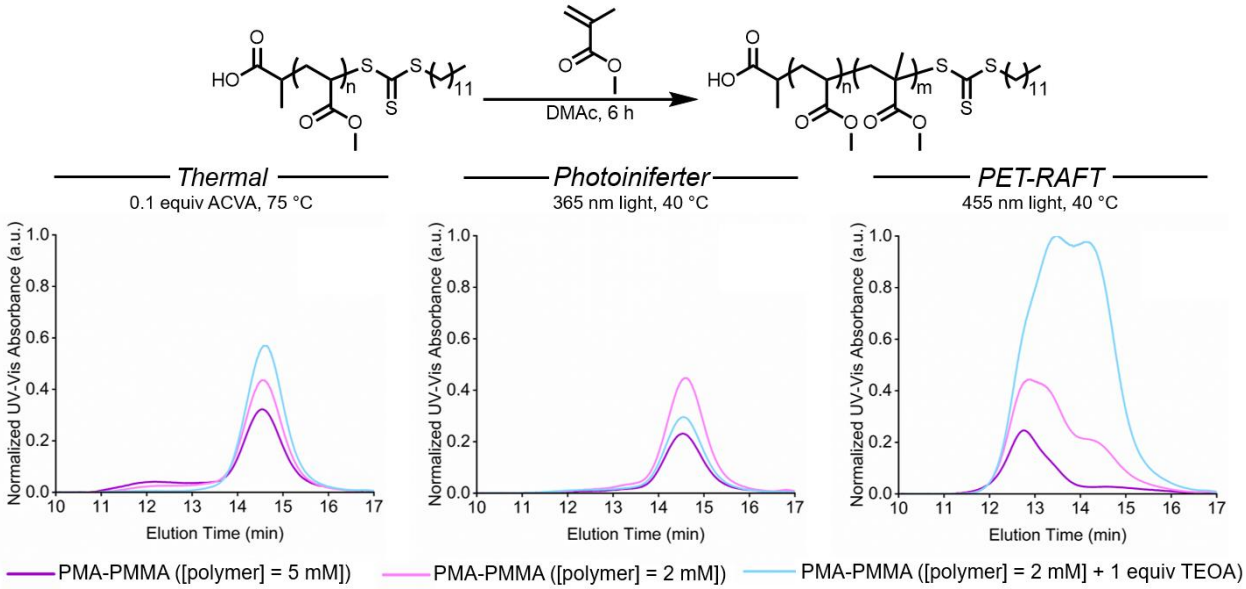

Figure B2. Normalized UV-Vis absorbance of thermal, photoiniferter, and PET initiation pathways tested across three conditions.

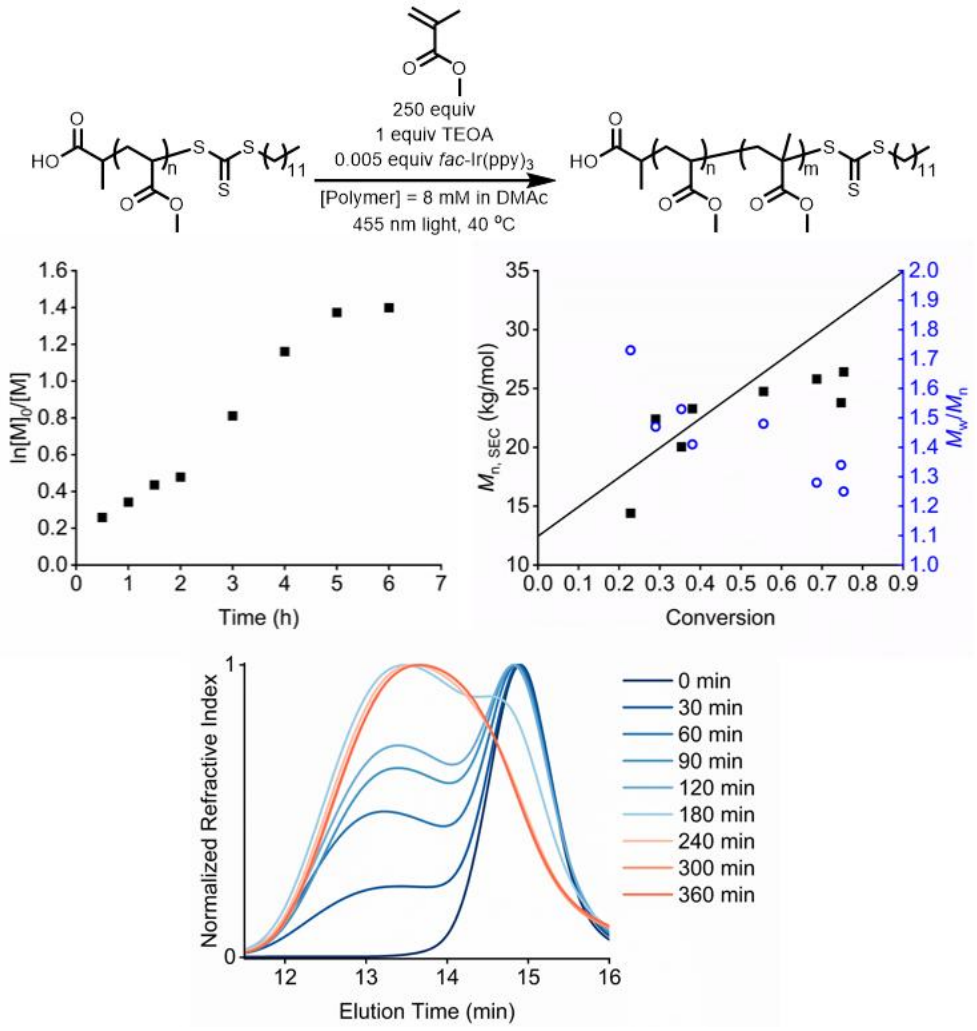

Figure B3. Kinetic data of the reverse blocking order polymerization using 0.005 equiv $Ir(ppy)_3$ at an 8 mM polymer concentration.

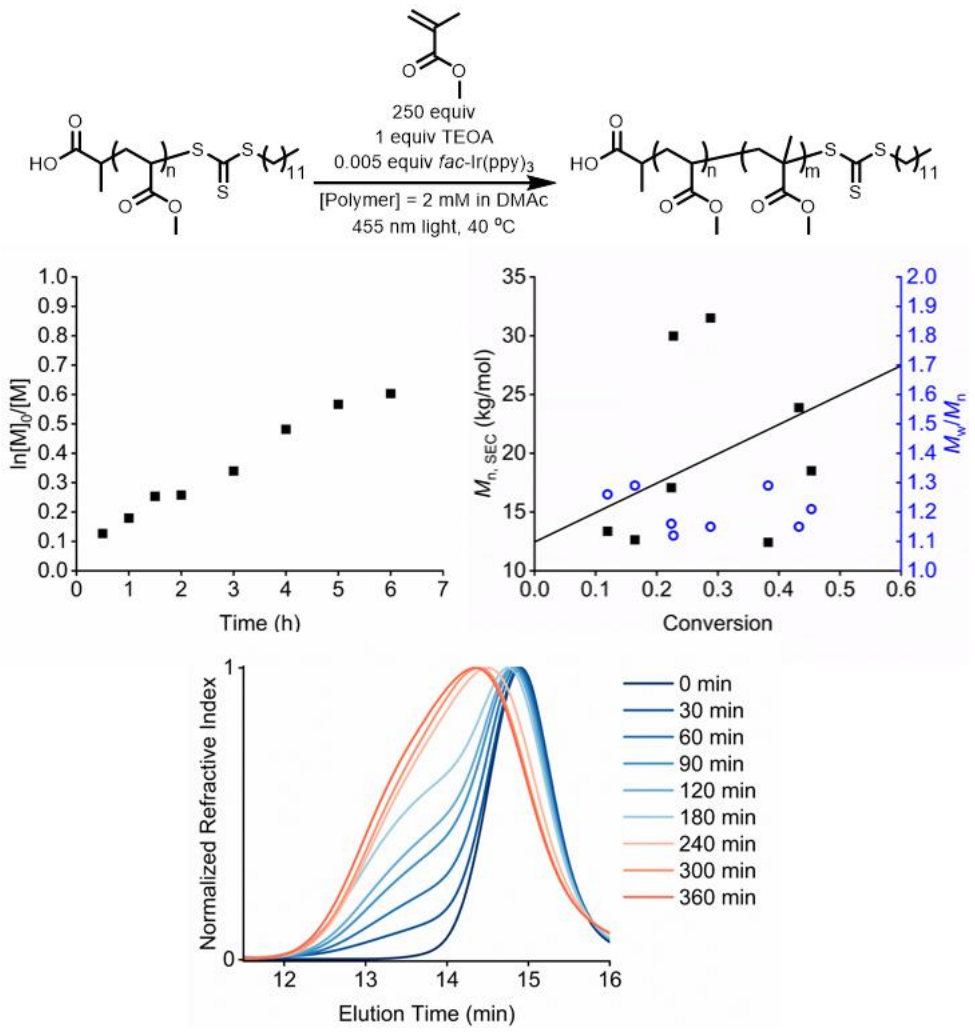

Figure B4. Kinetic data of the reverse blocking order polymerization using 0.005 equiv $Ir(ppy)_3$ at a 2 mM polymer concentration.

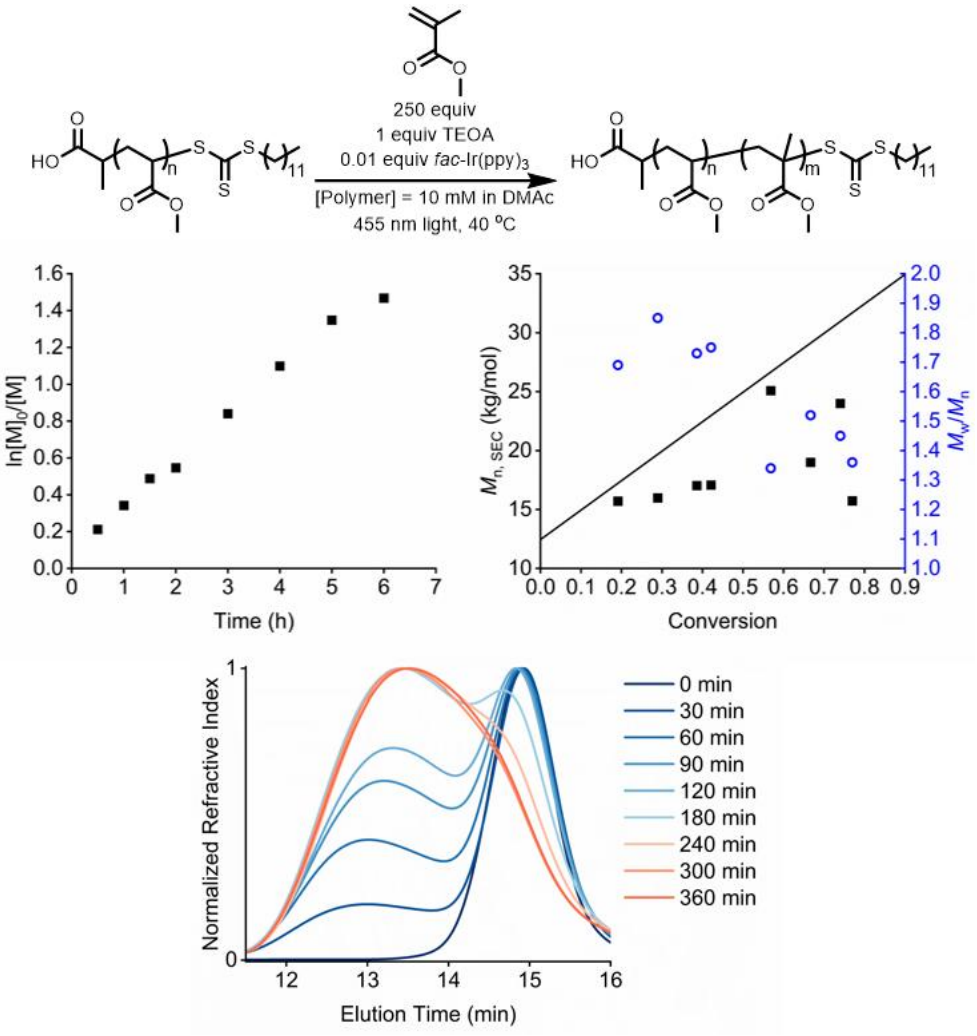

Figure B5. Kinetic data of the reverse blocking order polymerization using 0.01 equiv $Ir(ppy)_3$ at a 10 mM polymer concentration.

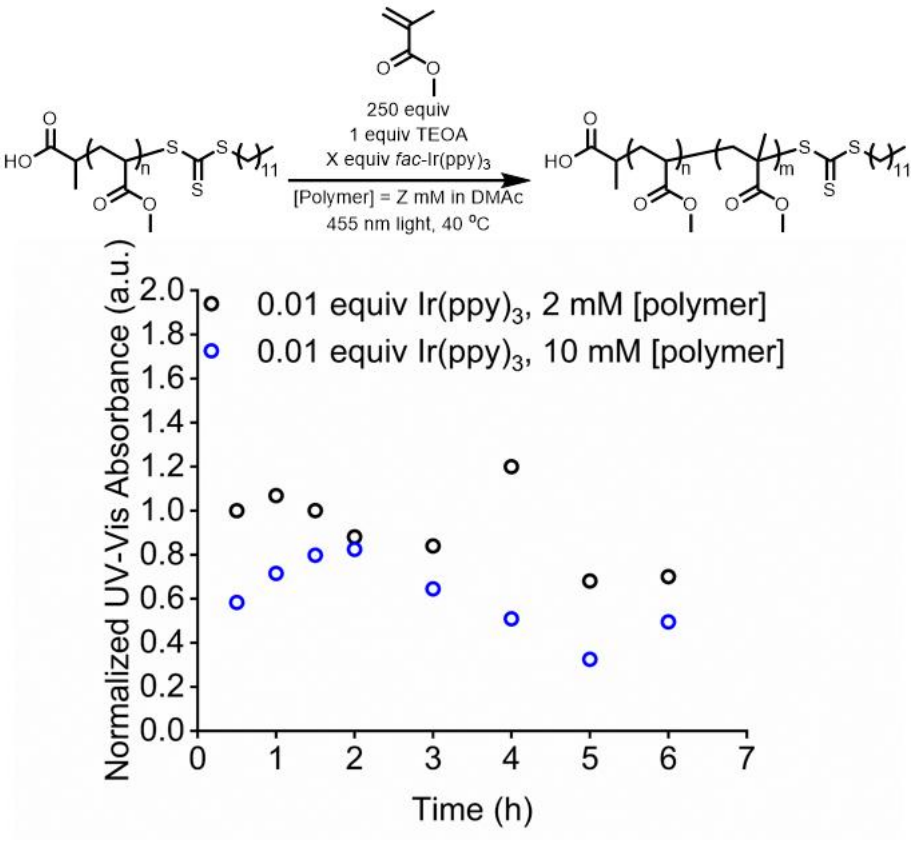

Figure B6. Normalized UV-Vis absorbance kinetic data comparing the impact of polymer concentration (2 mM vs 10 mM) on chain-end retention.

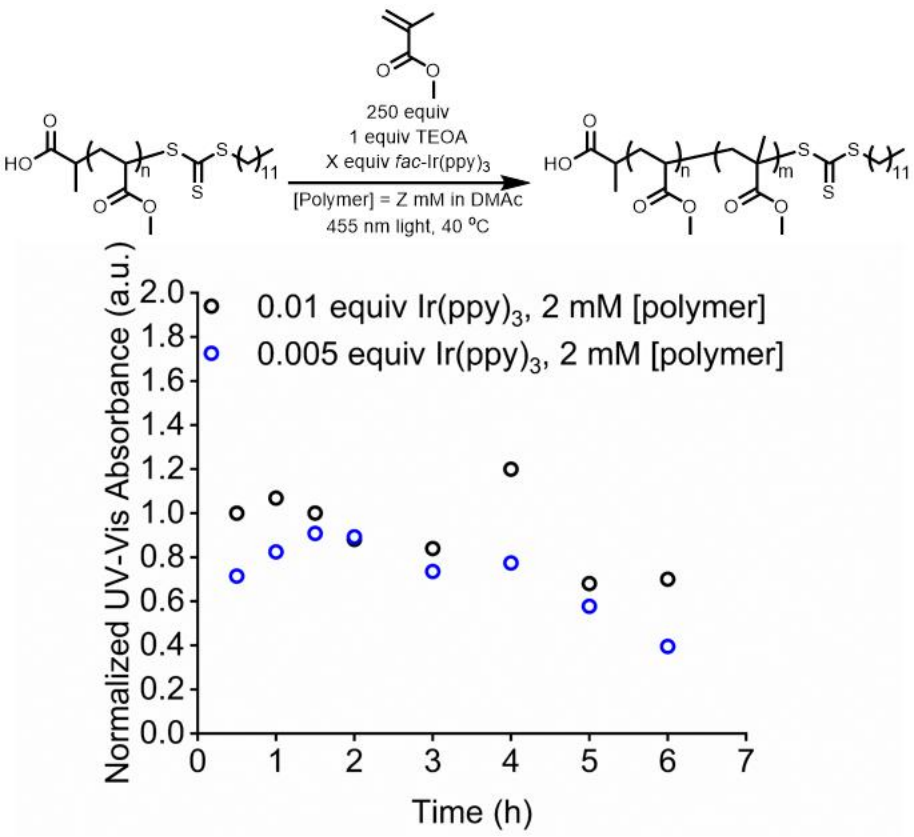

Figure B7. Normalized UV-Vis absorbance kinetic data comparing the impact of $Ir(ppy)_3$ equivalents (0.01 equivalents vs 0.005 equivalents) on chain-end retention.

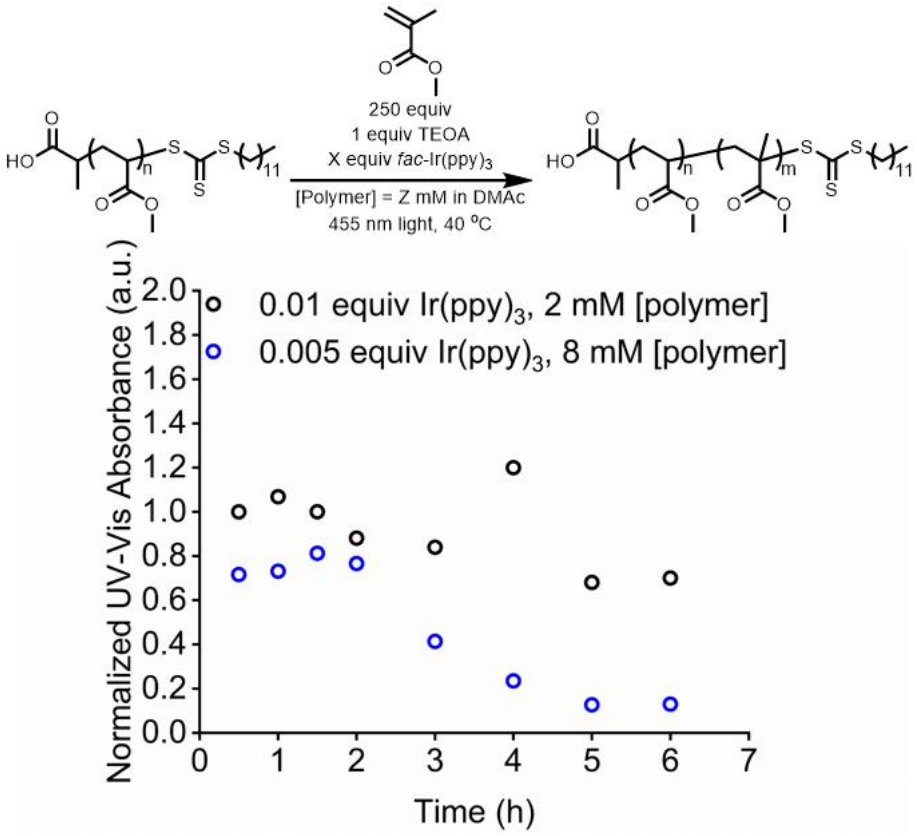

Figure B8. Normalized UV-Vis absorbance kinetic data comparing the impact of polymer concentration and $Ir(ppy)_3$ equivalents (2 mM, 0.01 equivalents vs 8 mM, 0.005 equivalents) on chain-end retention.

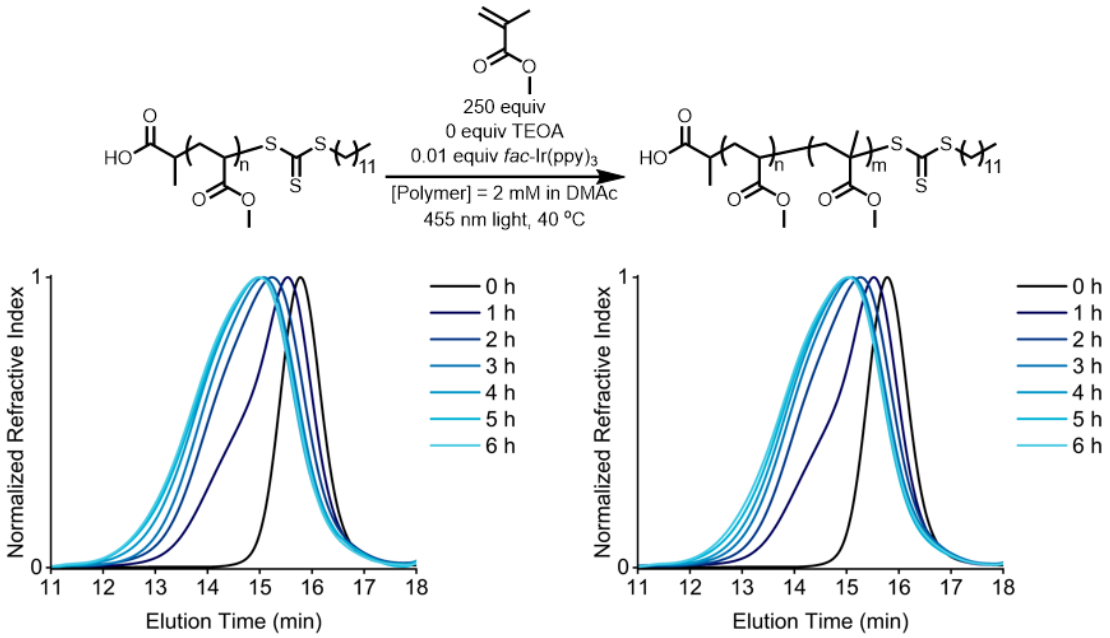

Figure B9. Additional refractive indices of the reverse blocking order polymerization using PMA, 0.01 equiv $Ir(ppy)_3$ at a 2 mM polymer concentration with no TEOA (n=3) from Figure 3C.

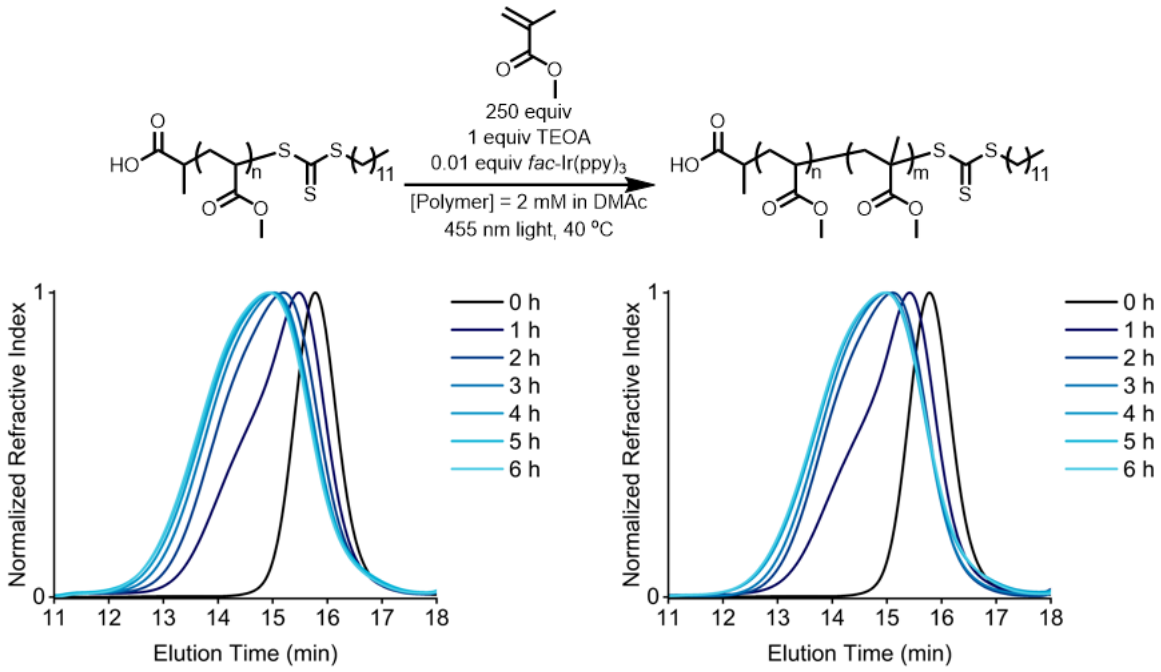

Figure B10. Additional refractive indices of the reverse blocking order polymerization using PMA, 0.01 equiv $Ir(ppy)_3$ at a 2 mM polymer concentration with TEOA (n=3) from Figure 3F.

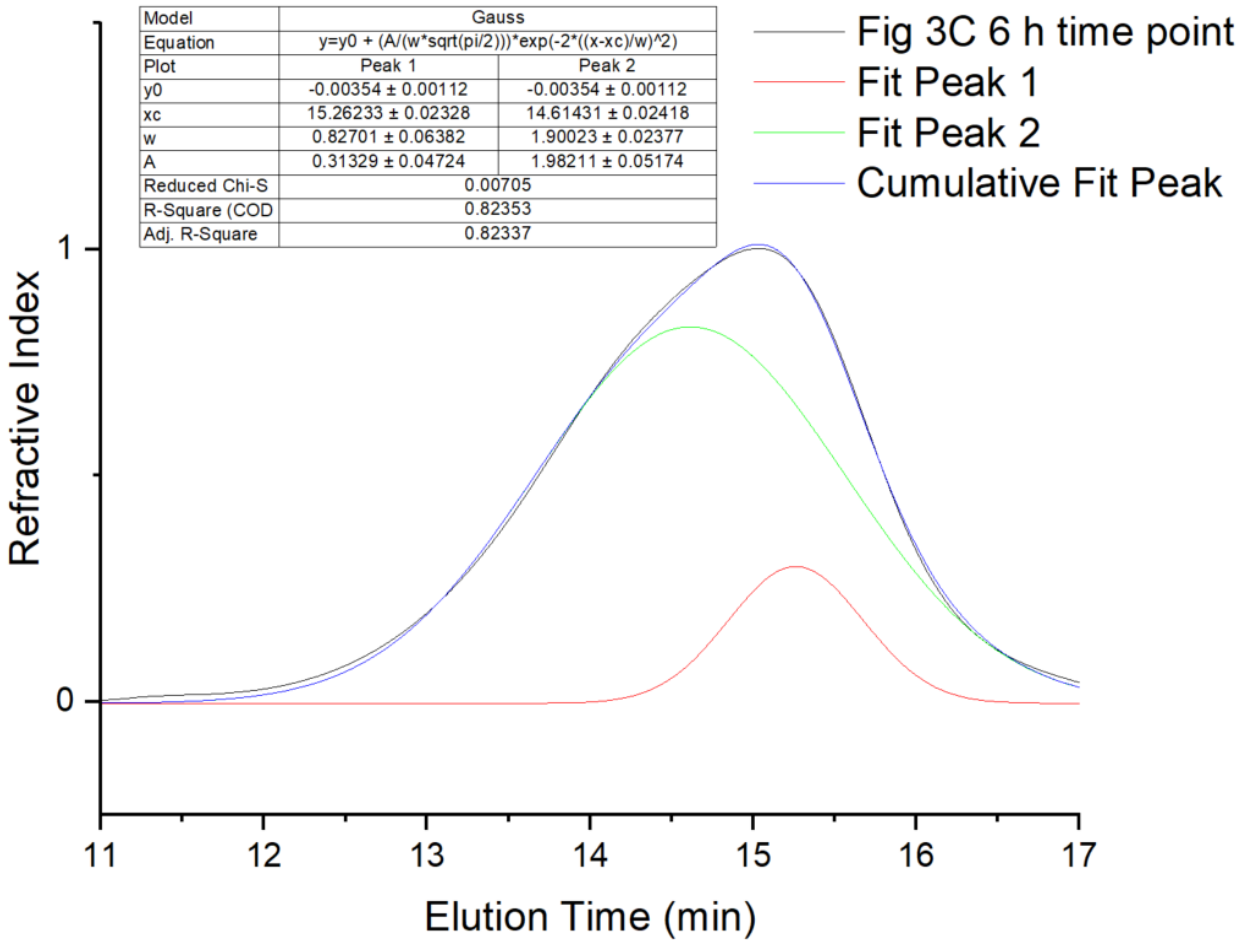

Figure B11. Peak analysis of the 6 h time point from **Figure 3C** P(MA-*b*-MMA) block copolymers with no TEOA using deconvolution to assess percentages of chain-extended vs. unextended chains using Origin Pro and a Gauss model. A in the table indicates the area under the curve of each respective fitting.

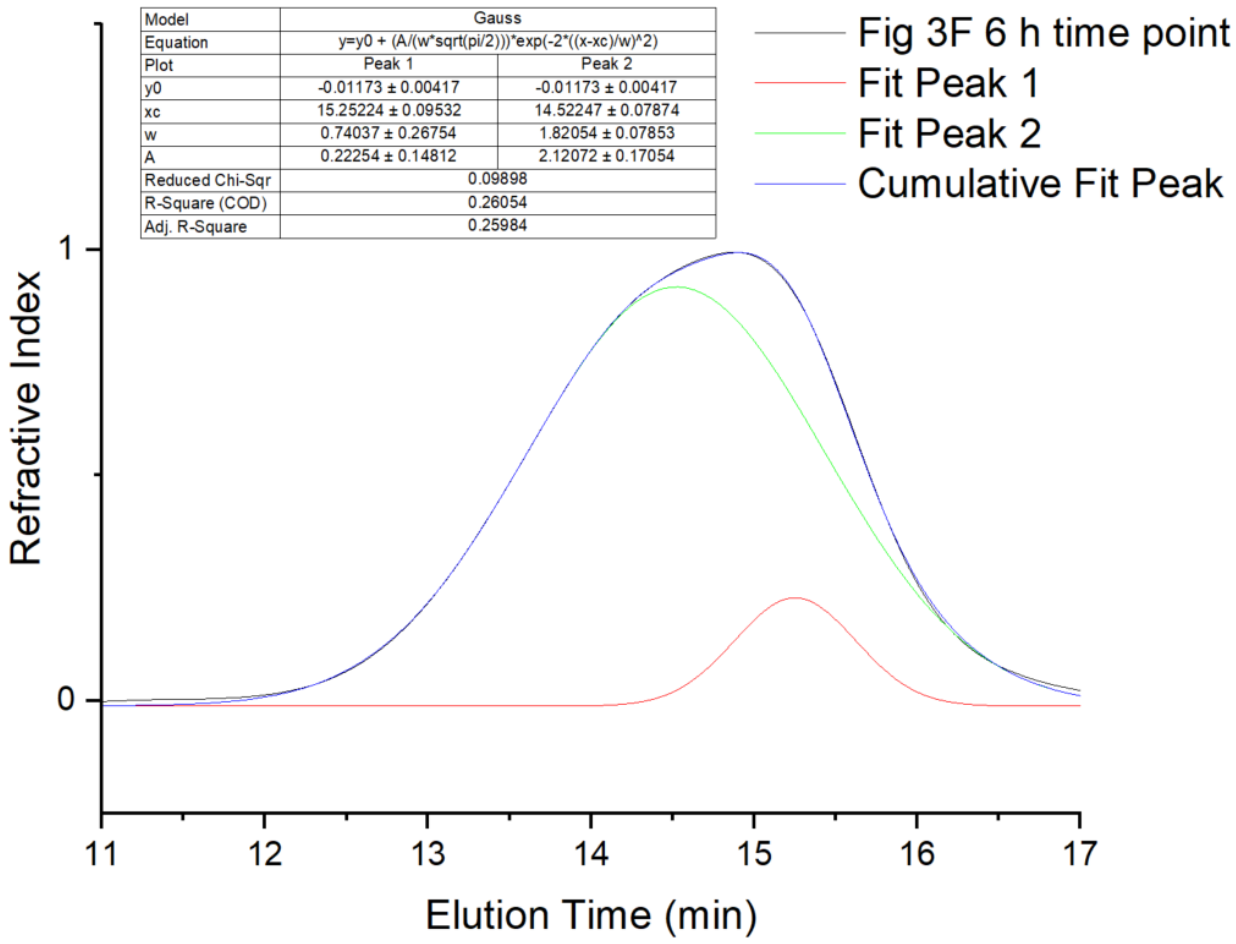

Figure B12. Peak analysis of the 6 h time point from **Figure 3F** P(MA-*b*-MMA) block copolymers with TEOA using deconvolution to assess percentages of chain-extended vs. unextended chains using Origin Pro and a Gauss model. A in the table indicates the area under the curve of each respective fitting.

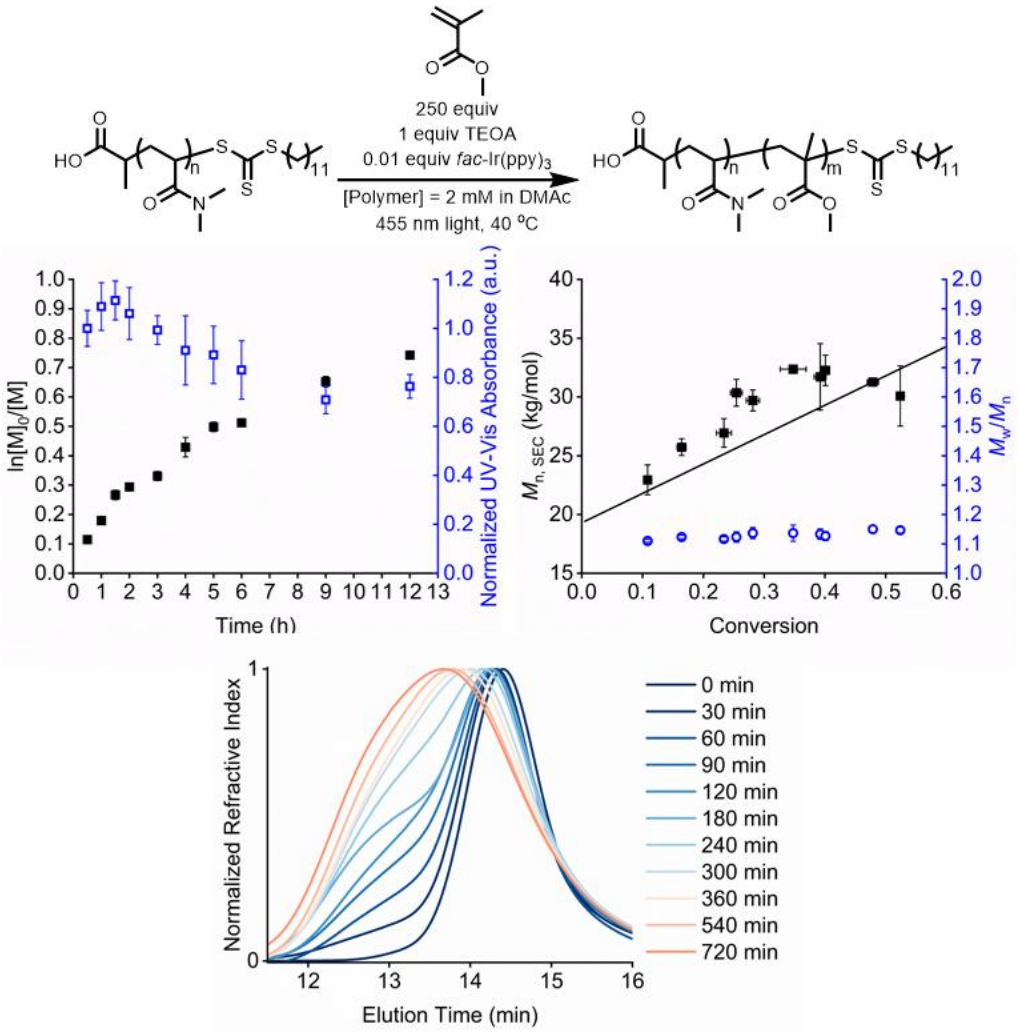

Figure B13. Kinetic data of the reverse blocking order polymerization using PDMA, 0.01 equiv $Ir(ppy)_3$ at a 2 mM polymer concentration (n=3).

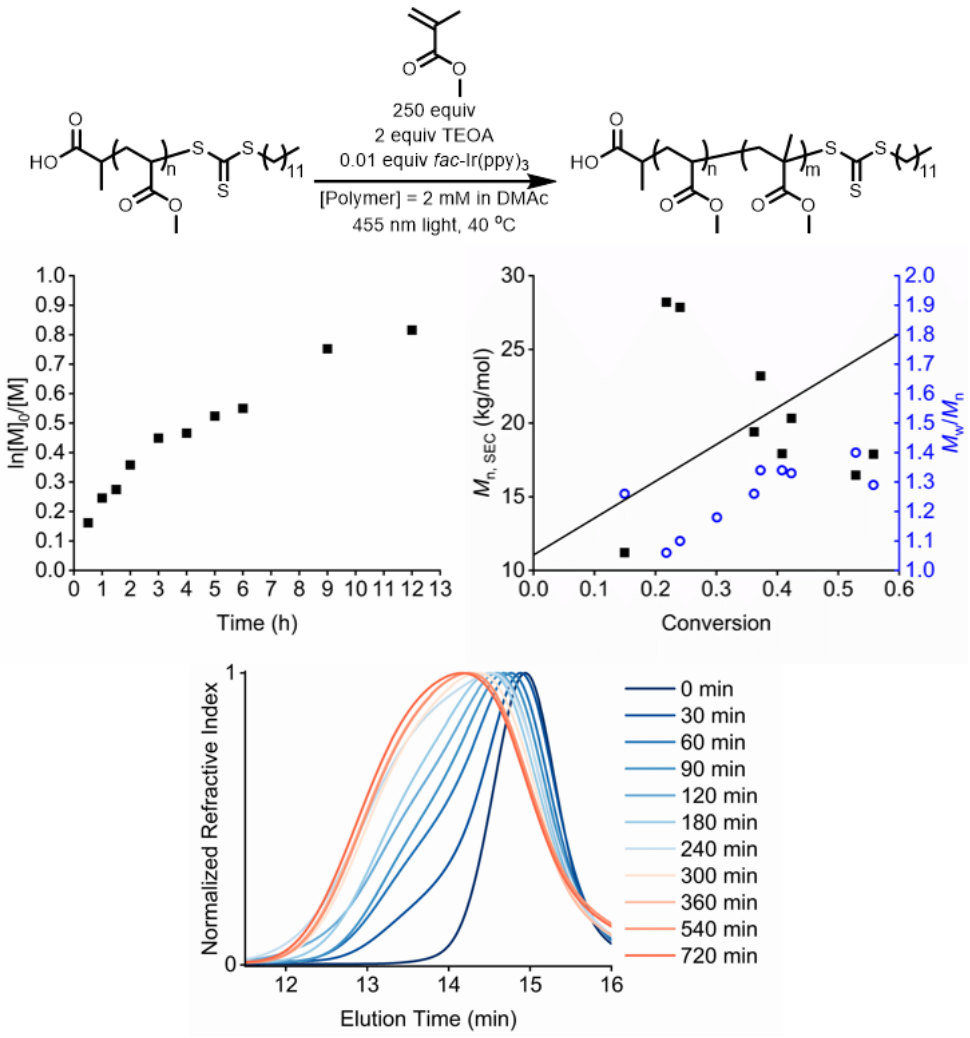

Figure B14. Kinetic data of the reverse blocking order polymerization using PMA, 0.01 equiv $Ir(ppy)_3$ at a 2 mM polymer concentration, but 2 equivalents of TEOA.

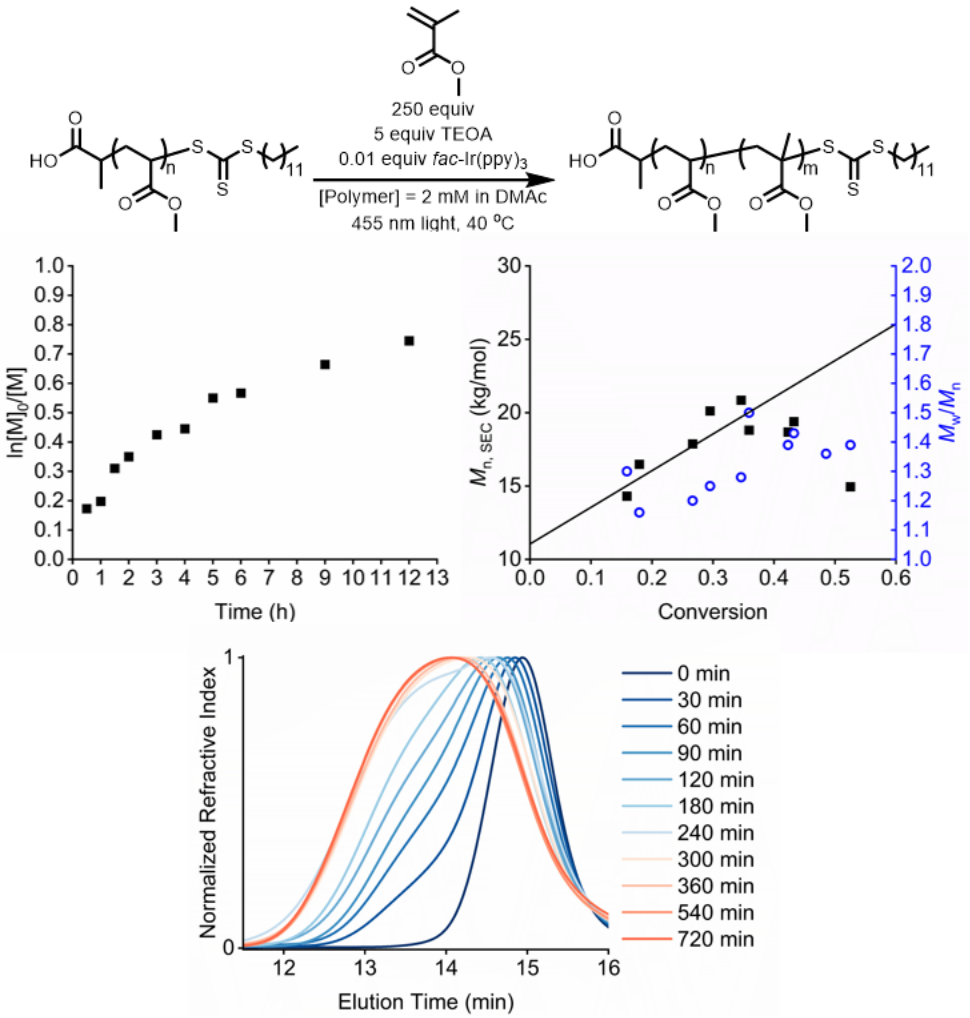

Figure B15. Kinetic data of the reverse blocking order polymerization using PMA, 0.01 equiv $Ir(ppy)_3$ at a 2 mM polymer concentration, but 5 equivalents of TEOA.

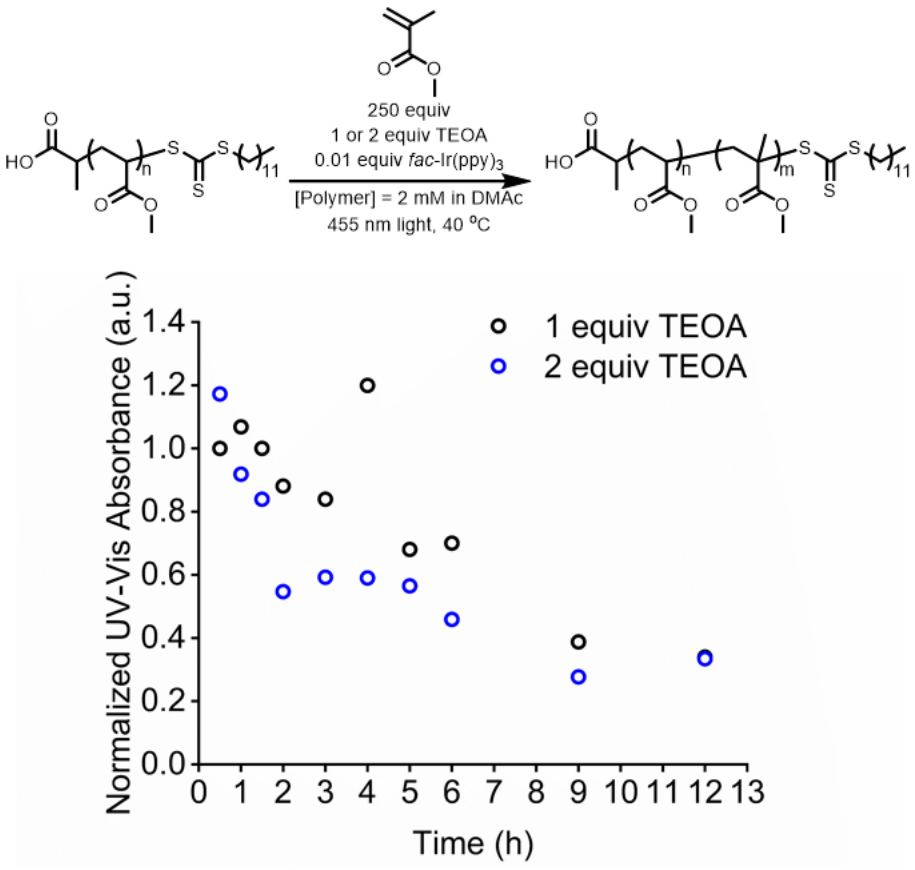

Figure B16. Normalized UV-Vis absorbance kinetic data comparing the impact of TEOA equivalents (1 equivalents vs 2 equivalents) on chain-end retention.

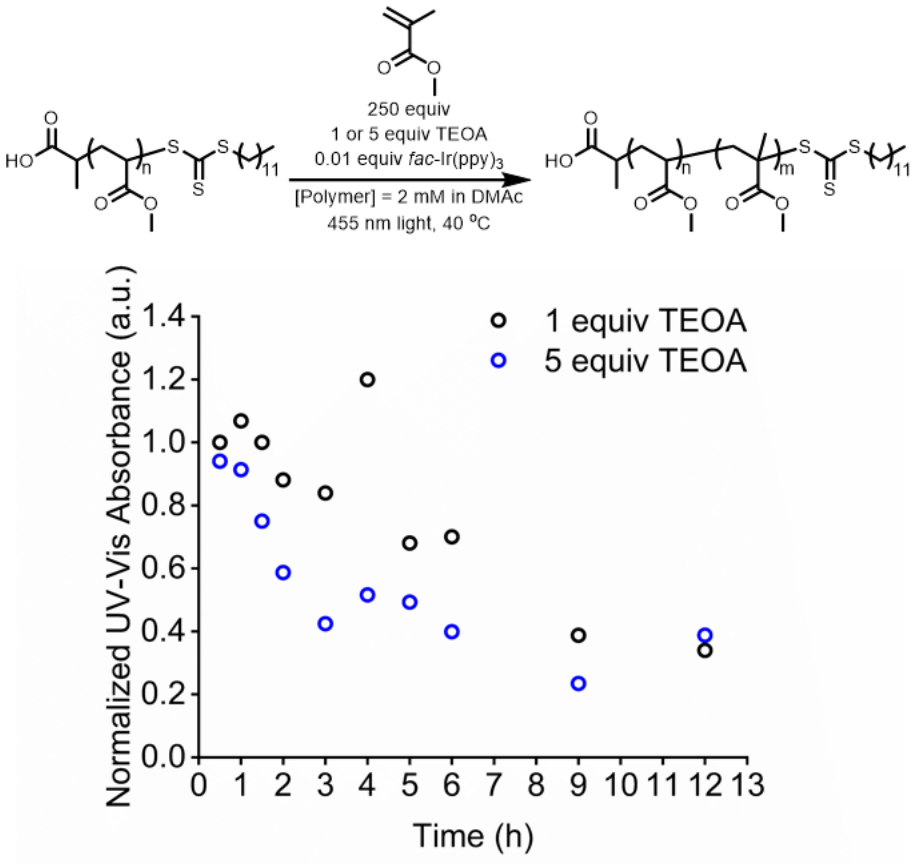

Figure B17. Normalized UV-Vis absorbance kinetic data comparing the impact of TEOA equivalents (1 equivalents vs 5 equivalents) on chain-end retention.

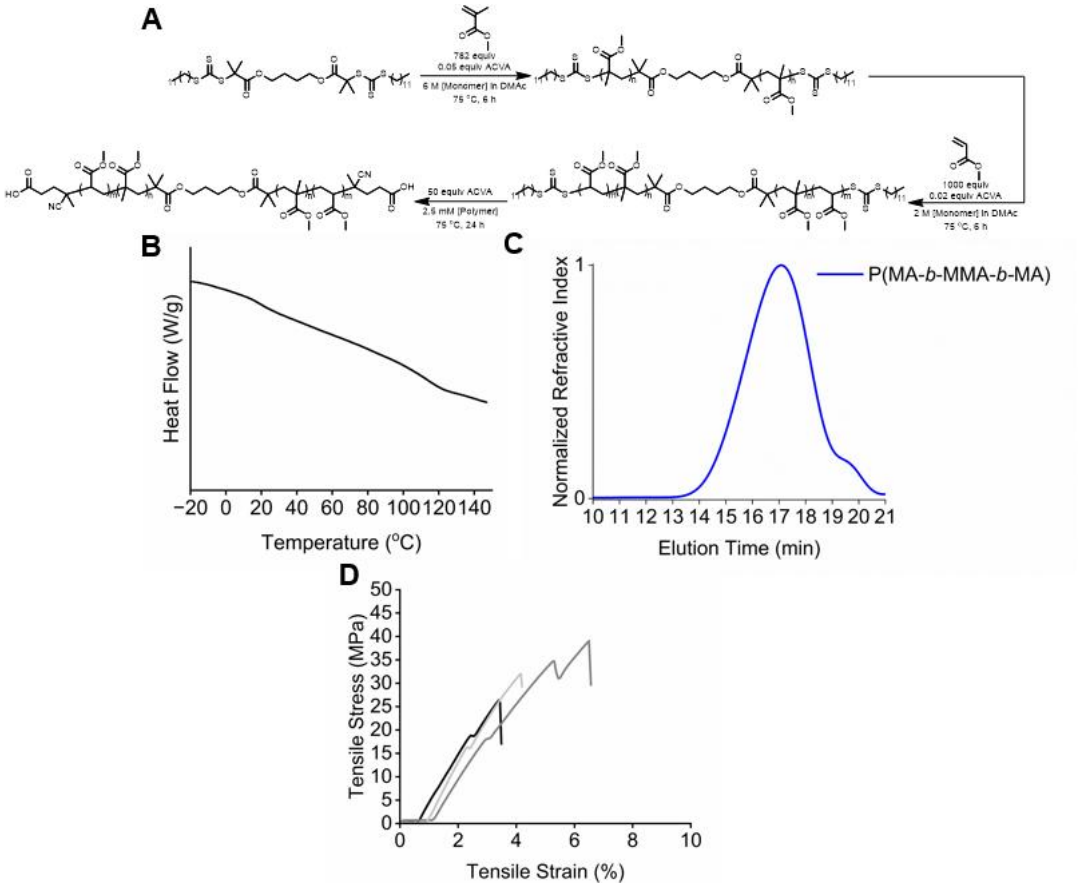

Figure B18. A) Synthesis scheme**,** B) DSC trace (exo up), C) normalized RI traces using a higher molecular weight column (separation limit for column = 0-1×10^6 g/mol) for P(MA-*b*-MMA-*b*-MA) using the bis-TTC, and D) tensile testing traces.

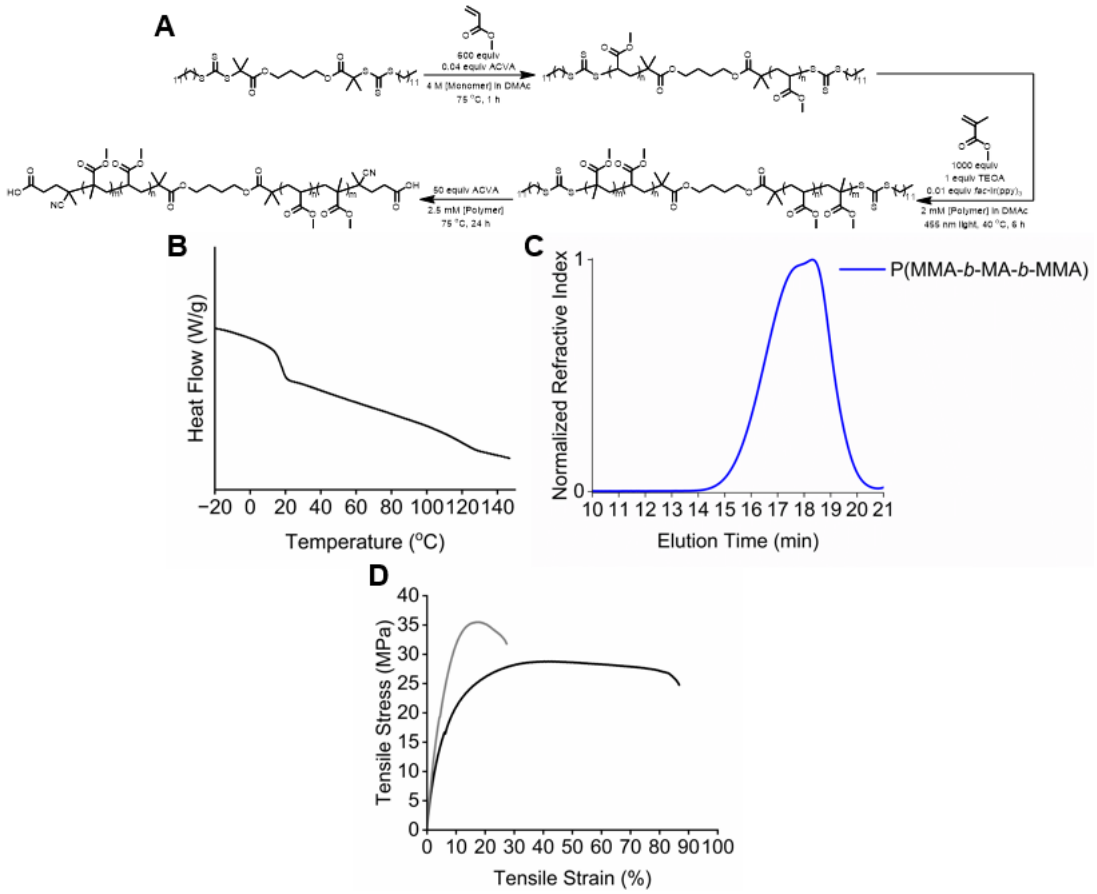

Figure B19. A) Synthesis scheme**,** B) DSC trace (exo up), C) normalized RI traces using a higher molecular weight column (separation limit for column = 0-1×10^6 g/mol) for P(MMA-*b*-MA-*b*-MMA) using the bis-TTC, and D) tensile testing traces.

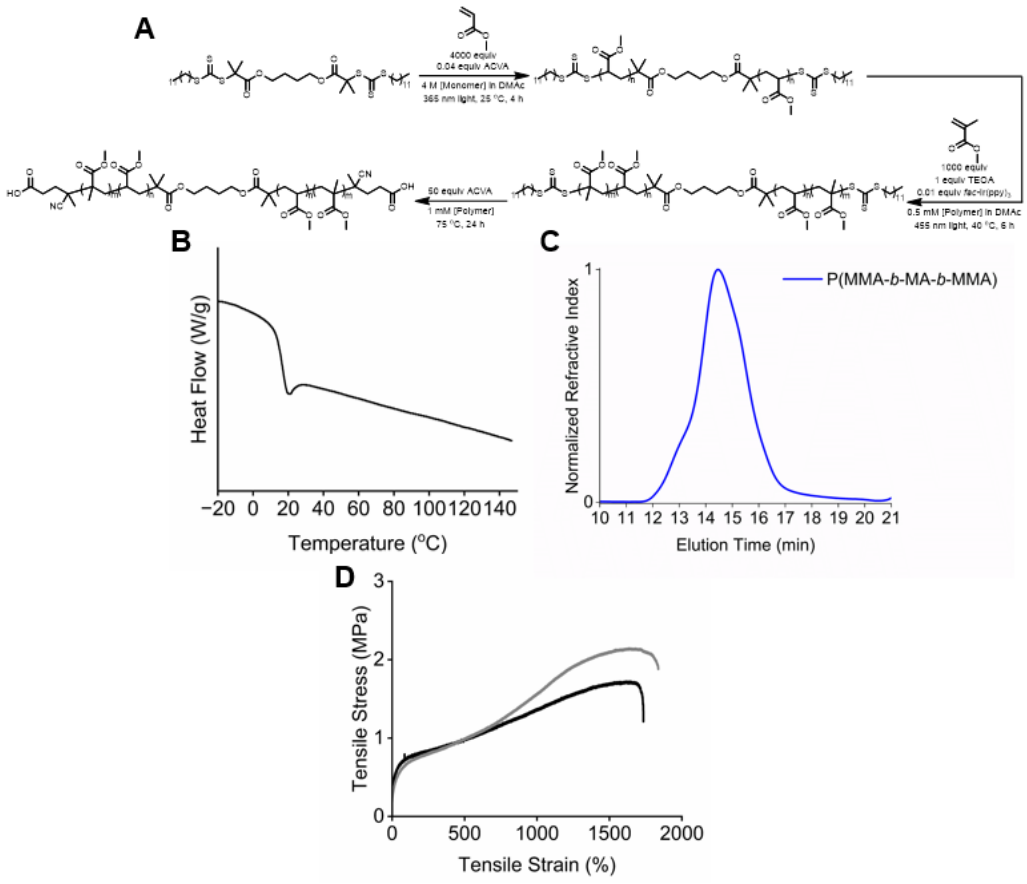

Figure B20. A) Synthesis scheme**,** B) DSC trace (exo up), C) normalized RI traces using a higher molecular weight column (separation limit for column = 0-1×10^6 g/mol) for the high-molecular weight P(MMA-*b*-MA-*b*-MMA) using the bis-TTC, and D) tensile testing traces.

XYZ Coordinates (Angstrom) of Optimum Geometries in DFT Calculations

CS2

C	0.000000000	0.000000000	0.000000000
S	0.000000000	0.000000000	1.553220000
S	0.000000000	0.000000000	-1.553220000

TCT anion

C	-2.719415000	-0.128486000	-0.805893000
C	-2.044379000	0.249838000	0.502836000
S	-0.468928000	1.138242000	0.292174000
S	2.309134000	0.612749000	-0.285696000
C	0.798772000	-0.090657000	0.043983000
S	0.472378000	-1.739357000	0.165874000
H	-2.666516000	0.941513000	1.077532000
H	-1.852629000	-0.627063000	1.123331000
H	-3.663802000	-0.643667000	-0.602070000
H	-2.088304000	-0.798661000	-1.394432000
H	-2.939963000	0.757561000	-1.407545000

TCT-MMA

C	-3.980007000	-1.561575000	0.000807000
C	-2.506042000	-1.839075000	-0.281681000
H	-4.188584000	-1.493399000	1.070799000
H	-4.581846000	-2.379100000	-0.403347000
H	-4.320634000	-0.637400000	-0.475391000
C	-1.544948000	-0.741599000	0.249412000
H	-2.360957000	-1.943094000	-1.360642000
H	-2.218327000	-2.787813000	0.181489000
C	-1.923018000	0.566951000	-0.456351000
O	-1.784798000	0.760671000	-1.638583000

O	-2.527349000	1.414237000	0.367426000
C	-2.976610000	2.647227000	-0.207874000
H	-3.709239000	2.459573000	-0.994677000
H	-2.131289000	3.205626000	-0.613838000
H	-3.435728000	3.200862000	0.608659000
S	0.100266000	-1.328533000	-0.357150000
C	-1.560061000	-0.677655000	1.773455000
C	1.287659000	-0.100874000	0.050271000
S	2.876976000	-0.816336000	-0.136288000
C	4.027150000	0.586817000	0.037518000
C	5.448609000	0.082699000	-0.163176000
H	3.893697000	1.013057000	1.032063000
H	3.761602000	1.337753000	-0.707754000
H	5.721123000	-0.671486000	0.579611000
H	6.135193000	0.925648000	-0.052564000
H	5.592917000	-0.339955000	-1.160679000
S	0.986182000	1.453352000	0.492503000
H	-0.831106000	0.036791000	2.156033000
H	-2.544245000	-0.372820000	2.130736000
H	-1.336585000	-1.666727000	2.179428000

TCT radical

S	0.727901000	-0.878074000	-0.000077000

C	-0.782936000	-0.073759000	-0.000013000
S	-1.085721000	1.576858000	0.000052000
S	-2.254449000	-0.897368000	0.000043000
C	1.951146000	0.483380000	-0.000299000
H	1.782483000	1.090101000	0.890477000
H	1.783145000	1.089330000	-0.891739000
C	3.348551000	-0.117246000	0.000266000
H	4.075026000	0.698710000	0.000442000
H	3.527726000	-0.727660000	-0.888262000
H	3.527354000	-0.727398000	0.889062000

Intermediate 1 in RAFT equilibrium

C	4.845262000	-1.138418000	-0.289300000
C	3.606394000	-1.029367000	-1.174114000
H	5.125639000	-0.159804000	0.112264000
H	5.690802000	-1.520146000	-0.867149000
H	4.683499000	-1.818007000	0.552052000
C	2.413853000	-0.455366000	-0.414708000
H	3.347189000	-2.010840000	-1.582149000
H	3.817101000	-0.369744000	-2.020014000
C	1.947532000	-1.358004000	0.709888000
O	1.985873000	-2.563871000	0.686904000

O	1.483943000	-0.648244000	1.736894000
C	0.938031000	-1.392222000	2.835151000
H	1.706940000	-2.018962000	3.289886000
H	0.104260000	-2.008074000	2.497371000
H	0.591189000	-0.648543000	3.549836000
S	0.998567000	-0.210181000	-1.573678000
H	2.655338000	0.528930000	-0.012670000
C	0.157884000	1.186110000	-0.931708000
S	1.064644000	2.649744000	-0.616114000
C	0.303326000	3.261981000	0.934675000
C	0.896953000	4.613766000	1.295406000
H	0.495983000	2.523597000	1.713588000
H	-0.772997000	3.335397000	0.773616000
H	1.977112000	4.552131000	1.454343000
H	0.441494000	4.967940000	2.223994000
H	0.702242000	5.358819000	0.519169000
S	-1.563451000	1.295894000	-1.226900000
C	-2.342099000	0.102227000	-0.017559000
C	-2.071515000	-1.319573000	-0.518139000
C	-3.853372000	0.381567000	-0.144083000
C	-1.822626000	0.375965000	1.387826000
C	-4.714412000	-0.520590000	0.736560000
H	-4.151138000	0.260321000	-1.189074000

H	-4.024026000	1.427831000	0.126738000
H	-4.558700000	-1.579883000	0.509105000
H	-5.771226000	-0.300526000	0.565738000
H	-4.510362000	-0.366322000	1.798882000
O	-2.490963000	-1.758408000	-1.561353000
O	-1.354421000	-2.037133000	0.342162000
C	-1.058240000	-3.384309000	-0.046948000
H	-0.481725000	-3.807283000	0.771747000
H	-0.468176000	-3.393247000	-0.964187000
H	-1.981343000	-3.947800000	-0.194039000
H	-0.734975000	0.320744000	1.424815000
H	-2.223974000	-0.350472000	2.096999000
H	-2.133587000	1.375290000	1.701675000

TS to products 2 in RAFT equilibrium

S	-1.493111000	2.636507000	0.465770000
C	-0.320595000	1.340402000	0.346033000
S	-0.722341000	-0.090840000	1.089384000
S	1.121126000	1.694492000	-0.576631000
C	2.199291000	0.190816000	-0.557493000
C	2.412730000	-0.288744000	0.883432000
O	2.651489000	0.443860000	1.811565000

O	2.412729000	-1.613327000	0.967569000
C	2.658538000	-2.166875000	2.266216000
H	1.891622000	-1.837802000	2.969430000
H	2.612127000	-3.246338000	2.137446000
H	3.644963000	-1.872171000	2.628318000
C	1.641796000	-0.864174000	-1.507043000
H	2.274720000	-1.752283000	-1.510206000
H	1.612119000	-0.458157000	-2.521174000
H	0.636209000	-1.166627000	-1.221684000
C	3.559420000	0.747245000	-1.056948000
H	3.868544000	1.563579000	-0.398753000
H	3.401932000	1.170926000	-2.053941000
C	4.668859000	-0.298757000	-1.120996000
H	4.426316000	-1.113402000	-1.806990000
H	4.881031000	-0.729860000	-0.138128000
H	5.587500000	0.173770000	-1.477102000
C	-0.825856000	4.059914000	-0.471909000
H	-0.666781000	3.757476000	-1.508062000
H	0.126847000	4.357278000	-0.030878000
C	-1.834549000	5.196954000	-0.392613000
H	-2.794050000	4.916939000	-0.835138000
H	-1.444083000	6.052866000	-0.948531000
H	-2.004215000	5.514850000	0.639382000

C	-2.518046000	-1.057292000	-0.223006000
C	-3.739315000	-0.841463000	0.612717000
C	-5.004994000	-1.315281000	-0.114555000
C	-1.964899000	-2.404478000	-0.334160000
O	-2.103279000	-3.292192000	0.486324000
O	-1.239580000	-2.557124000	-1.457488000
C	-0.515344000	-3.781813000	-1.588836000
H	-1.195468000	-4.634974000	-1.627168000
H	0.033059000	-3.701721000	-2.525969000
H	0.182328000	-3.907833000	-0.757857000
H	-2.383107000	-0.422873000	-1.093885000
H	-3.637822000	-1.376807000	1.560527000
H	-3.832093000	0.222675000	0.843958000
H	-5.136681000	-0.782334000	-1.060943000
H	-5.888741000	-1.131646000	0.503266000
H	-4.960140000	-2.386523000	-0.331079000

TS to products 3 in RAFT equilibrium

C	5.190315000	-0.216326000	0.041705000
C	4.036080000	-0.250169000	-0.956157000
H	5.238640000	0.751057000	0.550854000
H	6.140495000	-0.373336000	-0.474887000

H	5.091757000	-0.996708000	0.801451000
C	2.692960000	0.011094000	-0.278410000
H	4.009352000	-1.216299000	-1.468641000
H	4.184767000	0.520121000	-1.717209000
C	2.316535000	-1.074574000	0.713970000
O	2.584034000	-2.243965000	0.581160000
O	1.641055000	-0.576850000	1.745004000
C	1.150429000	-1.521838000	2.707369000
H	1.978443000	-2.071926000	3.157162000
H	0.452239000	-2.212528000	2.233681000
H	0.639737000	-0.930119000	3.464196000
S	1.364839000	0.042604000	-1.561812000
H	2.712924000	0.975723000	0.226730000
C	0.123822000	1.167237000	-1.000376000
S	0.655234000	2.520219000	-0.030049000
C	-0.852618000	3.513203000	0.217127000
C	-0.523131000	4.687384000	1.126614000
H	-1.615876000	2.873712000	0.660123000
H	-1.201460000	3.851196000	-0.759394000
H	-0.185552000	4.353785000	2.111290000
H	-1.426756000	5.286275000	1.265338000
H	0.244793000	5.334482000	0.694667000
S	-1.426525000	0.912539000	-1.536294000

C	-2.531737000	-0.450881000	0.171035000
C	-2.122728000	-1.737241000	-0.425071000
C	-3.955760000	-0.036576000	-0.061758000
C	-1.870621000	-0.016914000	1.440534000
C	-4.916992000	-0.749131000	0.900048000
H	-4.244683000	-0.257457000	-1.091949000
H	-4.036663000	1.044392000	0.085488000
H	-4.859973000	-1.834958000	0.782949000
H	-5.946641000	-0.440627000	0.699332000
H	-4.689119000	-0.505228000	1.941426000
O	-2.747613000	-2.340348000	-1.275339000
O	-0.960484000	-2.182887000	0.075238000
C	-0.428523000	-3.370304000	-0.513989000
H	0.510724000	-3.559570000	0.001175000
H	-0.244340000	-3.219933000	-1.579778000
H	-1.112545000	-4.210329000	-0.376625000
H	-0.784516000	0.023042000	1.343230000
H	-2.094939000	-0.730127000	2.244062000
H	-2.241711000	0.962188000	1.751456000

MA radical

C	-3.171616000	-0.365010000	-0.270164000

C	-1.941876000	0.381465000	0.244963000
H	-4.063071000	0.261834000	-0.188094000
H	-3.346842000	-1.278943000	0.304963000
H	-3.049148000	-0.643899000	-1.320615000
C	-0.705658000	-0.432759000	0.197384000
H	-2.115351000	0.681206000	1.291209000
H	-1.789494000	1.314980000	-0.305017000
C	0.599902000	0.164325000	0.037432000
H	-0.759504000	-1.508723000	0.328143000
O	0.816775000	1.357033000	-0.095340000
O	1.581229000	-0.758675000	0.051430000
C	2.915032000	-0.268609000	-0.100697000
H	3.033195000	0.245716000	-1.056796000
H	3.557346000	-1.147080000	-0.069493000
H	3.174137000	0.411568000	0.713483000

MMA radical

C	-2.734388000	-0.548226000	0.711886000
C	-1.860591000	-0.437504000	-0.548644000
H	-3.641137000	-1.119206000	0.494589000
H	-3.034357000	0.439157000	1.074382000
H	-2.194485000	-1.057287000	1.515469000

C	-0.631061000	0.367740000	-0.301876000
H	-2.445189000	0.047967000	-1.339197000
H	-1.590556000	-1.436785000	-0.894395000
C	0.637729000	-0.316582000	-0.152064000
C	-0.734612000	1.839952000	-0.103663000
O	0.800530000	-1.523198000	-0.255288000
O	1.654649000	0.525465000	0.121622000
C	2.942451000	-0.068627000	0.286609000
H	2.943111000	-0.769913000	1.123837000
H	3.623647000	0.755461000	0.492772000
H	3.251359000	-0.588365000	-0.622804000
H	0.011415000	2.379678000	-0.695191000
H	-0.553800000	2.111724000	0.944594000
H	-1.728611000	2.198925000	-0.378208000

Triethylamine cation

N	0.360054	0.546499	0.294813
C	0.230942	1.479447	-0.800516
C	-0.112658	0.913051	1.611189
C	1.004660	-0.730789	0.081094
C	0.109573	-1.695899	-0.703664
H	1.920048	-0.530850	-0.485261
H	1.263702	-1.144799	1.054839

C	-1.311066	0.054213	2.025265
H	0.717175	0.757046	2.307688
H	-0.378877	1.968988	1.593459
H	0.305878	0.927312	-1.736335
C	1.335135	2.541676	-0.717461
H	-0.753512	1.947513	-0.723456
H	0.657887	-2.631569	-0.827127
H	-0.815041	-1.899147	-0.161775
H	-0.131659	-1.304084	-1.693207
H	1.262962	3.115496	0.208124
H	2.320559	2.076059	-0.779602
H	1.211859	3.221294	-1.562472
H	-1.038882	-0.999712	2.103259
H	-1.647044	0.399687	3.004543
H	-2.130176	0.165155	1.312152

Triethylamine-TCT complex

S	-2.092534	0.335670	1.115589
C	-1.805268	-0.977876	-0.053753
S	-2.368070	-0.898478	-1.637306
S	-0.947949	-2.269806	0.643630
C	-2.885305	1.703787	0.211119
H	-3.389936	2.274486	0.995593

H	-3.650518	1.277328	-0.439480
C	-1.920054	2.586075	-0.564778
H	-1.432699	2.026067	-1.365652
H	-1.150040	3.003862	0.089651
H	-2.466737	3.418384	-1.019697
N	2.239421	0.094215	-0.051947
C	1.931760	0.051280	1.357856
C	1.302594	0.760970	-0.930403
C	3.367132	-0.596095	-0.631961
H	1.103299	-0.677281	1.446064
C	3.079995	-0.308910	2.275301
H	1.497603	1.024209	1.610844
H	4.225128	-0.488214	0.031386
C	3.027827	-2.078416	-0.837692
H	3.586195	-0.118959	-1.587515
H	0.323713	0.743525	-0.451329
C	1.748447	2.204321	-1.180001
H	1.263969	0.201320	-1.866705
H	2.806886	-2.564665	0.114281
H	2.171235	-2.189176	-1.505304
H	3.894468	-2.564068	-1.290002
H	2.728191	2.233543	-1.661274
H	1.019354	2.677454	-1.840103

H	1.789888	2.763015	-0.242711
H	3.900424	0.407272	2.188752
H	2.708808	-0.277606	3.301416
H	3.459043	-1.315137	2.086570

Triethylamine

N	0.196028	0.411163	0.247930
C	1.123843	0.855948	1.290212
C	0.908474	0.051190	-0.979988
C	-0.834644	1.418702	-0.011589
C	-2.098281	0.837922	-0.630505
H	-1.102010	1.887072	0.938287
H	-0.433750	2.223861	-0.653396
C	1.565053	-1.320514	-0.911981
H	0.190489	0.047376	-1.803233
H	1.662027	0.820389	-1.227976
H	2.031201	0.251722	1.220934
C	0.559774	0.711551	2.696734
H	1.432145	1.901784	1.110978
H	-2.837629	1.629094	-0.787700
H	-1.907924	0.368216	-1.599438
H	-2.536859	0.085661	0.031819
H	1.298072	1.042262	3.433500

H	-0.343770	1.309251	2.845163
H	0.313643	-0.334154	2.903804
H	0.813710	-2.094722	-0.730247
H	2.066246	-1.544594	-1.858484
H	2.315681	-1.382590	-0.119274

Thiolate anion

C	-1.618046000	-0.351391000	-0.000002000
C	-0.457950000	0.636739000	-0.000010000
S	1.206181000	-0.153940000	-0.000002000
H	-0.546206000	1.286626000	-0.877575000
H	-0.546116000	1.286572000	0.877618000
H	-2.583704000	0.170954000	-0.000314000
H	-1.583598000	-0.996345000	0.884402000
H	-1.583290000	-0.996853000	-0.884026000

Thiyl radical in the decomposition of the TCT-radical

C	-1.619952000	-0.335954000	0.000004000
C	-0.437161000	0.617359000	0.000144000
S	1.189678000	-0.158631000	0.000073000
H	-0.456143000	1.281733000	-0.872553000
H	-0.457930000	1.284555000	0.870361000
H	-2.554370000	0.234061000	0.000301000

H	-1.611815000	-0.975459000	0.886391000
H	-1.611917000	-0.975219000	-0.886551000

TS for the decomposition of TCT anion to CS2 and thiolate

C	-3.030545000	0.312278000	0.786613000
C	-2.210270000	0.055155000	-0.472531000
S	-0.954707000	-1.254897000	-0.309149000
S	2.456839000	-0.858293000	0.264228000
C	1.395644000	0.285208000	0.017962000
S	0.832887000	1.747092000	-0.159771000
H	-2.881815000	-0.177306000	-1.306159000
H	-1.684648000	0.981884000	-0.746770000
H	-3.752446000	1.123746000	0.628479000
H	-2.382434000	0.595111000	1.622619000
H	-3.587954000	-0.581710000	1.084635000

TS for the decomposition of TCT radical to CS2 and thiyl radical

S	-0.797101000	-0.461902000	1.069473000
C	1.169531000	0.181695000	-0.013952000
S	2.196431000	-0.961918000	-0.373208000
S	0.677574000	1.710337000	0.001094000
C	-1.767145000	-0.853939000	-0.417766000
H	-2.218036000	-1.826947000	-0.192455000

H	-1.075697000	-1.009735000	-1.249362000
C	-2.836655000	0.169374000	-0.759706000
H	-3.395860000	-0.171601000	-1.636133000
H	-2.394657000	1.140377000	-0.996943000
H	-3.540603000	0.300849000	0.065694000

TS for the addition of TCT radical to MMA monomer

S	-0.010020	2.373591	1.843393
C	0.506692	1.729437	0.318782
S	0.291053	2.422269	-1.174204
S	1.338365	0.216497	0.328985
C	-0.836014	3.941748	1.414843
H	-1.649702	3.718806	0.723751
H	-0.109431	4.582128	0.913341
C	-1.354631	4.585674	2.692281
H	-1.846281	5.526188	2.432039
H	-0.545273	4.812018	3.391067
H	-2.087508	3.951827	3.197977
C	1.419079	-0.565134	2.664956
C	1.980017	-1.807503	2.531849
C	3.454836	-1.993848	2.610764
O	3.993034	-3.071147	2.485524
O	4.117774	-0.860079	2.835053

C	5.545085	-0.958653	2.919414
C	1.175052	-3.022142	2.220649
H	5.835717	-1.608850	3.746371
H	5.958200	-1.342198	1.985025
H	5.897745	0.055203	3.097125
H	1.448306	-3.421447	1.237333
H	1.369743	-3.816284	2.947299
H	0.109298	-2.790561	2.221572
H	0.341448	-0.491176	2.764275
H	2.015643	0.272344	3.004138

MMA monomer

C	0.499511	2.874090	0.442359
C	0.961381	1.769367	-0.143239
C	0.933561	1.542246	-1.626081
C	1.552092	0.657708	0.663269
O	1.560303	0.893046	1.976260
C	2.113501	-0.133288	2.807543
O	1.983112	-0.361451	0.172016
H	0.072313	3.675987	-0.151808
H	0.532863	3.010462	1.516619
H	0.487853	2.399008	-2.134256
H	0.354746	0.648148	-1.874535

H	1.943205	1.389545	-2.017858
H	1.548484	-1.061143	2.701672
H	2.031024	0.239920	3.826580
H	3.161140	-0.309238	2.556821

Appendix C: Maximizing Activation versus Termination Characterization

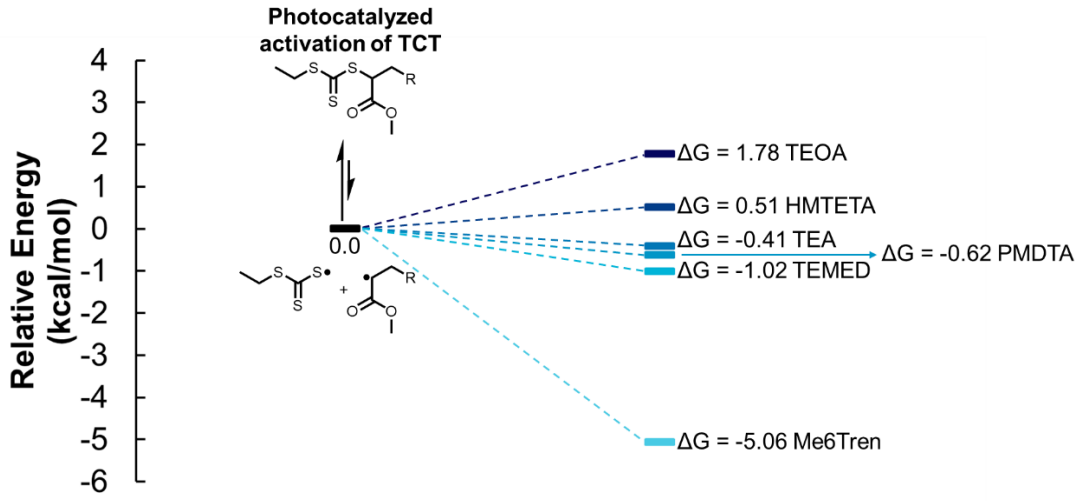

Figure C1. Density functional theory (DFT) calculations for the reduction of a trithiocarbonate radical to a trithiocarbonate anion with different tertiary amines.

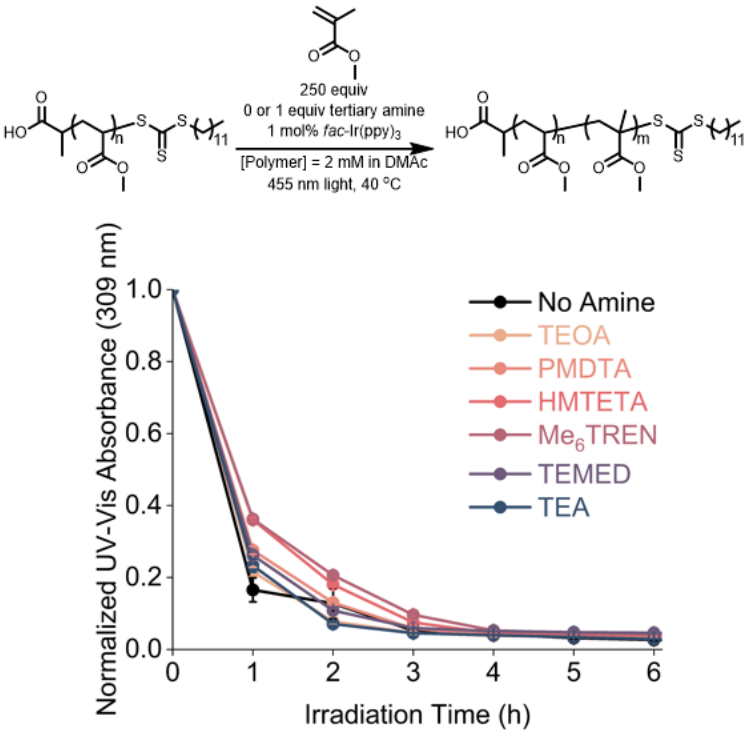

Figure C2. Normalized UV-Visible absorbance of 6 different amines and no amine over the course of 6 hours in the reverse blocking order photoinduced electron/energy transfer reversible addition–fragmentation chain transfer polymerization system.

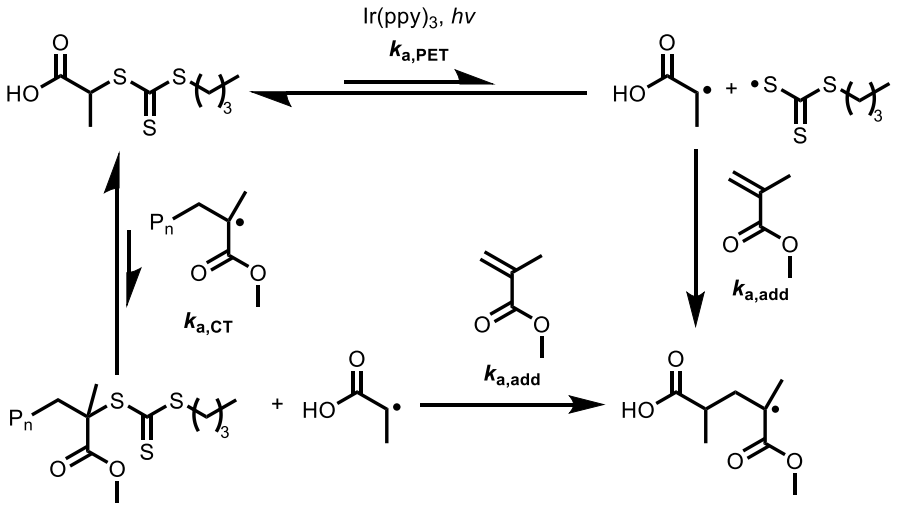

Figure C3. Activation pathways for methyl acrylate mimic R-group trithiocarbonates (TTC) with methyl methacrylate via photoinduced electron/energy transfer reversible addition–fragmentation chain transfer (PET-RAFT) polymerization.

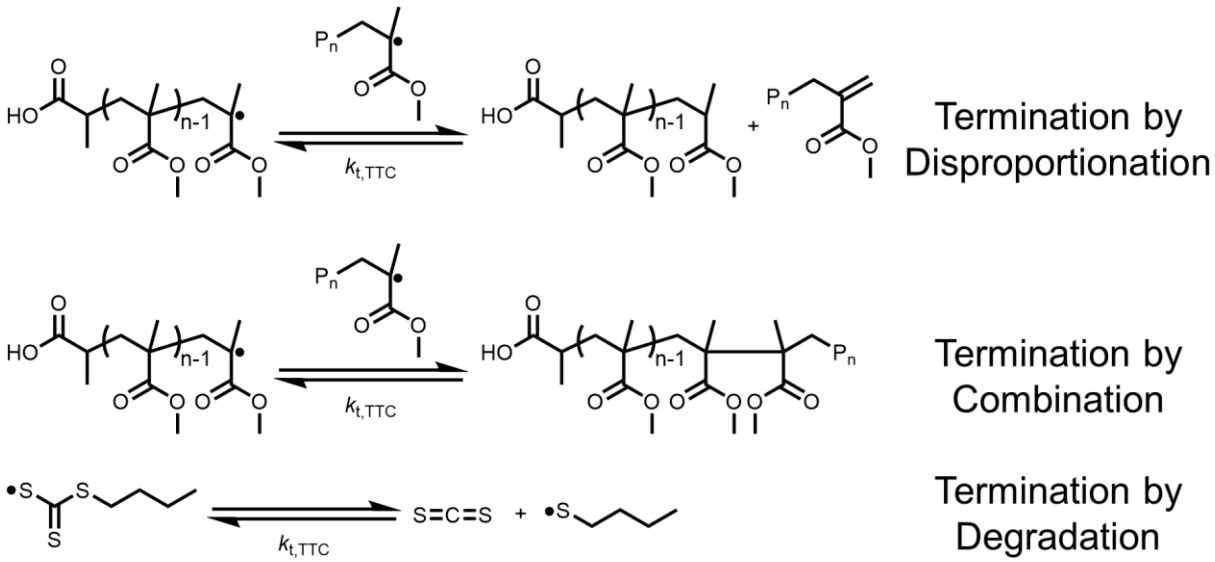

Figure C4. Termination pathways for methyl methacrylate polymerizations via photoinduced electron/energy transfer reversible addition–fragmentation chain transfer (PET-RAFT) polymerization.

Activation and Termination Data for Trials of 250 MMA Equivalents:

Table C1. Consumption of BTPA and degradation of TTC in the presence of 250 equivalents of MMA, 2.5 mol% of *fac*-Ir(ppy)$_3$, and 0.1 mM BTPA at 23 ^{o}C.

Time (h)	BTPA Conversion	ln([BTPA]$_0$ / [BTPA])	Average	TTC Loss	ln([TTC]$_0$/ [TTC])	Average
1	0.2855	0.2855		0.2033	0.2272	
	0.2168	0.2168		0.3628	0.4506	
	0.2330	0.2330		0.2186	0.2467	
	0.2097	0.2097	0.27 ± 0.05	0.1556	0.1691	0.3 ± 0.1
2	0.4419	0.4419		0.4228	0.5495	
	0.3998	0.3998		0.3263	0.3950	
	0.4552	0.4552		0.3176	0.3821	
	0.3760	0.3760	0.54 ± 0.06	0.5346	0.7648	0.5 ± 0.2
4	0.7658	0.7658		0.6978	1.1966	
	0.7266	0.7266		0.6678	1.1020	
	0.7115	0.7115		0.4642	0.6241	
	0.7103	0.7103	1.3 ± 0.1	0.5565	0.8130	0.9 ± 0.2
8	0.9091	0.9091		0.7503	1.3875	
	0.8135	0.8135		*	*	
	0.7871	0.7871		0.5682	0.8398	
	0.9038	0.9038	2.0 ± 0.4	0.8353	1.8034	1.3 ± 0.5

Table C2. Consumption of BTPA and degradation of TTC in the presence of 250 equivalents of MMA, 1.0 mol% of *fac*-Ir(ppy)$_3$, and 0.1 mM BTPA at 23 °C.

Time (h)	BTPA Conversion	ln([BTPA]$_0$ / [BTPA])	Average	TTC Loss	ln([TTC]$_0$/ [TTC])	Average
1	0.1261	0.1348		0.0805	0.0839	
	0.1700	0.1864		0.0790	0.0823	
	0.1638	0.1789		0.1176	0.1252	
	0.1341	0.1439	0.16 ± 0.03	0.1141	0.1212	0.10 ± 0.02
2	0.1966	0.2189		0.2658	0.3090	
	0.2128	0.2393		0.1634	0.1784	
	0.2270	0.2575		0.1785	0.1966	
	0.3160	0.3798	0.27 ± 0.07	0.2077	0.2328	0.23 ± 0.06
4	0.4913	0.6759		0.2654	0.3085	
	0.3378	0.4122		0.2056	0.2302	
	0.5012	0.6956		0.2471	0.2839	
	0.5330	0.7615	0.6 ± 0.2	0.3607	0.4474	0.32 ± 0.09
8	0.5979	0.9111		0.3678	0.4586	
	0.5921	0.8968		0.3890	0.4926	
	0.4599	0.6161		0.2898	0.3422	
	0.6775	1.1317	0.9 ± 0.2	0.4883	0.6700	0.5 ± 0.1

Table C3. Consumption of BTPA and degradation of TTC in the presence of 250 equivalents of MMA, 0.1 mol% of *fac*-Ir(ppy)$_3$, and 0.1 mM BTPA at 23 °C.

Time (h)	BTPA Conversion	ln([BTPA]$_0$ / [BTPA])	Average	TTC Loss	ln([TTC]$_0$/ [TTC])	Average
1	0.0619	0.0639		0.0192	0.0194	
	0.0203	0.0206		0.0109	0.0110	
	0.0681	0.0706		0.0413	0.0422	
	0.0266	0.0269	0.05 ± 0.03	0.0062	0.0062	0.02 ± 0.02
2	0.0762	0.0793		0.0251	0.0255	
	0.0604	0.0623		0.0339	0.0345	
	0.1406	0.1515		0.0646	0.0668	
	0.1264	0.1352	0.11 ± 0.04	0.0165	0.0167	0.03 ± 0.02
4	0.0319	0.0325		0.0334	0.0340	
	0.2065	0.2313		0.1059	0.1119	
	0.0933	0.0979		0.0472	0.0483	
	0.1798	0.1982	0.14 ± 0.09	0.0877	0.0918	0.07 ± 0.04
8	0.1362	0.1464		0.0523	0.0537	
	0.0702	0.0728		0.0276	0.0280	
	0.1088	0.1152		0.0671	0.0695	
	0.1490	0.1614	0.12 ± 0.04	0.1112	0.1179	0.07 ± 0.04

Table C4. Consumption of BTPA and degradation of TTC in the presence of 250 equivalents of MMA, 2.5 mol% of *fac*-Ir(ppy)$_3$, and 0.5 mM BTPA at 23 °C.

Time (h)	BTPA Conversion	ln([BTPA]$_0$ / [BTPA])	Average	TTC Loss	ln([TTC]$_0$/ [TTC])	Average
0.5	0.2989	0.3551		0.2892	0.3414	
	0.2484	0.2855		0.0966	0.1015	
	0.2835	0.3334		0.2637	0.3061	
	0.2632	0.3054	0.32 ± 0.03	0.2386	0.2726	0.3 ± 0.1
1	0.4613	0.6185		0.4130	0.5327	
	0.3526	0.4348		0.3322	0.4037	
	0.5195	0.7329		0.4745	0.6433	
	0.4553	0.6076	0.6 ± 0.1	0.4162	0.5382	0.5 ± 0.1
2	0.8161	1.6932		0.7306	1.3116	
	0.6543	1.0621		0.5553	0.8104	
	0.8454	1.8668		0.7704	1.4713	
	0.7450	1.3664	1.5 ± 0.4	0.6278	0.9883	1.1 ± 0.3
4	*	*		0.9278	2.6287	
	*	*		0.8945	2.2492	
	*	*		0.9298	2.6564	
	*	*		0.9609	3.2420	2.7 ± 0.4

Table C5. Consumption of BTPA and degradation of TTC in the presence of 250 equivalents of MMA, 1.0 mol% of *fac*-Ir(ppy)$_3$, and 0.5 mM BTPA at 23 °C.

Time (h)	BTPA Conversion	ln([BTPA]$_0$ / [BTPA])	Average	TTC Loss	ln([TTC]$_0$/ [TTC])	Average
0.5	0.1344	0.1443		0.1055	0.1115	
	0.1415	0.1526		0.0585	0.0603	
	0.1233	0.1316		0.0999	0.1053	
			0.142 ±			
	0.1296	0.1388	0.009	0.1237	0.1320	0.10 ± 0.03
1	0.1997	0.2227		0.1540	0.1672	
	0.2535	0.2924		0.1950	0.2169	
	0.2826	0.3321		0.2036	0.2276	
	0.2851	0.3356	0.30 ± 0.05	0.2110	0.2370	0.21 ± 0.03
2	0.4639	0.6234		0.3354	0.4086	
	0.4946	0.6823		0.3871	0.4895	
	0.5185	0.7308		0.3972	0.5062	
	0.5508	0.8004	0.71 ± 0.07	0.4212	0.5469	0.49 ± 0.06
4	0.6573	1.0709		0.5320	0.7592	
	0.7337	1.3233		0.6335	1.0038	
	0.7472	1.3753		0.6164	0.9582	
	0.7924	1.5723	1.3 ± 0.2	0.7050	1.2208	1.0 ± 0.2

Table C6. Consumption of BTPA and degradation of TTC in the presence of 250 equivalents of MMA, 0.1 mol% of *fac*-Ir(ppy)$_3$, and 0.5 mM BTPA at 23 °C.

Time (h)	BTPA Conversion	ln([BTPA]$_0$ / [BTPA])	Average	TTC Loss	ln([TTC]$_0$/ [TTC])	Average
0.5	0.0434	0.0444		0.0402	0.0410	
	0.0405	0.0414		0.0638	0.0659	
	0.0380	0.0387		0.0438	0.0448	
	0.0138	0.0139	0.03 ± 0.01	0.0446	0.0456	0.05 ± 0.01
1	0.0536	0.0551		0.0173	0.0175	
	0.0434	0.0444		0.0335	0.0341	
	0.0517	0.0531		0.0434	0.0444	
			0.053 ±			
	0.0591	0.0609	0.007	0.0528	0.0542	0.04 ± 0.02
2	0.1403	0.1512		0.0787	0.0819	
	0.1076	0.1139		0.0797	0.0831	
	0.1961	0.2183		0.0738	0.0766	
	0.1519	0.1647	0.16 ± 0.04	0.0929	0.0975	0.09 ± 0.01
4	0.2885	0.3404		0.1490	0.1614	
	0.1598	0.1741		0.0985	0.1037	
	0.3402	0.4158		0.1711	0.1877	
	0.2799	0.3284	0.3 ± 0.1	0.1714	0.1880	0.16 ± 0.04

Table C7. Consumption of BTPA and degradation of TTC in the presence of 250 equivalents of MMA, 2.5 mol% of *fac*-Ir(ppy)$_3$, and 1.0 mM BTPA at 23 °C.

Time (h)	BTPA Conversion	ln([BTPA]$_0$ / [BTPA])	Average	TTC Loss	ln([TTC]$_0$/ [TTC])	Average
0.5	0.2959	0.3508		0.1544	0.168	
	0.2691	0.3135		0.2429	0.278	
	0.3372	0.4113		0.3202	0.386	
			0.34 ±			
	0.2733	0.3193	0.04	0.2974	0.353	0.3 ± 0.1
1	0.5292	0.7533		0.5034	0.700	
	0.3981	0.5077		0.3648	0.454	
	0.5573	0.8149		0.5460	0.790	
	0.4813	0.6564	0.7 ± 0.1	0.4702	0.635	0.6 ± 0.1
2	0.8987	2.2892		0.8348	1.801	
	0.7086	1.2330		0.6606	1.081	
	0.9623	3.2790		0.9066	2.370	
	0.8581	1.9525	2.2 ± 0.8	0.8201	1.715	1.7 ± 0.5
3	*	*		0.9614	3.255	
	*	*		0.9475	2.947	
	*	*		0.9405	2.821	
	*	*		0.9670	3.410	3.1 ± 0.3

Table C8. Consumption of BTPA and degradation of TTC in the presence of 250 equivalents of MMA, 1.0 mol% of *fac*-Ir(ppy)$_3$, and 1.0 mM BTPA at 23 °C.

Time (h)	BTPA Conversion	ln([BTPA]$_0$ / [BTPA])	Average	TTC Loss	ln([TTC]$_0$/ [TTC])	Average
0.5	0.1178	0.1253		0.1300	0.1393	
	*	*		0.0993	0.1045	
	0.1470	0.1590		0.1212	0.1292	
			0.14 ±			
	0.1321	0.1417	0.02	0.1447	0.1563	0.13 ± 0.02
1	0.2311	0.2628		0.2331	0.2654	
	0.3326	0.4043		0.2922	0.3457	
	0.3442	0.4219		0.1646	0.1798	
			0.37 ±			
	0.3256	0.3940	0.07	0.2952	0.3499	0.29 ± 0.08
2	0.4833	0.6603		0.3978	0.5072	
	0.5586	0.8179		0.4987	0.6906	
	0.5798	0.8670		0.5372	0.7705	
	0.6278	0.9882	0.8 ± 0.1	0.5595	0.8198	0.7 ± 0.1
3	0.6467	1.0405		0.5760	0.8580	
	0.7539	1.4019		0.6973	1.1949	
	0.7295	1.3074		0.6681	1.1030	
	0.7774	1.5025	1.3 ± 0.2	0.7139	1.2513	1.1 ± 0.2

Table C9. Consumption of BTPA and degradation of TTC in the presence of 250 equivalents of MMA, 0.1 mol% of *fac*-Ir(ppy)$_3$, and 1.0 mM BTPA at 23 °C.

Time (h)	BTPA Conversion	ln([BTPA]$_0$ / [BTPA])	Average	TTC Loss	ln([TTC]$_0$/ [TTC])	Average
0.5	0.0683	0.0707		0.0493	0.0506	
	*	*		0.0816	0.0851	
	0.0551	0.0566		0.0768	0.0799	
			0.04 ±			
	0.0120	0.0120	0.03	0.0977	0.1028	0.08 ± 0.02
1	0.1220	0.1301		0.1025	0.1082	
	0.0414	0.0423		0.0659	0.0681	
	0.1066	0.1128		0.0655	0.0677	
			0.10 ±			
	0.0958	0.1007	0.04	0.0727	0.0755	0.08 ± 0.02
2	0.1929	0.2144		0.1270	0.1358	
	0.2087	0.2340		0.1171	0.1246	
	0.1092	0.1156		0.1089	0.1153	
			0.17 ±			
	0.1263	0.1350	0.06	0.1271	0.1359	0.13 ± 0.01
3	0.2391	0.2732		0.1737	0.1908	
	0.0862	0.0902		0.1505	0.1631	
	*	*		0.1557	0.1693	
	0.2569	0.2969	0.2 ± 0.1	0.1687	0.1848	0.18 ± 0.01

Table C10. Consumption of BTPA and degradation of TTC in the presence of 250 equivalents of MMA, 2.5 mol% of *fac*-Ir(ppy)$_3$, and 5.0 mM BTPA at 23 °C.

Time (h)	BTPA Conversion	ln([BTPA]$_0$ / [BTPA])	Average	TTC Loss	ln([TTC]$_0$/ [TTC])	Average
0.5	0.3210	0.3872		0.2135	0.2401	
	0.1722	0.1890		0.1570	0.1708	
	0.3149	0.3782		0.2093	0.2349	
	0.3464	0.4252	0.3 ± 0.1	0.2508	0.2888	0.23 ± 0.05
1	0.4159	0.5377		0.4852	0.6640	
	0.2044	0.2286		0.3899	0.4941	
	0.3113	0.3730		0.3880	0.4911	
	0.2725	0.3181	0.4 ± 0.1	0.5021	0.6973	0.6 ± 0.1
1.5	0.6708	1.1111		0.8435	1.8545	
	0.4693	0.6335		0.6362	1.0111	
	0.5635	0.8290		0.8067	1.6433	
	0.4776	0.6494	0.8 ± 0.2	0.8971	2.2744	1.7 ± 0.5
2	0.7028	1.2133		0.9634	3.3066	
	0.6870	1.1617		0.9425	2.8562	
	0.7802	1.5149		0.9684	3.4557	
	0.7789	1.5093	1.3 ± 0.2	0.9190	2.5131	3.0 ± 0.4

Table C11. Consumption of BTPA and degradation of TTC in the presence of 250 equivalents of MMA, 1.0 mol% of *fac*-Ir(ppy)$_3$, and 5.0 mM BTPA at 23 °C.

Time (h)	BTPA Conversion	ln([BTPA]$_0$ / [BTPA])	Average	TTC Loss	ln([TTC]$_0$/ [TTC])	Average
0.5	*	*		0.1125	0.1194	
	0.1411	0.1521		0.1088	0.1152	
	0.0833	0.0870		0.1061	0.1122	
			0.12 ±			
	0.1146	0.1217	0.03	0.1522	0.1651	0.13 ± 0.02
1	0.1872	0.2073		0.2286	0.2595	
	0.2808	0.3296		0.0480	0.0492	
	0.2116	0.2378		0.2296	0.2609	
			0.26 ±			
	*	*	0.06	0.1999	0.2230	0.2 ± 0.1
1.5	0.3740	0.4685		0.3729	0.4667	
	0.2658	0.3089		0.2490	0.2864	
	0.2606	0.3019		0.5505	0.7996	
			0.36 ±			
	0.2958	0.3507	0.08	0.4563	0.6093	0.5 ± 0.2
2	0.4036	0.5169		0.5564	0.8128	
	0.5768	0.8599		0.6204	0.9687	
	*	*		0.7334	1.3221	
	0.5108	0.7151	0.7 ± 0.2	0.6311	0.9971	1.0 ± 0.2

Table C12. Consumption of BTPA and degradation of TTC in the presence of 250 equivalents of MMA, 0.1 mol% of *fac*-Ir(ppy)$_3$, and 5.0 mM BTPA at 23 °C.

Time (h)	BTPA Conversion	ln([BTPA]$_0$ / [BTPA])	Average	TTC Loss	ln([TTC]$_0$/ [TTC])	Average
0.5	0.0191	0.0192		0.0974	0.1025	
	0.0296	0.0300		0.0808	0.0843	
	0.1722	0.1889		0.0786	0.0819	
	0.0927	0.0973	0.08 ± 0.08	0.0759	0.0789	0.08 ± 0.01
1	0.1468	0.1587		0.0519	0.0533	
	0.1501	0.1626		0.1123	0.1191	
	*	*		0.1132	0.1201	
			0.161 ±			
	*	*	0.003	0.0702	0.0727	0.09 ± 0.03
1.5	0.1693	0.1854		0.0934	0.0981	
	*	*		0.0980	0.1032	
	*	*		0.1204	0.1283	
			0.190 ±			
	0.1771	0.1949	0.007	0.0916	0.0961	0.11 ± 0.01
2	0.1428	0.1540		0.1322	0.1418	
	*	*		0.0725	0.0752	
	0.2544	0.2936		0.1214	0.1294	
	0.1862	0.2060	0.22 ± 0.07	0.1569	0.1707	0.13 ± 0.04

Table C13. Apparent rate constants of BTPA activation (k_a) and termination (k_t) for each set of conditions in the presence of 250 equivalents of monomer.

[BTPA] (mM)	Catalyst Loading (mol%)	Temperature (°C)	$k_{a,TTC}$ (10^{-5} s^{-})	$k_{t,TTC}$ (10^{-5} s^{-})	$k_{a,TTC}/k_{t,TTC}$
5	2.5	23	16 ± 1	34 ± 3	0.48 ± 0.05
	1.0		8.2 ± 0.6	12 ± 1	0.70 ± 0.09
	0.1		3.4 ± 0.4	2.1 ± 0.2	1.6 ± 0.2
1	2.5		27 ± 3	26 ± 1	1.1 ± 0.1
	1.0		11.2 ± 0.5	9.8 ± 0.4	1.14 ± 0.07
	0.1		2.2 ± 0.2	1.7 ± 0.1	1.3 ± 0.2
0.5	2.5		20 ± 1	17.9 ± 0.8	1.11 ± 0.09
	1.0		9.3 ± 0.3	6.7 ± 0.3	1.38 ± 0.07
	0.1		2.2 ± 0.2	1.14 ± 0.08	1.9 ± 0.2
0.1	2.5		7.4 ± 0.4	5.3 ± 0. 5	1.4 ± 0.2
	1.0		3.4 ± 0.2	1.9 ± 0.2	1.8 ± 0.2
	0.1		0.6 ± 0.1	0.30 ± 0.05	2.0 ± 0.5
0.1	0.1	40	1.4 ± 0.2	0.40 ± 0.03	3.6 ± 0.5
0.5	0.1		6.6 ± 0.4	2.1 ± 0.1	3.2 ± 0.3
5	0.1		8 ± 1	23 ± 2	0.36 ± 0.07
0.1	0.1	60	4.3 ± 0.3	1.05 ± 0.04	4.1 ± 0.3
0.5	0.1		4.8 ± 0.2	2.2 ± 0.2	2.2 ± 0.2
5	0.1		5.7 ± 0.4	1.6 ± 0.2	3.5 ± 0.4

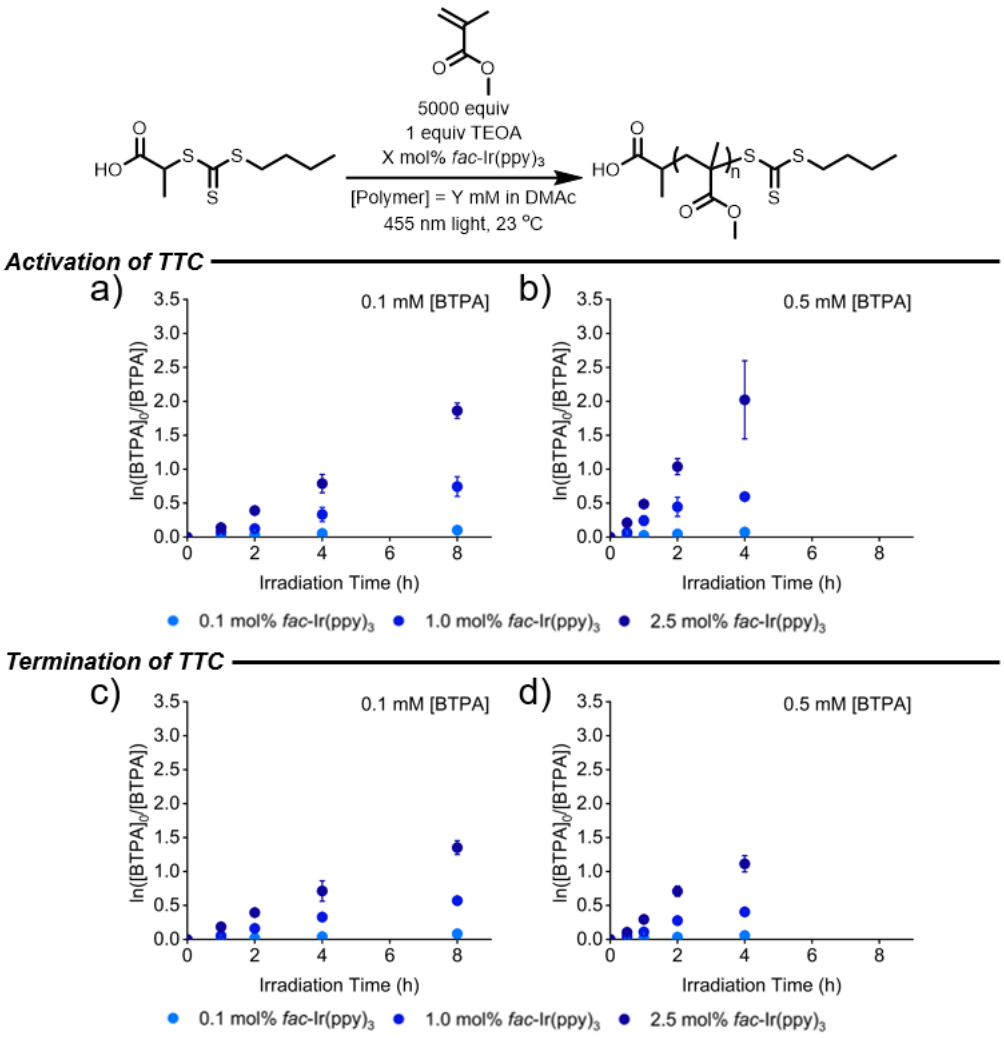

Figure C5. Pseudo-first-order kinetics plots for the activation of trithiocarbonate (TTC) with 5000 equivalents methyl methacrylate with a) 0.1 mM [TTC] or b) 0.5 mM [TTC] with 0.1, 1.0, or 2.5 mol% *fac*-Ir(ppy)$_3$. Pseudo-first-order kinetics plots for the termination of TTC with c) 0.1 mM [TTC] or d) 0.5 mM [TTC] with 0.1, 1.0, or 2.5 mol% *fac*-Ir(ppy)$_3$.

Table C14. Consumption of BTPA and degradation of TTC in the presence of 5000 equivalents of MMA, 2.5 mol% of *fac*-Ir(ppy)$_3$, and 0.5 mM BTPA at 23 °C.

Time (h)	BTPA Conversion	ln([BTPA]$_0$ / [BTPA])	Average	TTC Loss	ln([TTC]$_0$/ [TTC])	Average
0.5	0.1701	0.1865		0.0968	0.1018	
	0.1830	0.2021		0.0724	0.0752	
	0.2297	0.2609		0.1216	0.1297	
	0.1768	0.1946	0.21 ± 0.03	0.1071	0.1133	0.11 ± 0.02
1	0.3725	0.4660		0.2596	0.3006	
	0.4208	0.5461		0.2763	0.3234	
	0.3841	0.4847		0.2749	0.3214	
	0.3609	0.4478	0.49 ± 0.04	0.2094	0.2350	0.30 ± 0.04
2	0.6682	1.1031		0.5222	0.7386	
	0.6095	0.9403		0.4778	0.6497	
	0.6905	1.1729		0.5516	0.8021	
	0.6079	0.9362	1.0 ± 0.1	0.4761	0.6464	0.71 ± 0.08
3	0.9419	2.8461		0.7189	1.2691	
	0.7838	1.5316		0.6240	0.9782	
	0.8580	1.9519		0.6665	1.0981	
	0.8278	1.7590	2.0 ± 0.6	0.6694	1.1069	1.1 ± 0.1

Table C15. Consumption of BTPA and degradation of TTC in the presence of 5000 equivalents of MMA, 1.0 mol% of *fac*-Ir(ppy)$_3$, and 0.5 mM BTPA at 23 °C.

Time (h)	BTPA Conversion	ln([BTPA]$_0$ / [BTPA])	Average	TTC Loss	ln([TTC]$_0$/ [TTC])	Average
0.5	0.0403	0.0411		0.0434	0.0443	
	0.1242	0.1326		0.0578	0.0596	
	0.0351	0.0358		0.0347	0.0353	
	0.0566	0.0583	0.07 ± 0.04	0.0402	0.0410	0.05 ± 0.01
1	0.1922	0.2135		0.1161	0.1235	
	0.1546	0.1679		0.1265	0.1353	
	0.2840	0.3340		0.1392	0.1498	
	0.2275	0.2581	0.24 ± 0.07	0.0276	0.0280	0.11 ± 0.05
2	0.4074	0.5232		0.3010	0.3581	
	0.2675	0.3113		0.1973	0.2197	
	0.4534	0.6040		0.2417	0.2767	
	0.2917	0.3449	0.4 ± 0.1	0.2235	0.2530	0.28 ± 0.06
3	0.4625	0.6208		0.3437	0.4212	
	0.4412	0.5820		0.3234	0.3907	
	0.4559	0.6085		0.3114	0.3732	
	0.4359	0.5725	0.60 ± 0.02	0.3519	0.4337	0.40 ± 0.03

Table C16. Consumption of BTPA and degradation of TTC in the presence of 5000 equivalents of MMA, 0.1 mol% of *fac*-Ir(ppy)$_3$, and 0.5 mM BTPA at 23 °C.

Time (h)	BTPA Conversion	ln([BTPA]$_0$ / [BTPA])	Average	TTC Loss	ln([TTC]$_0$/ [TTC])	Average
0.5	0.0097	0.0097		0.0085	0.0086	
	0.0155	0.0156		0.0071	0.0071	
			0.016 ±			0.010 ± 0.005
	0.0213	0.0216	0.006	0.0161	0.0163	
1	0.0167	0.0169		0.0178	0.0180	
	0.0309	0.0314		0.0129	0.0130	
			0.026 ±			0.018 ± 0.006
	0.0324	0.0329	0.008	0.0239	0.0239	
2	0.0318	0.0324		0.0309	0.0314	
	0.0464	0.0475		0.0311	0.0316	
	0.0574	0.0591	0.05 ± 0.01	0.0368	0.0375	0.033 ± 0.003
3	0.0600	0.0619		0.0510	0.0524	
	0.0750	0.0780		0.0485	0.0497	
	0.0789	0.0822	0.07 ± 0.01	0.0645	0.0667	0.056 ± 0.009

Table C17. Consumption of BTPA and degradation of TTC in the presence of 5000 equivalents of MMA, 2.5 mol% of *fac*-Ir(ppy)$_3$, and 0.1 mM BTPA at 23 °C.

Time (h)	BTPA Conversion	ln([BTPA]$_0$ / [BTPA])	Average	TTC Loss	ln([TTC]$_0$/ [TTC])	Average
1	0.1595	0.1737		0.1975	0.2201	
	0.1244	0.1328		0.1790	0.1972	
	0.1263	0.1350		0.1553	0.1687	
	0.1117	0.1184	0.14 ± 0.02	0.1443	0.1559	0.19 ± 0.03
2	*	*		*	*	
	0.3153	0.3788		0.3231	0.3902	
	0.3352	0.4083		0.3418	0.4183	
	0.3210	0.3871	0.39 ± 0.02	0.3139	0.3767	0.40 ± 0.02
4	0.6250	0.9810		0.6086	0.9380	
	0.4917	0.6766		0.4676	0.6304	
	0.5394	0.7753		0.4729	0.6404	
	0.5131	0.7197	0.8 ± 0.1	0.4739	0.6422	0.71 ± 0.2
8	0.8493	1.8922		0.7331	1.3208	
	0.8353	1.8037		0.7772	1.5015	
	0.8653	2.0045		0.7304	1.3108	
	0.8255	1.7457	1.9 ± 0.1	0.7202	1.2735	1.4 ± 0.1

Table C18. Consumption of BTPA and degradation of TTC in the presence of 5000 equivalents of MMA, 1.0 mol% of *fac*-Ir(ppy)$_3$, and 0.1 mM BTPA at 23 °C.

Time (h)	BTPA Conversion	ln([BTPA]$_0$ / [BTPA])	Average	TTC Loss	ln([TTC]$_0$/ [TTC])	Average
1	*	*		0.0325	0.0331	
	*	*		0.0342	0.0348	
	0.0744	0.0773		0.0826	0.0862	
	*	*	0.0773*	0.0583	0.0601	0.05 ± 0.03
2	0.1650	0.1803		0.1576	0.1715	
	0.1380	0.1485		0.1665	0.1821	
	0.1010	0.1065		0.1522	0.1651	
	0.0645	0.0667	0.12 ± 0.05	0.1176	0.1252	0.16 ± 0.02
4	0.3861	0.4880		0.2982	0.3541	
	0.2358	0.2689		0.2801	0.3287	
	0.2626	0.3046		0.2945	0.3489	
	0.2383	0.2722	0.3 ± 0.1	0.2484	0.2856	0.33 ± 0.03
8	0.6132	0.9498		0.4110	0.5293	
	0.5094	0.7121		0.4506	0.5990	
	0.5064	0.7061		0.4265	0.5561	
	0.4563	0.6093	0.7 ± 0.1	0.4501	0.5981	0.57 ± 0.03

Table C19. Consumption of BTPA and degradation of TTC in the presence of 5000 equivalents of MMA, 0.1 mol% of *fac*-Ir(ppy)$_3$, and 0.1 mM BTPA at 23 °C.

Time (h)	BTPA Conversion	ln([BTPA]$_0$ / [BTPA])	Average	TTC Loss	ln([TTC]$_0$/ [TTC])	Average
1	0.0160	0.0161		0.0117	0.0118	
	0.0129	0.0130		0.0088	0.0088	
			0.013 ±			0.011 ±
	0.0120	0.0121	0.002	0.0152	0.0153	0.003
2	0.0384	0.0391		0.0204	0.0206	
	0.0268	0.0272		0.0135	0.0136	
			0.031 ±			0.019 ±
	0.0252	0.0255	0.007	0.0225	0.0227	0.005
4	0.0592	0.0610		0.0421	0.0430	
	0.0490	0.0503		0.0332	0.0337	
			0.053 ±			0.040 ±
	0.0476	0.0488	0.007	0.0421	0.0430	0.005
8	0.1083	0.1147		0.0790	0.0823	
	0.0941	0.0988		0.0740	0.0769	
	0.0883	0.0925	0.10 ± 0.01	0.0842	0.0880	0.082 ±
						0.006

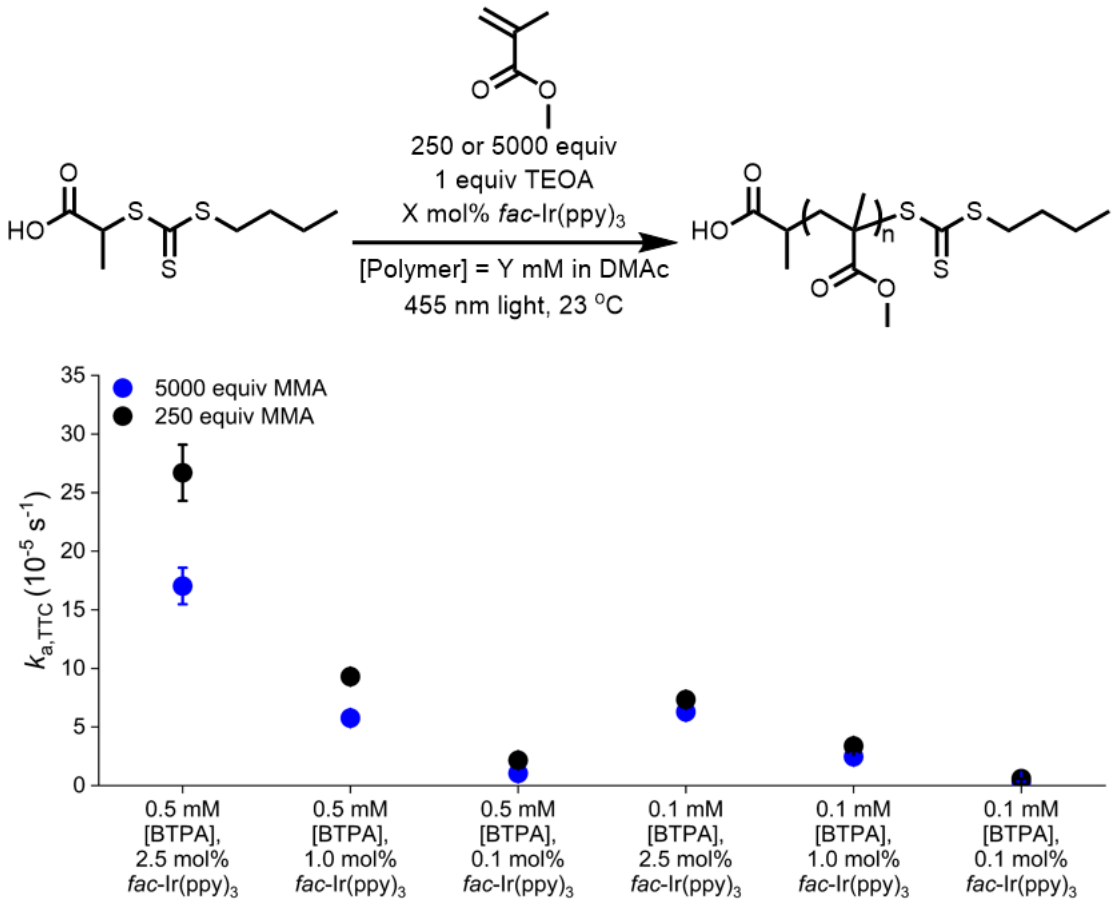

Figure C6. Comparison of 5000 equivalents of methyl methacrylate (MMA) versus 250 equivalents MMA across different [trithiocarbonate (TTC)] and *fac*-Ir(ppy)$_3$ loadings and the effect on the rate of activation of the TTC ($k_{a,TTC}$).

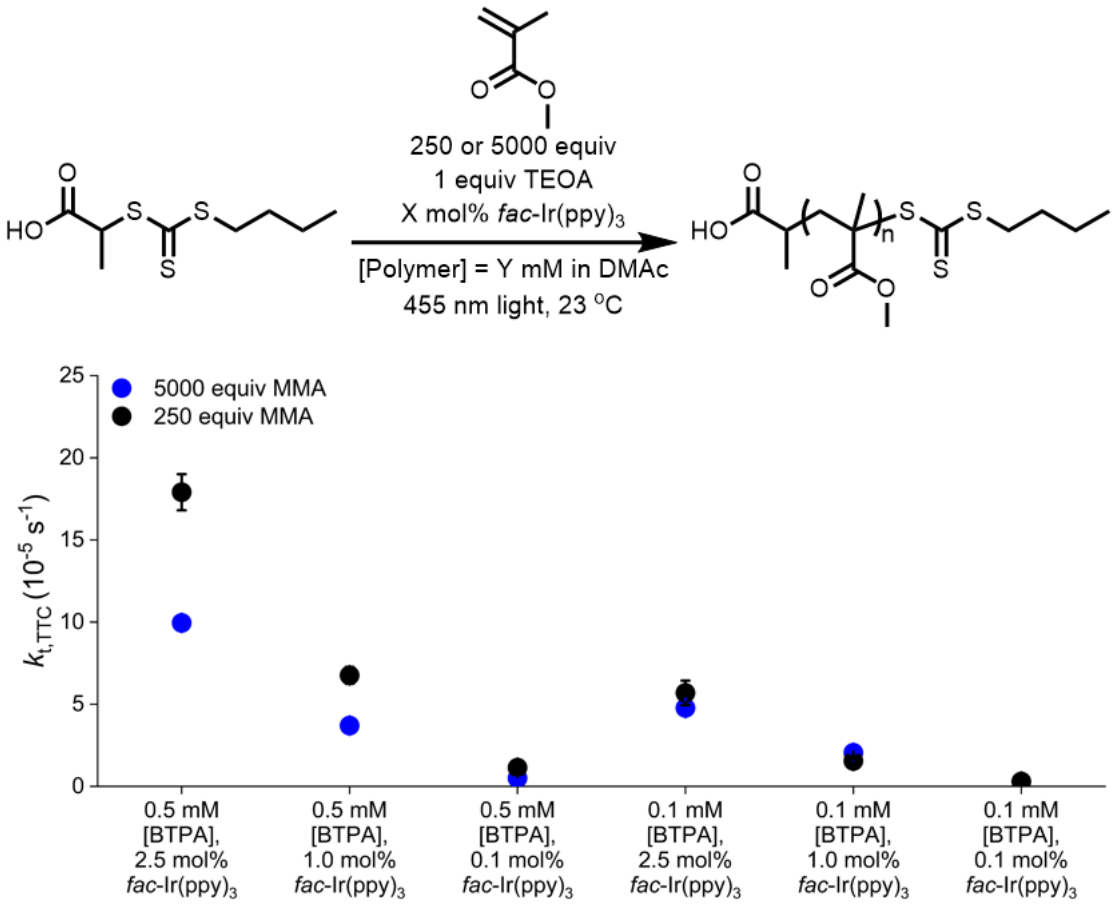

Figure C7. Comparison of 5000 equivalents of methyl methacrylate (MMA) versus 250 equivalents MMA across different [trithiocarbonate (TTC)] and *fac*-Ir(ppy)$_3$ loadings and the effect on the rate of termination of the TTC ($k_{t,TTC}$).

Table C20. Apparent rate constants of TTC activation (k_a) and termination (k_t) for each set of conditions in the presence of 5000 equivalents of MMA at 23 °C.

[BTPA] (mM)	Catalyst Loading (mol%)	$k_{a,TTC}$ (10^{-5} s^{-})	$k_{t,TTC}$ (10^{-5} s^{-})	$k_{a,TTC}/k_{t,TTC}$
0.5	2.5	17 ± 1	9.9 ± 0.3	1.7 ± 0.1
	1.0	5.8 ± 0.3	3.7 ± 0.2	1.6 ± 0.1
	0.1	0.67 ± 0.04	0.51 ± 0.02	1.3 ± 0.1
0.1	2.5	6.3 ± 0.3	4.8 ± 0.1	1.32 ± 0.07
	1.0	2.5 ± 0.2	2.04 ± 0.05	1.22 ± 0.08
	0.1	0.36 ± 0.01	0.284 ± 0.01	1.27 ± 0.05

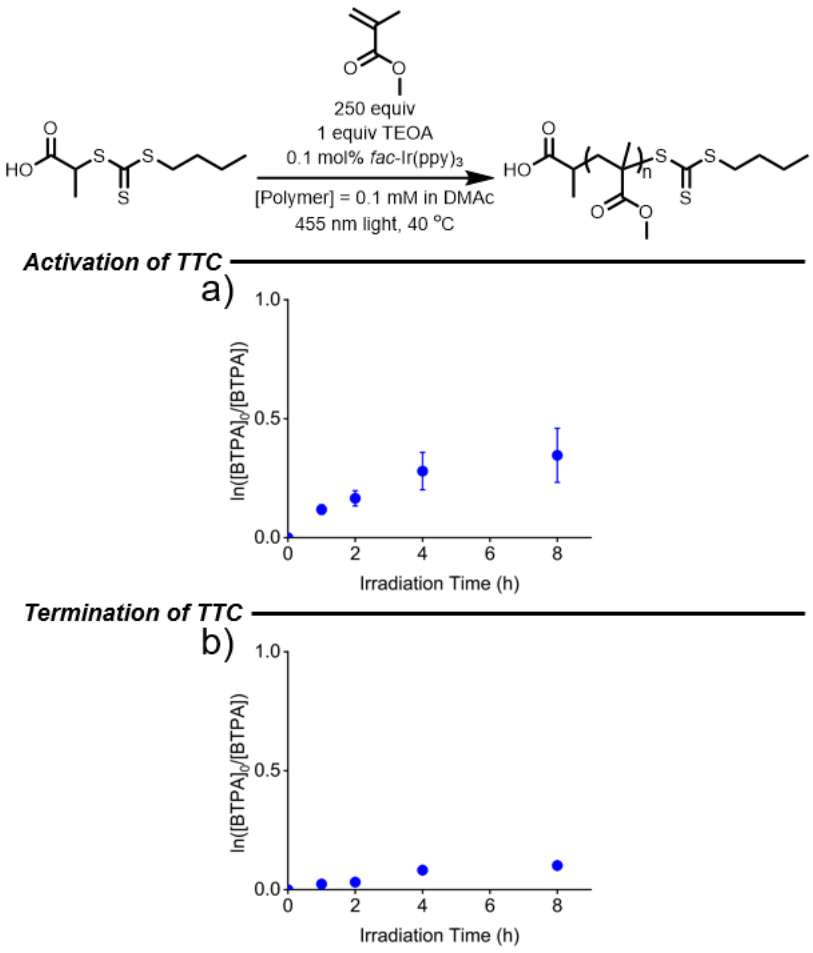

Figure C8. a) Pseudo-first-order kinetics plots for the activation of trithiocarbonate (TTC) with 250 equivalents methyl methacrylate at 40 °C with 0.1 mM [TTC] and 0.1 mol% *fac*-Ir(ppy)$_3$. b) Pseudo-first-order kinetics plots for the termination of trithiocarbonate (TTC) with 250 equivalents methyl methacrylate at 40 °C with 0.1 mM [TTC] and 0.1 mol% *fac*-Ir(ppy)$_3$.

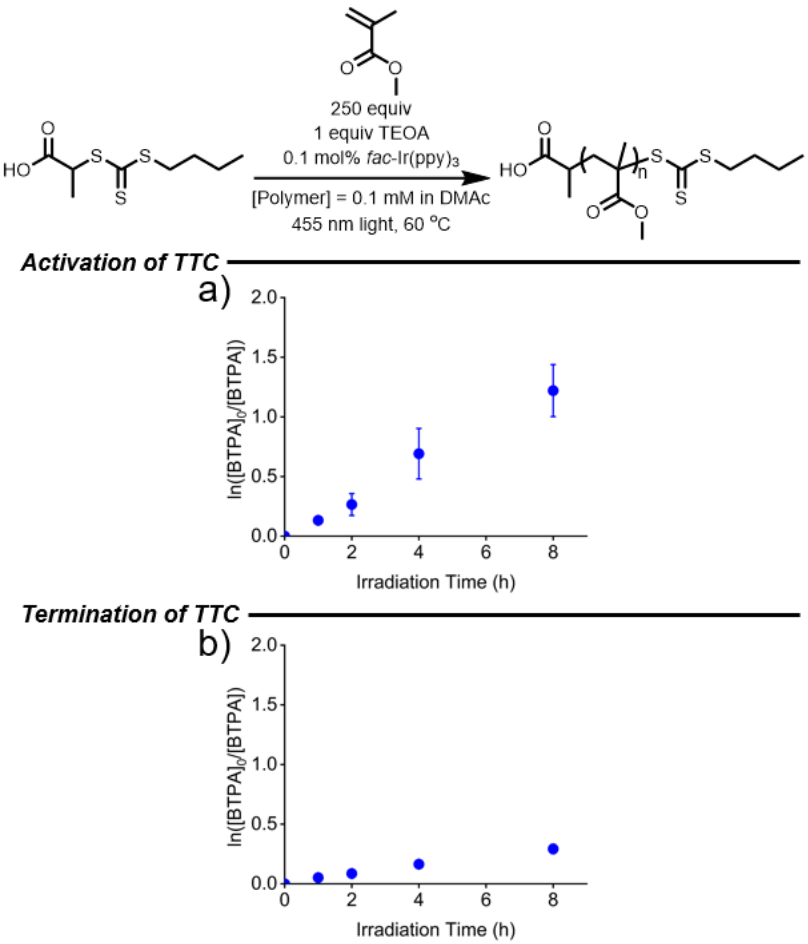

Figure C9. a) Pseudo-first-order kinetics plots for the activation of trithiocarbonate (TTC) with 250 equivalents methyl methacrylate at 60 °C with 0.1 mM [TTC] and 0.1 mol% *fac*-Ir(ppy)$_3$. b) Pseudo-first-order kinetics plots for the termination of trithiocarbonate (TTC) with 250 equivalents methyl methacrylate at 60 °C with 0.1 mM [TTC] and 0.1 mol% *fac*-Ir(ppy)$_3$. The rate constant of TTC activation and the rate constant of TTC termination were calculated using similar plots for 0.5 and 5 mM [TTC].

Table C21. Consumption of BTPA and degradation of TTC in the presence of 250 equivalents of MMA, 0.1 mol% of *fac*-Ir(ppy)$_3$, and 0.1 mM BTPA at 40 °C.

Time (h)	BTPA Conversion	ln([BTPA]$_0$ / [BTPA])	Average	TTC Loss	ln([TTC]$_0$/ [TTC])	Average
1	0.1182	0.1257		0.0013	0.0278	
	0.1246	0.1331		0.0219	0.0222	
			0.12 ±			
	0.0913	0.0958	0.02	0.0241	0.0207	0.024 ± 0.004
2	0.1825	0.2015		0.0287	0.0292	
	0.1432	0.1545		0.0359	0.0312	
			0.17 ±			
	0.1305	0.1399	0.03	0.0338	0.0339	0.031 ± 0.002
4	0.2626	0.3047		0.0961	0.0908	
	0.1744	0.1917		0.0737	0.0795	
			0.28 ±			
	0.2902	0.3427	0.08	0.0661	0.0752	0.082 ± 0.008
8	0.3314	0.4026		0.0847	0.1086	
	0.3432	0.4203		0.1340	0.1107	
	0.1936	0.2152	0.35 ±	0.1060	0.0849	0.10 ± 0.01
			0.11			

Table C22. Consumption of BTPA and degradation of TTC in the presence of 250 equivalents of MMA, 0.1 mol% of *fac*-Ir(ppy)$_3$, and 0.5 mM BTPA at 40 °C.

Time (h)	BTPA Conversion	ln([BTPA]$_0$ / [BTPA])	Average	TTC Loss	ln([TTC]$_0$/ [TTC])	Average
1	0.1787	0.1969		0.0673	0.0697	
	0.2092	0.2348		0.0969	0.1019	
	0.2004	0.2236		0.0523	0.0537	
			0.22 ±			
	0.2050	0.2294	0.02	0.0620	0.0640	0.07 ± 0.02
2	0.4049	0.5190		0.0576	0.0593	
	0.4825	0.6585		0.1260	0.1347	
	0.2702	0.3150		0.1046	0.1104	
	0.3896	0.4936	0.5 ± 0.1	0.1318	0.1413	0.11 ± 0.04
3	0.3112	0.3728		0.1842	0.2036	
	0.4034	0.5165		0.1260	0.1347	
	0.4447	0.5883		0.1046	0.1104	
			0.48 ±			
	0.3632	0.4512	0.09	0.2014	0.2249	0.2 ± 0.1
4	0.6983	1.1983		0.2931	0.3468	
	0.6585	1.0744		0.2671	0.3108	
	0.7187	1.2685		0.2437	0.2793	
	0.5881	0.8869	1.1 ± 0.2	0.2686	0.3128	0.31 ± 0.03

Table C23. Consumption of BTPA and degradation of TTC in the presence of 250 equivalents of MMA, 0.1 mol% of *fac*-Ir(ppy)$_3$, and 5 mM BTPA at 40 °C.

Time (h)	BTPA Conversion	ln([BTPA]$_0$ / [BTPA])	Average	TTC Loss	ln([TTC]$_0$/ [TTC])	Average
0.5	0.5540	0.8075		*	*	
	0.1619	0.1766		0.3774	0.4739	
	0.1953	0.2173		*	*	
	0.3539	0.4369	0.4 ± 0.3	0.3004	0.3572	0.42 ± 0.08
1	0.4169	0.5393		*	*	
	0.2041	0.2703		0.6019	0.9210	
	0.2136	0.2403		0.7581	1.4191	
	0.2049	0.2293	0.3 ± 0.2	0.6314	0.9981	1.1 ± 0.3
1.5	0.4623	0.6205		0.8475	1.881	
	0.2369	0.2703		0.7085	1.2328	
	0.3562	0.4404		0.4441	0.5871	
	0.2228	0.2293	0.4 ± 0.2	0.6966	1.1928	1.2 ± 0.5
2	0.5966	0.9078		0.7670	1.4567	
	0.3558	0.4397		0.9175	2.4955	
	0.3202	0.3859		0.7548	1.4058	
	0.3609	0.4477	0.5 ± 0.2	0.5641	0.8303	1.5 ± 0.7

Table C24. Consumption of BTPA and degradation of TTC in the presence of 250 equivalents of MMA, 0.1 mol% of *fac*-Ir(ppy)$_3$, and 0.1 mM BTPA at 60 °C.

Time (h)	BTPA Conversion	ln([BTPA]$_0$ / [BTPA])	Average	TTC Loss	ln([TTC]$_0$/ [TTC])	Average
1	0.1269	0.1357		0.0996	0.0546	
	0.1198	0.1277		0.0416	0.0483	
			0.132 ±			0.051 ±
	0.1255	0.1341	0.004	0.1432	0.0506	0.003
2	0.3084	0.3687		0.1667	0.0944	
	0.1761	0.1937		0.0935	0.0815	
						0.085 ±
	0.2077	0.2329	0.26 ± 0.09	0.0841	0.0819	0.007
4	0.5766	0.8594		0.2283	0.1842	
	0.3645	0.4534		0.1740	0.1497	
	0.5323	0.7600	0.7 ± 0.2	0.1972	0.1592	0.16 ± 0.02
8	0.7488	1.3815		0.3275	0.3151	
	0.6216	0.9718		0.3281	0.2475	
	0.7292	1.3064	1.2 ± 0.2	0.3079	0.3138	0.29 ± 0.04

Table C25. Consumption of BTPA and degradation of TTC in the presence of 250 equivalents of MMA, 0.1 mol% of *fac*-Ir(ppy)$_3$, and 0.5 mM BTPA at 60 °C.

Time (h)	BTPA Conversion	ln([BTPA]$_0$ / [BTPA])	Average	TTC Loss	ln([TTC]$_0$/ [TTC])	Average
1	0.1645	0.1797		0.0141	0.0142	
	0.2127	0.2391		*	*	
	0.1954	0.2174		0.0883	0.0925	
	0.2164	0.2438	0.22 ± 0.03	0.0797	0.0830	0.06 ± 0.04
2	0.3524	0.4344		0.0769	0.0800	
	0.3292	0.3993		0.1644	0.1796	
	0.2959	0.3508		0.1162	0.1235	
	0.2956	0.3505	0.38 ± 0.04	0.1303	0.1396	0.13 ± 0.04
3	0.3474	0.4269		0.1871	0.1962	
	0.3811	0.4798		0.2176	0.2454	
	0.4386	0.5777		0.2517	0.2899	
	0.4045	0.5184	0.50 ± 0.06	0.1858	0.2055	0.23 ± 0.04
4	0.4194	0.5436		0.2232	0.2525	
	0.5048	0.7027		0.2392	0.2734	
	0.5006	0.6943		0.3370	0.4110	
	0.5335	0.7626	0.67 ± 0.09	0.3586	0.4441	0.3 ± 0.1

Table C26. Consumption of BTPA and degradation of TTC in the presence of 250 equivalents of MMA, 0.1 mol% of *fac*-Ir(ppy)$_3$, and 5 mM BTPA at 60 °C.

Time (h)	BTPA Conversion	ln([BTPA]$_0$ / [BTPA])	Average	TTC Loss	ln([TTC]$_0$/ [TTC])	Average
0.5	0.1321	0.1417		0.0361	0.0368	
	0.1300	0.1392		0.0379	0.0386	
	0.1304	0.1397		0.0076	0.0077	
			0.144 ±			
	0.1439	0.1553	0.008	0.0379	0.0386	0.03 ± 0.02
1	0.2103	0.2362		0.0799	0.0832	
	0.1831	0.2022		0.0142	0.0143	
	0.2327	0.2649		0.0714	0.0741	
	0.2341	0.2667	0.24 ± 0.03	0.0485	0.0498	0.06 ± 0.03
1.5	0.3143	0.3773		0.1096	0.1161	
	0.3819	0.4812		0.0714	0.0741	
	0.2341	0.2667		0.0886	0.0928	
	0.2816	0.3307	0.37 ± 0.08	*	*	0.09 ± 0.02
2	0.3376	0.4119		0.1773	0.1951	
	0.2849	0.3354		0.1132	0.1202	
	0.2316	0.2634		0.0910	0.0955	
	0.2815	0.3306	0.34 ± 0.07	0.0500	0.0513	0.12 ± 0.06

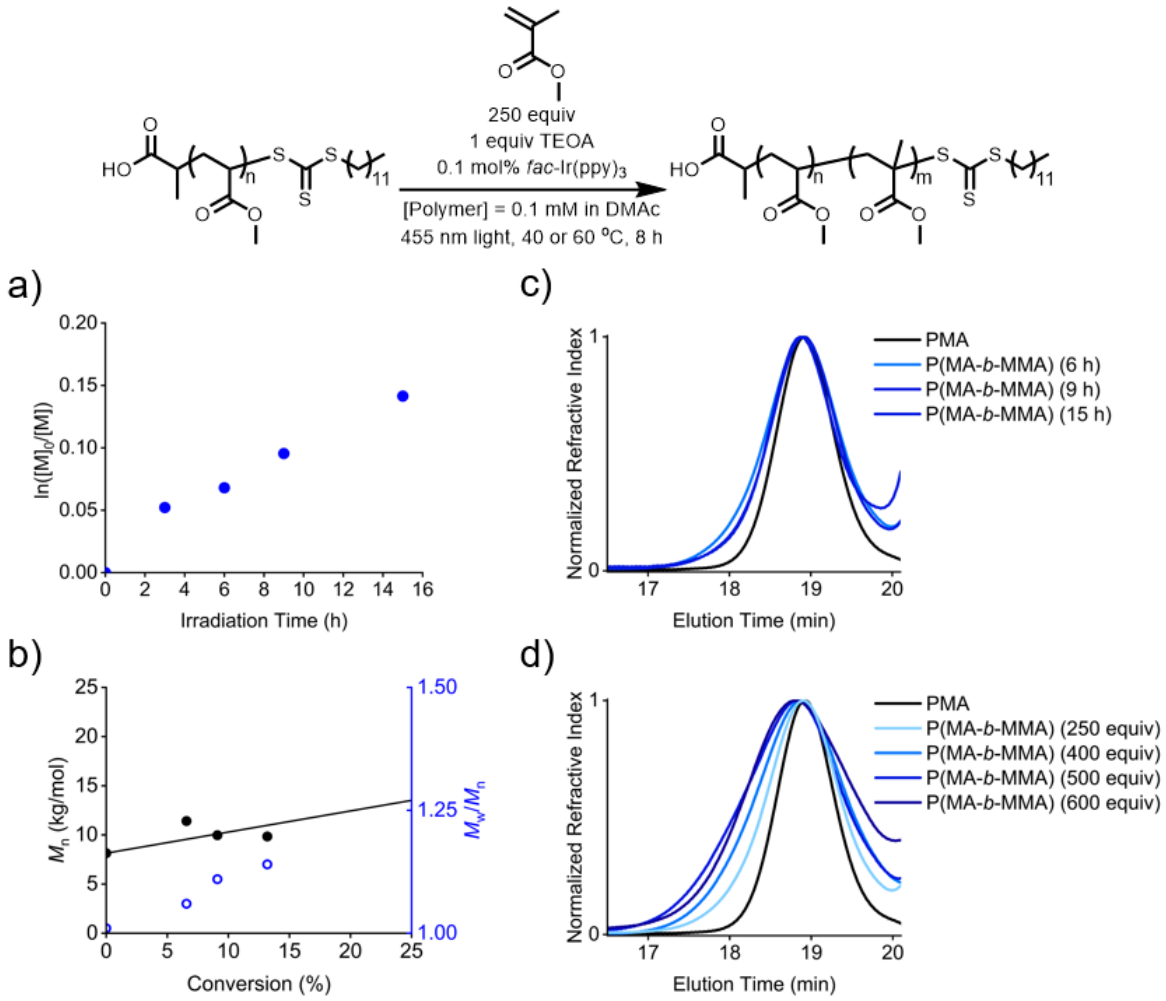

Figure C10. a) Pseudo-first-order kinetics plot for a chain extension of poly(methyl acrylate) with 250 equivalents of methyl methacrylate using 0.1 mol% *fac*-Ir(ppy)$_3$ and 0.1 mM [Polymer]. b) Molecular weight (M_n) and dispersity ($Đ$) versus conversion using multi-angle light scattering size exclusion chromatography (SEC-MALS). c) Refractive index (RI) traces from SEC-MALS of polymerization progress. d) RI traces from SEC-MALS of polymerizations using 250, 500, 750, or 1000 equivalents of methyl methacrylate.

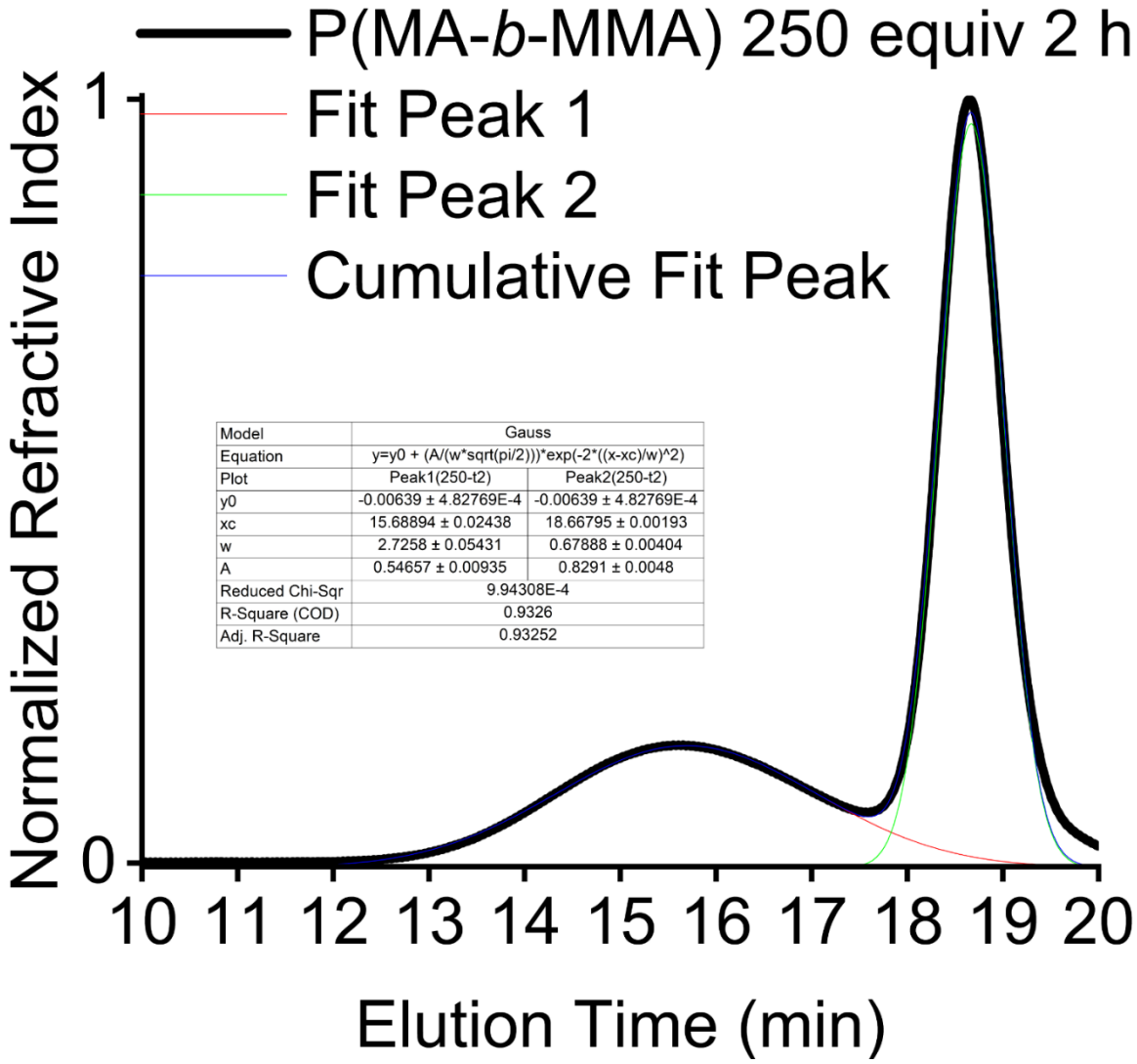

Model	Gauss	
Equation	y=y0 + (A/(w*sqrt(pi/2)))*exp(-2*((x-xc)/w)^2)	
Plot	Peak1(250-t2)	Peak2(250-t2)
y0	-0.00639 ± 4.82769E-4	-0.00639 ± 4.82769E-4
xc	15.68894 ± 0.02438	18.66795 ± 0.00193
w	2.7258 ± 0.05431	0.67888 ± 0.00404
A	0.54657 ± 0.00935	0.8291 ± 0.0048
Reduced Chi-Sqr	9.94308E-4	
R-Square (COD)	0.9326	
Adj. R-Square	0.93252	

Figure C11. Peak deconvolution for P(MA-b-MMA) synthesized from the chain extension of PMA with 250 equivalents of MMA after 2 hours. Approximately 40% of PMA chains were activated based on the fitted Gaussian model.

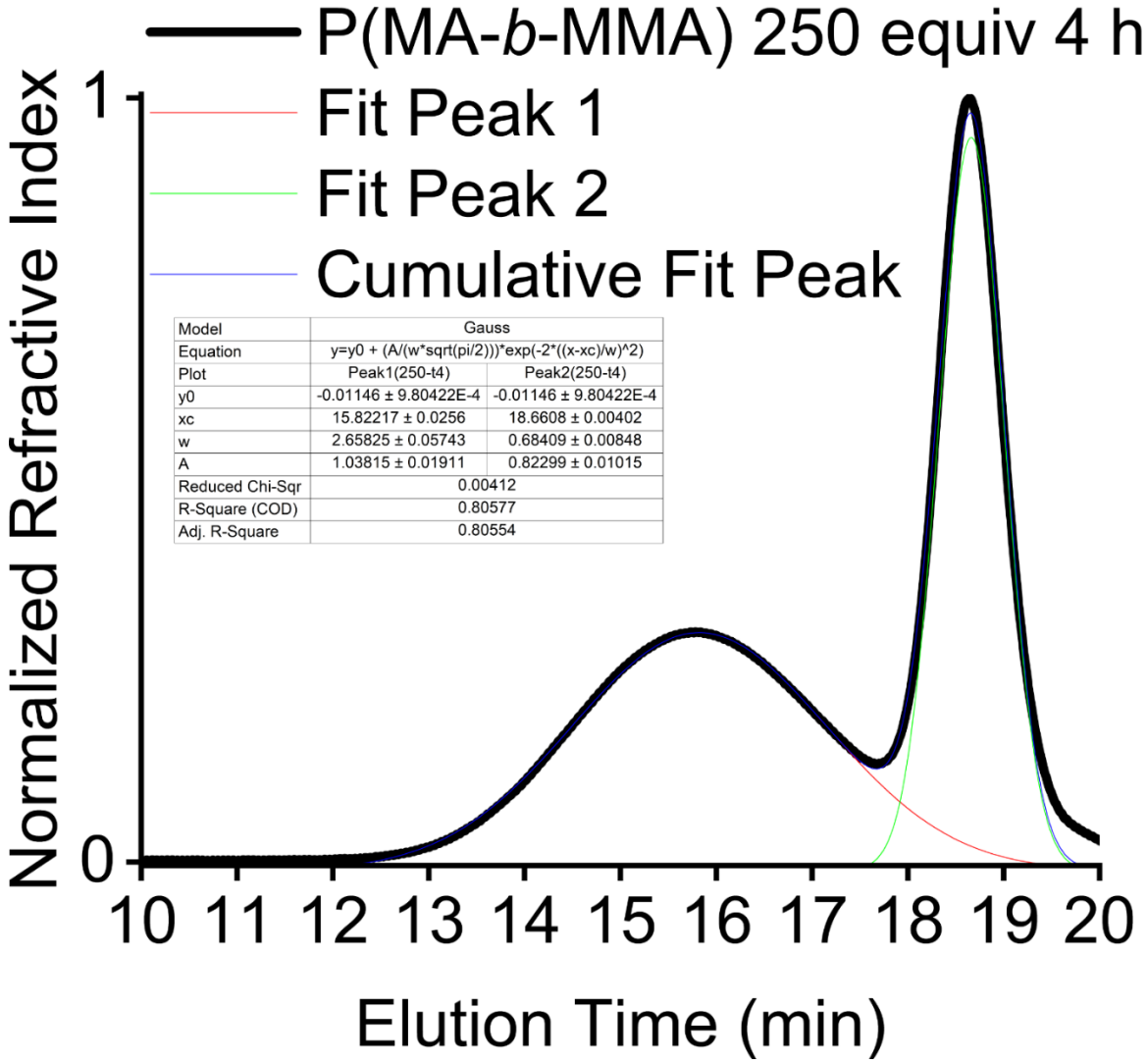

Model	Gauss	
Equation	y=y0 + (A/(w*sqrt(pi/2)))*exp(-2*((x-xc)/w)^2)	
Plot	Peak1(250-t4)	Peak2(250-t4)
y0	-0.01146 ± 9.80422E-4	-0.01146 ± 9.80422E-4
xc	15.82217 ± 0.0256	18.6608 ± 0.00402
w	2.65825 ± 0.05743	0.68409 ± 0.00848
A	1.03815 ± 0.01911	0.82299 ± 0.01015
Reduced Chi-Sqr	0.00412	
R-Square (COD)	0.80577	
Adj. R-Square	0.80554	

Figure C12. Peak deconvolution for P(MA-b-MMA) synthesized from the chain extension of PMA with 250 equivalents of MMA after 4 hours. Approximately 56% of PMA chains were activated based on the fitted Gaussian model.

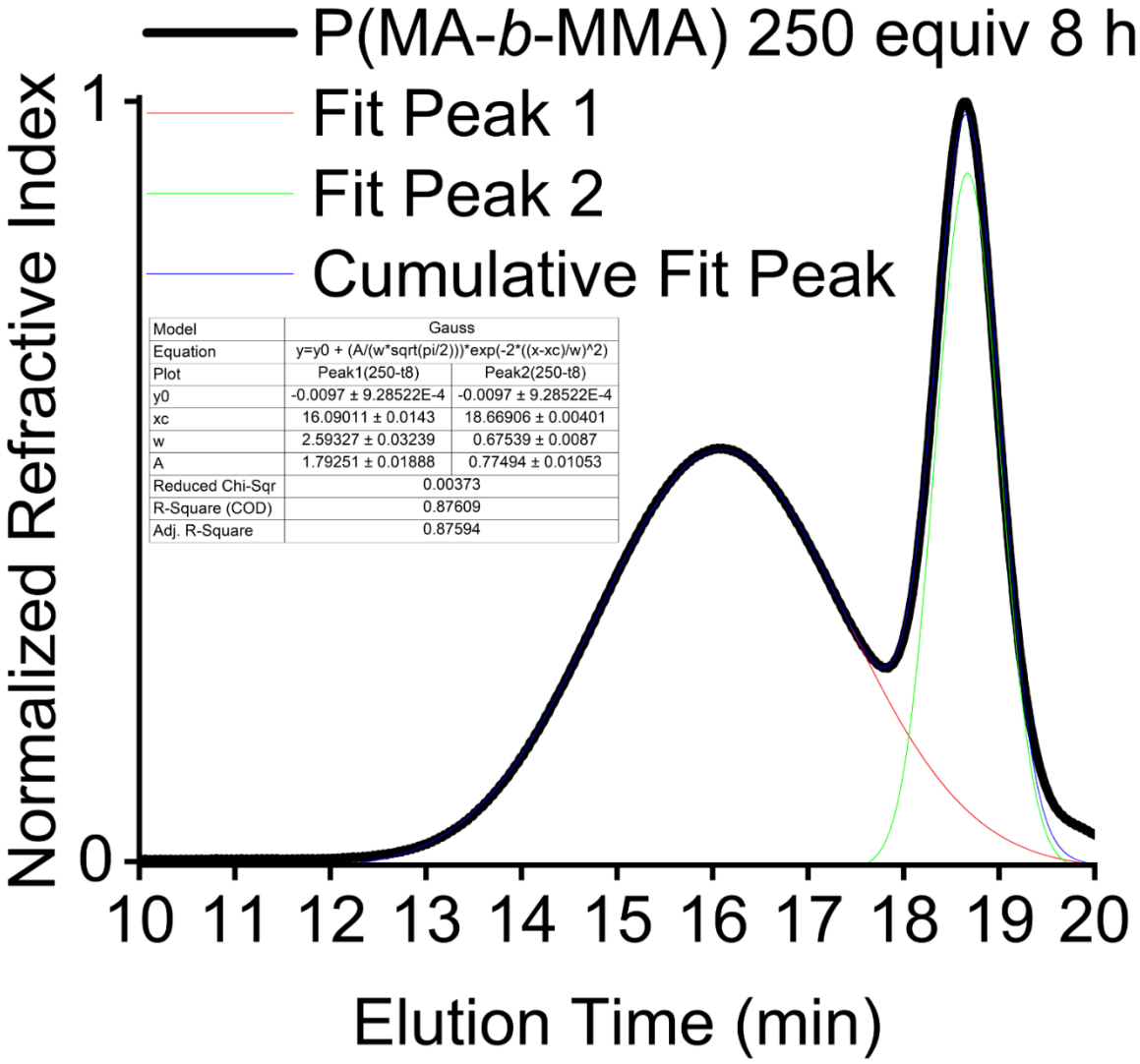

Model	Gauss	
Equation	y=y0 + (A/(w*sqrt(pi/2)))*exp(-2*((x-xc)/w)^2)	
Plot	Peak1(250-t8)	Peak2(250-t8)
y0	-0.0097 ± 9.28522E-4	-0.0097 ± 9.28522E-4
xc	16.09011 ± 0.0143	18.66906 ± 0.00401
w	2.59327 ± 0.03239	0.67539 ± 0.0087
A	1.79251 ± 0.01888	0.77494 ± 0.01053
Reduced Chi-Sqr	0.00373	
R-Square (COD)	0.87609	
Adj. R-Square	0.87594	

Figure C13. Peak deconvolution for P(MA-b-MMA) synthesized from the chain extension of PMA with 250 equivalents of MMA after 8 hours. Approximately 70% of PMA chains were activated based on the fitted Gaussian model.

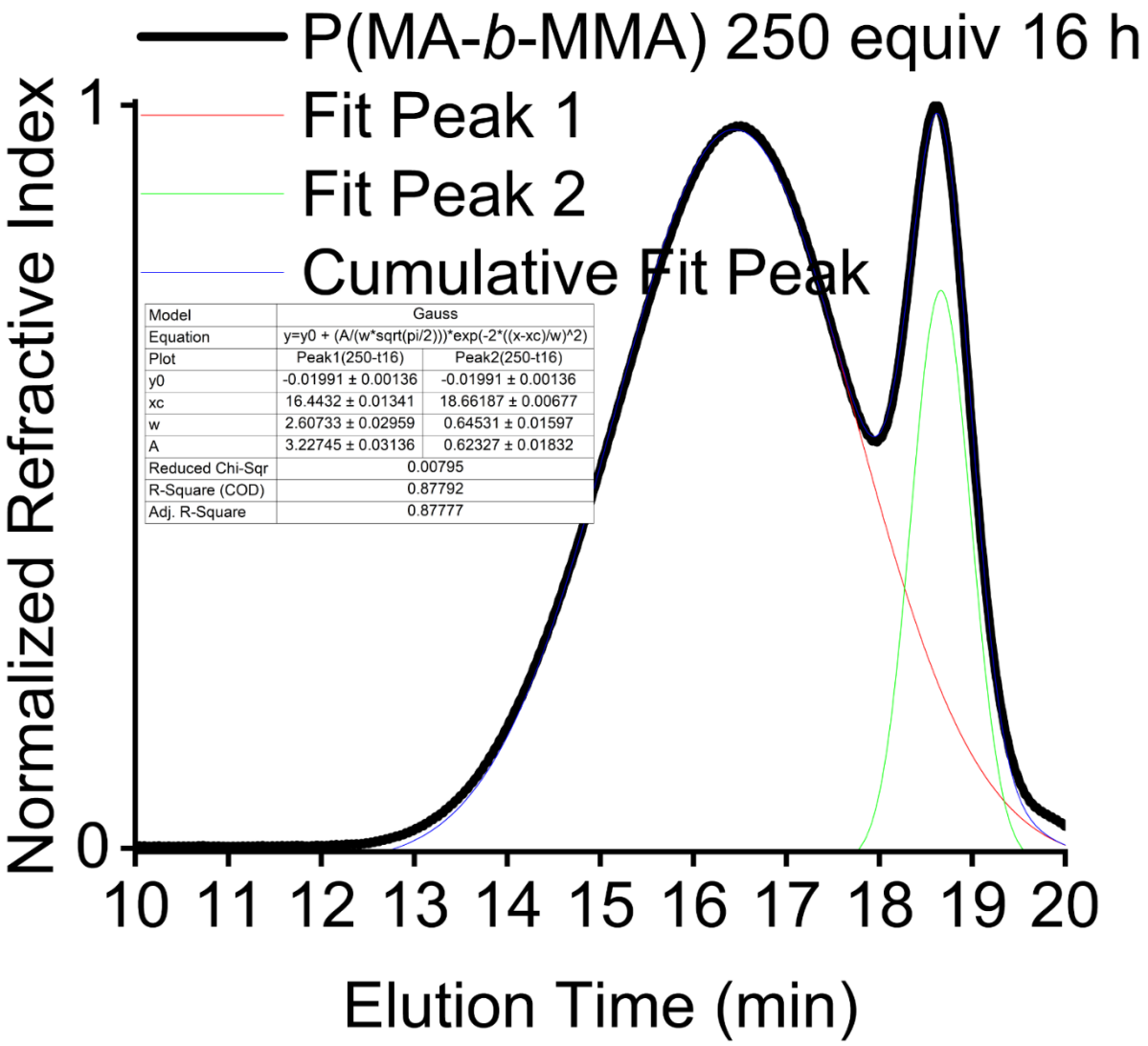

Model	Gauss	
Equation	y=y0 + (A/(w*sqrt(pi/2)))*exp(-2*((x-xc)/w)^2)	
Plot	Peak1(250-t16)	Peak2(250-t16)
y0	-0.01991 ± 0.00136	-0.01991 ± 0.00136
xc	16.4432 ± 0.01341	18.66187 ± 0.00677
w	2.60733 ± 0.02959	0.64531 ± 0.01597
A	3.22745 ± 0.03136	0.62327 ± 0.01832
Reduced Chi-Sqr	0.00795	
R-Square (COD)	0.87792	
Adj. R-Square	0.87777	

Figure C14. Peak deconvolution for P(MA-b-MMA) synthesized from the chain extension of PMA with 250 equivalents of MMA for 16 hours. Approximately 84% of PMA chains were activated based on the fitted Gaussian model.

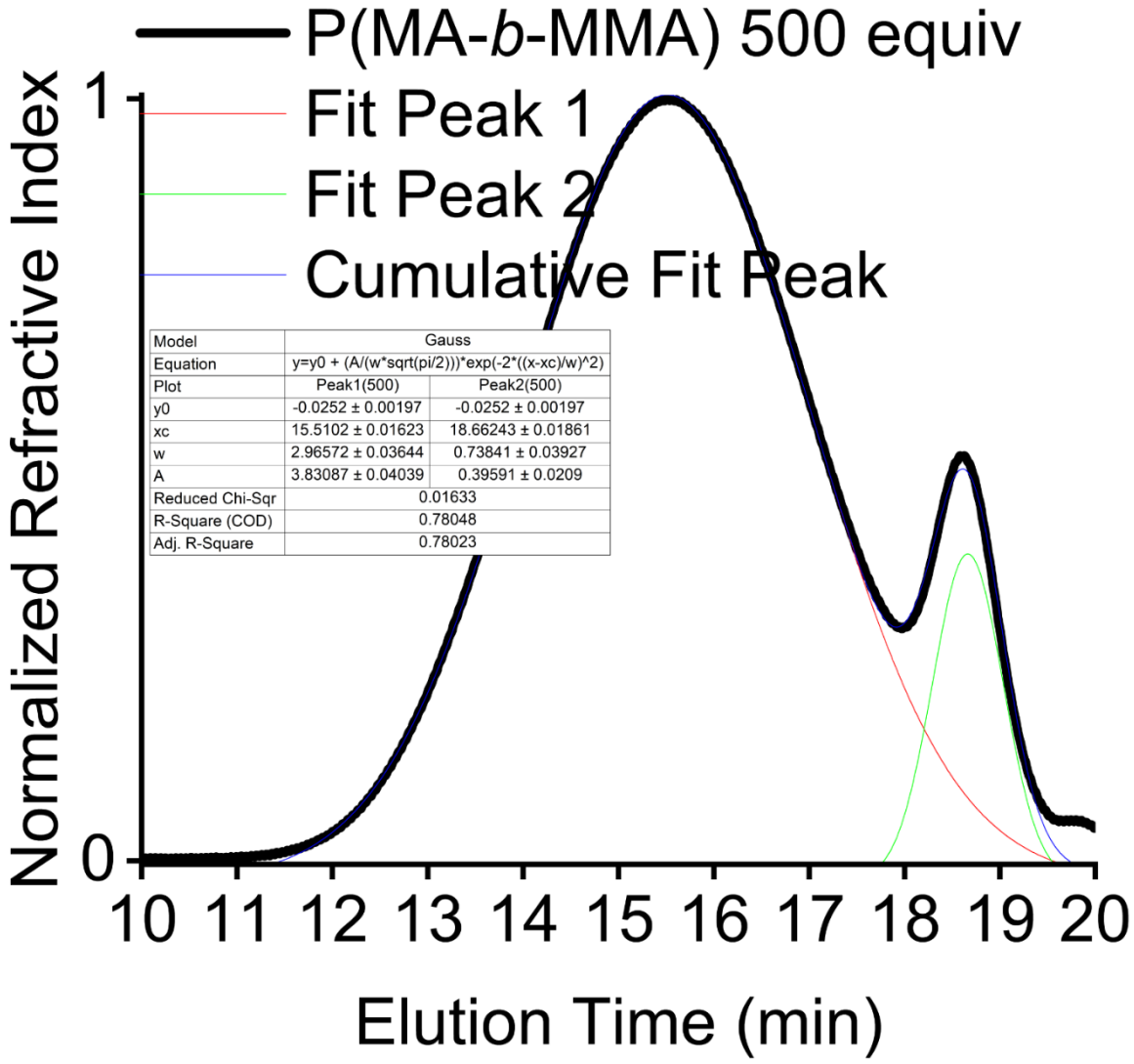

Model	Gauss	
Equation	y=y0 + (A/(w*sqrt(pi/2)))*exp(-2*((x-xc)/w)^2)	
Plot	Peak1(500)	Peak2(500)
y0	-0.0252 ± 0.00197	-0.0252 ± 0.00197
xc	15.5102 ± 0.01623	18.66243 ± 0.01861
w	2.96572 ± 0.03644	0.73841 ± 0.03927
A	3.83087 ± 0.04039	0.39591 ± 0.0209
Reduced Chi-Sqr	0.01633	
R-Square (COD)	0.78048	
Adj. R-Square	0.78023	

Figure C15. Peak deconvolution for P(MA-b-MMA) synthesized from chain extension of PMA with 500 equivalents of MMA. Approximately 91% of PMA chains were activated based on the fitted Gaussian model.

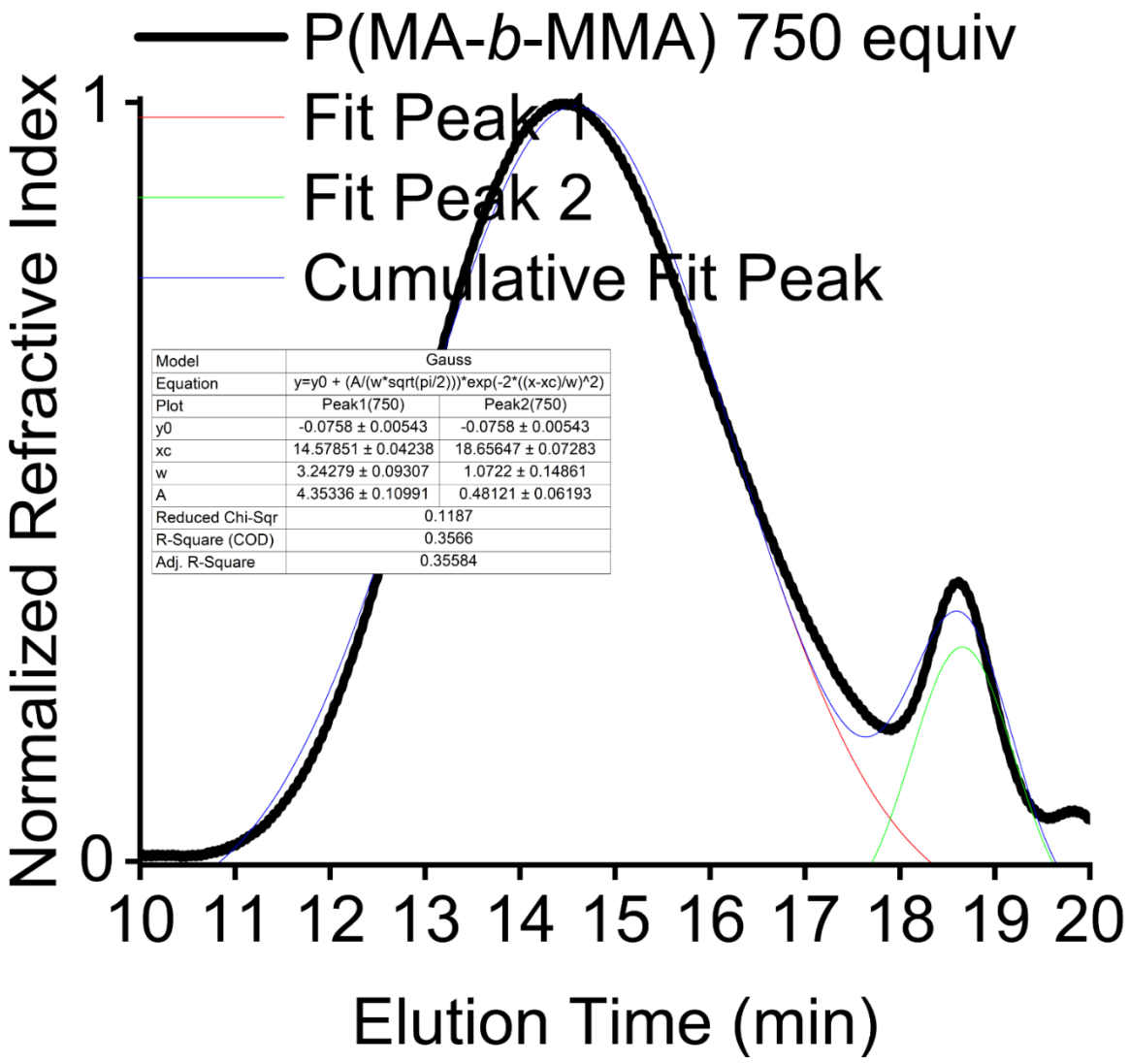

Figure C16. Peak deconvolution for P(MA-b-MMA) synthesized from chain extension of PMA with 750 equivalents of MMA. Approximately 90% of PMA chains were activated based on the fitted Gaussian model.

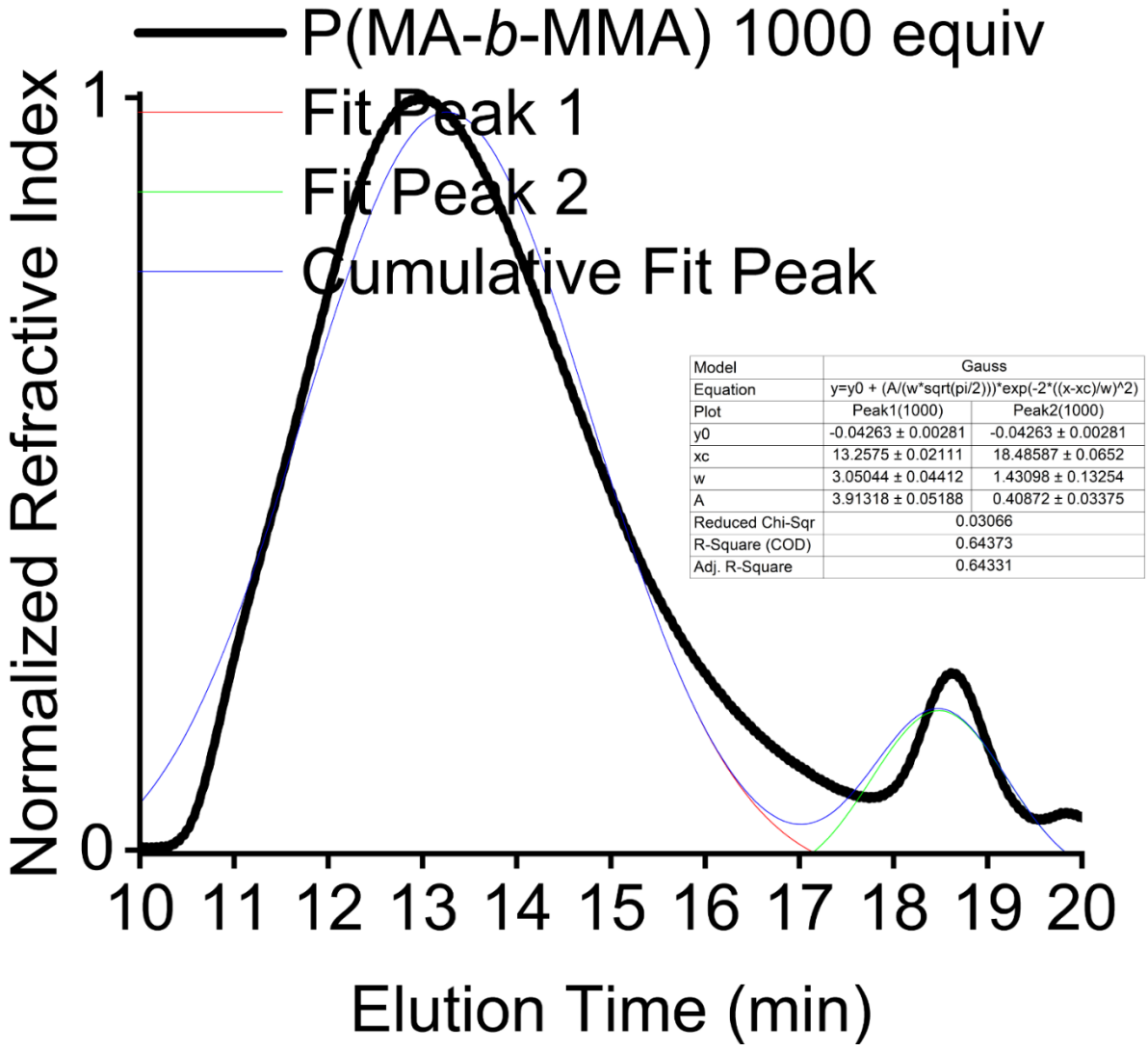

Figure C17. Peak deconvolution for P(MA-b-MMA) synthesized from chain extension of PMA with 1000 equivalents of MMA. Approximately 91% of PMA chains were activated based on the fitted Gaussian model.

Table C27. Number average molecular weights (M_n) and dispersities ($Đ$) for P(MA-b-MMA) synthesized from reverse blocking order chain extensions of PMA with MMA with 0.1 mol% *fac*-Ir(ppy)$_3$ and 5 mM [Polymer] at 60 °C.

Sample	M_n (kg/mol)	$Đ$
250 equiv, 2 h	14.16	6.11
250 equiv, 4 h	16.69	7.48
250 equiv, 8 h	21.21	5.56
250 equiv, 16 h	28.77	3.88
500 equiv	57.83	3.66
750 equiv	111.5	5.13
1000 equiv	257.3	4.23

XYZ Coordinates (Angstrom) of Optimum Geometries in DFT Calculations (with gibbs energies in hartrees)

TCT Radical (-1311.842102)

S	2.25439	-0.89750	0.00001
C	0.78310	-0.07370	-0.00000
S	1.08585	1.57688	-0.00000
S	-0.72797	-0.87797	-0.00001
C	-1.95116	0.48334	0.00000
C	-3.34864	-0.11726	0.00001
H	-1.78294	1.08978	-0.89106
H	-1.78293	1.08978	0.89106

H	-3.52760	-0.72754	-0.88866
H	-4.07507	0.69873	0.00002
H	-3.52759	-0.72755	0.88867

TCT Anion (-1312.026027)

S	-2.24238	-1.00785	0.00000
C	-0.90454	0.04066	0.00000
S	-0.95608	1.72584	0.00000
S	0.64062	-0.83480	0.00000
C	1.96177	0.42120	-0.00000
C	3.31475	-0.27797	0.00000
H	1.84508	1.04972	0.88404
H	1.84509	1.04972	-0.88405
H	3.44759	-0.90414	0.88680
H	4.10812	0.47448	-0.00001
H	3.44759	-0.90415	-0.88679

TEA - Ground State (-292.239227)

N	0.14815	-0.14827	-0.01867
C	1.46731	-0.67513	0.33764
C	2.60853	-0.09262	-0.48527
H	1.44114	-1.75452	0.16646
H	1.67519	-0.52724	1.41402

H	2.40355	-0.19875	-1.55511
H	3.53371	-0.63169	-0.26079
H	2.78890	0.96392	-0.27329
C	0.01609	1.26379	0.33648
C	-1.25091	1.91719	-0.19622
H	0.87466	1.79897	-0.07413
H	0.05779	1.39014	1.43532
H	-1.32372	1.79996	-1.28166
H	-1.23456	2.98712	0.03132
H	-2.15372	1.49805	0.25549
C	-0.93618	-0.96929	0.54051
C	-1.97894	-1.36709	-0.49734
H	-1.42054	-0.44627	1.37805
H	-0.50538	-1.88041	0.96608
H	-2.45812	-0.49234	-0.94352
H	-2.75825	-1.98608	-0.04028
H	-1.51300	-1.94407	-1.30212

TEA - Oxidized (-292.059214)

N	0.00031	-0.01140	-0.62348
C	-0.54904	-1.33174	-0.60465
C	-1.28437	-1.60935	0.71845
H	0.25862	-2.04388	-0.77339

H	-1.26061	-1.40923	-1.42813
H	-0.62115	-1.49436	1.58287
H	-1.66559	-2.62941	0.71146
H	-2.15015	-0.94574	0.82932
C	-0.87734	1.14445	-0.61471
C	-0.78153	1.90789	0.69594
H	-1.89205	0.79751	-0.82051
H	-0.54704	1.78418	-1.44367
H	0.21515	2.30201	0.88136
H	-1.48722	2.74744	0.63673
H	-1.06260	1.26702	1.54207
C	1.43515	0.15741	-0.61886
C	2.06343	-0.25425	0.72137
H	1.64694	1.19702	-0.83397
H	1.82322	-0.48969	-1.41091
H	1.65110	0.31388	1.55115
H	3.13625	-0.08345	0.64165
H	1.91521	-1.31994	0.91308

TEOA - Ground State (-517.889463)

N	0.14973	-0.53669	0.04361
C	1.54369	-0.81607	0.36460
C	2.48792	0.10402	-0.40201

H	1.76634	-1.84860	0.07756
H	1.74871	-0.72372	1.44506
H	2.32419	-0.02638	-1.47929
O	3.84794	-0.12773	-0.06098
H	2.29494	1.15183	-0.15973
C	-0.31991	0.72608	0.61831
C	-0.77319	1.70140	-0.46068
H	0.48653	1.19272	1.19841
H	-1.14794	0.55197	1.31398
H	0.04464	1.86421	-1.17505
O	-1.22132	2.93638	0.08456
H	-1.62193	1.27913	-1.00062
C	-0.73243	-1.67050	0.28892
C	-2.03428	-1.65294	-0.49938
H	-0.96305	-1.78635	1.36448
H	-0.20409	-2.57723	-0.01934
O	-2.98788	-0.68855	-0.06959
H	-2.47357	-2.65808	-0.45343
H	-1.82485	-1.42442	-1.54731
H	-3.21624	-0.88338	0.84332
H	-0.47640	3.35535	0.52401
H	4.07395	-1.02293	-0.32772

TEOA - Oxidized (-517.702707)

N	-0.01577	-0.09519	0.92401
C	1.24878	0.58837	0.89163
C	1.57446	1.11481	-0.53314
H	2.03064	-0.09131	1.23126
H	1.18251	1.44659	1.56585
H	1.61768	0.27680	-1.23447
O	2.77479	1.84260	-0.50612
H	0.78948	1.80023	-0.85532
C	-1.23822	0.65970	0.86198
C	-1.98387	0.47242	-0.48585
H	-1.00651	1.71367	1.01462
H	-1.89143	0.29968	1.66330
H	-1.33868	0.78497	-1.31144
O	-3.18657	1.19901	-0.45624
H	-2.25022	-0.57573	-0.62104
C	-0.06364	-1.53569	1.03889
C	0.68704	-2.25365	-0.08980
H	-1.10763	-1.84717	1.08102
H	0.42478	-1.79611	1.98686
O	0.17302	-1.95406	-1.36850
H	0.63698	-3.32393	0.13281
H	1.73830	-1.96298	-0.09522

H	-0.67581	-2.39385	-1.47450
H	-2.98680	2.13388	-0.56208
H	3.50993	1.22535	-0.44521

TEMED - Ground State (-347.555588)

N	1.78682	0.20379	-0.27501
C	0.43812	0.19746	0.28479
C	-0.57841	-0.50321	-0.62790
H	0.13803	1.24036	0.42207
H	0.43610	-0.27456	1.28464
H	-0.40030	-0.17367	-1.65754
N	-1.98490	-0.26558	-0.31636
H	-0.41833	-1.58561	-0.60094
C	2.34832	-1.13575	-0.36566
C	2.65874	1.06083	0.51246
C	-2.41568	1.10035	-0.55749
H	1.75556	-1.76334	-1.03376
H	2.39945	-1.63311	0.62065
H	3.36159	-1.08051	-0.77176
H	2.25149	2.07463	0.55008
H	3.64982	1.10617	0.05286
H	2.77877	0.69948	1.55029
H	-3.50576	1.15662	-0.48084

H	-2.12944	1.40697	-1.56735
H	-1.99685	1.83084	0.15563
C	-2.36704	-0.72211	1.00900
H	-2.03291	-1.75298	1.15728
H	-3.45684	-0.69907	1.10506
H	-1.94812	-0.10513	1.82199

TEMED - Oxidized (-347.373281)

N	1.82182	0.20064	-0.24440
C	0.50443	0.17316	0.35587
C	-0.56867	-0.16033	-0.71210
H	0.27789	1.16345	0.75721
H	0.43548	-0.55356	1.18153
H	-0.49736	0.55115	-1.53362
N	-1.87891	-0.06351	-0.12992
H	-0.44014	-1.18157	-1.07878
C	2.35589	-1.13512	-0.46853
C	2.74289	0.99920	0.55327
C	-2.66510	1.11571	-0.36189
H	1.69456	-1.71562	-1.11541
H	2.49091	-1.68972	0.47636
H	3.32593	-1.06005	-0.96509
H	2.35791	2.01573	0.66304

H	3.71067	1.05084	0.04874
H	2.90216	0.57514	1.55978
H	-3.57344	1.08892	0.23478
H	-2.90694	1.16711	-1.42948
H	-2.06104	1.99547	-0.11427
C	-2.34898	-1.06880	0.77987
H	-1.70245	-1.94238	0.74614
H	-3.37932	-1.32738	0.51957
H	-2.35799	-0.64034	1.79080

PMDTA - Ground State (-520.733723)

N	0.03956	0.69574	-0.19024
C	1.28926	0.06866	0.23778
C	2.49617	0.53476	-0.58773
H	1.17449	-1.01087	0.11069
H	1.47163	0.25476	1.31172
H	2.24173	0.43769	-1.64930
N	3.74414	-0.18533	-0.35486
H	2.69626	1.59338	-0.39792
C	0.04439	2.12622	0.09025
C	-1.11324	0.04126	0.42691
C	3.69520	-1.58672	-0.73270
H	0.80213	2.63786	-0.50582

H	0.24401	2.33256	1.15736
H	-0.91923	2.56984	-0.16462
H	-0.89351	-1.02658	0.49188
C	-2.38864	0.24543	-0.38778
H	-1.27639	0.40167	1.45839
H	4.70847	-1.99992	-0.73467
H	3.28550	-1.68537	-1.74187
H	3.08601	-2.20754	-0.05397
C	4.27815	-0.00879	0.98468
H	4.31571	1.05603	1.23144
H	5.29761	-0.40441	1.02701
H	3.68987	-0.52218	1.76396
H	-2.27003	-0.26093	-1.36432
H	-2.52539	1.31003	-0.59457
N	-3.58846	-0.21836	0.30057
C	-3.58973	-1.66123	0.49145
C	-4.77880	0.19203	-0.42746
H	-2.76890	-1.97095	1.14125
H	-3.49928	-2.20677	-0.46587
H	-4.52414	-1.96541	0.96972
H	-4.79620	1.27972	-0.53536
H	-5.67405	-0.11201	0.12151
H	-4.82966	-0.25461	-1.43731

PMDTA - Oxidized (-520.550778)

N	0.02146	0.65816	-0.18353
C	1.26363	0.18621	0.39197
C	2.35068	0.09625	-0.71410
H	1.12306	-0.81751	0.79742
H	1.62299	0.83384	1.20589
H	2.02913	-0.60927	-1.47873
N	3.59076	-0.35856	-0.15130
H	2.52398	1.08158	-1.15357
C	-0.01645	2.11297	-0.26149
C	-1.14292	0.10513	0.50569
C	3.97261	-1.73531	-0.30110
H	0.89986	2.49307	-0.71701
H	-0.12093	2.57469	0.73531
H	-0.84818	2.44380	-0.88543
H	-0.98014	-0.96918	0.60957
C	-2.44271	0.35188	-0.25612
H	-1.24209	0.52457	1.52248
H	4.84285	-1.95666	0.31209
H	4.19501	-1.91673	-1.35936
H	3.12476	-2.36996	-0.02416
C	4.39331	0.52376	0.64780

H	4.03566	1.54644	0.55475
H	5.43603	0.43918	0.32825
H	4.33577	0.19351	1.69299
H	-2.30688	0.05416	-1.31231
H	-2.67088	1.42030	-0.24938
N	-3.57579	-0.33923	0.35025
C	-3.55630	-1.77027	0.08340
C	-4.83292	0.23310	-0.10737
H	-2.65021	-2.23234	0.47939
H	-3.61148	-1.98972	-0.99839
H	-4.41150	-2.24513	0.57089
H	-4.87522	1.29663	0.14070
H	-5.66962	-0.26736	0.38736
H	-4.97050	0.12724	-1.19881

HMTETA - Ground State (-693.910713)

N	1.86179	0.62457	-0.41895
C	3.07816	0.20726	0.27634
C	4.35696	0.55508	-0.50051
H	3.02495	-0.87754	0.40267
H	3.12134	0.65009	1.28807
H	4.18905	0.32632	-1.55883
N	5.56700	-0.14234	-0.07497

H	4.56011	1.62781	-0.42768
C	1.78154	2.07568	-0.52224
C	0.68455	0.07057	0.24437
C	5.54849	-1.56941	-0.34448
H	0.89413	-0.98109	0.45370
C	-0.58300	0.17152	-0.60238
H	0.50367	0.56441	1.21679
H	6.54832	-1.98303	-0.18145
H	5.27396	-1.74584	-1.38813
H	4.84963	-2.13448	0.29555
C	5.94104	0.13880	1.30061
H	5.96239	1.21978	1.46614
H	6.94258	-0.25683	1.49469
H	5.25599	-0.30842	2.04086
H	-0.37738	-0.22152	-1.61390
H	-0.86208	1.22092	-0.71737
N	-1.71220	-0.52052	0.01727
C	-1.62475	-1.96126	-0.18478
C	-2.97916	0.01172	-0.47811
H	-0.64517	-2.33121	0.12165
H	-1.77977	-2.23720	-1.24345
H	-2.36819	-2.48461	0.41928
H	-2.94221	1.09771	-0.36480

C	-4.19192	-0.53193	0.27312
H	-3.10831	-0.20026	-1.55573
H	2.64034	2.46958	-1.06783
H	1.75175	2.55908	0.47155
H	0.88735	2.37260	-1.07247
H	-4.01023	-0.46065	1.36153
H	-4.32525	-1.59042	0.03836
N	-5.42314	0.15620	-0.10418
C	-5.52836	1.47165	0.50959
C	-6.58992	-0.64461	0.23296
H	-6.54349	-1.60965	-0.27791
H	-7.49846	-0.12955	-0.09058
H	-6.67371	-0.83179	1.31903
H	-4.68276	2.10309	0.23068
H	-5.56364	1.41107	1.61266
H	-6.44074	1.96568	0.16573

HMTETA - Oxidized (-693.735438)

N	1.47275	1.45648	-0.23601
C	2.61714	0.75409	-0.60489
C	3.45695	0.25545	0.73929
H	3.30589	1.38746	-1.16423
H	2.38510	-0.15579	-1.15649

H	3.78062	1.16950	1.23741
N	4.53598	-0.53035	0.36013
H	2.74425	-0.31164	1.33929
C	1.64441	2.81107	0.24898
C	0.34963	0.73644	0.34469
C	4.29609	-1.90079	-0.03300
H	0.55596	0.52385	1.40547
C	0.01845	-0.56836	-0.37339
H	-0.50641	1.41448	0.32096
H	5.20709	-2.48337	0.11473
H	4.02031	-1.95501	-1.09565
H	3.48854	-2.32106	0.56649
C	5.70891	0.10769	-0.19401
H	5.86402	1.07424	0.28533
H	5.58885	0.25774	-1.27613
H	6.58001	-0.52900	-0.02960
H	0.79615	-1.30649	-0.16175
H	0.01142	-0.40683	-1.46483
N	-1.25117	-1.10486	0.10251
C	-1.30784	-2.54913	-0.07778
C	-2.39745	-0.44253	-0.52121
H	-0.50151	-3.02666	0.48427
H	-1.21429	-2.84141	-1.13823

H	-2.25435	-2.94280	0.29803
H	-2.12215	0.58959	-0.74545
C	-3.61860	-0.45350	0.39379
H	-2.65095	-0.92036	-1.48264
H	2.43680	3.30714	-0.31251
H	1.90670	2.81741	1.31687
H	0.71027	3.36170	0.12204
H	-3.37405	0.10573	1.31664
H	-3.83629	-1.48305	0.69119
N	-4.81679	0.08291	-0.24145
C	-4.70456	1.51037	-0.50262
C	-5.98803	-0.18644	0.57819
H	-6.10147	-1.26306	0.72917
H	-6.88555	0.18601	0.07752
H	-5.92546	0.29592	1.57079
H	-3.89975	1.71720	-1.21073
H	-4.51033	2.08687	0.42056
H	-5.63537	1.87634	-0.94298

Me6Tren - Ground State (-693.911212)

N	0.08985	0.06730	-0.11512
C	-0.30877	-1.28221	0.28573
C	0.14476	-2.31921	-0.74986

H	-1.39792	-1.31307	0.36455
H	0.08685	-1.52441	1.28576
H	-0.38396	-2.11184	-1.68723
N	-0.07113	-3.72030	-0.40521
H	1.21300	-2.18902	-0.95211
C	1.47874	0.35426	0.24388
C	-0.82336	1.08015	0.41214
C	-1.46947	-4.04974	-0.18894
H	2.04718	-0.57796	0.20785
H	1.54573	0.72330	1.28052
C	2.10311	1.35827	-0.73420
H	-1.09469	0.84948	1.45481
C	-2.06489	1.22295	-0.46391
H	-0.31289	2.04637	0.43088
H	-1.58573	-5.13595	-0.12688
H	-2.06894	-3.69029	-1.03026
H	-1.88482	-3.61714	0.73724
C	0.76531	-4.18398	0.68863
H	1.81223	-3.94334	0.48356
H	0.67749	-5.27093	0.77926
H	0.49752	-3.74648	1.66511
H	-2.50718	0.23167	-0.67117
H	-1.74595	1.63431	-1.42584

N	-3.06183	2.12046	0.11241
C	-3.80754	1.47978	1.18618
C	-3.97686	2.60227	-0.91051
H	-3.13764	1.14590	1.98070
H	-4.37780	0.60340	0.82722
H	-4.51447	2.19193	1.61998
H	-3.42467	3.13938	-1.68603
H	-4.70086	3.29090	-0.46649
H	-4.53850	1.78141	-1.39286
H	2.18196	0.87203	-1.71321
N	3.41745	1.88116	-0.37734
H	1.42981	2.21286	-0.85670
C	4.43199	0.84897	-0.25059
C	3.39808	2.75741	0.78158
H	4.42582	0.21094	-1.13909
H	4.29391	0.20559	0.63514
H	5.41932	1.31375	-0.17043
H	2.63102	3.52614	0.65276
H	4.36728	3.25622	0.87851
H	3.19987	2.23086	1.73045

Me6Tren - Oxidized (-693.735352)

N	-0.20599	-0.04872	1.04798

C	0.27781	1.29278	0.99795
C	0.11978	1.91662	-0.44391
H	1.32676	1.29769	1.29290
H	-0.30722	1.89853	1.69490
H	0.51449	1.20872	-1.17486
N	0.79205	3.17479	-0.59728
H	-0.94872	2.05059	-0.63101
C	-1.60088	-0.31322	0.94742
C	0.73227	-1.15102	1.09094
C	2.24160	3.09124	-0.61999
H	-2.14879	0.60632	1.15192
H	-1.86478	-1.08007	1.68083
C	-1.98165	-0.86408	-0.48658
H	1.34839	-1.00812	1.98389
C	1.61146	-1.21114	-0.17093
H	0.17078	-2.07936	1.19248
H	2.65202	4.04141	-0.97184
H	2.55532	2.30458	-1.31014
H	2.68121	2.88407	0.36945
C	0.29831	4.23177	0.26590
H	-0.79123	4.28596	0.19847
H	0.71319	5.18915	-0.05949
H	0.57528	4.08647	1.32346

H	2.20148	-0.28342	-0.26156
H	0.95408	-1.27146	-1.04172
N	2.46356	-2.38738	-0.15269
C	3.56050	-2.25760	0.79674
C	2.97785	-2.66608	-1.48635
H	3.18554	-2.12885	1.81403
H	4.21538	-1.40125	0.55708
H	4.16479	-3.16756	0.77950
H	2.15056	-2.81687	-2.18411
H	3.57808	-3.57904	-1.46297
H	3.61219	-1.84815	-1.87083
H	-1.62864	-0.15241	-1.23416
N	-3.38979	-1.06727	-0.65863
H	-1.45763	-1.81224	-0.62995
C	-4.18324	0.14749	-0.70682
C	-3.96803	-2.08861	0.19399
H	-3.71920	0.86567	-1.38702
H	-4.30142	0.62564	0.27935
H	-5.18204	-0.08789	-1.08361
H	-3.35232	-2.99084	0.16253
H	-4.96862	-2.33880	-0.16805
H	-4.06246	-1.76730	1.24469

Appendix D: Chain Extension of PET-RAFT Organogels Characterization

Table D1. Kinetic data for the parent gel synthesis using PET-RAFT polymerization.

Time (h)	Conversion (%)	$Ln[M]_0/[M]$	Standard error
0	0	0	0
1	0	0	0
2	4.67	0.0479	0.00923
3	16.0	0.175	0.0183
4	21.5	0.243	0.0511
8	54.0	0.777	0.0251
20	81.7	1.70	0.0476

Table D2. Swelling ratios of the parent and daughter gels in DMAc performed in triplicate.

Network	Average Dry Weight (mg)	Average Swelled Weight (mg)	Swelling Ratio (%)	Standard error (%)
Parent	98.0	1430	1383	63.64
D-MA	63.3	820	1189	35.61
D-MAX	50.7	729	1329	52.88
D-DMA	48.0	808	1590	38.22
D-DMAX	54.0	719	1235	24.30

Table D3. Swelling ratios of the parent and daughter gels in water performed in triplicate.

Network	Average Dry Weight (mg)	Average Swelled Weight (mg)	Swelling Ratio (%)	Standard error (%)
Parent	177	192	8.185	0.4846
D-MA	42.7	58.3	36.70	2.107
D-MAX	44.0	66.3	50.25	3.210
D-DMA	45.7	283	518.8	16.69
D-DMAX	40.7	189	349.4	32.56

Figure D1. Additional images of the P(MA-*s*-DSDA) parent organogel network after synthesis.

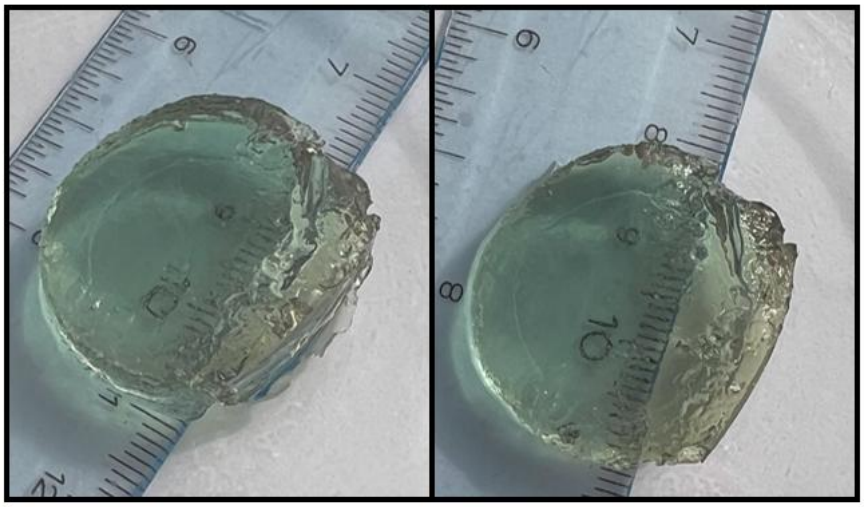

Figure D2. Additional images of the daughter gel D-MA swollen in DMAc.

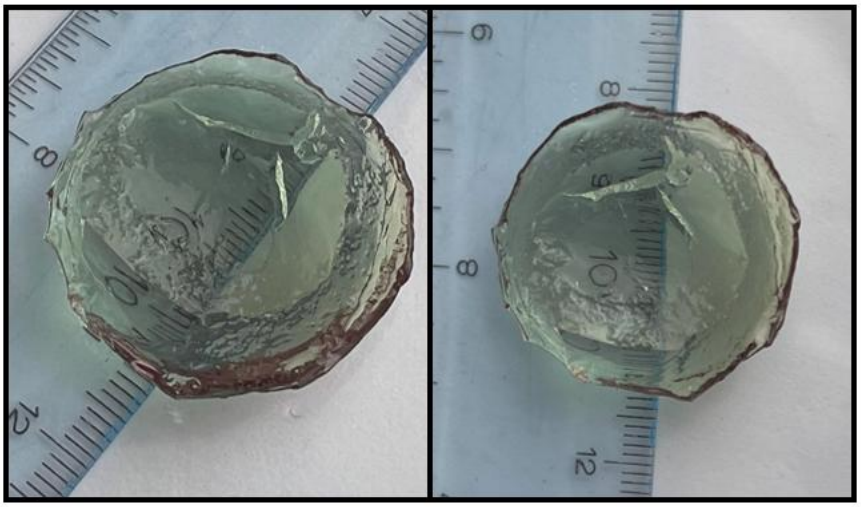

Figure D3. Additional images of the daughter gel D-MAX swollen in DMAc.

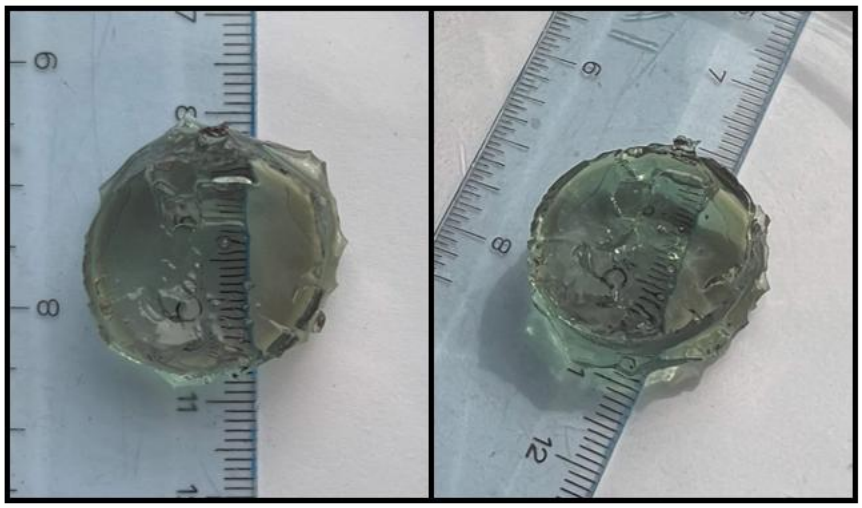

D-DMAX swollen in DMAc

Figure D4. Additional images of the daughter gel D-DMAX swollen in DMAc.

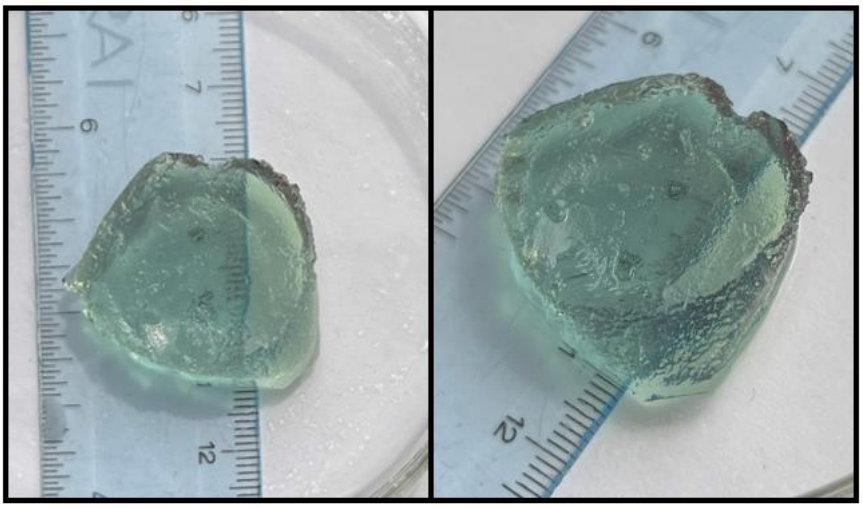

D-DMA swollen in DMAc

Figure D5. Additional images of the daughter gel D-DMA swollen in DMAc.

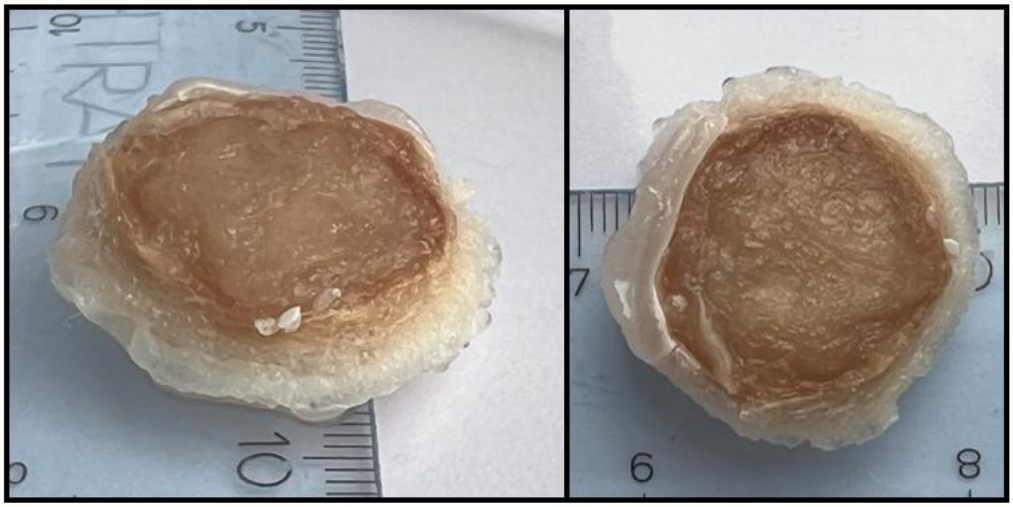

D-MA swollen in water

Figure D6. Additional images of the daughter gel D-MA swollen in water.

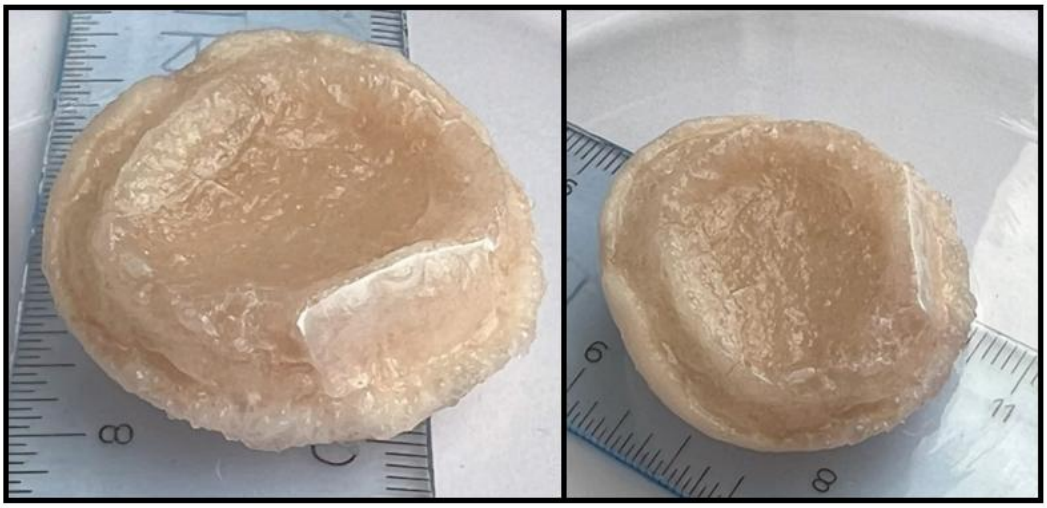

D-MAX swollen in water

Figure D7. Additional images of the daughter gel D-MAX swollen in water.

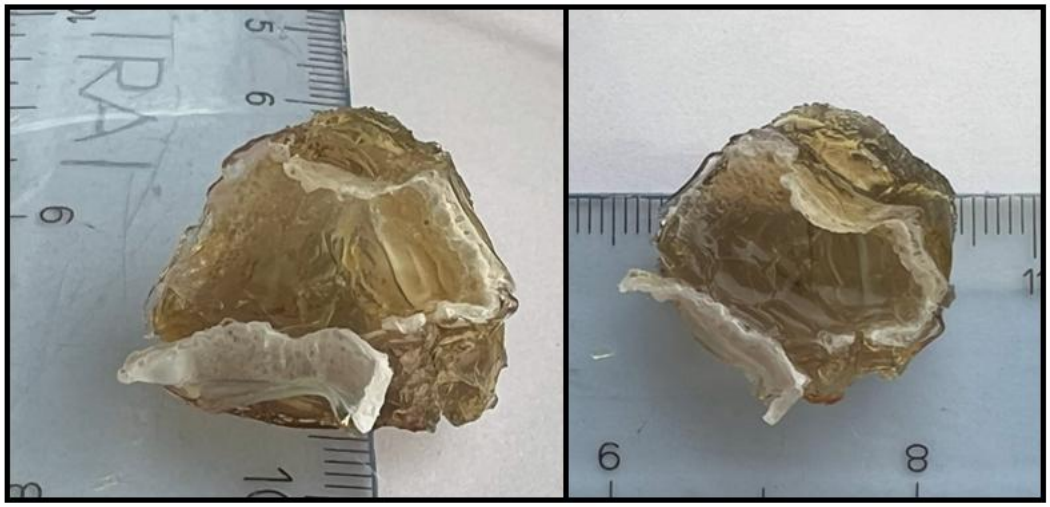

Figure D8. Additional images of the daughter gel D-DMA swollen in water.

Figure D9. Additional images of the daughter gel D-DMAX swollen in water.

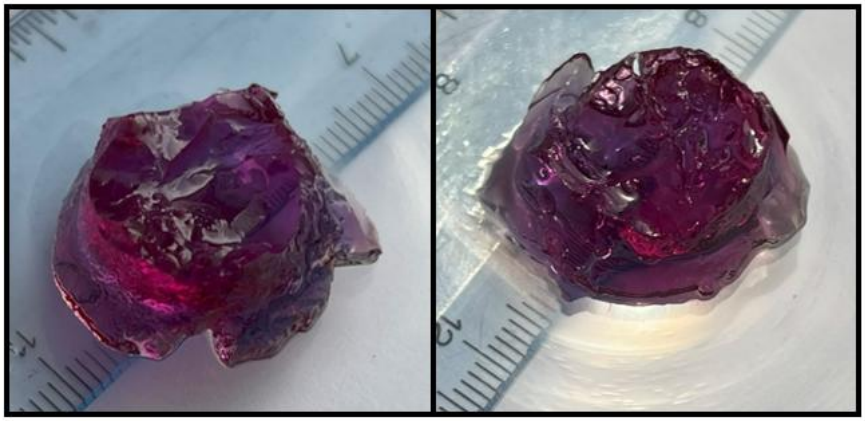

Figure D10. D-MA and D-MAX after irradiation showing asymmetric expansion of the network on the bottom.

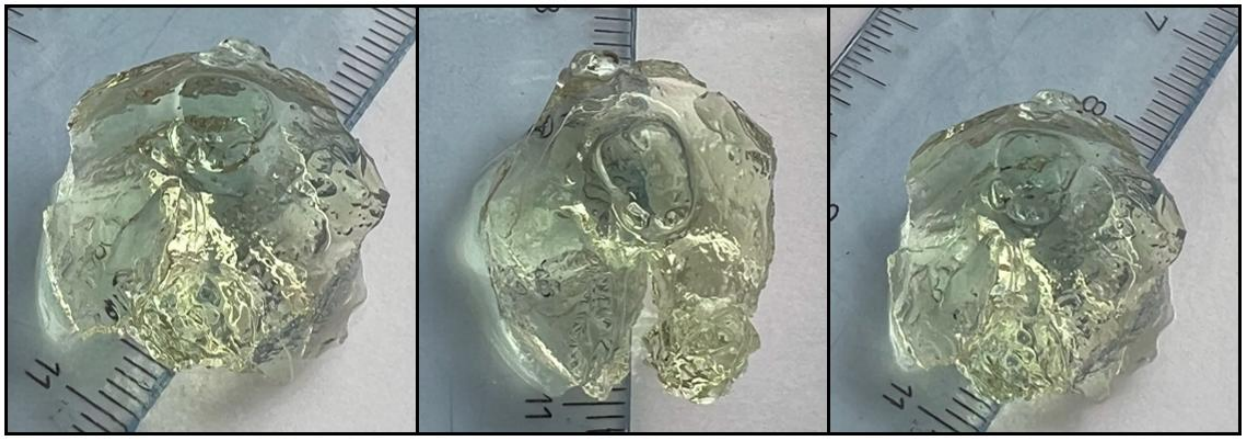

Figure D11. D-MA daughter gel synthesized with a checkerboard pattern on the bottom of the petri dish swollen in DMAc.

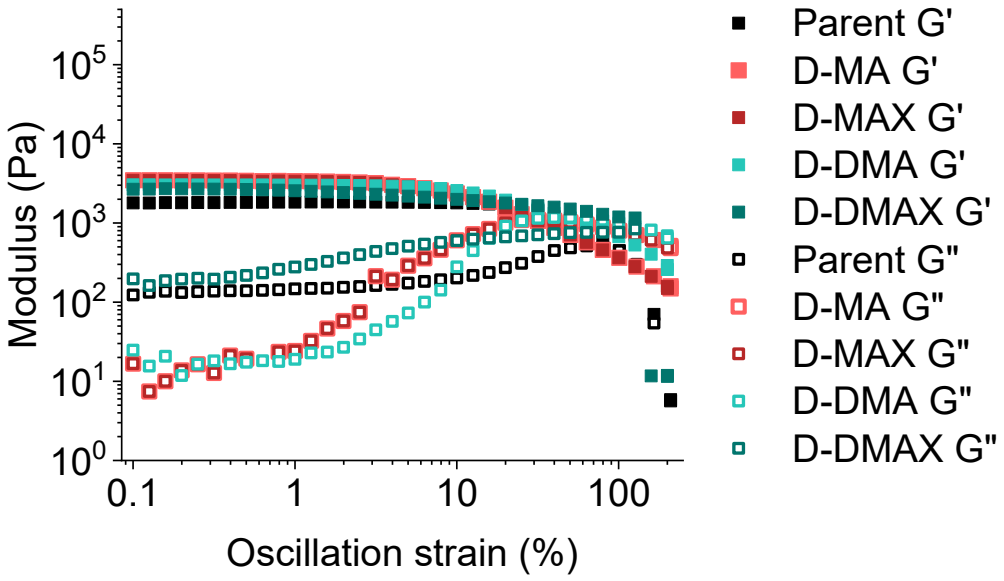

Figure D12. Full strain sweeps conducted on the parent and daughter gels with storage (filled squares, *G′*) and loss moduli (open squares, *G″*).

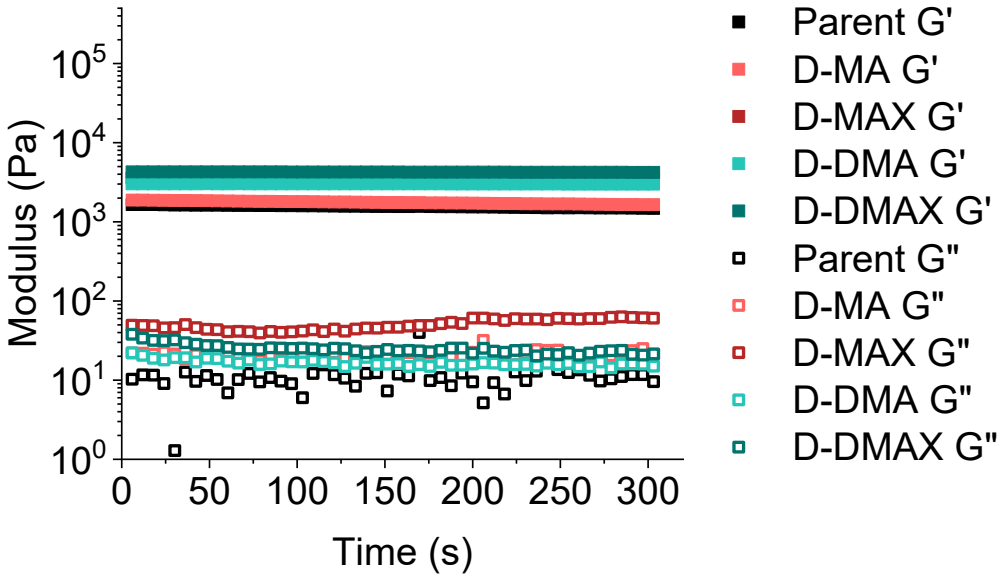

Figure D13. Time sweeps conducted on the parent and daughter gels with storage (filled squares, *G′*) and loss moduli (open squares, *G″*).

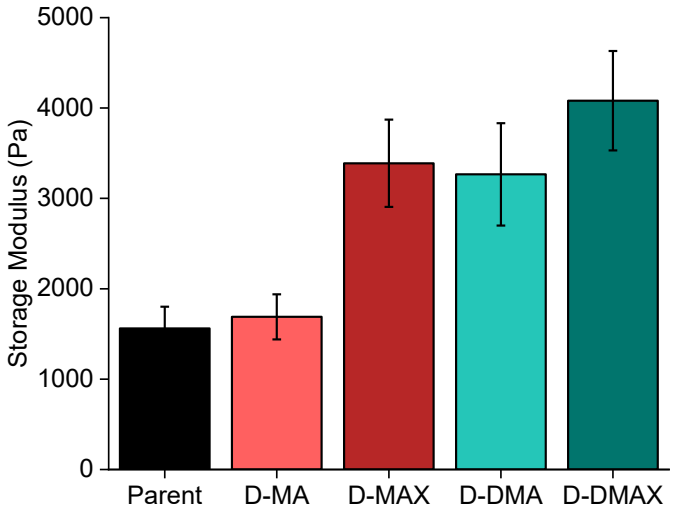

Figure D14. Parent and daughter gel average (n=3) storage moduli (*G′*) from time sweeps.

References:

(1) Hedstrand, D. M.; Kruizinga, W. H.; Kellogg, R. M. Light Induced and Dye Accelerated Reductions of Phenacyl Onium Salts by 1,4-Dihydropyridines. *Tetrahedron Lett.* **1978**, *19*, 1255–1258.

(2) Shaw, M. H.; Twilton, J.; MacMillan, D. W. C. Photoredox Catalysis in Organic Chemistry. *J. Org. Chem.* **2016**, *81*, 6898–6926.

(3) Romero, N. A.; Nicewicz, D. A. Organic Photoredox Catalysis. *Chem. Rev.* **2016**, *116*, 10075–10166.

(4) Marzo, L.; Pagire, S. K.; Reiser, O.; König, B. Visible-Light Photocatalysis: Does It Make a Difference in Organic Synthesis? *Angew. Chem., Int. Ed.* **2018**, *57*, 10034–10072.

(5) Wang, L.; Wang, T.; Cheng, G.-J.; Li, X.; Wei, J.-J.; Guo, B.; Zheng, C.; Chen, G.; Ran, C.; Zheng, C. Direct C–H Arylation of Aldehydes by Merging Photocatalyzed Hydrogen Atom Transfer with Palladium Catalysis. *ACS Catal.* **2020**, *10*, 7543–7551.

(6) Fan, X.; Rong, J.; Wu, H.; Zhou, Q.; Deng, H.; Tan, J. Da; Xue, C.; Wu, L.; Tao, H.; Wu, J. Eosin Y as a Direct Hydrogen-Atom Transfer Photocatalyst for the Functionalization of C−H Bonds. *Angew. Chem., Int. Ed.* **2018**, *57*, 8514–8518.

(7) Capaldo, L.; Ravelli, D.; Fagnoni, M. Direct Photocatalyzed Hydrogen Atom Transfer (HAT) for Aliphatic C–H Bonds Elaboration. *Chem. Rev.* **2022**, *122*, 1875–1924.

(8) Cavedon, C.; Seeberger, P. H.; Pieber, B. Photochemical Strategies for Carbon–Heteroatom Bond Formation. *Eur. J. Org. Chem.* **2020**, *2020*, 1379–1392.

(9) Tasker, S. Z.; Jamison, T. F. Highly Regioselective Indoline Synthesis under Nickel/Photoredox Dual Catalysis. *J. Am. Chem. Soc.* **2015**, *137*, 9531–9534.

(10) Terrett, J. A.; Cuthbertson, J. D.; Shurtleff, V. W.; MacMillan, D. W. C. Switching on Elusive Organometallic Mechanisms with Photoredox Catalysis. *Nature* **2015**, *524*, 330–334.

(11) Cannalire, R.; Pelliccia, S.; Sancineto, L.; Novellino, E.; Tron, G. C.; Giustiniano, M. Visible Light Photocatalysis in the Late-Stage Functionalization of Pharmaceutically Relevant Compounds. *Chem. Soc. Rev.* **2021**, *50*, 766–897.

(12) Douglas, J. J.; Sevrin, M. J.; Stephenson, C. R. J. Visible Light Photocatalysis: Applications and New Disconnections in the Synthesis of Pharmaceutical Agents. *Org. Process Res. Dev.* **2016**, *20*, 1134–1147.

(13) Zuo, Z.; Ahneman, D. T.; Chu, L.; Terrett, J. A.; Doyle, A. G.; MacMillan, D. W. C. Merging Photoredox with Nickel Catalysis: Coupling of α-Carboxyl Sp 3 -Carbons with Aryl Halides. *Science* **2014**, *345*, 437–440.

(14) Beatty, J. W.; Stephenson, C. R. J. Amine Functionalization via Oxidative Photoredox Catalysis: Methodology Development and Complex Molecule Synthesis. *Acc. Chem. Res.* **2015**, *48*, 1474–1484.

(15) Morcillo, S. P.; Dauncey, E. M.; Kim, J. H.; Douglas, J. J.; Sheikh, N. S.; Leonori, D. Photoinduced Remote Functionalization of Amides and Amines Using Electrophilic Nitrogen Radicals. *Angew. Chem., Int. Ed.* **2018**, *57*, 12945–12949.

(16) Leng, L.; Fu, Y.; Liu, P.; Ready, J. M. Regioselective, Photocatalytic α-Functionalization of Amines. *J. Am. Chem. Soc.* **2020**, *142*, 11972–11977.

(17) Brimioulle, R.; Lenhart, D.; Maturi, M. M.; Bach, T. Enantioselective Catalysis of Photochemical Reactions. *Angew. Chem., Int. Ed.* **2015**, *54*, 3872–3890.

(18) Genzink, M. J.; Kidd, J. B.; Swords, W. B.; Yoon, T. P. Chiral Photocatalyst Structures in Asymmetric Photochemical Synthesis. *Chem. Rev.* **2022**, *122*, 1654–1716.

(19) Han, B.; Li, Y.; Yu, Y.; Gong, L. Photocatalytic Enantioselective α-Aminoalkylation of Acyclic Imine Derivatives by a Chiral Copper Catalyst. *Nat. Commun.* **2019**, *10*, 3804.

(20) Li, P.; Terrett, J. A.; Zbieg, J. R. Visible-Light Photocatalysis as an Enabling Technology for Drug Discovery: A Paradigm Shift for Chemical Reactivity. *ACS Med. Chem. Lett.* **2020**, *11*, 2120–2130.

(21) Friedmann, D.; Hakki, A.; Kim, H.; Choi, W.; Bahnemann, D. Heterogeneous Photocatalytic Organic Synthesis: State-of-the-Art and Future Perspectives. *Green Chem.* **2016**, *18*, 5391–5411.

(22) Candish, L.; Collins, K. D.; Cook, G. C.; Douglas, J. J.; Gómez-Suárez, A.; Jolit, A.; Keess, S. Photocatalysis in the Life Science Industry. *Chem. Rev.* **2022**, *122*, 2907–2980.

(23) Corrigan, N.; Shanmugam, S.; Xu, J.; Boyer, C. Photocatalysis in Organic and Polymer Synthesis. *Chem. Soc. Rev.* **2016**, *45*, 6165-6212.

(24) Phommalysack-Lovan, J.; Chu, Y.; Boyer, C.; Xu, J. PET-RAFT Polymerisation: Towards Green and Precision Polymer Manufacturing. *Chem. Commun.* **2018**, *54*, 6591-6606.

(25) Corbin, D. A.; Miyake, G. M. Photoinduced Organocatalyzed Atom Transfer Radical Polymerization (O-ATRP): Precision Polymer Synthesis Using Organic Photoredox Catalysis. *Chem. Rev.* **2022**, *122*, 1830–1874.

(26) Peterson, G. I.; Schwartz, J. J.; Zhang, D.; Weiss, B. M.; Ganter, M. A.; Storti, D. W.; Boydston, A. J. Production of Materials with Spatially-Controlled Cross-Link Density via Vat Photopolymerization. *ACS Appl. Mater. Interfaces* **2016**, *8*, 29037–29043.

(27) Pagac, M.; Hajnys, J.; Ma, Q.-P.; Jancar, L.; Jansa, J.; Stefek, P.; Mesicek, J. A Review of Vat Photopolymerization Technology: Materials, Applications, Challenges, and Future Trends of 3D Printing. *Polymers* **2021**, *13*, 598.

(28) Bagheri, A.; Jin, J. Photopolymerization in 3D Printing. *ACS Appl. Polym. Mater.* **2019**, *1*, 593–611.

(29) Yan, W.; Dadashi-Silab, S.; Matyjaszewski, K.; Spencer, N. D.; Benetti, E. M. Surface-Initiated Photoinduced ATRP: Mechanism, Oxygen Tolerance, and Temporal Control during the Synthesis of Polymer Brushes. *Macromolecules* **2020**, *53*, 2801–2810.

(30) Krause, J. E.; Brault, N. D.; Li, Y.; Xue, H.; Zhou, Y.; Jiang, S. Photoiniferter-Mediated Polymerization of Zwitterionic Carboxybetaine Monomers for Low-Fouling and Functionalizable Surface Coatings. *Macromolecules* **2011**, *44*, 9213–9220.

(31) Du, W.; Jin, Y.; Shi, L.; Shen, Y.; Lai, S.; Zhou, Y. NIR-Light-Induced Thermoset Shape Memory Polyurethane Composites with Self-Healing and Recyclable Functionalities. *Compos. Part B Eng.* **2020**, *195*, 108092.

(32) Habault, D.; Zhang, H.; Zhao, Y. Light-Triggered Self-Healing and Shape-Memory Polymers. *Chem. Soc. Rev.* **2013**, *42*, 7244-7256.

(33) Shanmugam, S.; Cuthbert, J.; Kowalewski, T.; Boyer, C.; Matyjaszewski, K. Catalyst-Free Selective Photoactivation of RAFT Polymerization: A Facile Route for Preparation of Comblike and Bottlebrush Polymers. *Macromolecules* **2018**, *51*, 7776–7784.

(34) Corrigan, N.; Yeow, J.; Judzewitsch, P.; Xu, J.; Boyer, C. Seeing the Light: Advancing Materials Chemistry through Photopolymerization. *Angew. Chem., Int. Ed.* **2019**, *58*, 5170–5189.

(35) Wong, A. J.; Eades, C. B.; Bowman, J. I.; Davidson, C. L. G.; Sumerlin, B. S. Divergent Photoiniferter Polymerization-Induced Self-Assembly. *Polym. Chem.* **2025**, *16*, 620–625.

(36) Xu, J.; Shanmugam, S.; Fu, C.; Aguey-Zinsou, K. F.; Boyer, C. Selective Photoactivation: From a Single Unit Monomer Insertion Reaction to Controlled Polymer Architectures. *J. Am. Chem. Soc.* **2016**, *138*, 3094–3106.

(37) Xu, J.; Fu, C.; Shanmugam, S.; Hawker, C. J.; Moad, G.; Boyer, C. Synthesis of Discrete Oligomers by Sequential PET-RAFT Single-Unit Monomer Insertion. *Angew. Chem., Int.l Ed.* **2017**, *56*, 8376–8383.

(38) Matyjaszewski, K. Current Status and Outlook for ATRP. *Eur. Polym. J.* **2024**, *211*, 113001.

(39) Fors, B. P.; Hawker, C. J. Control of a Living Radical Polymerization of Methacrylates by Light. *Angew. Chem., Int. Ed.* **2012**, *51*, 8850–8853.

(40) Perrier, S. 50th Anniversary Perspective: RAFT Polymerization—A User Guide. *Macromolecules* **2017**, *50*, 7433–7447.

(41) Xu, J.; Jung, K.; Atme, A.; Shanmugam, S.; Boyer, C. A Robust and Versatile Photoinduced Living Polymerization of Conjugated and Unconjugated Monomers and Its Oxygen Tolerance. *J. Am. Chem. Soc.* **2014**, *136*, 5508–5519.

(42) Hughes, R. W.; Lott, M. E.; Olson S, R. A.; Sumerlin, B. S. Photoiniferter Polymerization: Illuminating the History, Ascendency, and Renaissance. *Prog. Polym. Sci.* **2024**, *156*, 101871.

(43) Beres, M. A.; Boyer, C.; Hartlieb, M.; Konkolewicz, D.; Qiao, G. G.; Sumerlin, B. S.; Perrier, S. RAFT with Light: A User Guide to Using Thiocarbonylthio Compounds in Photopolymerizations. *ACS Polym. Au* **2025**, *5*, 184–213.

(44) Dadashi-Silab, S.; Atilla Tasdelen, M.; Yagci, Y. Photoinitiated Atom Transfer Radical Polymerization: Current Status and Future Perspectives. *J. Polym. Sci. A Polym. Chem.* **2014**, *52*, 2878–2888.

(45) Xu, J.; Jung, K.; Boyer, C. Oxygen Tolerance Study of Photoinduced Electron Transfer–Reversible Addition–Fragmentation Chain Transfer (PET-RAFT) Polymerization Mediated by $Ru(Bpy)_3Cl_2$. *Macromolecules* **2014**, *47*, 4217–4229.

(46) Ng, G.; Yeow, J.; Xu, J.; Boyer, C. Application of Oxygen Tolerant PET-RAFT to Polymerization-Induced Self-Assembly. *Polym. Chem.* **2017**, *8*, 2841–2851.

(47) Gormley, A. J.; Yeow, J.; Ng, G.; Conway, Ó.; Boyer, C.; Chapman, R. An Oxygen-Tolerant PET-RAFT Polymerization for Screening Structure–Activity Relationships. *Angew. Chem., Int. Ed.* **2018**, *57*, 1557–1562.

(48) Wanasinghe, S. V.; Sun, M.; Yehl, K.; Cuthbert, J.; Matyjaszewski, K.; Konkolewicz, D. PET-RAFT Increases Uniformity in Polymer Networks. *ACS Macro Lett.* **2022**, *11*, 1156–1161.

(49) McCarthy, B. G.; Pearson, R. M.; Lim, C.-H.; Sartor, S. M.; Damrauer, N. H.; Miyake, G. M. Structure–Property Relationships for Tailoring Phenoxazines as Reducing Photoredox Catalysts. *J. Am. Chem. Soc.* **2018**, *140*, 5088–5101.

(50) Yang, H.; Lu, Z.; Fu, X.; Li, Q.; Xiao, L.; Zhao, R.; Zhao, Y.; Hou, L. Multipath Oxygen-Mediated PET-RAFT Polymerization by a Conjugated Organic Polymer Photocatalyst under Red LED Irradiation. *Polym. Chem.* **2021**, *12*, 6998–7004.

(51) Cao, H.; Wang, G.; Xue, Y.; Yang, G.; Tian, J.; Liu, F.; Zhang, W. Far-Red Light-Induced Reversible Addition–Fragmentation Chain Transfer Polymerization Using a Man-Made Bacteriochlorin. *ACS Macro Lett.* **2019**, *8*, 616–622.

(52) Shanmugam, S.; Xu, J.; Boyer, C. Light-Regulated Polymerization under Near-Infrared/Far-Red Irradiation Catalyzed by Bacteriochlorophyll *a*. *Angew. Chem., Int. Ed.* **2016**, *55*, 1036–1040.

(53) Wu, C.; Corrigan, N.; Lim, C.-H.; Jung, K.; Zhu, J.; Miyake, G.; Xu, J.; Boyer, C. Guiding the Design of Organic Photocatalyst for PET-RAFT Polymerization: Halogenated Xanthene Dyes. *Macromolecules* **2019**, *52*, 236–248.

(54) Wu, C.; Corrigan, N.; Lim, C.-H.; Liu, W.; Miyake, G.; Boyer, C. Rational Design of Photocatalysts for Controlled Polymerization: Effect of Structures on Photocatalytic Activities. *Chem. Rev.* **2022**, *122*, 5476–5518.

(55) Parnitzke, B.; Nwoko, T.; Bradford, K. G. E.; De Alwis Watuthanthrige, N.; Yehl, K.; Boyer, C.; Konkolewicz, D. Photons and Photocatalysts as Limiting Reagents for PET-RAFT Photopolymerization. *Chem. Eng. J.* **2023**, *456*, 141007.

(56) Kato, M.; Kamigaito, M.; Sawamoto, M.; Higashimura, T. Polymerization of Methyl Methacrylate with the Carbon Tetrachloride/Dichlorotris-(Triphenylphosphine)Ruthenium(II)/Methylaluminum Bis(2,6-Di-Tert-Butylphenoxide) Initiating System: Possibility of Living Radical Polymerization. *Macromolecules* **1995**, *28*, 1721–1723.

(57) Ando, T.; Kato, M.; Kamigaito, M.; Sawamoto, M. Living Radical Polymerization of Methyl Methacrylate with Ruthenium Complex: Formation of Polymers with Controlled Molecular Weights and Very Narrow Distributions. *Macromolecules* **1996**, *29*, 1070–1072.

(58) Kotani, Y.; Kato, M.; Kamigaito, M.; Sawamoto, M. Living Radical Polymerization of Alkyl Methacrylates with Ruthenium Complex and Synthesis of Their Block Copolymers. *Macromolecules* **1996**, *29*, 6979–6982.

(59) Wang, J.-S.; Matyjaszewski, K. Controlled/"living" Radical Polymerization. Atom Transfer Radical Polymerization in the Presence of Transition-Metal Complexes. *J. Am. Chem. Soc.* 1995, *117*, 5614–5615.

(60) Wang, J.-S.; Matyjaszewski, K. Controlled/"Living" Radical Polymerization. Halogen Atom Transfer Radical Polymerization Promoted by a Cu(I)/Cu(II) Redox Process. *Macromolecules* **1995**, *28*, 7901–7910.

(61) Tang, W.; Kwak, Y.; Braunecker, W.; Tsarevsky, N. V.; Coote, M. L.; Matyjaszewski, K. Understanding Atom Transfer Radical Polymerization: Effect of Ligand and Initiator Structures on the Equilibrium Constants. *J. Am. Chem. Soc.* **2008**, *130*, 10702–10713.

(62) Kwak, Y.; Magenau, A. J. D.; Matyjaszewski, K. ARGET ATRP of Methyl Acrylate with Inexpensive Ligands and Ppm Concentrations of Catalyst. *Macromolecules* **2011**, *44*, 811–819.

(63) Konkolewicz, D.; Magenau, A. J. D.; Averick, S. E.; Simakova, A.; He, H.; Matyjaszewski, K. ICAR ATRP with Ppm Cu Catalyst in Water. *Macromolecules* **2012**, *45*, 4461–4468.

(64) Dadashi-Silab, S.; Kim, K.; Lorandi, F.; Szczepaniak, G.; Kramer, S.; Peteanu, L.; Matyjaszewski, K. Red-Light-Induced, Copper-Catalyzed Atom Transfer Radical Polymerization. *ACS Macro Lett.* **2022**, *11*, 376–381.

(65) Ribelli, T. G.; Konkolewicz, D.; Pan, X.; Matyjaszewski, K. Contribution of Photochemistry to Activator Regeneration in ATRP. *Macromolecules* **2014**, *47*, 6316–6321.

(66) Ribelli, T. G.; Konkolewicz, D.; Bernhard, S.; Matyjaszewski, K. How Are Radicals (Re)Generated in Photochemical ATRP? *J. Am. Chem. Soc.* **2014**, *136*, 13303–13312.

(67) Konkolewicz, D.; Schröder, K.; Buback, J.; Bernhard, S.; Matyjaszewski, K. Visible Light and Sunlight Photoinduced ATRP with Ppm of Cu Catalyst. *ACS Macro Lett.* **2012**, *1*, 1219–1223.

(68) Treat, N. J.; Fors, B. P.; Kramer, J. W.; Christianson, M.; Chiu, C.-Y.; Read de Alaniz, J.; Hawker, C. J. Controlled Radical Polymerization of Acrylates Regulated by Visible Light. *ACS Macro Lett.* **2014**, *3*, 580–584.

(69) Miyake, G. M.; Theriot, J. C. Perylene as an Organic Photocatalyst for the Radical Polymerization of Functionalized Vinyl Monomers through Oxidative Quenching with Alkyl Bromides and Visible Light. *Macromolecules* **2014**, *47*, 8255–8261.

(70) Theriot, J. C.; Lim, C.-H.; Yang, H.; Ryan, M. D.; Musgrave, C. B.; Miyake, G. M. Organocatalyzed Atom Transfer Radical Polymerization Driven by Visible Light. *Science* **2016**, *352*, 1082–1086.

(71) Pan, X.; Fang, C.; Fantin, M.; Malhotra, N.; So, W. Y.; Peteanu, L. A.; Isse, A. A.; Gennaro, A.; Liu, P.; Matyjaszewski, K. Mechanism of Photoinduced Metal-Free Atom Transfer Radical Polymerization: Experimental and Computational Studies. *J. Am. Chem. Soc.* **2016**, *138*, 2411–2425.

(72) Treat, N. J.; Sprafke, H.; Kramer, J. W.; Clark, P. G.; Barton, B. E.; Read de Alaniz, J.; Fors, B. P.; Hawker, C. J. Metal-Free Atom Transfer Radical Polymerization. *J. Am. Chem. Soc.* **2014**, *136*, 16096–16101.

(73) Buss, B. L.; Lim, C.; Miyake, G. M. Dimethyl Dihydroacridines as Photocatalysts in Organocatalyzed Atom Transfer Radical Polymerization of Acrylate Monomers. *Angew. Chem., Int. Ed.* **2020**, *59*, 3209–3217.

(74) Xu, X.; Xu, X.; Zeng, Y.; Zhang, F. Oxygen-Tolerant Photo-Induced Metal-Free Atom Transfer Radical Polymerization. *J. Photochem. Photobiol. A Chem.* **2021**, *411*, 113191.

(75) Liu, X.; Zhang, L.; Cheng, Z.; Zhu, X. Metal-Free Photoinduced Electron Transfer–Atom Transfer Radical Polymerization (PET–ATRP) via a Visible Light Organic Photocatalyst. *Polym. Chem.* **2016**, *7*, 689–700.

(76) Luo, X.; Wan, J.; Meckbach, N.; Strehmel, V.; Li, S.; Chen, Z.; Strehmel, B. A Porphyrin-Based Organic Network Comprising Sustainable Carbon Dots for Photopolymerization. *Angew. Chem., Int. Ed.* **2022**, *61*, e202208180.

(77) Chiefari, J.; Chong, Y. K. (Bill); Ercole, F.; Krstina, J.; Jeffery, J.; Le, T. P. T.; Mayadunne, R. T. A.; Meijs, G. F.; Moad, C. L.; Moad, G.; Rizzardo, E.; Thang, S. H. Living Free-Radical Polymerization by Reversible Addition−Fragmentation Chain Transfer: The RAFT Process. *Macromolecules* **1998**, *31*, 5559–5562.

(78) Delduc, P.; Tailhan, C.; Zard, S. Z. A Convenient Source of Alkyl and Acyl Radicals. *J. Chem. Soc. Chem. Commun.* **1988**, *4*, 308–310.

(79) Turner, S. R.; Blevins, R. W. Photoinitiated Block Copolymer Formation Using Dithiocarbamate Free Radical Chemistry. *Macromolecules* **1990**, *23*, 1856–1859.

(80) Otsu, T.; Yoshida, M.; Tazaki, T. A Model for Living Radical Polymerization. *Makromol. Chem., Rapid Commun.* **1982**, *3*, 133–140.

(81) Konkolewicz, D.; Hawkett, B. S.; Gray-Weale, A.; Perrier, S. RAFT Polymerization Kinetics: Combination of Apparently Conflicting Models. *Macromolecules* **2008**, *41*, 6400–6412.

(82) Shanmugam, S.; Xu, J.; Boyer, C. Exploiting Metalloporphyrins for Selective Living Radical Polymerization Tunable over Visible Wavelengths. *J. Am. Chem. Soc.* **2015**, *137*, 9174–9185.

(83) Corrigan, N.; Xu, J.; Boyer, C. A Photoinitiation System for Conventional and Controlled Radical Polymerization at Visible and NIR Wavelengths. *Macromolecules* **2016**, *49*, 3274–3285.

(84) Xu, J.; Shanmugam, S.; Duong, H. T.; Boyer, C. Organo-Photocatalysts for Photoinduced Electron Transfer-Reversible Addition–Fragmentation Chain Transfer (PET-RAFT) Polymerization. *Polym. Chem.* **2015**, *6*, 5615–5624.

(85) Ma, Y.; Kottisch, V.; McLoughlin, E. A.; Rouse, Z. W.; Supej, M. J.; Baker, S. P.; Fors, B. P. Photoswitching Cationic and Radical Polymerizations: Spatiotemporal Control of Thermoset Properties. *J. Am. Chem. Soc.* **2021**, *143*, 21200–21205.

(86) Kottisch, V.; Michaudel, Q.; Fors, B. P. Cationic Polymerization of Vinyl Ethers Controlled by Visible Light. *J. Am. Chem. Soc.* **2016**, *138*, 15535–15538.

(87) Kottisch, V.; Michaudel, Q.; Fors, B. P. Photocontrolled Interconversion of Cationic and Radical Polymerizations. *J. Am. Chem. Soc.* **2017**, *139*, 10665–10668.

(88) Allegrezza, M. L.; Konkolewicz, D. PET-RAFT Polymerization: Mechanistic Perspectives for Future Materials. *ACS Macro Lett.* **2021**, *10*, 433–446.

(89) Baker, J. G.; Koehler, S. J.; Wood, K. J.; Troya, D.; Gloriod, J.; Anderson, I. C.; Gomez, D. C.; Figg, C. A. Reversing Blocking Order of Trithiocarbonate-Mediated RAFT Polymerizations Using Photocatalysis. *Angew. Chem., Int. Ed.* **2025**, *64*, e202509029.

(90) Shanmugam, S.; Xu, J.; Boyer, C. Utilizing the Electron Transfer Mechanism of Chlorophyll a under Light for Controlled Radical Polymerization. *Chem. Sci.* **2015**, *6*, 1341–1349.

(91) Figg, C. A.; Hickman, J. D.; Scheutz, G. M.; Shanmugam, S.; Carmean, R. N.; Tucker, B. S.; Boyer, C.; Sumerlin, B. S. Color-Coding Visible Light Polymerizations To Elucidate the Activation of Trithiocarbonates Using Eosin Y. *Macromolecules* **2018**, *51*, 1370–1376.

(92) Bell, K.; Freeburne, S.; Wolford, A.; Pester, C. W. Reusable Polymer Brush-Based Photocatalysts for PET-RAFT Polymerization. *Polym. Chem.* **2022**, *13*, 6120–6126.

(93) Anderson, I. C.; Gomez, D. C.; Zhang, M.; Koehler, S. J.; Figg, C. A. Catalyzing PET-RAFT Polymerizations Using Inherently Photoactive Zinc Myoglobin. *Angew. Chem., Int. Ed.* **2025**, *64*, e202414431.

(94) Bagheri, A.; Bainbridge, C. W. A.; Engel, K. E.; Qiao, G. G.; Xu, J.; Boyer, C.; Jin, J. Oxygen Tolerant PET-RAFT Facilitated 3D Printing of Polymeric Materials under Visible LEDs. *ACS Appl. Polym. Mater.* **2020**, *2*, 782–790.

(95) Bainbridge, C. W. A.; Engel, K. E.; Jin, J. 3D Printing and Growth Induced Bending Based on PET-RAFT Polymerization. *Polym. Chem.* **2020**, *11*, 4084–4093.

(96) Zhang, Z.; Corrigan, N.; Bagheri, A.; Jin, J.; Boyer, C. A Versatile 3D and 4D Printing System through Photocontrolled RAFT Polymerization. *Angew. Chem., Int. Ed.* **2019**, *58*, 17954–17963.

(97) Bagheri, A.; Ling, H.; Bainbridge, C. W. A.; Jin, J. Living Polymer Networks Based on a RAFT Cross-Linker: Toward 3D and 4D Printing Applications. *ACS Appl. Polym. Mater.* **2021**, *3*, 2921–2930.

(98) Bowman, Z.; Baker, J. G.; Hughes, M. J.; Nguyen, J. D.; Garcia, M.; Tamrat, N.; Worch, J. C.; Figg, C. A. Customizing STEM Organogels Using PET-RAFT Polymerization. *Polym. Chem.* **2024**, *15*, 3907–3915.

(99) Zhang, Z.; Corrigan, N.; Boyer, C. Effect of Thiocarbonylthio Compounds on Visible-Light-Mediated 3D Printing. *Macromolecules* **2021**, *54*, 1170–1182.

(100) Chen, M.; Gu, Y.; Singh, A.; Zhong, M.; Jordan, A. M.; Biswas, S.; Korley, L. T. J.; Balazs, A. C.; Johnson, J. A. Living Additive Manufacturing: Transformation of Parent Gels into Diversely Functionalized Daughter Gels Made Possible by Visible Light Photoredox Catalysis. *ACS Cent. Sci.* **2017**, *3*, 124–134.

(101) Lampley, M. W.; Tsogtgerel, E.; Harth, E. Nanonetwork Photogrowth Expansion: Tailoring Nanoparticle Networks' Chemical Structure and Local Topology. *Polym. Chem.* **2019**, *10*, 3841–3850.

(102) Bagheri, A.; Bainbridge, C.; Jin, J. Visible Light-Induced Transformation of Polymer Networks. *ACS Appl. Polym. Mater.* **2019**, *1*, 1896–1904.

(103) Cuthbert, J.; Beziau, A.; Gottlieb, E.; Fu, L.; Yuan, R.; Balazs, A. C.; Kowalewski, T.; Matyjaszewski, K. Transformable Materials: Structurally Tailored and Engineered Macromolecular (STEM) Gels by Controlled Radical Polymerization. *Macromolecules* **2018**, *51*, 3808–3817.

(104) Cuthbert, J.; Balazs, A. C.; Kowalewski, T.; Matyjaszewski, K. STEM Gels by Controlled Radical Polymerization. *Trends Chem.* **2020**, *2*, 341–353.

(105) Cuthbert, J.; Zhang, T.; Biswas, S.; Olszewski, M.; Shanmugam, S.; Fu, T.; Gottlieb, E.; Kowalewski, T.; Balazs, A. C.; Matyjaszewski, K. Structurally Tailored and Engineered Macromolecular (STEM) Gels as Soft Elastomers and Hard/Soft Interfaces. *Macromolecules* **2018**, *51*, 9184–9191.

(106) Li, M.; Fromel, M.; Ranaweera, D.; Rocha, S.; Boyer, C.; Pester, C. W. SI-PET-RAFT: Surface-Initiated Photoinduced Electron Transfer-Reversible Addition–Fragmentation Chain Transfer Polymerization. *ACS Macro Lett.* **2019**, *8*, 374–380.

(107) Poelma, J. E.; Fors, B. P.; Meyers, G. F.; Kramer, J. W.; Hawker, C. J. Fabrication of Complex Three-Dimensional Polymer Brush Nanostructures through Light-Mediated Living Radical Polymerization. *Angew. Chem., Int. Ed.* **2013**, *52*, 6844–6848.

(108) Kuzmyn, A. R.; Nguyen, A. T.; Teunissen, L. W.; Zuilhof, H.; Baggerman, J. Antifouling Polymer Brushes via Oxygen-Tolerant Surface-Initiated PET-RAFT. *Langmuir* **2020**, *36*, 4439–4446.

(109) Seera, S. D. K.; Pester, C. W. Surface-Initiated PET-RAFT via the Z-Group Approach. *ACS Polym. Au* **2023**, *3*, 428–436.

(110) Yan, J.; Pan, X.; Schmitt, M.; Wang, Z.; Bockstaller, M. R.; Matyjaszewski, K. Enhancing Initiation Efficiency in Metal-Free Surface-Initiated Atom Transfer Radical Polymerization (SI-ATRP). *ACS Macro Lett.* **2016**, *5*, 661–665.

(111) Ma, A.; Zhang, J.; Wang, N.; Bai, L.; Chen, H.; Wang, W.; Yang, H.; Yang, L.; Niu, Y.; Wei, D. Surface-Initiated Metal-Free Photoinduced ATRP of 4-Vinylpyridine from SiO_2 via Visible Light Photocatalysis for Self-Healing Hydrogels. *Ind. Eng. Chem. Res.* **2018**, *57*, 17417–17429.

(112) Fromel, M.; Pester, C. W. Polycarbonate Surface Modification via Aqueous SI-PET-RAFT. *Macromolecules* **2022**, *55*, 4907–4915.

(113) Rong, L.-H.; Cheng, X.; Ge, J.; Krebs, O. K.; Capadona, J. R.; Caldona, E. B.; Advincula, R. C. SI-PET-RAFT Polymerization via Electrodeposited Macroinitiator Thin Films: Toward Biomedical and Sensing Applications. *ACS Appl. Polym. Mater.* **2022**, *4*, 6449–6457.

(114) Ng, G.; Li, M.; Yeow, J.; Jung, K.; Pester, C. W.; Boyer, C. Benchtop Preparation of Polymer Brushes by SI-PET-RAFT: The Effect of the Polymer Composition and Structure on Inhibition of a *Pseudomonas* Biofilm. *ACS Appl. Mater. Interfaces* **2020**, *12*, 55243–55254.

(115) Chen, M.; Zhong, M.; Johnson, J. A. Light-Controlled Radical Polymerization: Mechanisms, Methods, and Applications. *Chem. Rev.* **2016**, *116*, 10167–10211.

(116) Menard, E.; Meitl, M. A.; Sun, Y.; Park, J.-U.; Shir, D. J.-L.; Nam, Y.-S.; Jeon, S.; Rogers, J. A. Micro- and Nanopatterning Techniques for Organic Electronic and Optoelectronic Systems. *Chem. Rev.* **2007**, *107*, 1117–1160.

(117) Feng, W.; Ueda, E.; Levkin, P. A. Droplet Microarrays: From Surface Patterning to High-Throughput Applications. *Adv. Mater.* **2018**, *30*, 1706111.

(118) Jung, M. W.; Myung, S.; Song, W.; Kang, M.-A.; Kim, S. H.; Yang, C.-S.; Lee, S. S.; Lim, J.; Park, C.-Y.; Lee, J.-O.; An, K.-S. Novel Fabrication of Flexible Graphene-Based Chemical Sensors with Heaters Using Soft Lithographic Patterning Method. *ACS Appl. Mater. Interfaces* **2014**, *6*, 13319–13323.

(119) Nie, Z.; Kumacheva, E. Patterning Surfaces with Functional Polymers. *Nat. Mater.* **2008**, *7*, 277–290.

(120) Hou, J.; Li, M.; Song, Y. Patterned Colloidal Photonic Crystals. *Angew. Chem., Int. Ed.* **2018**, *57*, 2544–2553.

(121) Fromel, M.; Benetti, E. M.; Pester, C. W. Oxygen Tolerance in Surface-Initiated Reversible Deactivation Radical Polymerizations: Are Polymer Brushes Turning into Technology? *ACS Macro Lett.* **2022**, *11*, 415–421.

(122) Poisson, J.; Polgar, A. M.; Fromel, M.; Pester, C. W.; Hudson, Z. M. Preparation of Patterned and Multilayer Thin Films for Organic Electronics via Oxygen-Tolerant SI-PET-RAFT. *Angew. Chem., Int. Ed.* **2021**, *60*, 19988–19996.

(123) Fromel, M.; Sweeder, D. M.; Jang, S.; Williams, T. A.; Kim, S. H.; Pester, C. W. Superhydrophilic Polymer Brushes with High Durability and Anti-Fogging Activity. *ACS Appl. Polym. Mater.* **2021**, *3*, 5291–5301.

(124) Jiang, X.; Xi, M.; Bai, L.; Wang, W.; Yang, L.; Chen, H.; Niu, Y.; Cui, Y.; Yang, H.; Wei, D. Surface-Initiated PET-ATRP and Mussel-Inspired Chemistry for Surface Engineering of MWCNTs and Application in Self-Healing Nanocomposite Hydrogels. *Mater. Sci. Eng. C* **2020**, *109*, 110553.

(125) Freeburne, S.; Sacco, J. L.; Gomez, E. W.; Pester, C. W. Effects of Surface-Immobilization on Photobleaching of Xanthene Dye Photocatalysts. *Macromol. Chem. Phys.* **2023**, *224*, 2300283.

(126) Polymeropoulos, G.; Zapsas, G.; Ntetsikas, K.; Bilalis, P.; Gnanou, Y.; Hadjichristidis, N. 50th Anniversary Perspective: Polymers with Complex Architectures. *Macromolecules* **2017**, *50*, 1253–1290.

(127) Zhang, C.; Ye, G.; Wang, W.; Ding, X.; Feng, Y.; Wang, R. Thermal, PH, and Photo Multistimuli Responsive Block Copolymer Self-Assembly Nanoparticles for Drug

Delivery Using Visible-Light-Induced PET-RAFT. *ACS Appl. Nano Mater.* **2024**, *7*, 370–381.

(128) Foster, H.; Stenzel, M. H.; Chapman, R. PET-RAFT Enables Efficient and Automated Multiblock Star Synthesis. *Macromolecules* **2022**, *55*, 5938–5945.

(129) Buss, B. L.; Beck, L. R.; Miyake, G. M. Synthesis of Star Polymers Using Organocatalyzed Atom Transfer Radical Polymerization through a Core-First Approach. *Polym. Chem.* **2018**, *9*, 1658–1665.

(130) Aydogan, C.; Yilmaz, G.; Yagci, Y. Synthesis of Hyperbranched Polymers by Photoinduced Metal-Free ATRP. *Macromolecules* **2017**, *50*, 9115–9120.

(131) Rong, L.; Cheng, X.; Ge, J.; Caldona, E. B.; Advincula, R. C. Synthesis of Hyperbranched Polymers via PET-RAFT Self-Condensing Vinyl Polymerization in a Flow Reactor. *Macromol. Chem. Phys.* **2022**, *223*, 2100342.

(132) Zhang, Y.; Zhao, R.; Qin, Y.; Yi, J.; Zhang, J.; Chen, X. Synthesis and Self-Assembly of Hyperbranched Multiarm Copolymer Peptide Conjugates Based on Light-Induced Metal-Free ATRP. *Polym. Chem.* **2023**, *14*, 2930–2939.

(133) Ng, G.; Yeow, J.; Chapman, R.; Isahak, N.; Wolvetang, E.; Cooper-White, J. J.; Boyer, C. Pushing the Limits of High Throughput PET-RAFT Polymerization. *Macromolecules* **2018**, *51*, 7600–7607.

(134) Theriot, J. C.; Miyake, G. M.; Boyer, C. A. *N*,*N*-Diaryl Dihydrophenazines as Photoredox Catalysts for PET-RAFT and Sequential PET-RAFT/O-ATRP. *ACS Macro Lett.* **2018**, *7*, 662–666.

(135) Ma, Q.; Wang, W.; Zhang, L.; Cao, H. RAFT Polymerization of Semifluorinated Monomers Mediated by a NIR Fluorinated Photocatalyst. *Macromol. Rapid Commun.* **2022**, *43*, 2200122.

(136) Shipp, D. A.; Wang, J.-L.; Matyjaszewski, K. Synthesis of Acrylate and Methacrylate Block Copolymers Using Atom Transfer Radical Polymerization. *Macromolecules* **1998**, *31*, 8005–8008.

(137) Easterling, C. P.; Xia, Y.; Zhao, J.; Fanucci, G. E.; Sumerlin, B. S. Block Copolymer Sequence Inversion through Photoiniferter Polymerization. *ACS Macro Lett.* **2019**, *8*, 1461–1466.

(138) Corrigan, N.; Trujillo, F. J.; Xu, J.; Moad, G.; Hawker, C. J.; Boyer, C. Divergent Synthesis of Graft and Branched Copolymers through Spatially Controlled Photopolymerization in Flow Reactors. *Macromolecules* **2021**, *54*, 3430–3446.

(139) Tucker, B. S.; Coughlin, M. L.; Figg, C. A.; Sumerlin, B. S. Grafting-From Proteins Using Metal-Free PET–RAFT Polymerizations under Mild Visible-Light Irradiation. *ACS Macro Lett.* **2017**, *6*, 452–457.

(140) Olson, R. A.; Korpusik, A. B.; Sumerlin, B. S. Enlightening Advances in Polymer Bioconjugate Chemistry: Light-Based Techniques for Grafting to and from Biomacromolecules. *Chem. Sci.* **2020**, *11*, 5142–5156.

(141) Niu, J.; Lunn, D. J.; Pusuluri, A.; Yoo, J. I.; O'Malley, M. A.; Mitragotri, S.; Soh, H. T.; Hawker, C. J. Engineering Live Cell Surfaces with Functional Polymers via Cytocompatible Controlled Radical Polymerization. *Nat. Chem.* **2017**, *9*, 537–545.

(142) Lian, S.; Li, R.; Chen, Y.; An, Z. Reversible Deactivation Radical Polymerization in Heterogeneous Systems: Enhancing Access to High Molecular Weight Polymers. *Macromolecules* **2025**, *58*, 5385–5394.

(143) An, Z. 100th Anniversary of Macromolecular Science Viewpoint: Achieving Ultrahigh Molecular Weights with Reversible Deactivation Radical Polymerization. *ACS Macro Lett.* **2020**, *9*, 350–357.

(144) Lee, Y.; Boyer, C.; Kwon, M. S. Photocontrolled RAFT Polymerization: Past, Present, and Future. *Chem. Soc. Rev.* **2023**, *52*, 3035–3097.

(145) Chou, Y.-T.; Lee, W.-R.; Yu, S.-S. Efficient Synthesis of Ultrahigh Molecular Weight Poly(Methyl Methacrylate) via Visible Light-Induced RAFT Polymerization in Deep Eutectic Solvent. *Macromolecules* **2024**, *57*, 9241–9249.

(146) Stacy, E. K.; McCormick, M. L.; Stevens, K. C.; Jankoski, P. E.; Aguinaga, J.; Patton, D. L.; Sumerlin, B. S.; Clemons, T. D. Aqueous Photoiniferter Polymerization of Acrylonitrile. *ACS Macro Lett.* **2024**, *13*, 1662–1669.

(147) Eades, C. B.; Stevens, K. C.; Cabrera, D. E.; Vereb, M. K.; Lott, M. E.; Bowman, J. I.; Sumerlin, B. S. Ultra-High Molecular Weight Polymer Synthesis *via* Aqueous Dispersion Polymerization. *Chem. Sci.* **2025**, *16*, 5573–5578.

(148) Zhu, S.; Kong, W.; Lian, S.; Shen, A.; Armes, S. P.; An, Z. Photocontrolled Radical Polymerization for the Synthesis of Ultrahigh-Molecular-Weight Polymers. *Nat. Synth.* **2025**, *4*, 15–30.

(149) Carmean, R. N.; Becker, T. E.; Sims, M. B.; Sumerlin, B. S. Ultra-High Molecular Weights via Aqueous Reversible-Deactivation Radical Polymerization. *Chem* **2017**, *2*, 93–101.

(150) Allison-Logan, S.; Karimi, F.; Sun, Y.; McKenzie, T. G.; Nothling, M. D.; Bryant, G.; Qiao, G. G. Highly Living Stars via Core-First Photo-RAFT Polymerization: Exploitation for Ultra-High Molecular Weight Star Synthesis. *ACS Macro Lett.* **2019**, *8*, 1291–1295.

(151) Carmean, R. N.; Sims, M. B.; Figg, C. A.; Hurst, P. J.; Patterson, J. P.; Sumerlin, B. S. Ultrahigh Molecular Weight Hydrophobic Acrylic and Styrenic Polymers through Organic-Phase Photoiniferter-Mediated Polymerization. *ACS Macro Lett.* **2020**, *9*, 613–618.

(152) Matyjaszewski, K.; Poli, R. Comparison of Bond Dissociation Energies of Dormant Species Relevant to Degenerative Transfer and Atom Transfer Radical Polymerization. *Macromolecules* **2005**, *38*, 8093–8100.

(153) Wu, Z.; Jung, K.; Wu, C.; Ng, G.; Wang, L.; Liu, J.; Boyer, C. Selective Photoactivation of Trithiocarbonates Mediated by Metal Naphthalocyanines and Overcoming Activation Barriers Using Thermal Energy. *J. Am. Chem. Soc.* **2022**, *144*, 995–1005.

(154) Gillies, M. B.; Matyjaszewski, K.; Norrby, P.-O.; Pintauer, T.; Poli, R.; Richard, P. A DFT Study of R−X Bond Dissociation Enthalpies of Relevance to the Initiation Process of Atom Transfer Radical Polymerization. *Macromolecules* **2003**, *36*, 8551–8559.

(155) Baker, J. G.; Zhang, R.; Figg, C. A. Installing a Single Monomer within Acrylic Polymers Using Photoredox Catalysis. *J. Am. Chem. Soc.* **2024**, *146*, 106–111.

(156) Moriceau, G.; Gody, G.; Hartlieb, M.; Winn, J.; Kim, H.; Mastrangelo, A.; Smith, T.; Perrier, S. Functional Multisite Copolymer by One-Pot Sequential RAFT Copolymerization of Styrene and Maleic Anhydride. *Polym. Chem.* **2017**, *8*, 4152–4161.

(157) Vandenbergh, J.; Reekmans, G.; Adriaensens, P.; Junkers, T. Synthesis of Sequence Controlled Acrylate Oligomers via Consecutive RAFT Monomer Additions. *Chem. Commun.* **2013**, *49*, 10358–10360.

(158) Huang, Z.; Noble, B. B.; Corrigan, N.; Chu, Y.; Satoh, K.; Thomas, D. S.; Hawker, C. J.; Moad, G.; Kamigaito, M.; Coote, M. L.; Boyer, C.; Xu, J. Discrete and Stereospecific Oligomers Prepared by Sequential and Alternating Single Unit Monomer Insertion. *J. Am. Chem. Soc.* **2018**, *140*, 13392–13406.

(159) Hakobyan, K.; Noble, B. B.; Xu, J. Solid-Phase Synthesis of Iterative RAFT Single Unit Monomer Insertion Adducts. *Polym. Chem.* **2023**, *14*, 4116–4125.

(160) Merrifield, B. Solid Phase Synthesis. *Science* **1986**, *232*, 341–347.

(161) Zhang, J.; Yang, Z.; Liu, C.; Wan, H.; Hao, Z.; Ji, X.; Wang, P.; Yi, H.; Lei, A. Tailoring Photocatalysts to Modulate Oxidative Potential of Anilides Enhances Para-Selective Electrochemical Hydroxylation. *Nat. Commun.* **2024**, *15*, 6954.

(162) Beil, S. B.; Bonnet, S.; Casadevall, C.; Detz, R. J.; Eisenreich, F.; Glover, S. D.; Kerzig, C.; Næsborg, L.; Pullen, S.; Storch, G.; Wei, N.; Zeymer, C. Challenges and Future Perspectives in Photocatalysis: Conclusions from an Interdisciplinary Workshop. *JACS Au* **2024**, *4*, 2746–2766.

(163) Reischauer, S.; Pieber, B. Emerging Concepts in Photocatalytic Organic Synthesis. *iScience* **2021**, *24*, 102209.

(164) Sun, H.; Kabb, C. P.; Dai, Y.; Hill, M. R.; Ghiviriga, I.; Bapat, A. P.; Sumerlin, B. S. Macromolecular Metamorphosis via Stimulus-Induced Transformations of Polymer Architecture. *Nat. Chem.* **2017**, *9*, 817–823.

(165) Bellotti, V.; Wang, H. S.; Truong, N. P.; Simonutti, R.; Anastasaki, A. Temporal Regulation of PET-RAFT Controlled Radical Depolymerization. *Angew. Chem., Int. Ed.* **2023**, *62*, e202313232.

(166) Bellotti, V.; Parkatzidis, K.; Wang, H. S.; De Alwis Watuthanthrige, N.; Orfano, M.; Monguzzi, A.; Truong, N. P.; Simonutti, R.; Anastasaki, A. Light-Accelerated Depolymerization Catalyzed by Eosin Y. *Polym. Chem.* **2023**, *14*, 253–258.

(167) Korpusik, A. B.; Adili, A.; Bhatt, K.; Anatot, J. E.; Seidel, D.; Sumerlin, B. S. Degradation of Polyacrylates by One-Pot Sequential Dehydrodecarboxylation and Ozonolysis. *J. Am. Chem. Soc.* **2023**, *145*, 10480–10485.

(168) Schué, E.; Rickertsen, D. R. L.; Korpusik, A. B.; Adili, A.; Seidel, D.; Sumerlin, B. S. Alternating Styrene–Propylene and Styrene–Ethylene Copolymers Prepared by Photocatalytic Decarboxylation. *Chem. Sci.* **2023**, *14*, 11228–11236.

(169) Adili, A.; Korpusik, A. B.; Seidel, D.; Sumerlin, B. S. Photocatalytic Direct Decarboxylation of Carboxylic Acids to Derivatize or Degrade Polymers. *Angew. Chem., Int. Ed.* 2022, *61*, e202209085.

(170) Delafresnaye, L.; Jung, K.; Boyer, C.; Barner-Kowollik, C. Two Colours of Light Drive PET–RAFT Photoligation. *Polym. Chem.* **2020**, *11*, 6453–6462.

(171) Xing, D.; Li, J.; Chen, M.; Li, N.; Pan, X.; Zhang, Z.; Zhu, J. Controlling Polymer Molecular Weight Distributions by Light through Reversible Addition-fragmentation Chain Transfer-hetero-Diels–Alder Click Conjugation. *J. Polym. Sci.* **2022**, *60*, 3463–3470.

(172) Aquib, M.; Yang, W.; Yu, L.; Kannaujiya, V. K.; Zhang, Y.; Li, P.; Whittaker, A.; Fu, C.; Boyer, C. Effect of Cyclic Topology *versus* Linear Terpolymers on Antibacterial

Activity and Biocompatibility: Antimicrobial Peptide Avatars. *Chem. Sci.* **2024**, *15*, 19057–19069.

(173) Kaupp, M.; Tischer, T.; Hirschbiel, A. F.; Vogt, A. P.; Geckle, U.; Trouillet, V.; Hofe, T.; Stenzel, M. H.; Barner-Kowollik, C. Photo-Sensitive RAFT-Agents for Advanced Microparticle Design. *Macromolecules* **2013**, *46*, 6858–6872.

(174) De Neve, J.; Haven, J. J.; Maes, L.; Junkers, T. Sequence-Definition from Controlled Polymerization: The next Generation of Materials. *Polym. Chem.* **2018**, *9*, 4692–4705.

(175) Hakobyan, K.; Xu, J.; Müllner, M. The Challenges of Controlling Polymer Synthesis at the Molecular and Macromolecular Level. *Polym. Chem.* **2022**, *13*, 5431-5446.

(176) Lutz, J. F.; Lehn, J. M.; Meijer, E. W.; Matyjaszewski, K. From Precision Polymers to Complex Materials and Systems. *Nat. Rev. Mater.* **2016**, *1*, 1–14.

(177) Lutz, J. F.; Ouchi, M.; Liu, D. R.; Sawamoto, M. Sequence-Controlled Polymers. *Science* **2013**, *341*, 1238149.

(178) Al Ouahabi, A.; Charles, L.; Lutz, J. F. Synthesis of Non-Natural Sequence-Encoded Polymers Using Phosphoramidite Chemistry. *J. Am. Chem. Soc.* **2015**, *137*, 5629–5635.

(179) Zhao, B.; Gao, Z.; Zheng, Y.; Gao, C. Scalable Synthesis of Positively Charged Sequence-Defined Functional Polymers. *J. Am. Chem. Soc.* **2019**, *141*, 4541–4546.

(180) Nguyen, H. V. T.; Jiang, Y.; Mohapatra, S.; Wang, W.; Barnes, J. C.; Oldenhuis, N. J.; Chen, K. K.; Axelrod, S.; Huang, Z.; Chen, Q.; Golder, M. R.; Young, K.; Suvlu, D.; Shen, Y.; Willard, A. P.; Hore, M. J. A.; Gómez-Bombarelli, R.; Johnson, J. A. Bottlebrush Polymers with Flexible Enantiomeric Side Chains Display Differential Biological Properties. *Nat. Chem.* **2021**, *14*, 85–93.

(181) Zhang, Z.; You, Y. Z.; Wu, D. C.; Hong, C. Y. Syntheses of Sequence-Controlled Polymers via Consecutive Multicomponent Reactions. *Macromolecules* **2015**, *48*, 3414–3421.

(182) Roy, R. K.; Meszynska, A.; Laure, C.; Charles, L.; Verchin, C.; Lutz, J.-F. Design and Synthesis of Digitally Encoded Polymers That Can Be Decoded and Erased. *Nat. Commun.* **2015**, *6*, 7237.

(183) Yang, C.; Wu, K. B.; Deng, Y.; Yuan, J.; Niu, J. Geared Toward Applications: A Perspective on Functional Sequence-Controlled Polymers. *ACS Macro Lett.* **2021**, *10*, 243–257.

(184) Gody, G.; Maschmeyer, T.; Zetterlund, P. B.; Perrier, S. Rapid and Quantitative One-Pot Synthesis of Sequence-Controlled Polymers by Radical Polymerization. *Nat. Commun.* **2013**, *4*, 2505.

(185) Gutekunst, W. R.; Hawker, C. J. A General Approach to Sequence-Controlled Polymers Using Macrocyclic Ring Opening Metathesis Polymerization. *J. Am. Chem. Soc.* **2015**, *137*, 8038–8041.

(186) Zhang, L.; Liu, R.; Lin, S.; Xu, J. PET-RAFT Single Unit Monomer Insertion of β-Methylstyrene Derivatives: RAFT Degradation and Reaction Selectivity. *Chem. Commun.* **2021**, *57*, 10759–10762.

(187) Huang, Z.; Corrigan, N.; Lin, S.; Boyer, C.; Xu, J. Upscaling Single Unit Monomer Insertion to Synthesize Discrete Oligomers. *J. Polym. Sci. A Polym. Chem.* **2019**, *57*, 1947–1955.

(188) Hoff, E. A.; De Hoe, G. X.; Mulvaney, C. M.; Hillmyer, M. A.; Alabi, C. A. Thiol–Ene Networks from Sequence-Defined Polyurethane Macromers. *J. Am. Chem. Soc.* **2020**, *142*, 6729–6736.

(189) Hoshino, Y.; Taniguchi, S.; Takimoto, H.; Akashi, S.; Katakami, S.; Yonamine, Y.; Miura, Y. Homogeneous Oligomeric Ligands Prepared via Radical Polymerization That Recognize and Neutralize a Target Peptide. *Angew. Chem., Int. Ed.* **2020**, *59*, 679–683.

(190) Xu, C.; He, C.; Li, N.; Yang, S.; Du, Y.; Matyjaszewski, K.; Pan, X. Regio- and Sequence-Controlled Conjugated Topological Oligomers and Polymers via Boronate-Tag Assisted Solution-Phase Strategy. *Nat. Commun.* **2021**, *12*, 5853.

(191) Sternhagen, G. L.; Gupta, S.; Zhang, Y.; John, V.; Schneider, G. J.; Zhang, D. Solution Self-Assemblies of Sequence-Defined Ionic Peptoid Block Copolymers. *J. Am. Chem. Soc.* **2018**, *140*, 4100–4109.

(192) Gody, G.; Zetterlund, P. B.; Perrier, S.; Harrisson, S. The Limits of Precision Monomer Placement in Chain Growth Polymerization. *Nat. Commun.* **2016**, *7*, 1–8.

(193) Elling, B. R.; Su, J. K.; Feist, J. D.; Xia, Y. Precise Placement of Single Monomer Units in Living Ring-Opening Metathesis Polymerization. *Chem* **2019**, *5*, 2691–2701.

(194) Foster, J. C.; Damron, J. T.; Zhang, H. Simple Monomers for Precise Polymer Functionalization During Ring-Opening Metathesis Polymerization. *Macromolecules* **2023**, *56*, 7931–7938.

(195) Berthet, M. A.; Zarafshani, Z.; Pfeifer, S.; Lutz, J. F. Facile Synthesis of Functional Periodic Copolymers: A Step toward Polymer-Based Molecular Arrays. *Macromolecules* **2010**, *43*, 44–50.

(196) Zamfir, M.; Lutz, J. F. Ultra-Precise Insertion of Functional Monomers in Chain-Growth Polymerizations. *Nat. Commun.* **2012**, *3*, 1–8.

(197) Benoit, D.; Hawker, C. J.; Huang, E. E.; Lin, Z.; Russell, T. P. One-Step Formation of Functionalized Block Copolymers. *Macromolecules* **2000**, *33*, 1505–1507.

(198) Spick, M. P.; Bingham, N. M.; Li, Y.; de Jesus, J.; Costa, C.; Bailey, M. J.; Roth, P. J. Fully Degradable Thioester-Functional Homo- and Alternating Copolymers Prepared through Thiocarbonyl Addition–Ring-Opening RAFT Radical Polymerization. *Macromolecules* **2020**, *53*, 539–547.

(199) Hill, M. R.; Kubo, T.; Goodrich, S. L.; Figg, C. A.; Sumerlin, B. S. Alternating Radical Ring-Opening Polymerization of Cyclic Ketene Acetals: Access to Tunable and Functional Polyester Copolymers. *Macromolecules* **2018**, *51*, 5079–5084.

(200) Sugihara, S.; Yoshida, A.; Kono, T. aki; Takayama, T.; Maeda, Y. Controlled Radical Homopolymerization of Representative Cationically Polymerizable Vinyl Ethers. *J. Am. Chem. Soc.* **2019**, *141*, 13954–13961.

(201) Aoshima, H.; Uchiyama, M.; Satoh, K.; Kamigaito, M. Interconvertible Living Radical and Cationic Polymerization through Reversible Activation of Dormant Species with Dual Activity. *Angew. Chem., Int. Ed.* **2014**, *53*, 10932–10936.

(202) Gruendling, T.; Kaupp, M.; Blinco, J. P.; Barner-Kowollik, C. Photoinduced Conjugation of Dithioester-and Trithiocarbonate-Functional RAFT Polymers with Alkenes. *Macromolecules* **2011**, *44*, 166–174.

(203) Keddie, D. J. A Guide to the Synthesis of Block Copolymers Using Reversible-Addition Fragmentation Chain Transfer (RAFT) Polymerization. *Chem. Soc. Rev.* 2014, *43*, 496–505.

(204) Chen, M.; MacLeod, M. J.; Johnson, J. A. Visible-Light-Controlled Living Radical Polymerization from a Trithiocarbonate Iniferter Mediated by an Organic Photoredox Catalyst. *ACS Macro Lett.* **2015**, *4*, 566–569.

(205) Otsu, T.; Matsunaga, T.; Kuriyama, A.; Yoshioka, M. Living Radical Polymerization through the Use of Iniferters: Controlled Synthesis of Polymers. *Eur. Polym. J.* **1989**, *25*, 643–650.

(206) Gregg, R. A.; Mayo, F. R. Chain Transfer in the Polymerization of Styrene. II. The Reaction of Styrene with Carbon Tetrachloride 1. *J. Am. Chem. Soc.* **1948**, *70*, 2373–2378.

(207) Kuhn, L. R.; Allegrezza, M. L.; Dougher, N. J.; Konkolewicz, D. Using Kinetic Modeling and Experimental Data to Evaluate Mechanisms in PET-RAFT. *J. Polym. Sci.* **2020**, *58*, 139–144.

(208) Ng, G.; Jung, K.; Li, J.; Wu, C.; Zhang, L.; Boyer, C. Screening RAFT Agents and Photocatalysts to Mediate PET-RAFT Polymerization Using a High Throughput Approach. *Polym. Chem.* **2021**, *12*, 6548–6560.

(209) Sugihara, S.; Kawamoto, Y.; Maeda, Y. Direct Radical Polymerization of Vinyl Ethers: Reversible Addition–Fragmentation Chain Transfer Polymerization of Hydroxy-Functional Vinyl Ethers. *Macromolecules* **2016**, *49*, 1563–1574.

(210) Chiefari, J.; Mayadunne, R. T. A.; Moad, C. L.; Moad, G.; Rizzardo, E.; Postma, A.; Thang, S. H. Thiocarbonylthio Compounds (S=C(Z)S-R) in Free Radical Polymerization with Reversible Addition-Fragmentation Chain Transfer (RAFT Polymerization). Effect of the Activating Group Z. *Macromolecules* **2003**, *36*, 2273–2283.

(211) Skey, J.; O'Reilly, R. K. Facile One Pot Synthesis of a Range of Reversible Addition–Fragmentation Chain Transfer (RAFT) Agents. *Chem. Commun.* **2008**, *35*, 4183.

(212) Tang, C.; Lennon, E. M.; Fredrickson, G. H.; Kramer, E. J.; Hawker, C. J. Evolution of Block Copolymer Lithography to Highly Ordered Square Arrays. *Science* **2008**, *322*, 429–432.

(213) Jeong, S.-J.; Moon, H.-S.; Kim, B. H.; Kim, J. Y.; Yu, J.; Lee, S.; Lee, M. G.; Choi, H.; Kim, S. O. Ultralarge-Area Block Copolymer Lithography Enabled by Disposable Photoresist Prepatterning. *ACS Nano* **2010**, *4*, 5181–5186.

(214) Poelma, J. E.; Ono, K.; Miyajima, D.; Aida, T.; Satoh, K.; Hawker, C. J. Cyclic Block Copolymers for Controlling Feature Sizes in Block Copolymer Lithography. *ACS Nano* **2012**, *6*, 10845–10854.

(215) Yang, S. Y.; Yang, J.-A.; Kim, E.-S.; Jeon, G.; Oh, E. J.; Choi, K. Y.; Hahn, S. K.; Kim, J. K. Single-File Diffusion of Protein Drugs through Cylindrical Nanochannels. *ACS Nano* **2010**, *4*, 3817–3822.

(216) Khorsand, B.; Lapointe, G.; Brett, C.; Oh, J. K. Intracellular Drug Delivery Nanocarriers of Glutathione-Responsive Degradable Block Copolymers Having Pendant Disulfide Linkages. *Biomacromolecules* **2013**, *14*, 2103–2111.

(217) Yang, X.; Grailer, J. J.; Rowland, I. J.; Javadi, A.; Hurley, S. A.; Matson, V. Z.; Steeber, D. A.; Gong, S. Multifunctional Stable and PH-Responsive Polymer Vesicles Formed by Heterofunctional Triblock Copolymer for Targeted Anticancer Drug Delivery and Ultrasensitive MR Imaging. *ACS Nano* **2010**, *4*, 6805–6817.

(218) Sajjad, H.; Tolman, W. B.; Reineke, T. M. Block Copolymer Pressure-Sensitive Adhesives Derived from Fatty Acids and Triacetic Acid Lactone. *ACS Appl. Polym. Mater.* **2020**, *2*, 2719–2728.

(219) Pang, V.; Thompson, Z. J.; Joly, G. D.; Bates, F. S.; Francis, L. F. Adhesion Strength of Block Copolymer Toughened Epoxy on Aluminum. *ACS Appl. Polym. Mater.* **2020**, *2*, 464–474.

(220) Odnoroh, M.; Ivanchenko, O.; Fleury, G.; Guerre, M.; Destarac, M. New Generation of Thermoplastic Elastomers from Narrowly Dispersed All-(Meth)Acrylic ABA Triblock Copolymers Made by RAFT. *Macromolecules* **2024**, *57*, 9565–9575.

(221) Kurowska, I.; Odnoroh, M.; Ivanchenko, O.; Guerre, M.; Destarac, M. Synthesis of High Molar Mass All-(Meth)Acrylic Thermoplastic Elastomers by Photo-Iniferter RAFT Polymerisation. *Polym. Chem.* **2024**, *15*, 4888–4893.

(222) Lu, W.; Goodwin, A.; Wang, Y.; Yin, P.; Wang, W.; Zhu, J.; Wu, T.; Lu, X.; Hu, B.; Hong, K.; Kang, N.-G.; Mays, J. All-Acrylic Superelastomers: Facile Synthesis and Exceptional Mechanical Behavior. *Polym. Chem.* **2018**, *9*, 160–168.

(223) Lu, W.; Wang, Y.; Wang, W.; Cheng, S.; Zhu, J.; Xu, Y.; Hong, K.; Kang, N.-G.; Mays, J. All Acrylic-Based Thermoplastic Elastomers with High Upper Service Temperature and Superior Mechanical Properties. *Polym. Chem.* **2017**, *8*, 5741–5748.

(224) Ivanchenko, O.; Odnoroh, M.; Mallet-Ladeira, S.; Guerre, M.; Mazières, S.; Destarac, M. Azo-Derived Symmetrical Trithiocarbonate for Unprecedented RAFT Control. *J. Am. Chem. Soc.* **2021**, *143*, 20585–20590.

(225) Xiong, M.; Schneiderman, D. K.; Bates, F. S.; Hillmyer, M. A.; Zhang, K. Scalable Production of Mechanically Tunable Block Polymers from Sugar. *Proc. Natl. Acad. Sci.* **2014**, *111*, 8357–8362.

(226) Shanmugam, S.; Boyer, C. Stereo-, Temporal and Chemical Control through Photoactivation of Living Radical Polymerization: Synthesis of Block and Gradient Copolymers. *J. Am. Chem. Soc.* **2015**, *137*, 9988–9999.

(227) Mühlebach, A.; Gaynor, S. G.; Matyjaszewski, K. Synthesis of Amphiphilic Block Copolymers by Atom Transfer Radical Polymerization (ATRP). *Macromolecules* **1998**, *31*, 6046–6052.

(228) Soeriyadi, A. H.; Boyer, C.; Zetterlund, P. B.; Whittaker, M. R. High-Order Multiblock Copolymers via Iterative Cu(0)-Mediated Radical Polymerizations (SET-LRP): Toward Biological Precision. *J. Am. Chem. Soc.* **2011**, *133*, 11128–11131.

(229) Vazaios, A.; Lohse, D. J.; Hadjichristidis, N. Linear and Star Block Copolymers of Styrenic Macromonomers by Anionic Polymerization. *Macromolecules* **2005**, *38*, 5468–5474.

(230) Uchiyama, M.; Ohira, N.; Yamashita, K.; Sagawa, K.; Kamigaito, M. Proton Transfer Anionic Polymerization with C–H Bond as the Dormant Species. *Nat. Chem.* **2024**, *16*, 1630–1637.

(231) Takahata, K.; Aizawa, N.; Nagao, M.; Uchida, S.; Goseki, R.; Ishizone, T. Living Anionic Addition Reaction of 1,1-Diphenylethylene Derivatives: One-Pot Synthesis of ABC-Type Chain-End Sequence-Controlled Polymers. *J. Am. Chem. Soc.* **2021**, *143*, 11296–11301.

(232) Peterson, B. M.; Lin, S.; Fors, B. P. Electrochemically Controlled Cationic Polymerization of Vinyl Ethers. *J. Am. Chem. Soc.* **2018**, *140*, 2076–2079.

(233) Zhou, Y.; Faust, R. Synthesis of Poly(Cyclohexyl Vinyl Ether-b-Isobutylene-b-Cyclohexyl Vinyl Ether) Triblock Copolymer by Living Cationic Sequential Copolymerization. *Polym. Bull.* 2004, *52*, 421–428.

(234) Wan, Y.; He, J.; Zhang, Y. An Arbitrarily Regulated Monomer Sequence in Multi-Block Copolymer Synthesis by Frustrated Lewis Pairs. *Angew. Chem., Int. Ed.* **2023**, *62*, e202218248.

(235) Li, C.; Zhao, W.; He, J.; Zhang, Y.; Zhang, W. Single-Step Expeditious Synthesis of Diblock Copolymers with Different Morphologies by Lewis Pair Polymerization-Induced Self-Assembly. *Angew. Chem., Int. Ed.* **2022**, *61*, e202202448.

(236) Moad, G.; Chiefari, J.; Chong, Y. K.; Krstina, J.; Mayadunne, R. T. A.; Postma, A.; Rizzardo, E.; Thang, S. H. Living Free Radical Polymerization with Reversible Addition – Fragmentation Chain Transfer (the Life of RAFT). *Polym. Int.* **2000**, *49*, 993–1001.

(237) Eagan, J. M.; Xu, J.; Di Girolamo, R.; Thurber, C. M.; Macosko, C. W.; LaPointe, A. M.; Bates, F. S.; Coates, G. W. Combining Polyethylene and Polypropylene: Enhanced Performance with PE/ *i* PP Multiblock Polymers. *Science* **2017**, *355*, 814–816.

(238) Anderson, K. S.; Hillmyer, M. A. The Influence of Block Copolymer Microstructure on the Toughness of Compatibilized Polylactide/Polyethylene Blends. *Polymer* **2004**, *45*, 8809–8823.

(239) Self, J. L.; Zervoudakis, A. J.; Peng, X.; Lenart, W. R.; Macosko, C. W.; Ellison, C. J. Linear, Graft, and Beyond: Multiblock Copolymers as Next-Generation Compatibilizers. *JACS Au* **2022**, *2*, 310–321.

(240) Tomita, S.; Ishihara, S.; Kurita, R. Biomimicry Recognition of Proteins and Cells Using a Small Array of Block Copolymers Appended with Amino Acids and Fluorophores. *ACS Appl. Mater. Interfaces* **2019**, *11*, 6751–6758.

(241) McHale, R.; Patterson, J. P.; Zetterlund, P. B.; O'Reilly, R. K. Biomimetic Radical Polymerization via Cooperative Assembly of Segregating Templates. *Nat. Chem.* **2012**, *4*, 491–497.

(242) Lang, C.; Lloyd, E. C.; Matuszewski, K. E.; Xu, Y.; Ganesan, V.; Huang, R.; Kumar, M.; Hickey, R. J. Nanostructured Block Copolymer Muscles. *Nat. Nanotechnol.* **2022**, *17*, 752–758.

(243) Zhang, J.; Li, T.; Mannion, A. M.; Schneiderman, D. K.; Hillmyer, M. A.; Bates, F. S. Tough and Sustainable Graft Block Copolymer Thermoplastics. *ACS Macro Lett.* **2016**, *5*, 407–412.

(244) Kwak, Y.; Yamamura, Y.; Matyjaszewski, K. ATRP of Styrene and Methyl Methacrylate with Less Efficient Catalysts and with Alkyl Pseudohalides as Initiators/Chain Transfer Agents. *Macromol. Chem. Phys.* **2010**, *211*, 493–500.

(245) De Bon, F.; Lourenço Bernardino, T. J.; Serra, A. C.; Fantin, M.; Matyjaszewski, K.; Jordao Coelho, J. F. Synergistic Radical Taming by Concurrent Degenerative Transfer and Atom Transfer Radical Polymerization in Emulsion. *Macromolecules* **2024**, *57*, 10297–10310.

(246) Wang, Y.; Fantin, M.; Matyjaszewski, K. Electrochemically Mediated Atom Transfer Radical Polymerization with Dithiocarbamates as Alkyl Pseudohalides. *J. Polym. Sci. A Polym. Chem.* **2019**, *57*, 376–381.

(247) Tsarevsky, N. V.; Cooper, B. M.; Wojtyna, O. J.; Jahed, N. M.; Gao, H.; Matyjaszewski, K. *Polym. Prepr. (Am. Chem. Soc. Div. Polym. Chem.).* **2005**, *46*, 249–250.

(248) Mueller, L.; Jakubowski, W.; Matyjaszewski, K.; Pietrasik, J.; Kwiatkowski, P.; Chaladaj, W.; Jurczak, J. Synthesis of High Molecular Weight Polystyrene Using AGET ATRP under High Pressure. *Eur. Polym. J.* **2011**, *47*, 730–734.

(249) Huang, Z.; Chen, J.; Zhang, L.; Cheng, Z.; Zhu, X. ICAR ATRP of Acrylonitrile under Ambient and High Pressure. *Polymers* **2016**, *8*, 59.

(250) Simms, R. W.; Cunningham, M. F. High Molecular Weight Poly(Butyl Methacrylate) by Reverse Atom Transfer Radical Polymerization in Miniemulsion Initiated by a Redox System. *Macromolecules* **2007**, *40*, 860–866.

(251) Bernat, R.; Szczepaniak, G.; Kamiński, K.; Paluch, M.; Matyjaszewski, K.; Maksym, P. Visible-Light-Induced ATRP under High-Pressure: Synthesis of Ultra-High-Molecular-Weight Polymers. *Chem. Commun.* **2024**, *60*, 843–846.

(252) Szczepaniak, G.; Jeong, J.; Kapil, K.; Dadashi-Silab, S.; Yerneni, S. S.; Ratajczyk, P.; Lathwal, S.; Schild, D. J.; Das, S. R.; Matyjaszewski, K. Open-Air Green-Light-Driven ATRP Enabled by Dual Photoredox/Copper Catalysis. *Chem. Sci.* **2022**, *13*, 11540–11550.

(253) Wu, J.; Yang, T.; Wang, K.; Zhang, Q.; Fu, Q. Revealing the Role of Molecular Weight on Mechanical Reinforcement of Highly Oriented UHMWPE Fibers. *Polymer* **2025**, *317*, 127953.

(254) Zhao, B.; Li, J.; Xiu, Y.; Pan, X.; Zhang, Z.; Zhu, J. Xanthate-Based Photoiniferter RAFT Polymerization toward Oxygen-Tolerant and Rapid Living 3D Printing. *Macromolecules* **2022**, *55*, 1620–1628.

(255) Khan, M.; Guimarães, T. R.; Choong, K.; Moad, G.; Perrier, S.; Zetterlund, P. B. RAFT Emulsion Polymerization for (Multi)Block Copolymer Synthesis: Overcoming the Constraints of Monomer Order. *Macromolecules* **2021**, *54*, 736–746.

(256) Bates, F. S.; Hillmyer, M. A.; Lodge, T. P.; Bates, C. M.; Delaney, K. T.; Fredrickson, G. H. Multiblock Polymers: Panacea or Pandora's Box? *Science* **2012**, *336*, 434–440.

(257) Fine, J.; Diri, K.; Krylov, A. I.; Nemirow, C.; Lu, Z.; Wittig, C. Electronic Structure of Tris(2-Phenylpyridine)Iridium: Electronically Excited and Ionized States. *Mol. Phys.* **2012**, *110*, 1849–1862.

(258) Corrigan, N.; Xu, J.; Boyer, C.; Allonas, X. Exploration of the PET-RAFT Initiation Mechanism for Two Commonly Used Photocatalysts. *ChemPhotoChem* **2019**, *3*, 1193–1199.

(259) Junkers, T.; Theis, A.; Buback, M.; Davis, T. P.; Stenzel, M. H.; Vana, P.; Barner-Kowollik, C. Chain Length Dependent Termination in Butyl Acrylate Free-Radical Polymerization Studied via Stationary and Pulsed Laser Initiated RAFT Polymerization. *Macromolecules* **2005**, *38*, 9497–9508.

(260) Kerr, A.; Moriceau, G.; Przybyla, M. A.; Smith, T.; Perrier, S. Bis(Trithiocarbonate) Disulfides: From Chain Transfer Agent Precursors to Iniferter Control Agents in RAFT Polymerization. *Macromolecules* **2021**, *54*, 6649–6661.

(261) Fu, Q.; Xie, K.; McKenzie, T. G.; Qiao, G. G. Trithiocarbonates as Intrinsic Photoredox Catalysts and RAFT Agents for Oxygen Tolerant Controlled Radical Polymerization. *Polym. Chem.* **2017**, *8*, 1519–1526.

(262) Fu, Q.; McKenzie, T. G.; Tan, S.; Nam, E.; Qiao, G. G. Tertiary Amine Catalyzed Photo-Induced Controlled Radical Polymerization of Methacrylates. *Polym. Chem.* **2015**, *6*, 5362–5368.

(263) Nomeir, B.; Fabre, O.; Ferji, K. Effect of Tertiary Amines on the Photoinduced Electron Transfer-Reversible Addition–Fragmentation Chain Transfer (PET-RAFT) Polymerization. *Macromolecules* **2019**, *52*, 6898–6903.

(264) Zou, F.; Mao, Y.; Li, X.; Burger, C.; Hsiao, B. S.; Chen, H.; Marchand, G. R. Effects of Block Architecture on Structure and Mechanical Properties of Olefin Block Copolymers under Uniaxial deformation. *Macromolecules* **2011**, *44*, 3670-3673.

(265) Martin, D. J.; Meijs, G. F.; Renwick, G. M.; Mccarthy, S. J.; Gunatillake, P. A. The Effect of Average Soft Segment Length on Morphology and Properties of a Series of Polyurethane Elastomers. I. Characterization of the Series. *J. Appl. Polym. Sci.* **1996**, *62*, 1377-1386.

(266) Martin, D. J.; Meijs, G. F.; Gunatillake, P. A.; Mccarthy, S. J.; Renwick, G. M. The Effect of Average Soft Segment Length on Morphology and Properties of a Series of Polyurethane Elastomers. II. SAXS-DSC Annealing Study. *J. Appl. Polym. Sci.* **1997**, *64*, 803-817.

(267) Gisselfalt, K.; Helgee, B. Effect of Soft Segment Length and Chain Extender Structure on Phase Separation and Morphology in Poly(urethane urea)s. *Macromol. Mater. Eng.* **2003**, *288*, 265-271.

(268) Chu, B.; Gao, T.; Li, Y.; Desper, C. R.; Byrne, C. A. Microphase Separation Kinetics in Segmented Polyurethanes: Effects of Soft Segment Length and Structure. *Macromolecules* **1992**, *25*, 5724-5729.

(269) Kong, X.; Tan, S.; Yang, X.; Li, G.; Zhou, E.; Ma, D. Isothermal Crystallization Kinetics of PEO in Poly(ethylene terephthalate)-poly(ethylene oxide) Segmented Copolymers. I. Effect of the Soft-Block Length. *J. Polym. Sci. B Polym. Phys.* **2000**, *38*, 3230-3238.

(270) Miller, J. A.; Lin, S. B.; Hwang, K. K. S.; Wu, K. S.; Gibson, P. E.; Cooper, S. L. Properties of Polyether-Polyurethane Block Copolymers: Effects of Hard Segment Length Distribution. *Macromolecules* **1985**, *18*, 32-44.

(271) Versteegen, R. M.; Kleppinger, R.; Sijbesma, R. P.; Meijer, E. W. Properties and Morphology of Segment Copoly(ether urea)s with Uniform Hard Segments. *Macromolecules* **2006**, *39*, 772-783.

(272) Chen, S.; Hu, J.; Liu, Y.; Liem, H.; Zhu, Y.; Liu, Y. Effect of SSL and HSC on Morphology and Properties of PHA Based SMPU Synthesized by Bulk Polymerization Method. *J. Polym. Phys. B. Polym. Phys.* **2007**, *45*, 444-454.

(273) Kong, D.-C.; Yang, M.-H.; Zhang, X.-S.; Du, Z.-C.; Fu, Q.; Gao, X.-Q.; Gong, J.-W. Control of Polymer Properties by Entanglement: A Review. *Macromol. Mater. Eng.* **2021**, *306*, 2100536.

(274) Nunes, R. W.; Martin, J. R.; Johnson, J. F. Influence of Molecular Weight and Molecular Weight Distribution on Mechanical Properties of Polymers. *Polym. Eng. Sci.* **1982**, *22*, 205-228.

(275) Wan, Y.; He, J.; Zhang, Y.; Chen, E. Y. -X. One-Step Synthesis of Lignin-Based Triblock Copolymers as High-Temperature and UV-Blocking Thermoplastic Elastomers. *Angew. Chem., Int. Ed.* 2022, *61*, e202124946.

(276) Ooi, H. W.; Jack, K. S.; Whittaker, A. K.; Peng, H. Photo-Initiated Thiol-Ene "Click" Hydrogels from RAFT-Synthesized Poly(*N*-Isopropylacrylamide). *J. Polym. Sci. A Polym. Chem.* **2013**, *51*, 4626–4636.

(277) Chai, J.-D.; Head-Gordon, M. Long-Range Corrected Hybrid Density Functionals with Damped Atom–Atom Dispersion Corrections. *Phys. Chem. Chem. Phys.* **2008**, *10*, 6615.

(278) Frisch, M. J.; Trucks, G. W.; Schlegel, H. B.; Scuseria, G. E.; Robb, M. A.; Cheeseman, J. R.; Scalmani, G.; Barone, V.; Mennuscci, B.; Petersson, G. A. Gaussian 09 Rev. E0.1; Gaussian Inc: Wallingford, CT, 2009.

(279) Marenich, A. V.; Cramer, C. J.; Truhlar, D. G. Universal Solvation Model Based on Solute Electron Density and on a Continuum Model of the Solvent Defined by the Bulk Dielectric Constant and Atomic Surface Tensions. *J. Phys. Chem. B* **2009**, *113*, 6378–6396.

(280) Capets, J. A.; Yost, S. F.; Vogt, B. D.; Pester, C. W. Rapid Self-Healing of Robust Surface-Tethered Covalent Adaptable Coatings. *Adv. Funct. Mater.* **2024**, *34*, 2406277.

(281) Lee, S.; Park, J.; Ma, H.; Kim, W.; Song, Y. K.; Lee, D. W.; Noh, S. M.; Yoon, S.-J.; Yang, C. Multifunctional Acrylic Polymers with Enhanced Adhesive Property Serving as Excellent Edge Encapsulant for Stable Optoelectronic Devices. *ACS Appl. Mater. Interfaces* **2024**, *16*, 5138–5148.

(282) Krys, P.; Ribelli, T. G.; Matyjaszewski, K.; Gennaro, A. Relation between Overall Rate of ATRP and Rates of Activation of Dormant Species. *Macromolecules* **2016**, *49*, 2467–2476.

(283) Tang, W.; Matyjaszewski, K. Effects of Initiator Structure on Activation Rate Constants in ATRP. *Macromolecules* **2007**, *40*, 1858–1863.

(284) Seeliger, F.; Matyjaszewski, K. Temperature Effect on Activation Rate Constants in ATRP: New Mechanistic Insights into the Activation Process. *Macromolecules* **2009**, *42*, 6050–6055.

(285) Tang, W.; Matyjaszewski, K. Effect of Ligand Structure on Activation Rate Constants in ATRP. *Macromolecules* **2006**, *39*, 4953–4959.

(286) Matyjaszewski, K.; Nanda, A. K.; Tang, W. Effect of [CuII] on the Rate of Activation in ATRP. *Macromolecules* **2005**, *38*, 2015–2018.

(287) Payne, K. A.; D'hooge, D. R.; Van Steenberge, P. H. M.; Reyniers, M.-F.; Cunningham, M. F.; Hutchinson, R. A.; Marin, G. B. ARGET ATRP of Butyl Methacrylate: Utilizing Kinetic Modeling To Understand Experimental Trends. *Macromolecules* **2013**, *46*, 3828–3840.

(288) Fantin, M.; Isse, A. A.; Gennaro, A.; Matyjaszewski, K. Understanding the Fundamentals of Aqueous ATRP and Defining Conditions for Better Control. *Macromolecules* **2015**, *48*, 6862–6875.

(289) Wang, Y.; Kwak, Y.; Buback, J.; Buback, M.; Matyjaszewski, K. Determination of ATRP Equilibrium Constants under Polymerization Conditions. *ACS Macro Lett.* **2012**, *1*, 1367–1370.

(290) Vana, P.; Davis, T. P.; Barner-Kowollik, C. Kinetic Analysis of Reversible Addition Fragmentation Chain Transfer (RAFT) Polymerizations: Conditions for Inhibition, Retardation, and Optimum Living Polymerization. *Macromol. Theory Simul.* **2002**, *11*, 823–835.

(291) Rizzardo, E.; Chen, M.; Chong, B.; Moad, G.; Skidmore, M.; Thang, S. H. RAFT Polymerization: Adding to the Picture. *Macromol. Symp.* **2007**, *248*, 104–116.

(292) Destarac, M. On the Critical Role of RAFT Agent Design in Reversible Addition-Fragmentation Chain Transfer (RAFT) Polymerization. *Polym. Rev.* **2011**, *51*, 163–187.

(293) Barner-Kowollik, C.; Buback, M.; Charleux, B.; Coote, M. L.; Drache, M.; Fukuda, T.; Goto, A.; Klumperman, B.; Lowe, A. B.; Mcleary, J. B.; Moad, G.; Monteiro, M. J.; Sanderson, R. D.; Tonge, M. P.; Vana, P. Mechanism and Kinetics of Dithiobenzoate-Mediated RAFT Polymerization. I. The Current Situation. *J. Polym. Sci. A Polym. Chem.* **2006**, *44*, 5809–5831.

(294) Moad, G. Mechanism and Kinetics of Dithiobenzoate-Mediated RAFT Polymerization – Status of the Dilemma. *Macromol. Chem. Phys.* **2014**, *215*, 9–26.

(295) Coote, M. L.; Krenske, E. H.; Izgorodina, E. I. Computational Studies of RAFT Polymerization–Mechanistic Insights and Practical Applications. *Macromol. Rapid Commun.* **2006**, *27*, 473–497.

(296) Konkolewicz, D.; Hawkett, B. S.; Gray-Weale, A.; Perrier, S. RAFT Polymerization Kinetics: How Long Are the Cross-terminating Oligomers? *J. Polym. Sci. A Polym. Chem.* **2009**, *47*, 3455–3466.

(297) Kwak, Y.; Goto, A.; Fukuda, T. Rate Retardation in Reversible Addition−Fragmentation Chain Transfer (RAFT) Polymerization: Further Evidence for Cross-Termination Producing 3-Arm Star Chain. *Macromolecules* **2004**, *37*, 1219–1225.

(298) Vana, P.; Davis, T. P.; Barner-Kowollik, C. Easy Access to Chain-Length-Dependent Termination Rate Coefficients Using RAFT Polymerization. *Macromol. Rapid Commun.* **2002**, *23*, 952–956.

(299) Bradford, K. G. E.; Petit, L. M.; Whitfield, R.; Anastasaki, A.; Barner-Kowollik, C.; Konkolewicz, D. Ubiquitous Nature of Rate Retardation in Reversible Addition–

Fragmentation Chain Transfer Polymerization. *J. Am. Chem. Soc.* **2021**, *143*, 17769–17777.

(300) Nwoko, T.; Zhang, B.; Vargo, T.; Junkers, T.; Konkolewicz, D. Temperature Effects in Conventional and RAFT Photopolymerization. *Macromolecules* **2025**, *58*, 488–494.

(301) Rahane, S. B.; Kilbey, S. M.; Metters, A. T. Kinetics of Surface-Initiated Photoiniferter-Mediated Photopolymerization. *Macromolecules* **2005**, *38*, 8202–8210.

(302) Antonopoulou, M.; Truong, N. P.; Egger, T.; Kroeger, A. A.; Coote, M. L.; Anastasaki, A. Acid-Enhanced Photoiniferter Polymerization under Visible Light. *Angew. Chem., Int. Ed.* **2025**, *64*, e202420733.

(303) Bereś, M. A.; Zhang, B.; Junkers, T.; Perrier, S. Kinetic Investigation of Photoiniferter-RAFT Polymerization in Continuous Flow Using Inline NMR Analysis. *Polym. Chem.* **2024**, *15*, 3166–3175.

(304) Allegrezza, M. L.; De Alwis Watuthanthrige, N.; Wang, Y.; Garcia, G. A.; Ren, H.; Konkolewicz, D. Substituent Effects in Iniferter Photopolymerization: Can Bond Homolysis Be Enhanced by Electronics? *Polym. Chem.* **2020**, *11*, 6129–6133.

(305) Wylie, R. A. L.; Jafari, V. F.; Qiao, G. G. Photoiniferter RAFT Accelerated by Ionic Liquids in Organic Solvent Systems. *Macromolecules* **2024**, *57*, 3731–3740.

(306) Hartlieb, M. Photo-Iniferter RAFT Polymerization. *Macromol. Rapid Commun.* **2022**, *43*, 2100514.

(307) Hughes, R. W.; Lott, M. E.; Bowman, J. I.; Sumerlin, B. S. Excitation Dependence in Photoiniferter Polymerization. *ACS Macro Lett.* **2023**, *12*, 14–19.

(308) Tang, X.; Meng, L.; Li, R.; Zhu, S.; Lian, S.; Jia, B.; An, Z. Triplet-Enhanced Photoiniferter Polymerization: Ultrafast, Oxygen-Tolerant, and Biocompatible Synthesis of Well-Defined Polymers Under Visible Light. *Angew. Chem., Int. Ed.* **2025**, e22611.

(309) Fu, C.; Xu, J.; Kokotovic, M.; Boyer, C. One-Pot Synthesis of Block Copolymers by Orthogonal Ring-Opening Polymerization and PET-RAFT Polymerization at Ambient Temperature. *ACS Macro Lett.* **2016**, *5*, 444–449.

(310) Liu, Z.; Liu, X.; Tao, W.; Wei, Z.; Zhang, Y.; Liu, G. Streamlined Synthesis of Sequence-Defined Oligomers and In-Chain Multifunctionalized Polymers via Sequential Dual Monomer Insertion. *Macromolecules* **2025**, *58*, 8205–8216.

(311) Baker, J. G.; Gloriod, J.; Figg, C. A. Leveraging Reactivity to Gain Precise Control over Macromolecular Structures with Photocatalysis in Reversible-Deactivation Radical Polymerizations. *Chem. Sci.* **2025**, *16*, 15298–15309.

(312) Li, Z.; Lian, Q.; Xu, Y.; Zhang, Y.; Zhang, P.; Geng, J. Aggregation-Induced Emission Luminogen Catalyzed Photocontrolled Reversible Addition–Fragmentation Chain Transfer Polymerization in an Aqueous Environment. *Macromolecules* **2022**, *55*, 2904–2910.

(313) McKenzie, T. G.; Costa, L. P. da M.; Fu, Q.; Dunstan, D. E.; Qiao, G. G. Investigation into the Photolytic Stability of RAFT Agents and the Implications for Photopolymerization Reactions. *Polym. Chem.* **2016**, *7*, 4246–4253.

(314) Jazani, A. M.; Yilmaz, G.; Baumer, M.; Sobieski, J.; Bernhard, S.; Matyjaszewski, K. Unraveling the Roles of Amines in Atom Transfer Radical Polymerization in the Dark. *J. Am. Chem. Soc.* **2025**, *147*, 12562-12573.

(315) Nwoko, T.; Nguyen, K.; Saha, N. K.; Barner-Kowollik, C.; Konkolewicz, D. Rate Retardation Trends in RAFT – an Emerging Monomer Classification Tool? *Polym. Chem.* **2024**, *15*, 1052–1061.

(316) Trachsel, L.; Levkovsky, I. O.; Hu, X.; Murata, H.; Matyjaszewski, K. Red Light-Driven, Oxygen-Tolerant RAFT Polymerization Enabled by Methylene Blue. *J. Am. Chem. Soc.* **2025**, *147*, 32096–32109.

(317) Bocos-Bintintan, V.; Ratiu, I. A. Hunting for Toxic Industrial Chemicals: Real-Time Detection of Carbon Disulfide Traces by Means of Ion Mobility Spectrometry. *Toxics* **2020**, *8*, 121.

(318) Gu, Y.; Zhao, J.; Johnson, J. A. Polymer Networks: From Plastics and Gels to Porous Frameworks. *Angew. Chem., Int. Ed.* **2020**, *59*, 5022–5049.

(319) Zeng, L.; Lin, X.; Li, P.; Liu, F.-Q.; Guo, H.; Li, W.-H. Recent Advances of Organogels: From Fabrications and Functions to Applications. *Prog. Org. Coat.* **2021**, *159*, 106417.

(320) Kuzina, M. A.; Kartsev, D. D.; Stratonovich, A. V.; Levkin, P. A. Organogels versus Hydrogels: Advantages, Challenges, and Applications. *Adv. Funct. Mater.* **2023**, *33*, 2301421.

(321) Beemer, D. L.; Wang, W.; Kota, A. K. Durable Gels with Ultra-Low Adhesion to Ice. *J. Mater. Chem. A Mater.* **2016**, *4*, 18253–18258.

(322) Zhuo, Y.; Chen, J.; Xiao, S.; Li, T.; Wang, F.; He, J.; Zhang, Z. Gels as Emerging Anti-Icing Materials: A Mini Review. *Mater. Horiz.* **2021**, *8*, 3266–3280.

(323) Eslami, B.; Irajizad, P.; Jafari, P.; Nazari, M.; Masoudi, A.; Kashyap, V.; Stafslien, S.; Ghasemi, H. Stress-Localized Durable Anti-Biofouling Surfaces. *Soft Matter* **2019**, *15*, 6014–6026.

(324) Scartazzini, R.; Luisi, P. L. Organogels from Lecithins. *J. Phys. Chem.* **1988**, *92*, 829–833.

(325) Chaulagain, B.; Jain, A.; Tiwari, A.; Verma, A.; Jain, S. K. Passive Delivery of Protein Drugs through Transdermal Route. *Artif. Cells Nanomed. Biotechnol.* **2018**, *46*, 472–487.

(326) Kumar, R.; Katare, O. P. Lecithin Organogels as a Potential Phospholipid-Structured System for Topical Drug Delivery: A Review. *AAPS PharmSciTech* **2005**, *6*, 298–310.

(327) Shakeel, A.; Farooq, U.; Gabriele, D.; Marangoni, A. G.; Lupi, F. R. Bigels and Multi-Component Organogels: An Overview from Rheological Perspective. *Food Hydrocoll.* **2021**, *111*, 106190.

(328) Aguilar-Zárate, M.; Macias-Rodriguez, B. A.; Toro-Vazquez, J. F.; Marangoni, A. G. Engineering Rheological Properties of Edible Oleogels with Ethylcellulose and Lecithin. *Carbohydr. Polym.* **2019**, *205*, 98–105.

(329) Achilleos, M.; Legge, T. M.; Perrier, S.; Patrickios, C. S. Poly(Ethylene Glycol)-based Amphiphilic Model Conetworks: Synthesis by RAFT Polymerization and Characterization. *J. Polym. Sci. A Polym. Chem.* **2008**, *46*, 7556–7565.

(330) Krasia, T. C.; Patrickios, C. S. Amphiphilic Polymethacrylate Model Co-Networks: Synthesis by RAFT Radical Polymerization and Characterization of the Swelling Behavior. *Macromolecules* **2006**, *39*, 2467–2473.

(331) Shanmugam, S.; Cuthbert, J.; Flum, J.; Fantin, M.; Boyer, C.; Kowalewski, T.; Matyjaszewski, K. Transformation of Gels *via* Catalyst-Free Selective RAFT Photoactivation. *Polym. Chem.* **2019**, *10*, 2477–2483.

(332) Bagheri, A.; Engel, K. E.; Bainbridge, C. W. A.; Xu, J.; Boyer, C.; Jin, J. 3D Printing of Polymeric Materials Based on Photo-RAFT Polymerization. *Polym. Chem.* **2020**, *11*, 641–647.

(333) Imrie, P.; Diegel, O.; Jin, J. Direct-Ink-Write 3D Printing of "Living" Polymer Hydrogels via Type I Photoinitiated RAFT Polymerization. *Polymer* **2023**, *276*, 125944.

(334) Anderson Bainbridge, C. W.; Hye Lee, C. E.; Broderick, N.; Jin, J. Mechanical Modification of RAFT-Based Living Polymer Networks by Photo-Growth with Crosslinker. *Pure Appl. Chem.* **2023**, *95*, 99–107.

(335) Beziau, A.; Fortney, A.; Fu, L.; Nishiura, C.; Wang, H.; Cuthbert, J.; Gottlieb, E.; Balazs, A. C.; Kowalewski, T.; Matyjaszewski, K. Photoactivated Structurally Tailored and Engineered Macromolecular (STEM) Gels as Precursors for Materials with Spatially Differentiated Mechanical Properties. *Polymer* **2017**, *126*, 224–230.

(336) Lampley, M. W.; Harth, E. Photocontrolled Growth of Cross-Linked Nanonetworks. *ACS Macro Lett.* **2018**, *7*, 745–750.

(337) Cuthbert, J.; Martinez, M. R.; Sun, M.; Flum, J.; Li, L.; Olszewski, M.; Wang, Z.; Kowalewski, T.; Matyjaszewski, K. Non-Tacky Fluorinated and Elastomeric STEM Networks. *Macromol. Rapid Commun.* **2019**, *40*, 1800876.

(338) Corrigan, N.; Jung, K.; Moad, G.; Hawker, C. J.; Matyjaszewski, K.; Boyer, C. Reversible-Deactivation Radical Polymerization (Controlled/Living Radical Polymerization): From Discovery to Materials Design and Applications. *Prog. Polym. Sci.* **2020**, *111*, 101311.

(339) Cuthbert, J.; Wanasinghe, S. V.; Matyjaszewski, K.; Konkolewicz, D. Are RAFT and ATRP Universally Interchangeable Polymerization Methods in Network Formation? *Macromolecules* **2021**, *54*, 8331–8340.

(340) Liu, Q.; Zhang, P.; Qing, A.; Lan, Y.; Lu, M. Poly(N-Isopropylacrylamide) Hydrogels with Improved Shrinking Kinetics by RAFT Polymerization. *Polymer* **2006**, *47*, 2330–2336.

(341) Norisuye, T.; Morinaga, T.; Tran-Cong-Miyata, Q.; Goto, A.; Fukuda, T.; Shibayama, M. Comparison of the Gelation Dynamics for Polystyrenes Prepared by Conventional and Living Radical Polymerizations: A Time-Resolved Dynamic Light Scattering Study. *Polymer* **2005**, *46*, 1982–1994.

(342) Zhou, H.; Johnson, J. A. Photo-controlled Growth of Telechelic Polymers and End-linked Polymer Gels. *Angew. Chem., Int. Ed.* **2013**, *52*, 2235–2238.

(343) Imrie, P.; Jin, J. Mechanical Property Modification of "Living" Networks via PET-RAFT Photopolymerization. *Macromol. Symp.* 2023, *408*, 2100506.

(344) Liu, J.; Miao, J.; Zhao, L.; Liu, Z.; Leng, K.; Xie, W.; Yu, Y. Versatile Bilayer Hydrogel for Wound Dressing through PET-RAFT Polymerization. *Biomacromolecules* **2022**, *23*, 1112–1123.

(345) Wan, D.; Zhou, Q.; Pu, H.; Yang, G. Controlled Radical Polymerization of *N* -vinylcaprolactam Mediated by Xanthate or Dithiocarbamate. *J. Polym. Sci. A Polym. Chem.* **2008**, *46*, 3756–3765.

(346) Weidner, S. M.; Trimpin, S. Mass Spectrometry of Synthetic Polymers. *Anal. Chem.* **2010**, *82*, 4811–4829.

(347) Gies, A. P.; Hercules, D. M.; Ellison, S. T.; Nonidez, W. K. MALDI-TOF MS Study of Poly(*p*-Phenylene Terephthalamide) Fibers. *Macromolecules* **2006**, *39*, 941–947.

(348) Marie, A.; Fournier, F.; Tabet, J. C. Characterization of Synthetic Polymers by MALDI-TOF/MS: Investigation into New Methods of Sample Target Preparation and Consequence on Mass Spectrum Finger Print. *Anal. Chem.* **2000**, *72*, 5106–5114.